Radio-Frequency Spectroscopy of Ultracold Atomic Fermi Gases

by

Andre Schirotzek

Submitted to the Department of Physics
in partial fulfillment of the requirements for the degree of

Doctor of Philosophy

at the

MASSACHUSETTS INSTITUTE OF TECHNOLOGY

February 2010

Author . . . .
Department of Physics
February 8, 2010

Certified by . . . .
Wolfgang Ketterle
John D. MacArthur Professor of Physics
Thesis Supervisor

Certified by . . . .
Martin W. Zwierlein
Assistant Professor of Physics
Thesis Supervisor

Accepted by . . . .
Krishna Rajagopal
Professor of Physics, Associate Department Head for Education

Radio-Frequency Spectroscopy of Ultracold Atomic Fermi Gases

by

Andre Schirotzek

Submitted to the Department of Physics
on February 8, 2010, in partial fulfillment of the
requirements for the degree of
Doctor of Philosophy

Abstract

This thesis presents experiments investigating the phase diagram of ultracold atomic Fermi gases using radio-frequency spectroscopy. The tunability of many experimental parameters including the temperature, the interparticle interaction strength and the relative population of different fermions allows to access very different physical regimes. Radio-frequency spectroscopy has been developed into an ideal tool to probe correlations between particles in these different phases.

In particular, radio-frequency spectroscopy of highly population imbalanced atomic Fermi systems gives access to the impurity problem: A single fermion, or boson, immersed in a sea of fermions constitutes a polaron, which can be described by Landau's Fermi liquid theory. A critical interaction strength can be identified separating the regime of a fermionic polaron and a bosonic polaron. Radio-frequency spectroscopy of the polarized superfluid phase allows an accurate measure of the superfluid gap Δ and allows to identify the importance of Hartree Mean-field energies. Furthermore, it is shown how these different physical regimes are connected.

Thesis Supervisor: Wolfgang Ketterle
Title: John D. MacArthur Professor of Physics

Thesis Supervisor: Martin W. Zwierlein
Title: Assistant Professor of Physics

To Larry...

Acknowledgments

Five years is a long time but it certainly seems short when you are having a good time. And I will miss the cordial, open and driven environment in our hallway. I would like to thank everyone in building 26 for making my PhD a memorable experience I will always look back to with great fondness. A few people I would like to thank in particular:

First and foremost, I want to thank Wolfgang for giving me the opportunity to do research in his lab and for being an inspirational figure throughout the years.

There are not enough words to express my gratitude to Martin for being the best friend, colleague, former room mate, and supervisor one could wish for. I will remember countless nights inside and outside the lab spent discussing physics and more worldly things, appropriate and inappropriate, be it at Bertucci's, in the Student Center or in the bathroom. There are more than a few things I admire and appreciate about Martin: His deep and intuitive understanding of physics, his boundless energy and excitement, his body's ability to trade sleep for coffee for a week or longer, his endearing outbursts of deafening laughter followed by an equally deafening "YEAH!", his ability to outrun frat-boy opponents on the soccer field right after consumption of a large Big-Mac value meal and the fact that you can always count on him when you need him.

I have always had the luck to share the lab with great people - not only are they outstanding physicists but I have always truly enjoyed working with them during every day and many a long night. My recent labmates Ariel and Mark are no exception to this rule and they are possibly the two nicest people on the face of the earth. It has been a pleasure to see Ariel "growing up" to take over BECI in no time. His thorough and critical way of thinking, his understanding and grasp of physics have amazed me more than once. I am also indebted to him for enduring my proclivities to listening to loud metal music as well as wrap- and unwrap music followed by "Wrong!".

I am glad to have had a few months overlap with Mark. Besides being the gentle, caring and thoughtful person that he is, he has already proven to be an integral and productive member of the group. With these two at the helm, I have no doubt that BECI will be a place of excellent spirit and research for the years to come.

The contest for the nicest person would be a close one with my former lab mate Christian. Always smiling, always helpful, always positive and calm. Some my dearest memories at MIT include Christian, Martin and me having the best of times in the middle of the night, working in the lab.

My special thanks go out to my loved and loving girlfriend Paige. I am not sure where she took the patience from to endure the unusual work hours and my passion for working out when I was not in the lab, but I am grateful that she did.

Most of all, I would like to thank my parents who have always believed in me and who have been supportive and patient with me all my life. Without them, I would not be where I am today.

Contents

List of Figures

Chapter 1

Introduction

All particles in nature are fermions. Fermions have half-integer spin and according to the spin-statistics theorem [1, 2] the wavefunction of indistinguishable fermions is antisymmetric with respect to exchange of two particles. The Pauli exclusion principle [3] is a direct result, which states that two identical fermions can not occupy the same quantum state. Therefore, the ground state of fermions consists of particles "stacked up" in momentum space to the Fermi momentum. We will call this ground state a Fermi sea in the following. For all temperatures, the distribution of fermions over energy states is described by Fermi-Dirac statistics.

Bosons are either exchange particles mediating interactions between fermions or composite particles comprised of an even number of fermions and have integer spin. Bosons obey Bose-Einstein statistics and can all occupy the same quantum state. Below a critical temperature, bosons occupy the ground state of the system in large numbers, forming a Bose-Einstein Condensate (BEC) [4].

Fermions and bosons thus exhibit a very different behavior at low temperatures. This immediately raises the question what makes a "composite particle"? To compose a particle, interactions between fermions are required. Physically, it is clear that the energy scale characterizing the interactions must be compared to the kinetic energy of the Fermi sea. If there is a bound state between two fermions whose binding energy is much larger than the kinetic energy, we arrive at the simplest case of stable composite bosons which can subsequently form a BEC. For bound state energies comparable to or lower than the Fermi energy, one expects no such stable composite particles as surrounding fermions can trade places with one of the constituents of the pair. This is a highly correlated state of interacting fermions. The limit of weak attractive interactions compared to the Fermi energy is again well understood and is characterized by the formation of Cooper pairs of fermions [5]. The ground state

is a BCS superfluid, named after the authors of the seminal paper [6] providing a theoretical framework for the understanding of conventional superconductors.

For arbitrary interaction strength, temperature and particle numbers of a two-component fermion system, the phase diagram is still poorly understood on a quantitative and even qualitative level. Here, experimental data is of crucial importance to gain a deeper insight into interacting Fermi systems. Since the experimental realization of Bose-Einstein Condensation in 1995 [7, 8] and degenerate Fermi gases in 1998 [9] the field of ultracold atoms has been developed into a powerful toy model for many-body theories. Experiments with ultracold atoms offer the unique possibility to control almost any parameter of the system at will, including the interaction strength, temperature, density imbalance, dimensionality, disorder, lattice parameters and more. In particular, controlling the interaction strength between fermions allows the experimenter to access the BEC regime of strongly bound diatomic molecules as well as the regime of BCS pairing. The crossover region connecting these two regimes is called the BEC-BCS crossover.

In this thesis, we will summarize experiments with ultracold atomic Fermi gases performed at MIT in the past few years. In particular, the emphasis will be on quantitative studies of the BEC-BCS crossover using radiofrequency spectroscopy. In the remainder of this chapter we will give a brief overview of the experimental efforts in BEC1 at MIT over the past five years. This overview will be followed by a few basics, concepts and tools relevant to experiments with ultracold atomic Fermi gases. Chapter 2 deals with the theoretical and experimental investigation of the phase diagram of interacting fermions. In chapter 3 and 4 we present a quantitative study of two limits of particular interest: The highly imbalanced normal phase allowing access to Fermi liquid properties of the system in its normal state and the moderately imbalanced superfluid region allowing access to the superfluid gap and the Hartree energy. In chapter 5 an ongoing effort will be presented on the extraction of the equation of state of a unitary Fermi gas.

1.1 A Brief History of Time from 2005 to 2010: Ultracold Fermions in BEC1

The field of ultracold atomic Fermi gases has matured considerably over the past five years. When I joined the BEC1 lab in 2005, condensates of bosonic Feshbach molecules comprised of two fermionic atoms had been created [10, 11] a little over a
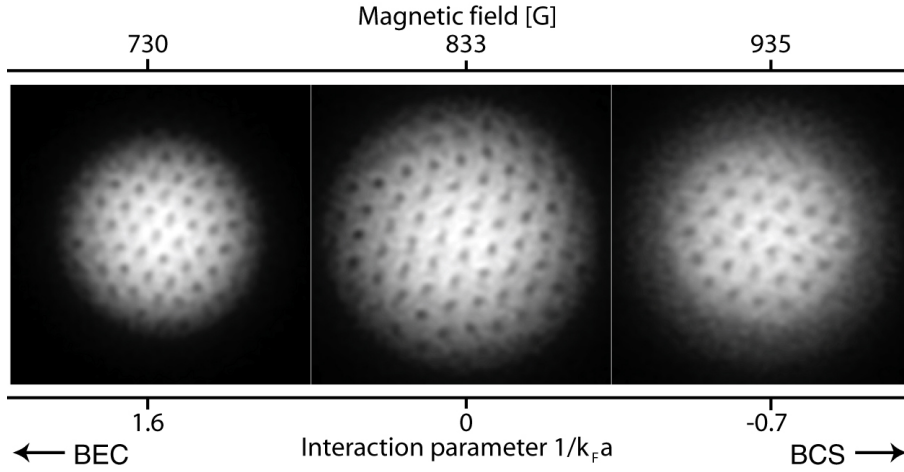
Figure 1-1: The presence of vortex lattices is evidence for superfluidity throughout the BEC-BCS crossover.

year earlier. However, in the unitary limit, where there is no two-body bound state and pairing is a many-body affair, evidence for superfluidity of ultracold fermionic atoms remained elusive. There were several observations consistent with superfluidity [12, 13, 14] but conclusive evidence was only provided by the observation of vortex lattices, see figure 1-1, in our lab in the spring of 2005 [15].
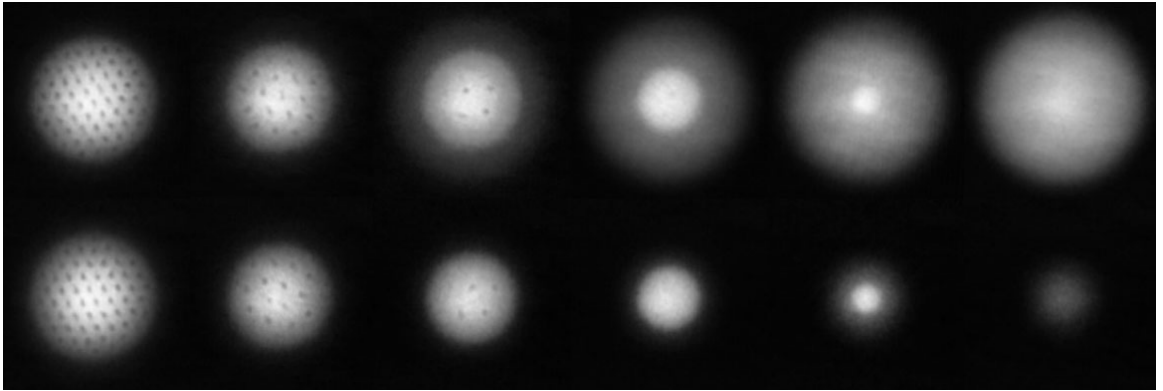
Figure 1-2: The presence of vortex lattices is evidence for superfluidity in imbalanced Fermi mixtures. Superfluidity is stable against number imbalance up to a critical value of 70(5)%. For higher number imbalance, the Fermi mixture is in the normal phase.

Using the presence of vortex lattices as a marker for superfluidity, see figure 1-2, it was possible for the first time to test for superfluidity with unequal numbers of $|\uparrow\rangle$ and $|\downarrow\rangle$ fermions [16], thus opening a door to the new and exciting field of imbalanced Fermi

gases. Exploring the phase diagram of imbalanced Fermi mixtures as a function of interaction strength, density imbalance and temperature was the major task we had set out to accomplish and this would keep us busy for the next five years, still with many questions left to answer today.

Up to this point, much of the information obtained from ultracold atomic Fermi gases relied on two experimental techniques: 1.) The rapid field ramp technique [12], "projecting" fermion pairs onto molecules and 2.) the density distributions were obtained after time-of-flight, meaning the atoms were released from the trapping potential before imaging.

Employing these techniques was necessary to observe resonance superfluidity but it was not entirely clear how they would affect the physics quantitatively and qualitatively.
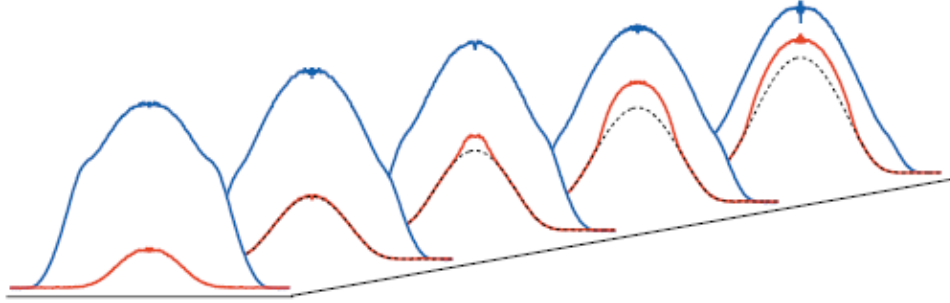
Figure 1-3: Direct observation of superfluidity in the unitary limit. Shown are radially averaged density profiles for the majority component (blue) and minority component (red). The bimodal feature in the minority density profile clearly shows the onset of the formation of a superfluid core.

We subsequently circumvented the "projection method" by preparing a number imbalanced Fermi gas which enabled us to *directly* observe the superfluid phase transition [17]: If the core of the atomic sample is in the superfluid phase at equal density, it is surrounded by unpaired fermions at unequal density. Therefore, the number imbalanced Fermi gas shows a bimodal density distribution, see figure 1-3, similar to a BEC surrounded by a thermal cloud.

Beginning around 2006/2007 we have started concentrating our efforts on quantitative studies of the BEC-BCS crossover using in-situ density distributions and radiofrequency spectroscopy.

Employing phase-contrast imaging allowed us to overcome the "problem" of the high optical density of the trapped atoms and gave us immediate access to the density difference between the two spin states. This way, we were able to demonstrate in-situ
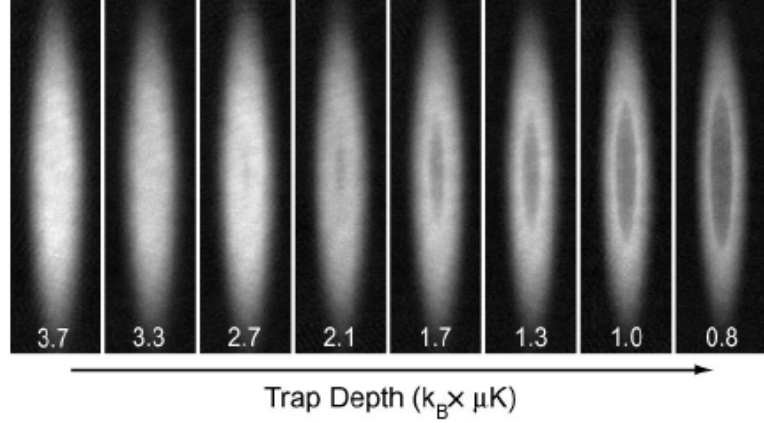
Figure 1-4: Phase separation in a strongly interacting Fermi gas. As the trap depth of the potential, and therefore the temperature, is lowered, excess majority atoms are expelled out of the center of the Fermi mixture. The superfluid core of the sample is characterized by equal densities of majority and minority components. It is surrounded by a density imbalanced Fermi gas in the normal phase.

the phase separation of a number imbalanced Fermi mixture into a superfluid core surrounded by a polarized normal gas [18], see figure 1-4.

This, however, gave us access only to the density difference and not the individual density of each spin state. With the upgrade to a new camera, which allowed us to take two consecutive images separated by only a few tens of μs, we were able to image not only the density difference $n_\uparrow - n_\downarrow$ but a different linear combination of the densities $a\,n_\uparrow - b\,n_\downarrow$ with a second phase contrast image[1]. We were thus able to determine both the majority and the minority density, see figure 1-5. Using the local density approximation and three-dimensional density reconstruction, we were able to map out the phase diagram of the unitary Fermi gas [19] and the zero temperature phase diagram of imbalanced Fermi gases for various interaction strengths in the BEC-BCS crossover. The results will be presented in parts in chapter 2.

At the same time we performed experiments on radiofrequency spectroscopy in BEC1. Our first publication on radiofrequency spectroscopy of highly imbalanced Fermi gases in the normal state in 2007 raised the question of the nature of this normal state: We have observed a spectral gap in the normal phase even at the lowest temperatures achievable in the experiment. Initially, we have interpreted this as

---

[1]In our previous setup this had not been possible due to the heating of the cloud as a result of the first phase contrast image. The typical detuning of 40MHz is not sufficient to suppress absorption of the first imaging pulse. With a sufficiently short delay time between the images, the cloud can be imaged before heating distorts the density profiles.
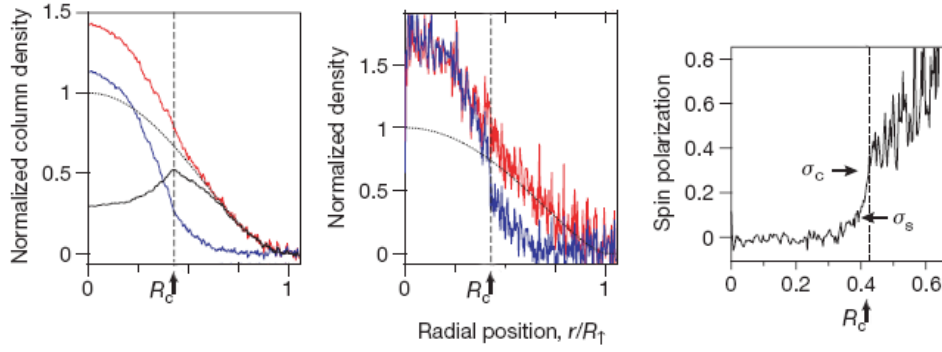
Figure 1-5: In-situ three-dimensional density profiles in the unitary limit at low temperature $T/T_F \simeq 0.03$. The plot on the left shows the radially averaged column density profiles of majority (red) and minority (blue). Also shown are the column density difference profile (solid black) and the non-interacting density profile (dashed black) fit to the wings of the majority density distribution in order to determine the temperature. The center plot shows the three-dimensional density distributions of majority and minority. The plot on the right shows the local density imbalance $\sigma = (n_\uparrow - n_\downarrow)/(n_\uparrow + n_\downarrow)$. R_c denotes the radius of the superfluid core.

evidence for paired fermions which remain in the normal state even at zero temperature [20]. It became clear after experiments performed a year later that, in fact, the spectral gap is a signature of the normal Fermi liquid. This topic will be the subject of chapter 3.

Up to this point, experiments on radiofrequency spectroscopy in ^{6}Li had been plagued by several complications described below in chapter 1.5.1 and in the PhD thesis of my long-time colleague Christian Schunck [21]. In the following years we overcame these problems and developed radiofrequency spectroscopy into a powerful tool for quantitative studies. The first step was the introduction of tomographic radiofrequency spectroscopy [22]: Taking an image immediately after the radiofrequency population transfer and reconstructing the three-dimensional density allowed us to overcome the problem of trap-averaged radiofrequency spectra and to probe the local excitation spectrum. The next improvement was the introduction of a new strongly interacting Fermi mixture, comprised of hyperfine states $|1\rangle$ and $|3\rangle$ of ^{6}Li, see figure 1-10. This overcame the problem of strong final state interactions and furthermore allowed taking spectra of both spin states. This paved the road for quantitative studies using radiofrequency spectroscopy and therefore the most recent results presented in chapters 3 and 4.

Before proceeding to the presentation of our experimental results, a few concepts and their underlying physics will be discussed in the next few sections.

1.2 Feshbach Resonances

Feshbach resonances are now a standard tool in in the field of ultracold atomic physics as they are the mechanism allowing to tune the interaction strength between atoms in different states. For an extensive treatment please refer to [23]. The principle of a Feshbach resonance in the case of ^{6}Li is shown in figure 1-6: Two free neutral atoms in the triplet configuration at a relative kinetic energy of $E \simeq 0$ interacting through the van der Waals potential are coupled to a quasibound state. The singlet and triplet states of the interatomic potential are coupled by the hyperfine interaction $V_{HF} = a_{\text{HF}}(\mathbf{s}_1 \cdot \mathbf{i}_1 + \mathbf{s}_2 \cdot \mathbf{i}_2)$. Since singlet and triplet state have different magnetic moments the energy of the incoming colliding atoms can be tuned with respect to a bound state in the singlet potential. A scattering resonance occurs when the energy of the incoming atoms is resonant with that of the bound state.
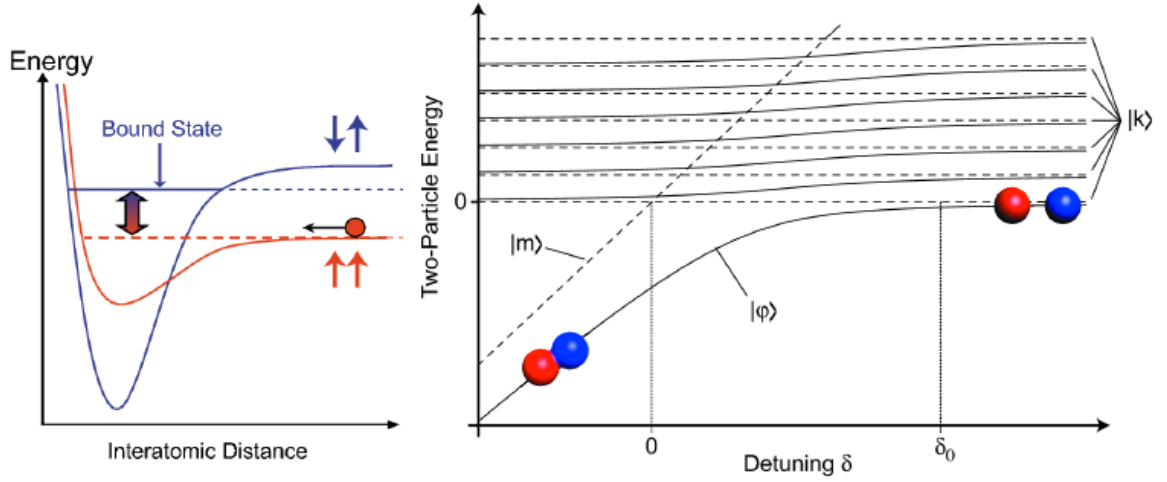
Figure 1-6: a) A Feshbach resonance occurs when the energy of two free atoms is coupled to and resonant with a bound state in the interatomic potential. b) The resulting energy level structure for two particles in a box

The s-wave scattering length, completely characterizing the interactions between atoms at low enough temperatures ($T < 1\text{mK}$), can be shown to diverge and change its sign around a Feshbach resonance. Below the Feshbach resonance, where the interatomic potential supports a bound state[2] of energy $E_{\text{b}} = \frac{\hbar^2}{ma^2}$, the excited states in figure 1-6b) consist of free atoms interacting repulsively, corresponding to a positive scattering length $a > 0$. The metastable ground state consists of molecular dimers

---

[2]The experimentally relevant bound state in the singlet potential is the vibrational state with quantum number $n = 38$.

whose residual interaction depends on four-body physics and can be calculated exactly and is given by $a_{dd} \simeq 1.18a$. Above the Feshbach resonance the interatomic potential does not support a bound state and colliding atoms simply acquire a phase shift in the scattering event given by the usual result $\delta = \arctan(-ka)$ corresponding to attractive interactions between the atoms.

It is important to note that the bound state in the interatomic potential is only populated when the magnetic field is adiabatically ramped from above the Feshbach resonance to below the Feshbach resonance if three-body interactions are suppressed. This is the case if the Franck-Condon factor, quantifying the wavefunction overlap between the incoming free atoms and the bound molecular state, is small enough for the time scale of three-body relaxation to be longer than other relevant time scales of the experiment, like the inverse Fermi energy $\hbar/\epsilon_F$. Therefore, a sample prepared below the Feshbach resonance represents a repulsive Fermi gas. This has important implications for the experiments presented in this thesis and has been used recently in search for ferromagnetic states in ultracold Fermi gases [24].

It is insightful to compare the above model of a Feshbach resonance to the more familiar case of a discrete state coupled to a continuum, e.g. an atom in an excited electronic state. A simple model has been presented in [25] based on a discrete state coupled to an unbounded continuum ($-\infty < E_{\text{cont}} < \infty$) of scattering states. Let us now remove the unphysical restriction of the absence of a lower bound for the free wave states. The resulting energy level structure corresponds the above single-channel model for a Feshbach resonance once the bound state energy E_{b} crosses the lower bound $E_{\text{kin}} = 0$ to negative energies.

Before proceeding to the mean-field treatment of a many-body system, whose interactions can be tuned through the strongly interacting regime, let us review a simple toy model capturing many qualitative features of the many-body treatment [26]: A particle interacting with a δ-potential characterized by the scattering length a, into which Pauli blocking effects are incorporated by confining it to a spherical box of the size of the interparticle spacing, see figure 1-7.

One of the important features that can be reproduced is the existence of an excitation gap between the ground state and the excited states above the Feshbach resonance, where pairing is a many-body effect. This model also demonstrates that there is a smooth crossover between the different physical regimes in spite of the diverging scattering length around the Feshbach resonance.
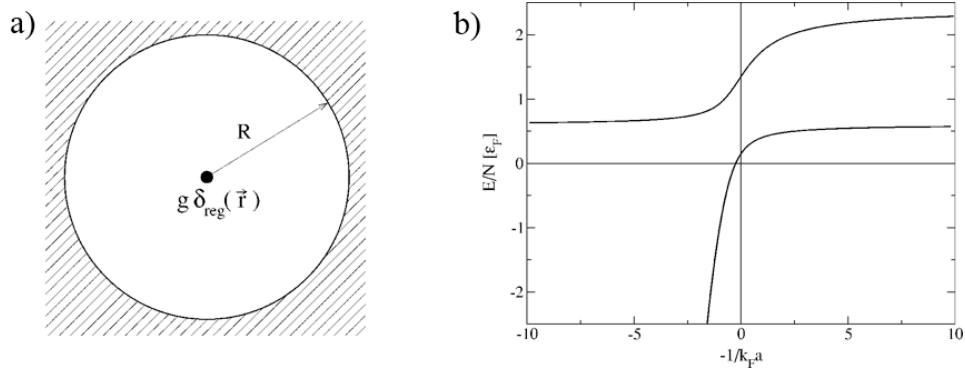
Figure 1-7: a) Toy model of a Fermi mixture with tunable interactions $1/k_\mathrm{F}a$: The interaction strength is characterized by the pseudo-potential $V(r) = 4\pi\hbar^2 a/m\delta_\mathrm{reg}$ and Pauli blocking is mimicked by choosing a box of the size of the interparticle spacing R. b) Many qualitative features of the many-body treatment can be reproduced. Taken from [26]

1.3 BEC-BCS Crossover: A Mean-Field Description

The tunability of the interaction strength by simply changing the external magnetic field gives ultracold atomic physics a unique advantage over condensed matter experiments. Let us consider a many-body system comprised of two fermionic species, $|\uparrow\rangle$ and $|\downarrow\rangle$. Without interactions, the momentum distributions are simply given by $\Theta(k = k_\mathrm{F})$, with the Fermi momentum k_F.

For small positive interactions, corresponding to $a < 0$, there is no bound state in the interatomic potential but the presence of the Fermi sea results in Cooper pairing [5], a many-body bound state. It was shown that the ground state of this system is not a Fermi Liquid, see chapter 3, but a Superfluid described by the famous BCS-wavefunction, named after the authors of their seminal paper [6], Bardeen, Cooper and Schrieffer. A simple picture for the effect of the presence of the Fermi seas is a restriction of phase space available for particles above the Fermi surface to scatter into. The Fermi sea makes this essentially a two-dimensional system[3], in which a bound state exists for arbitrarily small interactions.

For a deeply bound molecular state with small residual repulsive interactions, corresponding to $a > 0$, the system is comprised of composite bosons. The ground state is a Bose-Einstein condensate (BEC) of dimers and can be described by the

---

[3]The naïve picture does not hold for N-dimensional space. The figure of merit is a constant density of states and *not* the restriction of the phase space to $N - 1$ dimensions.

BEC mean-field description.

A mean-field description of the entire BEC-BCS crossover regime, including the strongly interacting regime $|a| \to \infty$, based on [27, 28] can be found in [23]. Here we will review a few of the results. The generalized BCS-wavefunction takes the same form as in the limit $a \to 0^-$:

$$|\psi_{\text{BCS}}\rangle = \prod_{\mathbf{k}} (u_k + v_k c^\dagger_{\mathbf{k}\uparrow} c^\dagger_{\mathbf{-k}\downarrow})|0\rangle \qquad (1.1)$$

where the u_k, v_k are variational parameters obeying the normalization condition $|u_k|^2 + |v_k|^2 = 1$ and the $c^\dagger_{\mathbf{k}\sigma}$ are the creation operators for a particle in spin state σ.
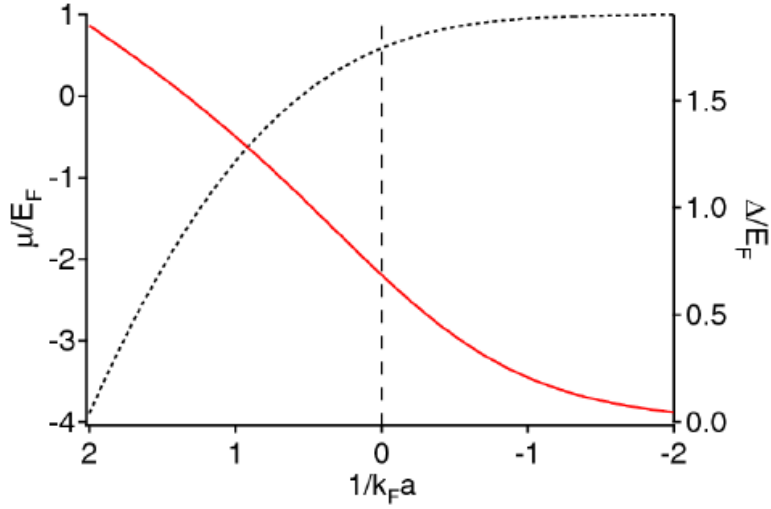
Figure 1-8: Chemical potential μ (black dashed) and the superfluid gap Δ (red) as a function of interaction strength in the BEC-BCS crossover regime in a mean-field description based on the seminal work of Nozières Schmitt-Rink [28].

We use the Hamiltonian

$$
\begin{aligned}
H &= \sum_{\mathbf{k},\sigma} \epsilon_{\mathbf{k}} c^\dagger_{\mathbf{k}\sigma} c_{\mathbf{k}\sigma} + \frac{V_0}{V} \sum_{\mathbf{k},\mathbf{k}',\mathbf{q}} c^\dagger_{\mathbf{k}+\frac{\mathbf{q}}{2}\uparrow} c^\dagger_{-\mathbf{k}+\frac{\mathbf{q}}{2}\downarrow} c_{\mathbf{k}'+\frac{\mathbf{q}}{2}\downarrow} c_{-\mathbf{k}'+\frac{\mathbf{q}}{2}\uparrow} \\
&\to \sum_{\mathbf{k},\sigma} \epsilon_{\mathbf{k}} c^\dagger_{\mathbf{k}\sigma} c_{\mathbf{k}\sigma} + \frac{V_0}{V} \sum_{\mathbf{k},\mathbf{k}'} c^\dagger_{\mathbf{k}\uparrow} c^\dagger_{-\mathbf{k}\downarrow} c_{\mathbf{k}'\downarrow} c_{-\mathbf{k}'\uparrow} \qquad (1.2)
\end{aligned}
$$

where V_0 is a measure of the interaction strength between the particles, V is the volume of the system. The second row represents the standard BCS approximation in which only terms of $\mathbf{q} = 0$ are retained in the interaction, thereby neglecting finite

momentum Cooper pairs[4]

The energy can be minimized under variation of $E - \mu N$ with respect to u_k, v_k. The results are:

$$u_k^2 = \frac{1}{2}\left(1 + \frac{\xi_k}{E_k}\right) \tag{1.3}$$

$$v_k^2 = \frac{1}{2}\left(1 - \frac{\xi_k}{E_k}\right) \tag{1.4}$$

$$\tag{1.5}$$
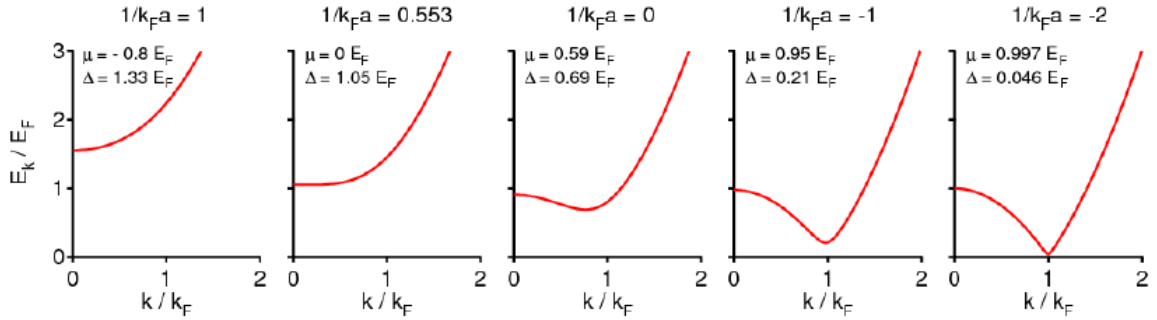
Figure 1-9: Quasiparticle excitation spectrum $E_k = \sqrt{\xi_k^2 + \Delta^2}$ for various interaction strengths in a mean-field description. A qualitative change can be observed at $1/k_{\mathrm{F}}a = 0.553$.

Physically, v_k^2 represents the momentum distribution of particles and u_k^2 represents the distribution of holes. Here we have defined the kinetic energy $\xi_k = \epsilon_k - \mu$ with respect to the chemical potential μ and the quasiparticle excitation energy $E_k = \sqrt{\xi_k^2 + \Delta^2}$, Δ being the superfluid gap. The above equations are identical to the usual BCS result, the difference for atomic gases with arbitrary interactions strength being that the chemical potential *and* the superfluid gap have to be solved self-consistently as a function of interaction strength $1/k_{\mathrm{F}}a$:

$$-\frac{1}{V_0} = \int \frac{d^3k}{(2\pi)^3}\frac{1}{2E_k} \tag{1.6}$$

$$n = 2\int \frac{d^3k}{(2\pi)^3}v_k^2 \tag{1.7}$$

The results for μ and Δ are plotted in figure 1-8.

---

[4]This is a severe approximation with important results. See discussion below and in chpater 4.1.

The resulting quasiparticle excitation spectrum is shown in figure 1-9

Although the above picture provides valuable qualitative insight, the results have been shown to be quantitatively inaccurate: a) In the deep BEC limit the residual interaction between molecules, characterized by the dimer-dimer scattering length can be shown to be $a_{dd} = 2a$, differing from the exact result [29] $a_{dd} \simeq 0.6a$. b) Even in the BCS limit, the mean-field result overestimates of the superfluid gap by a factor of $\sim$ 2.2 - see discussion in 4.1. The reason for both of the above discrepancies is the reduction of the Hamiltonian 1.2 by setting $q = 0$. The same inaccuracy can be observed in the unitary limit: c) The chemical potential in the unitary limit in the mean-field treatment is $\mu \simeq 0.59\epsilon_F$, while it has been shown theoretically to range between $0.32\epsilon_F$ and $0.45\epsilon_F$ [30, 31, 32, 33, 34, 35, 36, 37] and experimentally to range between $0.32\epsilon_F$ and $0.51\epsilon_F$ [38, 39, 14, 40]. c) The superfluid gap is $\Delta \simeq 0.69\epsilon_F$ in the above mean-field theory and has been theoretically predicted to be on the order of $0.45\epsilon_F - 0.54\epsilon_F$ [41, 42]. An experimental determination of the gap using momentum-resolved radiofrequency spectroscopy has found $\Delta \simeq 0.8\epsilon_F$ close to the critical temperature [43]. In chapter 4 we will use radiofrequency spectroscopy of Fermi systems characterized by a small density imbalance between $|\uparrow\rangle$ and $|\downarrow\rangle$ to determine the superfluid gap to be $\Delta \simeq 0.44\epsilon_F$ [44]. d) Another point of quantitative interest is the critical interaction at which the character of the system changes from fermionic to bosonic. This should be related to the position of the minimum in the quasiparticle dispersion, figure 1-9. For interactions stronger than $1/k_F a = 0.553$, the lowest single-particle excitation energy is at finite momentum $k > 0$ and costs an energy Δ, whereas for weaker interactions the lowest excitation energy is at $k = 0$ at an energy of $\sqrt{\Delta^2 + \mu^2}$. The interaction strength at which this transition happens is the one at which the chemical potential μ is zero, see definition for E_k. The critical interaction strength determining the change of character from fermionic to bosonic will be discussed in more detail in chapter 3.

We will discuss the approximations made in the above treatment and its shortcomings in chapter 4, in which we present a determination of the superfluid gap in the unitary regime using radiofrequency spectroscopy.

1.4   Experiment

The experimental setup and production of a strongly interacting degenerate gas of ^{6}Li has been described in detail in [45, 23]. Here, we will only briefly review the procedure: An atomic beam is created in an oven containing ^{23}Na, a boson, and ^{6}Li,

a fermion. After a Zeeman slowing stage, $\sim 10^{10}$ ^{23}Na atoms and $\sim 10^9$ ^{6}Li atoms are loaded into a dual species Magneto-Optical Trap (MOT) for a typically one second. After optically pumping ^{23}Na and ^{6}Li into their respective stretched states in order to avoid spin exchange collisions and for their magnetic trapping properties, the atoms are loaded into a magnetic trap of the Ioffe-Pritchard type. Both ^{23}Na and ^{6}Li are subsequently evaporated within 20s using microwave/radiofrequency radiation. At this point the ^{6}Li atoms are typically in the quantum degenerate regime at a temperature of $T \simeq 0.3T_F$ with typically a few 10^7 ^{6}Li atoms and no ^{23}Na atoms left. The ^{6}Li atoms are subsequently loaded into an optical dipole trap (ODT) with a waist size of $\sim 70\mu$m and an power of a few Watts, resulting in a typical trap depth of a few ten μK. Next the magnetic field is ramped up to around 690G within 2s, where there is a Feshbach resonance between the hyperfine states $|1\rangle$ and $|3\rangle$[5]. Here a spin mixture of the states $|1\rangle$ and $|3\rangle$ of variable number imbalance is created using a Landau-Zener sweep. For the experiments on radiofrequency spectroscopy presented in this thesis, the $|1\rangle$-$|3\rangle$ mixture is preferred over the $|1\rangle$-$|2\rangle$ mixture because the final state interactions are weak and can easily be accounted for [46]. Next the power of the ODT is ramped down for evaporative cooling in 4s to a typical trap depth of a few μK. For the experiments presented in this thesis the typical atom number for highly imbalanced samples is $5 \cdot 10^6$ at a temperature of $T \simeq 0.15T_F$ and for the balanced or moderately imbalanced samples $1 \cdot 10^7$ at a temperature of $T \simeq 0.05T_F$.

1.5 Radiofrequency Spectroscopy: An Overview

1.5.1 A Little Bit of History

Radiofrequency spectroscopy has been experimentally realized on trapped cold neutral atoms for the first time a little over 20 years ago [47], from which the authors were able to deduce the temperature. Subsequently, forced evaporative cooling of neutral atoms using radiofrequency has been suggested [48, 49]. This was a crucial step to in order to increase phase space density [50, 51] and eventually made the realization of Bose-Einstein condensation possible [7, 8]. Radiofrequency induced transitions have also been used as an output coupler in order to create the first atom Laser [52] and to create spinor condensates [53, 54].

In the years following, radiofrequency spectroscopy has developed into a powerful

---

[5]We have realized strongly interacting superfluid Fermi gases in other combinations of hyperfine states [46]: There is the much employed Feshbach resonance between states $|1\rangle$ and $|2\rangle$ at 834G, and also the $|2\rangle$-$|3\rangle$ Feshbach resonance at 810G

tool to study single-particle excitations in degenerate quantum gases. The first density dependent radiofrequency spectrum has been observed in Bose-Einstein condensates [55, 56], a clear signature of a mean-field shift due to interactions between the atoms.

With the advent of mixtures of degenerate Fermi gases [57, 58, 59, 60, 61, 62] radiofrequency spectroscopy has been used to study a variety of aspects of this new system: In the first radiofrequency spectroscopy experiments performed at JILA [63] and at MIT [64] the scattering length around a Feshbach resonance has been determined by an observation of the mean-field shift and was shown to switch sign around the Feshbach resonance. The authors of [64] also found an absence of the mean-field shift in a two-level system, in spite of the strong interactions between the atoms induced by a Feshbach resonance. This can be shown to be a direct consequence of the asymmetry of the fermionic wavefunction [65]. In the same year, the JILA group has verified the creation of molecules consisting of two fermions below the Feshbach resonance [10] using radiofrequency dissociation spectra. The binding energy was shown to closely follow $E_\mathrm{b} = \frac{\hbar^2}{ma^2}$. In 2004, the Innsbruck group [13] observed bimodal radiofrequency spectra throughout the entire BEC-BCS crossover, see chapter 1.3: At low enough temperatures a second peak appeared in the radiofrequency spectra. This was interpreted as evidence for pairing and superfluidity throughout the BEC-BCS crossover. Three years later, after the experimental realization of number imbalanced mixtures of Fermi gases [16, 40], it was found that the minority component in a highly imbalanced normal mixture also shows a gap in the excitation spectrum [20]. This spectral gap was initially interpreted as a signature of pairing of fermions in the imbalanced ground state.

At this time, a few shortcomings of standard radiofrequency spectroscopy became obvious. Up to this point spectra were obtained by radiofrequency transfer to a third state and subsequent time-of-flight for an accurate measure of the transferred atom number. Quantitative, and even qualitative, interpretation of the spectra was difficult due a variety of factors (for a detailed discussion see [21]), which have all been overcome by our group in the past few years:

1. **Problem**: Inhomogeneous trapping potential. Since many-body effects depend on the density, the spatially varying density yields a spatially varying gap Δ, mean-field shift, interaction strength $1/k_\mathrm{F}a$ and normalized temperature T/T_F. Even separate phases can exist within the trap [18].

   Solution: We have performed spatially resolved radiofrequency spectroscopy [22]. Immediately after the radiofrequency pulse an absorption image of the

final state is taken, projecting the three-dimensional density distribution onto a two-dimensional image. The three-dimensional density distribution can be obtained using the Inverse Abel Transform[6][66]. The resulting spectra represent the response of a homogeneous system in the local density approximation.

2. **Problem**: Strong final state interactions alter radiofrequency spectra qualitatively and quantitatively. If the atoms in the final state are non-interacting, or at least weakly interacting, the spectrum shows the typical dissociative shape $I(\omega \propto \frac{\sqrt{\omega - \omega_{th}}}{\omega^2})$, see 1.5.2. If the final state is also strongly interacting, the line shape is altered. Furthermore, bound-bound transitions [46, 67] appear.

   Solution: We have a created a degenerate fermion mixture using the hyperfine states $|1\rangle$ and $|3\rangle$. State $|2\rangle$ is only weakly interacting with both states $|1\rangle$ and $|3\rangle$. The local spectra can be used to determine the pair size of fermion pairs in the unitary regime [46, 21].

3. **Problem**: Hartree energy: Mean-field shifts usually neglected in interpretations can shift radiofrequency spectra. These are difficult to predict theoretically in the strongly interacting regime.

   Solution: Hartree terms can be identified and quantified in radiofrequency spectra of imbalanced mixtures. This is discussed in chapter 4.

4. **Problem**: Absence of majority spectra: The qualitative and quantitative interpretation of the minority spectra requires comparison to the majority spectra.

   Solution: The use of $|1\rangle$-$|3\rangle$ mixtures has the additional advantage of allowing us to perform spectroscopy on both majority and minority components of the mixture using state $|2\rangle$ as the final state. In previous experiments, obtaining radiofrequency spectra from both states $|1\rangle$ and $|3\rangle$ would have required a two-photon transition from state $|1\rangle$ to state $|3\rangle$.

Recently, momentum resolved radiofrequency spectroscopy has been performed at JILA [43] allowing to extract information about the spectral function of strongly interacting fermions, see also 3.3.2.

---

[6]The inverse Abel transform is given by $f(x, z) = -\frac{1}{\pi} \int_x^\infty dy \frac{\frac{dn_{2D}(y,z)}{dy}}{\sqrt{y^2 - x^2}}$, where $n_{2D}(y, z)$ is the column density measured in a typical experiment

1.5.2 A Little Bit of Theory

Radiofrequency is broadly defined as electromagnetic radiation in the frequency range from 300Hz to 3GHz[7]. Since the ^{6}Li $|1\rangle$-$|3\rangle$ Feshbach resonance is located at a magnetic field of 690G and the hyperfine constant for ^{6}Li is $a_{\mathrm{HF}} \sim 152$MHz, typical transition frequencies in our experiments are around 80MHz, corresponding to a wavelength of $3-4$m. As a consequence the momentum of the radiofrequency photon is negligible compared to the recoil of the atom. Another consequence is that radiofrequency transitions are typically magnetic dipole transitions - they act as a spin-flip operator[8].
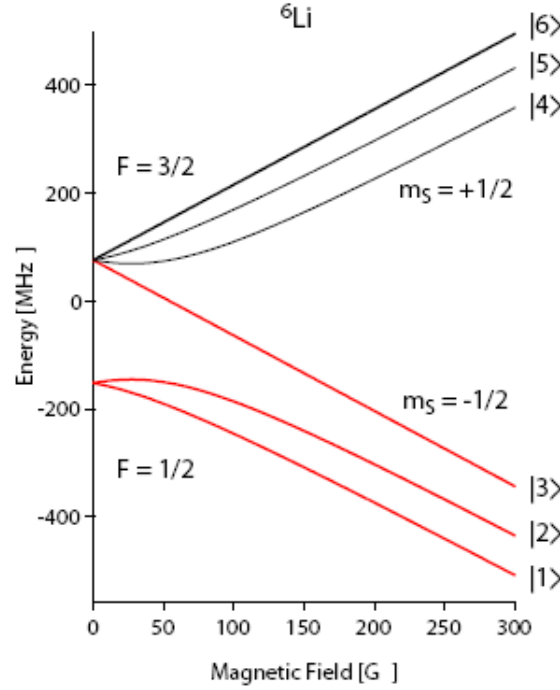
Figure 1-10: Energy level structure of ^{6}Li as a function of magnetic field. The relatively small hyperfine constant $a_{\mathrm{HF}} \simeq 152$MHz results in a small splitting between the ground states with $F = 3/2$ and $F = 1/2$ of $3/2\, a_{\mathrm{HF}} \simeq 228$MHz and in entering the Paschen-Back region at relatively low field (state $|2\rangle$ has a maximum at ~ 27G). However, the admixture of the upper hyperfine levels is still large enough to ensure efficient radiofrequency transfer, see text.

Looking at the energy level structure in figure 1-10 of ^{6}Li, one might be tempted to assume that the magnetic field around 690G would bring ^{6}Li deep into the Paschen-Back regime and that the radiofrequency radiation flips the nuclear spin. However,

---

[7]Wikipedia entry: http://en.wikipedia.org/wiki/Radio_spectrum

[8]There are, however, electric dipole transitions in the radiofrequency range, e.g. The $^2S_{1/2}$ to $^2P_{1/2}$ transition at a frequency of 1000MHz in hydrogen.

using perturbation theory it can be shown that the hyperfine interaction $V = a_{\mathrm{HF}} \mathbf{S} \cdot \mathbf{I}$ results in an admixture to the wavefunction[9] of the upper manifold $m_s = 1/2$ into the lower manifold $m_s = -1/2$, containing the experimentally relevant states $|1\rangle$ and $|2\rangle$, on the order of ten percent. Since the magnetic moment of the nucleus is a few thousand times smaller than that of the electron, the transitions are mostly due to electronic spin-flip. This raises the question whether, for the same radiofrequency power, a $|1\rangle$-$|2\rangle$ transition will have a matrix-element similar to the $|3\rangle$-$|2\rangle$ transition. Using the Breit-Rabi formula [68] it can be shown that the matrix elements, and hence Rabi frequencies $\Omega_{\mathrm{R}} = \mu \cdot \mathbf{B}/\hbar$, are equal to within a few percent ($\Omega_{\mathrm{R}}^{|1\rangle \to |2\rangle}/\Omega_{\mathrm{R}}^{|3\rangle \to |2\rangle} \simeq 0.94$). Using fully spin-polarized atomic samples we were able to confirm the close agreement of the Rabi frequencies experimentally by directly measuring the Rabi frequency of spin transfer. This point is of importance for both experiments presented in chapters 3 and 4.

1.5.3 Radiofrequency Spectroscopy on the Microscopic Level

After establishing the nature of radiofrequency spectroscopy as a spin-flip operator, one can immediately define the corresponding interaction operator:

$$
\begin{aligned}
V_{\mathrm{rf}} &= 2\pi\hbar\Omega_{\mathrm{R}}^2 \sum_{\mathbf{k}} \left(c_{\mathbf{k}3}^{\dagger} c_{\mathbf{k}\uparrow} + c_{\mathbf{k}\uparrow}^{\dagger} c_{\mathbf{k}3} \right) \\
&\to 2\pi\hbar\Omega_{\mathrm{R}}^2 \sum_{\mathbf{k}} c_{\mathbf{k}3}^{\dagger} c_{\mathbf{k}\uparrow}
\end{aligned}
\tag{1.9}
$$

where Ω_{R} is the Rabi frequency, $c_{\mathbf{k}2}^{\dagger}$ is the creation operator for a free particle in the final state and $c_{\mathbf{k}\uparrow}$ the annihilation operator for a single particle in the initial state. The second line holds if the final state is empty, which is the case in a typical exper-

---

[9]In first order perturbation theory, the admixture to state $|1\rangle$ (good quantum numbers: $m_s = -1/2, m_I = +1$) is given by

$$
\begin{aligned}
|n^{(1)}\rangle &= a_{HF} \sum_{k \neq n} \frac{\langle k^{(0)}| \mathbf{S} \cdot \mathbf{I} |n^{(0)}\rangle}{E_n^{(0)} - E_k^{(0)}} |k^{(0)}\rangle \\
&= a_{HF} \frac{\langle \frac{1}{2}, \frac{1}{2}, 1, 0| S_+ I_- |\frac{1}{2}, -\frac{1}{2}, 1, 1\rangle}{2\mu_B B} |\frac{1}{2}, \frac{1}{2}, 1, 0\rangle
\end{aligned}
\tag{1.8}
$$

where we have used $\mathbf{S} \cdot \mathbf{I} = S_z I_z - S_+ I_- - S_- I_+$ and only kept the relevant states in the second equality. Therefore, the admixture is $\frac{\sqrt{2} a_{HF}}{2\mu_B \mathbf{B}} \simeq 0.1$

iment[10]. From equation 1.9 it can be seen that the radiofrequency operator probes the single-particle excitation spectrum: One particle is removed from its environment and the energy cost, including interaction and kinetic energy, is provided by the radiofrequency photon: $\hbar\omega_{\mathrm{RF}} \equiv E_k + \epsilon_k - \mu$. Using the generalized BCS-wavefunction $|\psi_{\mathrm{BCS}}\rangle$, see section 1.3, and Fermi's Golden Rule one can calculate the radiofrequency spectrum in linear response [23]:

$$I(\omega) = \frac{2\pi}{\hbar} \sum_f |\langle f|V_{\mathrm{rf}}|\psi_{\mathrm{BCS}}\rangle|^2 \delta(\hbar\omega - E_f) \tag{1.10}$$

which can be written as [23]:

$$I(\omega) \propto \frac{\sqrt{\omega - \omega_{\mathrm{th}}}}{\omega^2} \sqrt{1 + \frac{\omega_{\mathrm{th}}}{\omega} + \frac{\mu}{\hbar\omega}} \tag{1.11}$$

with μ the chemical potential of the generalized BCS state and the definition for the threshold frequency $\omega_{\mathrm{th}} \equiv \sqrt{\mu^2 + \Delta^2} - \mu$. The first square-root factor is the dominant feature of the spectrum and quite generic, with the square-root representing the three-dimensional density of states and the $1/\omega^2$ dependence can be understood in the limit of high energy: It has been shown recently [69] that the momentum distribution of any system of fermions interacting through a δ-potential behaves as C/k^4 for high momenta. C is the called the contact coefficient. In this limit, the kinetic energy dominates the dispersion relation and $\omega \propto k^2$. The contact coefficient will be the subject of chapter 3.7.4.

---

[10]Transitions from states other than the approximately resonant one, state $|3\rangle$ in the above case, are usually highly suppressed as a typical linewidth of an experimental radiofrequency transition is on the order of kilohertz, whereas other hyperfine states are typically detuned by hundreds of Megahertz.

Chapter 2

Imbalanced Fermi Systems and the Phase Diagram

2.1 BEC-BCS Crossover with Density Imbalance: A Mean-Field Description (and Beyond)

In a mean-field description, the results of chapter 1.3, see also 4.3 are readily generalized, see [70, 71] and references therein. For imbalanced Fermi systems $n_\uparrow \neq n_\downarrow$ the free energy to be minimized now takes the form $\langle H - \mu n - h\Delta n \rangle$, where H is the Hamiltonian defined previously in equation 1.2, μ is the systems chemical potential fixing the total density $n = n_\uparrow + n_\downarrow$, h is the species-imbalance chemical potential, fixing a constant density difference Δn just as μ fixes the total particle density. By comparison to electrons in a metal subject to a magnetic field it is clear that h plays the role of an effective Zeeman field and Δn can be regarded as an effective magnetic moment. From now on we will refer to h as the Zeeman field. The dimensionless normalized density difference $\sigma = \Delta n/n$ is typically used as a parameter of the system. σ is usually referred to as the polarization.

It can be shown that the excitation spectrum 1-9 takes the form:

$$
\begin{aligned}
E_\uparrow(\mathbf{k}) &= \sqrt{\xi_k^2 + \Delta^2} - h & (2.1) \\
E_\downarrow(\mathbf{k}) &= \sqrt{\xi_k^2 + \Delta^2} + h & (2.2)
\end{aligned}
$$

where, as before, $\xi_k = \epsilon_k - \mu$. Now the coherence factors v_k, u_k are modified to:

$$
u_k^2 = 1 - v_k^2 = \frac{E_\uparrow(\mathbf{k}) - \xi_k - h}{E_\uparrow + E_\downarrow} \tag{2.3}
$$
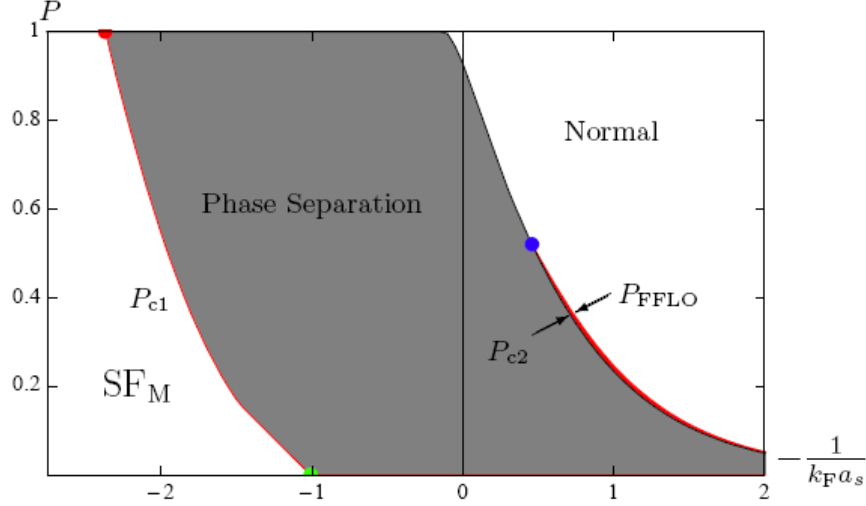
Figure 2-1: Zero temperature mean-field phase diagram of fermions in the BEC-BCS crossover. Plotted is the phase as a function of number imbalance $P = \frac{N_\uparrow - N_\downarrow}{N_\uparrow + N_\downarrow}$ and interaction strength $1/k_\mathrm{F}a$ (taken from [71]). The grey area is a phase separated state between a superfluid of equal densities and a partially polarized normal phase. SF_M stands for a polarized superfluid. P_{c1} and P_{c2} denote the phase boundaries separating the different phases.

And the number and gap equations 1.7 are:

$$-\frac{1}{V_0} = \int \frac{d^3k}{(2\pi)^3} \frac{1 - f(E_\uparrow) - f(E_\downarrow)}{E_\uparrow(\mathbf{k}) + E_\downarrow(\mathbf{k})} \tag{2.4}$$

$$n = 2 \int \frac{d^3k}{(2\pi)^3} \left(u_k^2 f(E_\sigma) + v_k^2 f(-E_{-\sigma}) \right) \tag{2.5}$$

It can be seen that in the limit of equal densities $\sigma = 0$ the above equations reduce to the familiar BCS results of chapter 1.3.

2.2 Theoretical Phase Diagrams

With the above equations one can produce the zero-temperature phase diagram in the BEC-BCS crossover shown in figure 2-1.

This treatment has been generalized to finite temperatures [72].

Just as in the balanced case presented in chapter 1.3, the above mean-field treatment for the imbalanced case exhibits many of the qualitative features of the phase
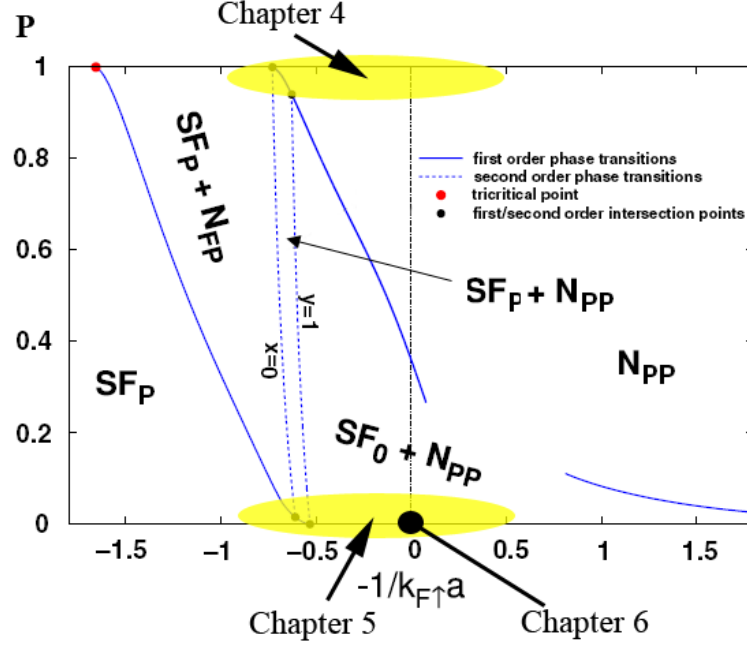
Figure 2-2: Zero temperature phase diagram obtained by fixed-node Monte Carlo calculations, including interactions in the normal phase (taken from [73] and modified). Plotted is the phase as a function of number imbalance $P = \frac{N_\uparrow - N_\downarrow}{N_\uparrow + N_\downarrow}$ and interaction strength $1/k_{\mathrm{F}}a$. The arrows point to the qualitatively very different regimes, which will be presented in the following chapters. The nomenclature is as follows: Polarized superfluid SF_P, balanced superfluid SF_0, partially polarized normal phase N_{PP}, fully polarized normal phase N_{FP}. The different phases are discussed in chapter 2.3.

diagram. But the mean-field treatment fails when put to the test quantitatively. A discussion of the shortcomings of a mean-field treatment have been provided at the end of chapter 1.3 and will be discussed in more detail in chapter 4.1. In essence, the quantitative inaccuracy can be traced back to neglecting interactions in the normal phase. The authors of [73] perform fixed-node Monte Carlo simulations taking the interactions in the normal phase into account [74, 75], see figure 2-2. These normal state interactions will be the subject of chapter 3, in which we use radiofrequency spectroscopy to experimentally determine the properties of this Landau Fermi Liquid of a strongly interacting Fermi system.

As is indicated in figure 2-2, in the following chapters 4 and 5 we will focus on quantitative studies of the single-particle excitation spectrum using radiofrequency spectroscopy in two different physical regimes: The highly imbalanced normal phase and the (almost) balanced superfluid phase. In chapter 6 we will present another

quantitative study, in which we use the density distribution in a non-homogeneous potential to determine the equation of state for finite temperature at unitarity.

2.3   Discussion of the Theoretical Phase Diagram

$T = 0$:   The phase diagram in figure 2-2 shows a very rich structure and here we will discuss the different phases based on [71, 73, 76].

The line $P = 1$ or $N_\downarrow = 0$ is the fully polarized non-interacting Fermi gas (N_{FP}). Here, the system consists of fermions filled up to momentum k_F, resulting in the well-known equation of state:

$$E_{N_{FP}} = \frac{3}{5} N_\uparrow E_{F\uparrow} \tag{2.6}$$

with the Fermi energy $E_{F\uparrow} = \frac{\hbar^2 k_F^2}{2m}$.

The limit of a single impurity ($P = 1^-$) is the line infinitesimally below $P = 1$. This polaronic phase, a phase of dressed quasiparticles interacting with a Fermi sea, already yields rich information about the interacting system. In particular, in chapter 3 we will show that a dilute gas of such Fermi-polarons (more than a single impurity) is characterized by a binding energy, an effective mass $m^* \neq m$ and weak interactions and essentially follows the physics of the single impurity limit. This allows to extrapolate into the much more complicated partially polarized normal phase (N_{PP}). We encounter this phase at finite imbalance (concentration $x \equiv N_\downarrow/N_\uparrow > 0$) if the two-body bound state energy is not too large. In the regime $x \ll 1$ the equation of state can be expanded as [74]:

$$E_{N_{PP}} = N_\uparrow E_{F\uparrow} \left(\frac{3}{5} - Ax + \frac{3}{5}\frac{m}{m^*}x^{5/3} + \frac{3}{5}Fx^2 \right) \tag{2.7}$$

The first term is the energy of the majority Fermi sea, assumed not to be appreciably perturbed by the presence of a few minority particles. The second term represents the interaction energy of polarons with the majority particles. It is attractive and quite significant in the unitary limit: $A \simeq 0.6\epsilon_F$. The third term represents the energy of a Fermi sea of non-interacting polarons since[1] $(E_{F\downarrow} N_\downarrow)/(E_{F\uparrow} N_\uparrow) = \frac{m}{m^*}x^{5/3}$. The effective mass renormalization has been shown to be fairly small and on the order of $m^* = 1.17m$ in the unitary limit [77, 74, 78]. The fourth term represents the

---

[1]Since the effective mass might depend on the density, the third term in the parametrization in equation 2.7 might have to be modified to depend on $x^{7/3}$ instead of $x^{5/3}$.

(weak) interactions between polarons and has been calculated to be $F = 0.14$ using fixed-node Monte Carlo calculations [74].

Once the density imbalance between majority and minority becomes smaller, the system enters a phase separated state ($SF_0 + N_{PP}$) with a balanced superfluid separated from a partially polarized normal phase. The unitary limited balanced superfluid state is described by the equation of state:

$$\mu = \xi E_F \tag{2.8}$$

where $\xi = 1 + \beta$ with the Bertsch parameter β. The value of ξ is still subject to discussion, ranging between $0.32 < \xi < 0.49$ [30, 31, 32, 33, 34, 35, 36, 37, 38, 39, 14, 40]. In this regime of equal densities, the existence of the superfluid gap expels all excess particles out of the superfluid as their presence would "cost" an energy Δ. It is obvious that the phase diagram depends strongly on the precise energetics of the normal and the superfluid phase and they will be the subject of the following chapters.

In the deep BEC regime, it is clear that the imbalanced ground state consists of a BEC of strongly bound molecules weakly interacting with excess majority atoms (*all* minority atoms are bound into molecules). The interactions between fermionic atoms and the bosonic molecules are characterized by the scattering length $a_{ad} \sim 1.18a$ [79] and the typical mean-field energy $U_{\mathrm{MF}} = \frac{4\pi\hbar^2 a_{ad}}{m} n_d$. In this regime, the superfluid is called partially polarized (SF_P).

If U_{MF} is increased beyond a critical value, the system will phase separate into a partially polarized superfluid and a fully polarized normal cloud ($SF_P + N_{FP}$). In a homogeneous system the phase separation would be evident. For the experimentally relevant harmonic trapping potential, this transition would be less obvious as the majority cloud extends beyond the size of the superfluid. Since the superfluid density continuously approaches zero and the transition is of first order, it can only be observable through a kink in the trapped three-dimensional majority density distribution at the interface, a signature very hard to detect experimentally.

For increasing interactions one might enter a small sliver of a phase separated state between a partially polarized superfluid and a partially polarized normal region ($SF_P + N_{PP}$). This phase does not exist in a mean-field description and the authors of [73] concede that this phase might not be realized.

A further increase in the interaction strength results in a phase separated state between a balanced superfluid and a partially polarized normal gas. The critical density imbalance σ_c in the normal phase at the interface between the superfluid

and the normal region was calculated [73] and experimentally confirmed [19] to be $\sigma_c \simeq 0.36$.

2.4   Experimental Phase Diagram

As is intuitively obvious and as can be seen from figure 2-2, as $1/k_F a$ is increased towards the BEC side of the Feshbach resonance, more and more minority particles pair up with majority particles, thereby increasing the critical polarization σ_c in the normal phase. At a certain critical interaction strength, *all* minority particles will be bound in generalized molecules, no matter how high the density imbalance - this is the polarized superfluid regime.

Its experimental signature is immediately accessible through the majority and minority density profiles, see figure 2-3. The top row shows elliptically averaged column density profiles and the column density difference. The reconstructed three-dimensional density profiles of majority and minority are shown in the second row. As the BEC limit is approached, one can indeed clearly see the region of the partially polarized normal region shrinking until all minority particles are paired into a Bose-Einstein condensate of molecules, phase separated from a fully polarized normal region. The density imbalance $\sigma = (n_\uparrow - n_\downarrow)/(n_\uparrow + n_\downarrow)$ is shown in the third row, confirming that the critical imbalance indeed approaches unity. This critical imbalance is plotted in figure 2-4 as a function of interaction strength and compared to the Monte Carlo phase diagram, as well as to the data in the following chapters using a different method: Radiofrequency spectroscopy.

2.5   Phase Diagram at Finite Temperatures

So far we have limited the discussion to the zero-temperature case. Theoretically, making a quantitative prediction at finite temperature for a density imbalanced system remains a formidable challenge even within the realm of mean-field theory as one must include the effect of thermally excited molecules and quasiparticle excitations (see also chapter 4), which might be strongly interacting in the unitary regime. Again, one must resort to Monte Carlo calculations[2] and experiments [19, 80] to test the accuracy of theories. In fact, even the balanced two-component Fermi mixture at

---

[2]While there have been various Monte Carlo calculations for the imbalanced case at zero temperature and the balanced case at finite temperature, to date the treatment of imbalanced Fermi gases at finite temperature remains elusive.
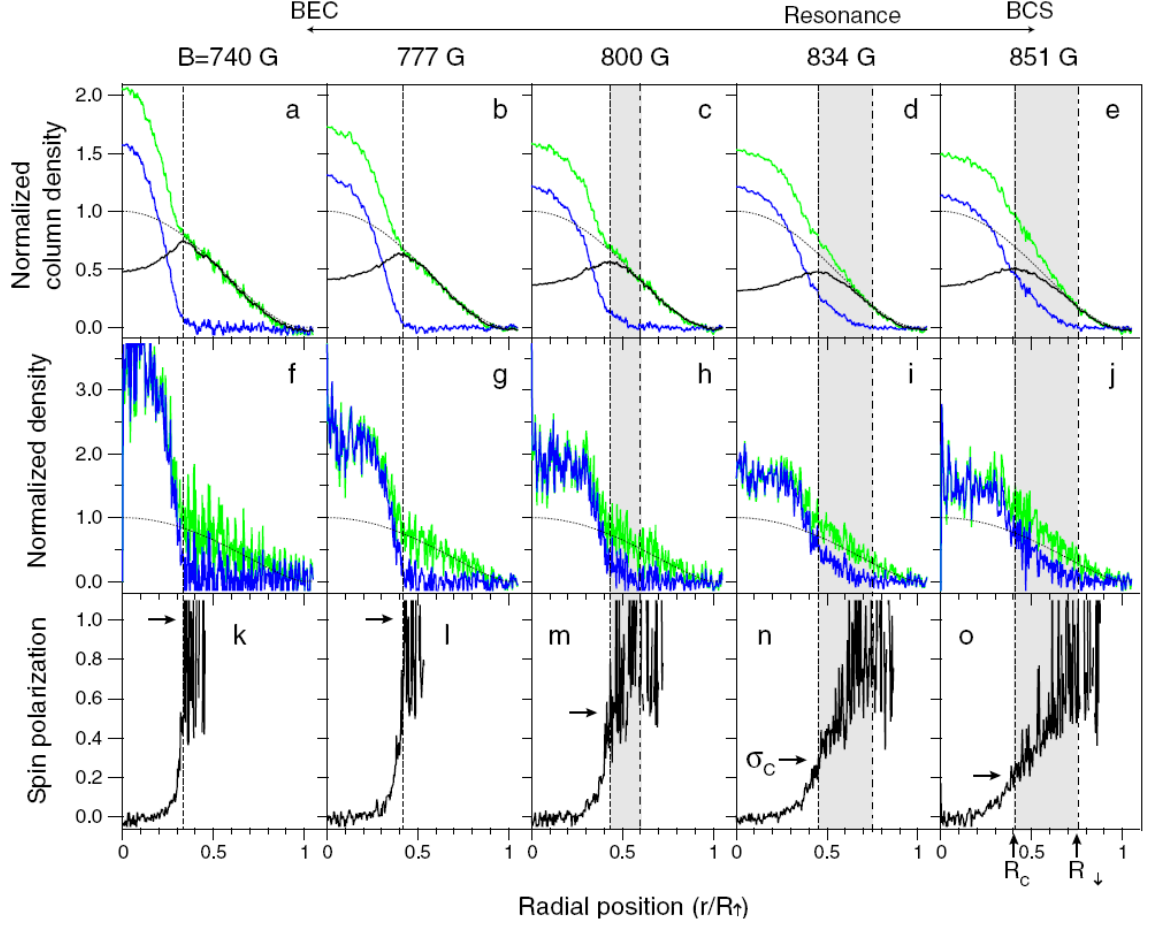
Figure 2-3: Density profiles of imbalanced Fermi mixtures in a harmonic trap. The top row (a)(e) shows the averaged column-density profiles for various magnetic fields. Green: Majority, blue: Minority, black: Column density difference. The black dotted line is a zero-temperature Thomas-Fermi distribution fit to the majority wing ($r > R_\downarrow$). The middle row (f)(j) and the bottom row (k)(o) show the reconstructed three-dimensional density distributions and the spin polarizations obtained from the profiles in the top row. The critical polarizations σ_c at the phase boundary $r = R_c$ are indicated by the right-pointing arrows. The values for $R_\uparrow$ (in μm), $R_c/R_\uparrow$, and $R_\downarrow/ = R_\uparrow$ were respectively: for (a), (f), (k), 381, 0.33, 0.33; for (b), (g), (l), 380, 0.33, 0.33; for (c), (h), (m), 362, 0.35, 0.59; for (d), (i), (n), 371, 0.44, 0.72; for (e), (j), (o), 367, 0.41, 0.76. $T/T_{F0} \simeq 0.05$, and $T_{F0} \simeq 1.0\mu$K (see the text for definitions).

finite temperatures in the unitary regime is still under current theoretical and experimental investigation. We will present an outlook on our recent experimental efforts in this regard in chapter 5.

For completeness, we will briefly present our results on the finite temperature phase diagram in the unitary limit. For more details refer to [19] and Christian

36
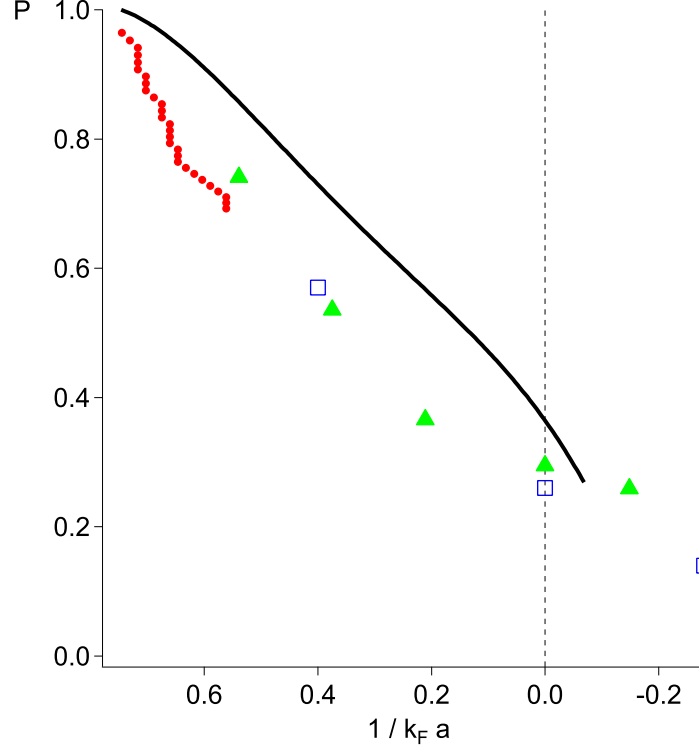
Figure 2-4: Experimental phase diagram approaching zero temperature. Critical interaction strength determined by several methods: Solid green triangles: Density distribution. Solid red circles: Radiofrequency spectroscopy of polarons, chapter 3. Open blue squares: Radiofrequency spectroscopy of moderately imbalanced Fermi mixtures based on figure 4-9 in chapter 4. For comparison, the first order phase transition line from Monte Carlo calculations is added as solid black line, see figure 2-2.

Schunck's thesis [21].

We have used an analysis of the density profiles of majority and minority components and recorded the critical density imbalance in the normal (σ_c) and in the superfluid (σ_c) region, this time as a function of the normalized local temperature T/T_F. The resulting finite temperature phase diagram is shown in figure 2-5.

The fact that at finite temperature the superfluid supports finite polarizations σ in the form of thermally excited quasiparticles will be used in chapter 4 to determine the superfluid gap Δ and the Hartree energy U.

Furthermore, finite temperatures make the superfluid less robust against imbalance, for instance the critical polarization is reduced from $\sigma_c \simeq 0.36$ at zero temperature to $\sigma_c \simeq 0.2$ at $T/T_F \simeq 0.07$, see figure 2-5. This might explain the discrepancy between the Monte Carlo calculations and our data in figure 2-4. For an accurate
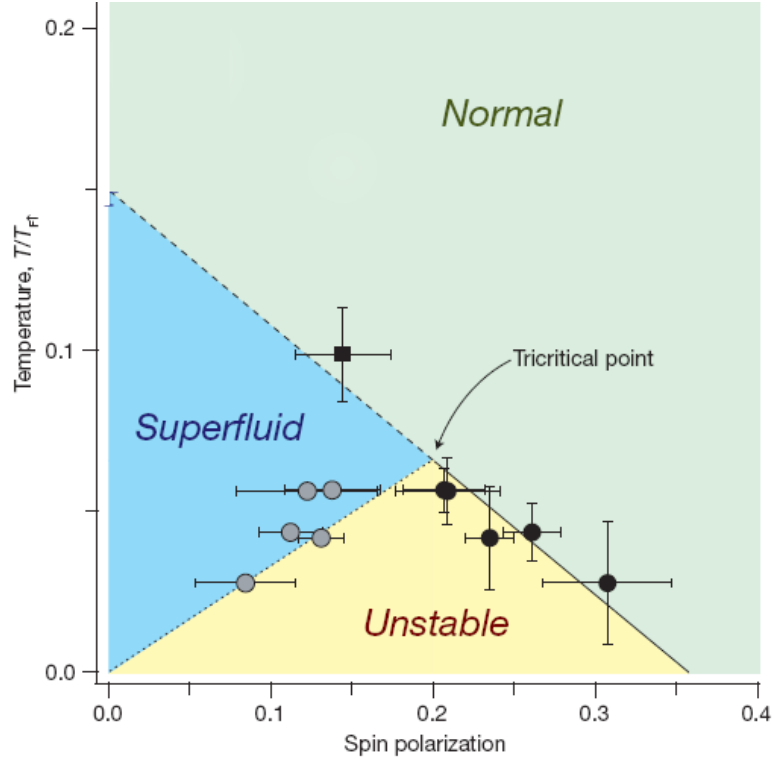
Figure 2-5: Experimental phase diagram at finite temperature in the unitary limit. The critical polarizations σ_c (black solid circles and square) and σ_c (grey solid circles) are displayed along the local T/T_F at the phase boundary. The yellow area ($\sigma_s < \sigma < \sigma_c$) represents a thermodynamically unstable region, leading to the phase separation, see chapter 2.3. We identify the tricritical point, separating a first order phase transition ($T/T_F < 0.07$) from a second order phase transition ($T/T_F > 0.07$). The linear fit to the σ_c values is shown as a guide to the eye for the normal-to-superfluid phase transition line. Each data point consists of five independent measurements and error bars indicate the standard deviation.

comparison, a theoretical phase diagram is needed for finite temperatures.

Chapter 3

The Fermi-Polaron

3.1   N+1 = The Impurity Problem

A seemingly simple problem: What is the energy of a single $|\downarrow\rangle$ particle (fermion or boson) interacting with an environment of $|\uparrow\rangle$ fermions, composing a Fermi sea, which we will denote as $|FS\rangle_\uparrow$? Apart from the universal interest the impurity problem has as discussed below, we have seen in the previous chapter that the interactions in the normal state have substantial impact on the phase diagram of imbalanced Fermi mixtures. This becomes obvious when a quantitative comparison is made between the mean-field phase diagram, neglecting normal phase interactions, and the Monte Carlo calculations including these interactions, see figures 2-1 and 2-2.

In general, no real physical system is free of imperfections and impurities. Modeling the ions in a metal as having a perfect crystalline structure and treating the electrons as free waves in Bloch bands is surprisingly successful in describing many properties at high temperature. However, at low temperatures, on the order of the interaction energy between impurity and environment, new phenomena appear. A famous example is the Kondo effect, where immobile magnetic impurities decrease the mobility of conduction electrons, therefore giving rise to an enhanced resistance in metals below the Kondo temperature [81]. Without the presence of an impurity, the resistance decreases quadratically with the temperature, the usual signature of Pauli blocking.

A different example for an impurity problem is an electron moving in a crystal lattice creating a localized polarization, or phonon wavepackets, by displacing the ions in a crystal from their respective equilibrium positions. The electron dressed by phonons forms the lattice polaron [82]. The difference to the above examples and the experimental system presented later in this chapter is that the fermion is interacting

with a bosonic environment, the lattice phonons.

The phonons, or lattice polarization, created by one electron can, in turn, interact with another electron giving rise to the small attractive interaction responsible for Cooper pairing [5] and are therefore an essential ingredient for the formation of the superfluid phase. This immediately raises the question of the connection between interacting polarons (the limit of $T \to 0$ and $\sigma \to 1$ in 2-5) and the normal state of a balanced Fermi gas above the superfluid transition temperature T_C (the limit of $\sigma \to 0$ and $T > T_c$ in 2-5). If superfluidity can be regarded as condensation of interacting polarons, a good understanding of the normal polaronic phase might prove essential.

As interacting Fermi systems have been successfully described within the framework of Landau's Fermi Liquid Theory, we will introduce the basic concepts of quasiparticles and their properties below, largely based on [83].

3.2 Another Angle on the Impurity Problem

Above, the argument is made that the a single fermion interacting with a Fermi sea constitutes a quasiparticle which can be described in terms of Fermi liquid theory. One can look at this problem from the other end: Consider two fermions in a box at almost zero kinetic energy, whose interaction potential is close to supporting a bound state and that this bound state can be tuned above or below the energy of the incoming particles. This is a typical realization of a strongly interacting system around a Feshbach resonance and can be solved exactly [23]. Their energy is shown figure 3-1a: There exists a bound state in the interatomic potential below the Feshbach resonance (dashed line), above the Feshbach resonance the particles scatter off each other and acquire a phase shift related to the scattering length a.

How is the energy of the particles modified if one were to add particles of one kind to the system, one by one, building up a majority Fermi sea? The result is also shown in figure 3-1a as the solid black line. It can be seen that the energy changes substantially: At unitarity where we expect the binding energy to be zero, it is in fact a sizeable fraction of the majority Fermi energy. Away from the Feshbach resonance the modification reduces and eventually approaches the mean-field limit. The energy difference between two-body physics and many-body physics is shown in figure 3-1b. Another important result is that, even when the interatomic potential supports a bound state, no two-body bound state is formed. The particle remains a fermionic (quasi-) particle instead of forming a composite boson or molecule. Physically it
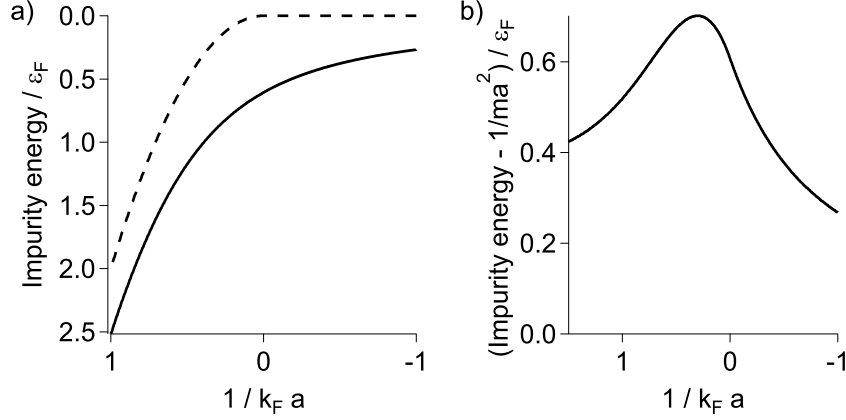
Figure 3-1: Two-body physics vs many-body physics: a) Dashed line: Binding energy $\frac{\hbar^2}{ma^2}$ as a function of interaction strength $\frac{1}{k_F a}$ according to the simple model of two particles interacting through a scattering resonance, see Feshbach resonance 1.2. Solid line: Energy from a variational many-body calculation, see equation 3.23. b) Energy difference between the two-body and many-body calculation.

is clear, though, that once the two-body binding energy reaches a critical value, a bosonic molecule will form regardless of the presence of a Fermi sea. We expect this critical interaction strength to be reached when the two-body binding energy $\frac{\hbar^2}{ma^2}$ is on the order of the Fermi energy of the Fermi sea. It is important to note, see also figure 3-11 and 3-1 that the energy of this bosonic quasiparticle is *not* described by $\frac{\hbar^2}{ma^2}$ but will also be modified due to the presence of the Fermi sea. We will discuss this "Molaron" below.

3.3 Landau's Fermi Liquid Theory

How is it possible that the naïve model for metals as free electrons moving in a lattice structure is so successful in describing the properties of solids when the electrons are, in fact, interacting through the Coulomb force, which is, although screened, still rather strong? The explanation and theoretical framework has been provided by L.D. Landau more than 50 years ago [82]. At the core of Fermi Liquid Theory is the notion of a quasiparticle, characterized by its effective mass m^*, its quasiparticle residue Z and the interaction parameters F_s and F_a.

In a non-interacting Fermi system free particles of wavevector $\mathbf{k}$ are the eigenstates. This, together with Pauli's exclusion principle, completely characterizes the ground and excited states: The ground state is just a filled Fermi sea - at zero temperature the

occupation probability is one for $k \leq k_F$ and it is zero for $k > k_F$. A particle added above the Fermi momentum k_F or a hole added below k_F constitutes an elementary excitation of the system. These excitations are also eigenstates of the system and therefore have an infinite lifetime.

Consider now a system of fermions in which the interactions are gradually, i.e. adiabatically, switched on. The system will remain in its ground state but now with an interaction term in the Hamiltonian. Free particles are no longer eigenstates of the system as particles will scatter and "dissolve" into the ground state by way of particle-hole excitations in the Fermi sea. Similarly, if interactions are switched on starting with a system in its ground state *plus* an elementary excitation at $k > k_F$, this excitation will be an approximate eigenstate of the real interacting system *if* its lifetime is long enough that it qualifies as an eigenstate. As the Pauli principle together with energy conservation restrict the available phase space for decay, one can see that the lifetime of an added particle of energy $\xi_k = \epsilon_k - \mu$, measured relative to the Fermi energy, has a scattering probability, or lifetime, proportional to $1/\tau(\xi) \propto \xi^2$. Hence, this excitation can be treated as an approximate eigenstate *if* its energy is close to the Fermi energy $\xi_k \to 0$. This elementary excitation is called a quasiparticle of momentum k to the real ground state. Similarly, an elementary excitation of $k < k_F$ is called a quasihole.

3.3.1 Quasiparticles

Quasiparticles are fermions since the system adiabatically evolves from a system of non-interacting fermions. In the ground state the real system can be represented as is shown as the solid black line in figure 3-2 - there are no quasiparticles present above k_F and no quasiholes below k_F. It is important to stress that figure 3-2 does not show the distribution of quasiparticles, as they are only well-defined entities close to the Fermi energy. In other words, quasiparticles are elementary excitations and give no information about the ground state of the system. Also shown is the effect of interactions on the distribution of the bare particles.

Just as in the non-interacting case, the excitation of the system can be characterized by the deviation from the ground state:

$$\delta n(k) = n(k) - n_0(k) \tag{3.1}$$

and for small densities of quasiparticles $N_{\mathrm{exc}} = \sum_k |\delta n(k)| \ll N$ and energies near the Fermi energy, the energy of the system can be expanded as:
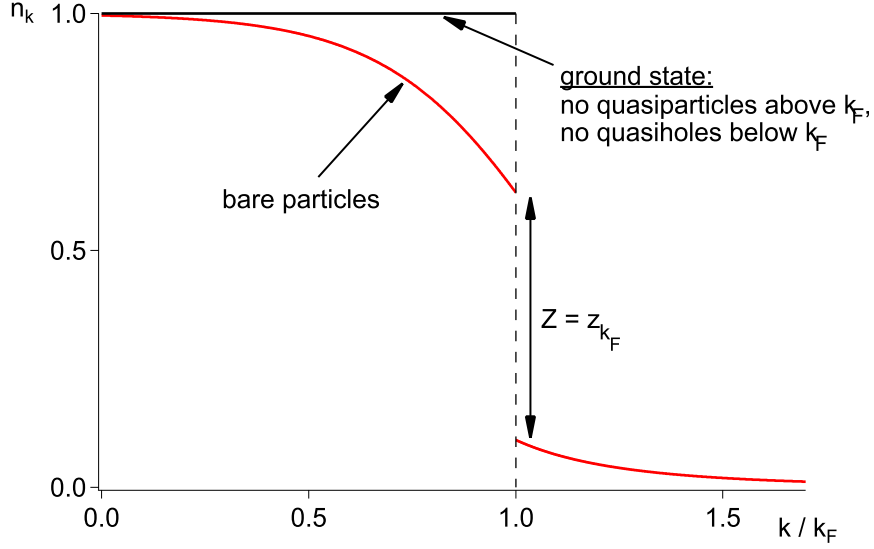
Figure 3-2: Cartoon picture of the ground state momentum distribution (solid black line) and bare particle momentum distribution (solid red line).

$$E[\delta n(k)] = E_0 + \sum_k \epsilon_k \delta n(k) + \frac{1}{2V} \sum_{k,k'} f(k, k') \delta n(k) \delta n(k') \qquad (3.2)$$

where E_0 is the (interacting) ground state energy, ϵ_k is the energy of non-interacting quasiparticles $\epsilon_k =: \frac{\hbar^2 k^2}{2m^*}$, with the definition of the effective mass m^* and $f(k, k')$ contains the interactions between quasiparticles.

The effective mass m^* will be different from the bare mass m due to the interactions between the bare particles. It is insightful to think of quasiparticles as bare particles being "dressed" by their surroundings - a quasiparticle is a superposition of different unperturbed states. In this picture it is easy to see why the effective mass of a quasiparticle differs from that of a free particle: It is dragging along a cloud of dressing particles. A quantity related to the effective mass is the quasiparticle residue Z, which quantifies how much "bare particle" is contained in a quasiparticle at momentum **k**. Z also gives the size of the "jump" in the bare particle distribution at $k = k_F$ called the Migdal discontinuity, see also figure 3-2. We will get back to this point in the next section on the microscopic description of interacting Fermi systems.

The function $f(k, k')$ in equation 3.2 is difficult and tedious to compute. However, it is generally clear that the interaction between quasiparticles is important in the description of collective excitations, such as sound waves, spin waves, etc. More specifically, $f(k, k')$ can be decomposed into a symmetric part $f^s(k, k')$, independent

43

of spin, and an antisymmetric part $f^a(k, k')$, and then expanded in Legendre polynomials. The resulting coefficients $F_l^{s,a}$ can be connected to parameters measurable in experiments, such as the effective mass m^* related to F_1^s, the speed of sound or the compressibility $\frac{\partial n}{\partial \mu}$ related to F_0^s and the paramagnetic spin susceptibility χ_p related to F_0^a.

3.3.2 Fermi Liquid Theory on a Microscopic Level

We begin with the definition of the single particle Green function $G(xt, x't')$. It contains all the information about one particle or one hole. It is defined as:

$$G(xt, x't') := i\langle\phi_0|T\{\psi(x, t)\psi^\dagger(x', t')\}|\phi_0\rangle \tag{3.3}$$

where $|\phi_0\rangle$ is the true ground state wavefunction of the system and generally unknown, $T\{...\}$ is the time ordering operator, and $\psi(x, t), \psi^\dagger(x, t)$ are the annihilation and creation at operator, respectively. The interpretation of formula 3.3 is immediately clear: $G(xt, x't')$ is the probability amplitude of finding a particle at x at time t, when a particle has been added at x' at time t'.

For simplicity, let us assume that the system is translationally invariant and that the time evolution is independent of the starting time t'. The Fourier transform is then $G(k, t)$. $G(k, 0^-)$ is proportional to the momentum distribution $n(k)$:

$$G(k, 0^-) = -in(k) \tag{3.4}$$

A hole is added at $t' = 0$: $a_k(0)|\phi_0\rangle$. If one were to measure at an infinitesimal time step later, one would have have measured the probability of *being able* to create a bare hole, which is proportional to the momentum distribution $n(k)$. Note that the added particle is a bare particle and therefore not an eigenstate. Eventually, for long enough times the particle will scatter and the according excitation will damped as expressed by the fact that $\lim_{t\to\infty} G(k, t) \to 0$.

At this point it is convenient to introduce the spectral function $A(\mathbf{k}, \omega)$:

$$A_+(\mathbf{k}, \omega) = \sum_n |\langle\phi_n|a_k^\dagger|\phi_0\rangle|^2 \delta(\omega - \epsilon_n) \tag{3.5}$$

$$A_-(\mathbf{k}, \omega) = \sum_n |\langle\phi_n|a_k|\phi_0\rangle|^2 \delta(\omega - \epsilon_n) \tag{3.6}$$

$$A(\mathbf{k}, \omega) = A_+(\mathbf{k}, \omega) + A_-(\mathbf{k}, \omega) \tag{3.7}$$

Similarly to the physical interpretation of equation 3.3, $A_{+/-}$ is the probability that adding/removing a particle with momentum k to the system will be associated with, in other words "costs", the energy $\hbar\omega$. For free particles the energies ϵ_n are just the $\epsilon_k = \frac{\hbar^2 k^2}{2m}$ and $A(\mathbf{k}, \omega)$ is a sum of discrete δ-functions as the fermionic excitations are eigenstates. Including interactions, an added particle is not an eigenstate any more but a superposition of the eigenstates of the interacting system. However, following the argument above, excitations close to the Fermi energy constitute quasiparticles and one can expect $A(\mathbf{k}, \omega)$ still to exhibit maxima at the new resonance frequencies ϵ_k spread out over a width Γ_k, determining the inverse lifetime of the quasiparticle. More explicitly, with the definition of the spectral function and the Green function above:

$$-iG(\mathbf{k}, t) = e^{-i\mu t} \int_0^\infty A_+(\mathbf{k}, \omega) e^{-i\omega t} d\omega \tag{3.8}$$

with the chemical potential μ. This can be rewritten deforming the contour of integration and choosing $\alpha \gg 1/t$:

$$-iG(\mathbf{k}, t) e^{i\mu t} \approx \int_0^{i\alpha} A_+(\mathbf{k}, \omega) e^{-i\omega t} d\omega - 2\pi i \sum_j \zeta_j e^{-i\omega_j t} \tag{3.9}$$

where ζ_j are the residues of $A_+(\mathbf{k}, \omega)$. One of the poles of $A(\mathbf{k}, \omega)$ will give a dominant contribution. The according frequency is $\omega = \xi_k - i\Gamma_k$. The other poles and the integral along the imaginary axis give contributions of various frequencies and very quickly decohere. Defining $z_k := 2\pi \iota \zeta_k$, the time evolution of an added bare particle is:

$$iG(\mathbf{k}, t) = z_k e^{-i\xi_k t - \Gamma_k t} + iG_{\text{inc}}(\mathbf{k}, t) \tag{3.10}$$

Therefore, with $A(\mathbf{k}, \omega) = -2\,\text{Im}G(\mathbf{k}, \omega)$ for $k \to k_F$ the spectral function can be written as:

$$A(\mathbf{k}, \omega) = Z\delta(\omega - \xi_k) + A_{inc}(\mathbf{k}, \omega) \tag{3.11}$$

From the equations above it is clear that $Z = z_{k_F}$ can be interpreted as the probability of free propagation of a quasiparticle. More generally, it can be shown that z_k measures how much bare particle is contained in a quasiparticle.

Inserting a complete set of eigenstates into 3.3 and using the above definitions 3.7 for the spectral function and performing the Fourier transform, one arrives at the Lehmann-representation for the Green function:

45

$$G(\mathbf{k}, \omega) = \int_0^\infty d\omega' \left(\frac{A_+(\mathbf{k}, \omega)}{\omega' - \omega + \mu - i0^+} - \frac{A_-(\mathbf{k}, \omega)}{\omega' + \omega - \mu - i0^+} \right) \tag{3.12}$$

which we will need in the next chapter when making the connection between the self-energy $\Sigma(\mathbf{k}, \omega)$ amd the spectral function.

3.3.3 Calculating m^* and Z

In order to explicitly calculate the properties of an interacting system described by a Hamiltonian of the form $H = H_0 + H_\mathrm{I}$, we not only need the single particle Green function but the two-particle Green function, which is defined similar to the one-particle Green function in equation 3.3:

$$K(\mathbf{x}_1, \mathbf{x}_2, \mathbf{x}_3, \mathbf{x}_4) := \langle \phi_0 | T\{\psi(\mathbf{x}_1)\psi(\mathbf{x}_2)\psi^\dagger(\mathbf{x}_3)\psi^\dagger(\mathbf{x}_4)\}|\phi_0\rangle \tag{3.13}$$

With this definition, the Schrödinger equation can be expressed in terms of the Green functions:

$$\left(\frac{\partial}{\partial t} - i\frac{\hbar^2 \nabla^2}{2m} \right) G(\mathbf{x}, \mathbf{x}') - \int d^3\mathbf{x}'' V(|\mathbf{x}| - |\mathbf{x}''|) K(\mathbf{x}'', \mathbf{x}, \mathbf{x}'', \mathbf{x}') = i\delta(\mathbf{x} - \mathbf{x}') \tag{3.14}$$

After Fourier-transforming this equation can be expressed as:

$$\left(\frac{\hbar^2 k^2}{2m} - \omega - \Sigma(\mathbf{k}, \omega) \right) G(\mathbf{k}, \omega) = 1 \tag{3.15}$$

The quantity $\Sigma(\mathbf{k}, \omega)$ is called the self-energy and contains all the effects of interactions in the system. It is in essence the correction to the free-particle kinetic energy ϵ_k by interactions and is therefore closely related to the effective mass m^* and the quasiparticle residue Z, see discussion following equation 3.2. Equation 3.15 and 3.10 can be combined to give the well-known result for the quasiparticle residue Z:

$$z_k = \frac{1}{2\pi i} \oint G(\mathbf{k}, \omega) d\omega \tag{3.16}$$

$$= \frac{1}{2\pi i} \oint \frac{d\omega}{\omega - \left(\frac{\hbar^2 k^2}{2m} - \Sigma(\mathbf{k}, \omega)\right)} \tag{3.17}$$

$$= \frac{1}{2\pi i} \oint d\omega' \frac{\left(1 + \frac{\partial \Sigma(\mathbf{k}, \omega)}{\partial \omega}|_{\omega = \epsilon_k}\right)^{-1}}{\omega'} \tag{3.18}$$

$$= \left(1 + \frac{\partial \Sigma(\mathbf{k}, \omega)}{\partial \omega}|_{\omega = \epsilon_k}\right)^{-1} \tag{3.19}$$

As mentioned above, one can relate the effective mass to the self-energy $\Sigma(\mathbf{k}, \omega)$ from equation 3.15. The pole of the Green function giving the dispersion relation satisfies $\omega = \epsilon_k + \Sigma(\mathbf{k}, \omega)$. Expanding around the ground state $k = 0$ and $\omega = \mu + \omega'$ gives:

$$\mu + \omega' = \epsilon_k + \underbrace{\Sigma(0,0)}_{\mu} + \frac{\partial \Sigma(\epsilon \mathbf{k}, \omega')}{\partial \epsilon_k} \epsilon_k + \frac{\partial \Sigma(\epsilon \mathbf{k}, \omega')}{\partial \omega'} \omega'$$

leading to:

$$\frac{m^*}{m} = \frac{1 - \frac{\partial \Sigma}{\partial \omega}}{1 + \frac{\partial \Sigma}{\partial \epsilon_k}} \tag{3.20}$$

Here we made the substitution $\epsilon_k = \frac{\hbar^2 k^2}{2m}$ and replaced $\Sigma(0,0)$ by μ, which is only true in the case of a single impurity particle as no momentum states are blocked.

Finally, for completeness let us make the connection between the self-energy $\Sigma(\mathbf{k}, \omega)$ and the spectral function $A(\mathbf{k}, \omega)$ by inserting the standard identity $\frac{1}{\omega \pm i\eta} = P\frac{1}{\omega} \mp i\pi\delta(\omega)$ into the Lehmann representation 3.12 and using equation 3.15:

$$A(\mathbf{k}, \omega) = -2\,\mathrm{Im}[G(\mathbf{k}, \omega)]$$

$$= \frac{-2\mathrm{Im}[\Sigma(\mathbf{k}, \omega)]}{(\omega - \frac{\hbar^2 k^2}{2m} - \mathrm{Re}[\Sigma(\mathbf{k}, \omega)])^2 + (\mathrm{Im}[\Sigma(\mathbf{k}, \omega)])^2} \tag{3.21}$$

The above equations for m^*, Z and $A(\mathbf{k}, \omega)$ from the self-energy will become important in the next section when the self-energy will be calculated for a particular

limit of a Fermi Liquid, namely a $|\downarrow\rangle$ impurity particle interacting with a $|\uparrow\rangle$ Fermi sea.

One result of the above equation is that the (bare) particle momentum distribution $n(k)$ can be written as, using 3.4 ($T = 0$):

$$n(k) = \int_{-\infty}^{0} d\omega A_-(k,\omega) \tag{3.22}$$

with the energy measured relative to the Fermi energy.

For the special case of a Fermi Liquid of a single particle immersed in a Fermi sea of majority particles, the according momentum distributions are plotted in figure 3-3.
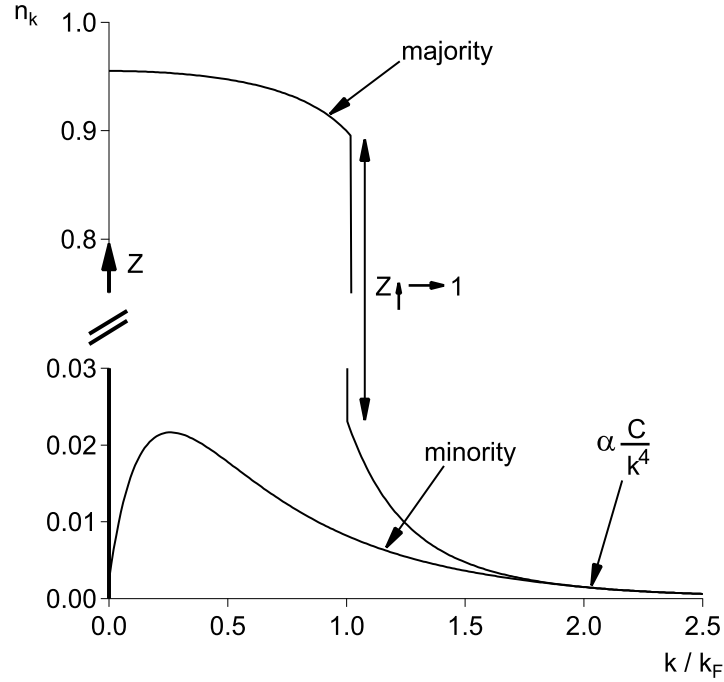
Figure 3-3: Momentum distribution for the polaron system at unitarity. It can be seen that the minority momentum distribution has a δ-peak of weight Z at $k = 0$ and a continuous momentum distribution at $k > 0$. The majority momentum distribution is described by a stepfunction only in the thermodynamic limit. For a finite volume V we see the particle-hole excitations in the ground state. The discontinuity in the majority momentum distribution is given by the quasiparticle residue of the majority $Z_\uparrow$. It approaches unity in the thermodynamic limit. At large momenta, the momentum distributions of majority and minority overlap and are characterized by the contact coefficient C, see chapter 3.7.4.

From the expression for the spectral function in equation 3.11 one can readily see another interpretation of the quasiparticle residue Z: At $T = 0$ the distribution of

the bare particles jumps by Z at $k = k_F$. If $k < k_F$, the δ-function is included with a weight of Z in the above integration as $\xi_k < 0$. If $k > k_F$, it is not included. The coherent part of the spectral function only determines the size of the jump in the momentum distribution and stems from the fact that excitations change in character from quasiparticles to quasiholes at $k = k_F$. The actual distribution is determined by the complicated integral over the incoherent part of the spectral function, see equation 3.11, and therefore not necessarily inflection symmetric around k_F. We will see this below in the specific example of an impurity particle interacting with a Fermi sea.

3.4 A Special Case: A $|\downarrow\rangle$ Swimming in a $|\uparrow\rangle$ Fermi sea

In this section we will use some of the results from the previous section and apply them to a particular limit of a Fermi Liquid: A $|\downarrow\rangle$ impurity particle strongly interacting with a Fermi sea of $|\uparrow\rangle$ particles. Of particular interest are the value of the self-energy $\Sigma(0,0) \equiv \mu$ and the Fermi liquid parameters m^* and Z as they are directly accessible in our experiments. The general cooking recipe to approach this problem would consist of the following steps:

- get vertex function Γ [84] describing the full interaction based on the Hamiltonian of the system

- T-matrix approximation for Γ: The impurity particle interacts repeatedly with only a single particle in the Fermi sea of $|\uparrow\rangle$ at a time. In other words, upon a scattering event the impurity particle creates only a single particle-hole pair. It can do so any number of times and hence perturbation theory can be carried out to arbitrarily high orders, giving the well-known ladder series (ladder approximation).

- get self-energy $\Sigma(\mathbf{k}, \omega)$ from Γ [84]

- extract physical quantities from $\Sigma(\mathbf{k}, \omega)$

In order to simplify the above calculation, in addition the non-selfconsistent approximation is often made of an undisturbed majority momentum distribution that can still be described by a step-function - it does not exhibit the characteristic C/k^4

behavior, see chapter 3.7.4 and figure 3-3. In the Chevy Ansatz, see below, the momentum distribution of the majority retains the high momentum tail for finite volume but approaches a step function in the thermodynamic limit, as one would expect for a single impurity particle interacting with a majority Fermi sea.

If the constraint of an undisturbed majority momentum distribution is released in the T-matrix approximation, however, the resulting minority energy is $E_\downarrow \simeq -0.9\epsilon_F$ [85][1] compared to the exact result $E_\downarrow \simeq -0.615\epsilon_F$ [87] and experimental result $E_\downarrow \simeq -0.64\epsilon_F$, see below.

A more insightful but mostly equivalent approach has been provided by F. Chevy: It is a variational calculation based on a trial wavefunction for the system in the vein of the T-matrix approximation, namely the impurity particle only interacting with single particle-hole pairs. It allows, however, for a modified majority momentum distribution. The Ansatz can be written as:

$$|\psi\rangle = \phi_0 |\mathbf{k}'\rangle_\downarrow |FS\rangle_\uparrow + \sum_{\substack{q<k_F \\ k>k_F}} \phi_{\mathbf{qk}} c^\dagger_{\mathbf{k}\uparrow} c_{\mathbf{q}\uparrow} |\mathbf{k}' + \mathbf{q} - \mathbf{k}\rangle_\downarrow |FS\rangle_\uparrow \qquad (3.23)$$

The Hamiltonian for this $N+1$ body system is:

$$\hat{H} = \sum_{\mathbf{k},\sigma} \epsilon_{\mathbf{k}} c^\dagger_{\mathbf{k}\sigma} c_{\mathbf{k}\sigma} + \frac{g_0}{\mathcal{V}} \sum_{\mathbf{k},\mathbf{k}',\mathbf{q}} c^\dagger_{\mathbf{k}+\frac{\mathbf{q}}{2}\uparrow} c^\dagger_{-\mathbf{k}+\frac{\mathbf{q}}{2}\downarrow} c_{\mathbf{k}'+\frac{\mathbf{q}}{2}\downarrow} c_{-\mathbf{k}'+\frac{\mathbf{q}}{2}\uparrow} \qquad (3.24)$$

where $\epsilon_{\mathbf{k}} = \hbar^2 k^2/2m$, $\mathcal{V}$ is the volume of the system and the $c^\dagger_{k\sigma}, c_{k\sigma}$ are the usual creation and annihilation operators for fermions with momentum $\mathbf{k}$ and spin σ.

In the standard way the variational parameters ϕ_0 and $\phi_{\mathbf{qk}}$ can then be found by minimizing the energy $\left\langle \Psi | \hat{H} | \Psi \right\rangle - E_\downarrow \left\langle \Psi | \Psi \right\rangle$ under the constraint $|\langle \Psi | \Psi \rangle|^2 = |\varphi_0|^2 + \sum_{q<k_F}^{k>k_F} |\varphi_{\mathbf{kq}}|^2 = 1$

Minimizing with respect to ϕ_0 and $\phi_{\mathbf{qk}}$ leads us to the following set of coupled equations:

$$E_\downarrow \phi_0 = \epsilon_{\mathbf{k}'} \phi_0 + \frac{g_0}{V} \sum_{q<k_F} \left(\phi_0 + \sum_{k>k_F} \phi_{\mathbf{qk}} \right) \qquad (3.25)$$

$$E_\downarrow \phi_{\mathbf{qk}} = \phi_{\mathbf{qk}} (\epsilon_{\mathbf{k}} - \epsilon_{\mathbf{q}} + \epsilon_{\mathbf{k}'+\mathbf{q}-\mathbf{k}} \frac{g_0}{V} \sum_{q<k_F} \left(\phi_0 + \sum_{k''>k_F} \phi_{\mathbf{qk}''} \right)) \qquad (3.26)$$

---

[1]This treatment is identical to the $1/N$ expansion and setting $N=1$ at the end of the calculation, where $N-1$ is the number of different spin states involved. Hence, the binding energy yields the same result as in [86].

Elimination of ϕ_0 and $\phi_{\mathbf{qk}}$ finally yields a self-consistent equation for the energy $E_\downarrow$:

$$E_\downarrow \;=\; \epsilon_{\mathbf{k'}} + \frac{1}{V}\sum_{q<k_F} \frac{1}{\frac{1}{g_0} + \frac{1}{V}\sum_{k>k_F}\frac{1}{\epsilon_{\mathbf{k}}-\epsilon_{\mathbf{q}}+\epsilon_{\mathbf{k'}+\mathbf{q}-\mathbf{k}}-E_\downarrow}} \tag{3.27}$$

$$\equiv\;\; \epsilon_{\mathbf{k'}} + \Sigma(\epsilon_{\mathbf{k'}}, E_\downarrow) \tag{3.28}$$

which can be cast into the more convenient form, using $\frac{1}{g_0} = \frac{m}{4\pi\hbar^2 a} - \frac{1}{\mathcal{V}}\sum_{\mathbf{k}}\frac{1}{2\epsilon_{\mathbf{k}}}$ [23]

$$\frac{E_\downarrow}{\epsilon_F} = \frac{\epsilon_{\mathbf{k'}}}{\epsilon_F} - 2\int_0^1 \mathrm{d}y \frac{y^2}{1 - \frac{\pi}{2k_F a} - I\left(\frac{E_\downarrow}{\epsilon_F}, y\right)} \tag{3.29}$$

with the definition for the integral $I(\epsilon, y)$

$$I(\epsilon, y) = \int_1^\infty \mathrm{d}x \left(\frac{x}{2y}\ln\left(\frac{2x^2 + 2xy - \epsilon}{2x^2 - 2xy - \epsilon}\right) - 1 \right) \tag{3.30}$$

In summary, we get for the self-energy $\Sigma(\epsilon_{\mathbf{k'}}, E_\downarrow) = E_\downarrow$:

$$\frac{E_\downarrow}{\epsilon_F} = -2\int_0^1 \mathrm{d}y \frac{y^2}{1 - \frac{\pi}{2k_F a} - I\left(\frac{E_\downarrow}{\epsilon_F}, y\right)} \tag{3.31}$$

In order to get the quasiparticle residue Z and the effective mass m^*, one can combine equations 3.31, 3.28 and 3.29. The results will be discussed in the section of the experimental results 3.7.2 and 3.7.3.

3.4.1 Radiofrequency Spectroscopy of a Fermi Liquid

From the discussion following equation 3.7, it can readily be seen that the spectral function has a central meaning in radiofrequency spectroscopy: The radiofrequency photon "asks" the system for its transition probability given an energy $\hbar\omega$. Since the radiofrequency photon induces a transition to the final state regardless of a particles initial momentum, the total transition probability will be a sum over all momentum states weighted by the distribution of particles:

$$I(\omega) = 2\pi\hbar\Omega_R^2 \sum_k A(k, \epsilon_k - \mu - \hbar\omega)n_F(\epsilon_k - \mu - \hbar\omega) \tag{3.32}$$

where Ω_R is the Rabi frequency, $\omega := \omega_{RF} - \omega_{HF}$ the energy of radiofrequency photon relative to the hyperfine transition energy and $n_F(\hbar\omega) = 1/(1 + \exp(\beta\hbar\omega))$. Using equation 3.11, we can immediately see the structure of the radiofrequency

spectrum for a single quasiparticle at $k = 0$:

$$I(\omega) = 2\pi\hbar\Omega_R^2 Z\delta(\hbar\omega + E_\downarrow) + I_{\text{inc}}(\omega) \tag{3.33}$$

and is given by a sharp peak plus an incoherent background. Using the definition 3.7 for the spectral function we obtain:

$$I_{\text{inc}}(\omega) = 2\pi\hbar\Omega_R^2 \sum_{\substack{q<k_F \\ k>k_F}} |\varphi_{\mathbf{kq}}|^2 \, \delta(\hbar\omega + E_\downarrow - \epsilon_{\mathbf{k}} + \epsilon_{\mathbf{q}} - \epsilon_{\mathbf{q-k}}) \tag{3.34}$$

which can be solved analytically, see appendix C.

3.5   Generalization of the Impurity Problem

The treatment of the previous section is, of course, an idealized one. Two important generalizations will be discussed in this section:

- We have only considered a single particle in an otherwise non-interacting Fermi sea, a situation which can not be realized in our physical system. Hence, the above treatment has to be generalized to the $N + M$-body case. For finite impurity concentration, effects of the presence of the minority Fermi sea have to be taken into account. Also, residual mediated interactions between the quasiparticles will exist, similar to the case of interacting lattice polarons discussed above. By construction of Chevy's wavefunction it does not contain quasiparticle interactions. The quasiparticle interactions should in principle be computable in the T-matrix approximation. Another approach [88] has been a variational approach of the $N + M$-body problem generalizing Chevy's wavefunction. In our case of an attractive interparticle potential, quasiparticle interactions also raise the question of the range of applicability of Fermi Liquid Theory at very low temperatures: At very low temperatures one might encounter the case of pairing and condensation of polarons.

- If the binding energy of the Feshbach molecular state between the $|\downarrow\rangle$ and an $|\uparrow\rangle$ particle exceeds the Fermi energy of the $|\uparrow\rangle$ Fermi sea, we expect many-body effects to be of less importance and we expect the formation of a molecule. At this point the quasiparticle changes from a fermionic quasiparticle to a bosonic quasiparticle. However, the energy and Fermi Liquid parameters of this quasiparticle, sometimes called "Molaron" reminiscent of the term "Polaron", are

still strongly modified by the presence of the Fermi sea. Again by construction, Chevy's wavefunction does not capture this behavior. However, one can define a generalized wavefunction taking molecule formation into account [76, 89, 90].

3.5.1 $N + M = M(\text{any})$ Impurities

One step towards extending the variational wavefunction Ansatz has been made in [88]:

$$|\psi\rangle = \phi_0 |FS\rangle_\downarrow |FS\rangle_\uparrow + \sum_{\substack{q < k_F \\ k > k_F \\ r = k_F}} \phi_{\mathbf{qkr}} \Theta_{\mathbf{qkr}} c^\dagger_{\mathbf{k}\uparrow} c_{\mathbf{q}\uparrow} c^\dagger_{\mathbf{r+q-k}\downarrow} c_{\mathbf{r}\downarrow} |FS\rangle_\downarrow |FS\rangle_\uparrow \qquad (3.35)$$

This Ansatz looks more intimidating than equation 3.23 but has a similarly simple interpretation: The first term describes two non-interacting Fermi seas, the second a particle-hole excitation in the majority Fermi sea by a minority particle *at the Fermi level.* The stepfunction $\Theta_{\mathbf{qkr}} = \Theta\left(|\mathbf{r} + \mathbf{q} - \mathbf{k}| - k_{F\downarrow}\right)$ ensures the restriction $|\mathbf{r} + \mathbf{q} - \mathbf{k}| > k_{F\downarrow}$ to satisfy Pauli exclusion. Therefore, the main difference between equations 3.23 and 3.35 is the decreased phase space available for the impurity particles to scatter into. Intuitively, one might therefore expect less dressing of the polarons by majority particles resulting in a decrease in binding energy. This would imply an effective repulsive interaction between polarons. This Ansatz neglects scattering of impurity particles inside the Fermi sea and can therefore be regarded as a first step towards symmetrization of the treatment using a variational wavefunction. Accordingly, the total energy of the system as a function of impurity concentration, the zero-temperature equation of state, can be found in [88] and will not be shown here. The results show good agreement with the Monte Carlo simulations of [73], which are shown in figure 3-18.

3.5.2 Radiofrequency Spectroscopy for Finite Impurity Concentration

In this section we will consider the effect of finite impurity concentration on the radiofrequency spectrum. We will neglect the effect of quasiparticle interactions as this is still a topic of discussion and concentrate on the effect of an effective mass m^* that is different from the bare mass m. The cartoon picture is shown in figure 3-4a): As different momentum states are occupied for finite impurity concentrations, the resonance frequency will depend on the momentum $\mathbf{k}$.
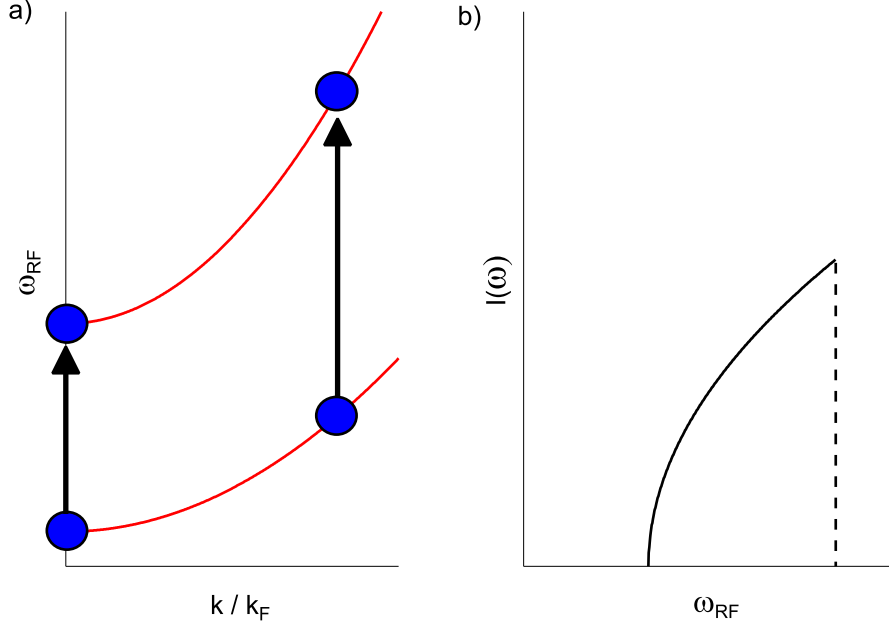
Figure 3-4: Effect of the effective mass on the minority radiofrequency spectrum. a) Different momenta will respond at different frequencies. b) The result is a continuous spectrum with a sudden drop, see equation 3.36.

The coherent part of the spectral function is thus $A_-^{\mathrm{coh}}(\mathbf{k}, \omega) = Z\delta(\hbar\omega + E(k))$ with $E(k) = -\hbar^2 k^2/2m^* = -\frac{m}{m^*}\epsilon_{\mathbf{k}}$ relative to the impurity Fermi energy. The coherent part of the spectrum then becomes

$$I_{\mathrm{coh.}}(\omega) = 2\pi\hbar\Omega_R^2 \sum_k A_-^{\mathrm{coh}}(\mathbf{k}, \epsilon_k - E_\downarrow - \hbar\omega)$$

where the sum extends up to the impurity Fermi momentum $k_{F\downarrow}$. With the free, 3D density of states $\rho(\epsilon)$, this is

$$
\begin{aligned}
I_{\mathrm{coh.}}(\omega) &= 2\pi\hbar\Omega_R^2 \int_0^{E_{F\downarrow}} \mathrm{d}\epsilon \, \rho(\epsilon) Z\delta(\epsilon - E_\downarrow - \hbar\omega - \frac{m}{m^*}\epsilon) \\
&= 2\pi\hbar\Omega_R^2 \frac{Z}{1 - \frac{m}{m^*}} \rho\left(\frac{\hbar\omega + E_\downarrow}{1 - \frac{m}{m^*}}\right) \times \\
&\quad \theta\left((1 - \frac{m}{m^*})E_{F\downarrow} - \hbar\omega - E_\downarrow\right)
\end{aligned}
\tag{3.36}
$$

This coherent part of the spectrum starts at the polaron ground state energy $\hbar\omega =$

$|E_\downarrow|$, then grows like a square root and jumps to zero when $\hbar\omega - |E_\downarrow| = (1 - \frac{m}{m^*})E_{F\downarrow}$. On resonance, where $m^* \approx 1.2$, this occurs at $\hbar\omega - |E_\downarrow| = 0.2x^{2/3}E_{F\uparrow} \approx 0.04E_{F\uparrow}$ for $x = 0.1$. This is still smaller than the Fourier width of the radiofrequency pulse used in the experiment of about $0.1\epsilon_F$. The size of the jump is given by $2\pi\hbar\Omega_R^2 \frac{Z}{1-\frac{m}{m^*}}\rho(E_{F\downarrow})$ and reflects the impurity Fermi surface in the radiofrequency spectrum. This behavior of the coherent part of the spectrum was treated in [91] and was discussed recently in [85]. Therefore, for an arbitrarily high spectral resolution the effective mass should be revealed both by the maximum and the shape in the radiofrequency spectrum.

3.5.3   Polaron vs Molaron or Fermi Liquid vs Bose Liquid

The variational wavefunction for the polaron describes, by construction, a Fermi Liquid. We expect, however, for a large bound state energy the formation of a composite boson, a molecule regardless of the presence of a Fermi sea. A rough estimate for the corresponding critical interaction strength is given by comparing the Fermi energy ϵ_F to the two-body binding energy $E_b = \frac{\hbar^2}{2m}$ resulting in $\frac{1}{(k_F a)_c} \simeq 0.7$. For higher binding energies, corresponding to smaller values of $\frac{1}{k_F a}$, the molecule will be similarly dressed by particle-hole excitations of the majority Fermi sea. Due to the internal structure of the molecule, however, the treatment shows a higher complexity and three-body physics is needed. The according variational wavefunction in the spirit of equation 3.23 is [76, 89, 90]:

$$|\psi\rangle = \left(\sum_{k>k_F} \xi_\mathbf{k} d^\dagger_{-\mathbf{k}} u^\dagger_\mathbf{k} + \sum_{\substack{q<k_F \\ k>k_F \\ k'>k_F}} \xi_{\mathbf{k}\mathbf{k'}\mathbf{q}} d^\dagger_{\mathbf{q}-\mathbf{k}-\mathbf{k'}} u^\dagger_{\mathbf{k'}} u^\dagger_\mathbf{k} u^\dagger_\mathbf{q} \right) |FS^{N-1}\rangle_\uparrow \qquad (3.37)$$

where $d^\dagger_\mathbf{k}$ and $u^\dagger_\mathbf{k}$ are the creation operators for a $|\downarrow\rangle$ particle and a $|\uparrow\rangle$ particle, respectively. The interpretation is similar to equation 3.23: Instead of a free $|\downarrow\rangle$ particle, a $|\downarrow\rangle$-$|\uparrow\rangle$ pair with zero center-of-mass momentum, a molecule, is created. The momentum, and spatial, distribution is determined by the function ξ_k. Note that the sum over the momentum states contained in the molecule is restricted to the volume outside of the majority Fermi sea due to Pauli blocking. The second term in equation 3.37 describes particle-hole excitations in the majority Fermi sea by way of imparting the momentum $\mathbf{q} - \mathbf{k}$ onto the molecule. This wavefunction can be shown to reproduce the weakly interacting limit, in which the energy is given by:
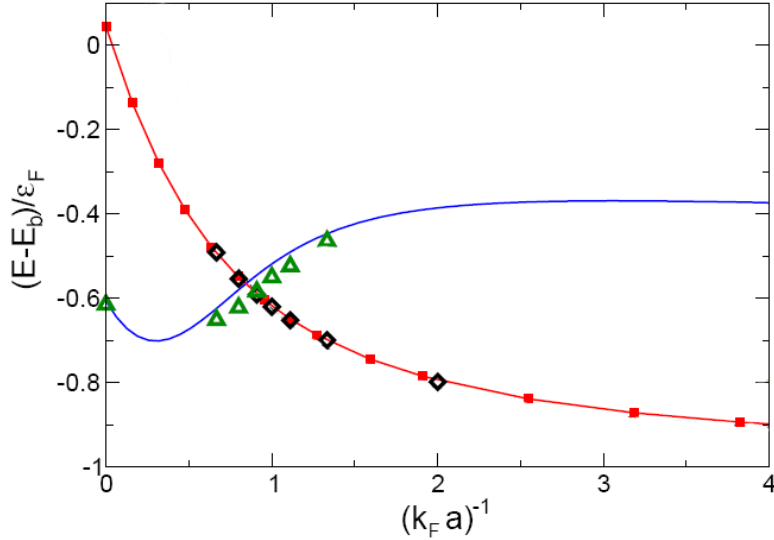
Figure 3-5: Energy of an impurity particle in a Fermi sea for various theories taken from [76]. The Ansatz 3.37 is shown as red line with full squares. For comparison, also shown are the diagrammatic Monte Carlo results (black/green diamonds) and the Ansatz 3.23 (blue line).

$$E_m = -\frac{\hbar^2}{2ma^2} + \frac{2\hbar^2\pi a_{ad}}{2/3m}n_\uparrow - \epsilon_F \qquad (3.38)$$

where a is the scattering length, $a_{ad} \simeq 1.18$ is the atom-molecule scattering length [79] and $n_\uparrow$ is the atom density. The first term is simply the two-body binding energy, the second term the density dependent mean-field shift. The full variational calculation has been done by the authors of [76, 89, 90] and is shown in Fig.3-5.

3.5.4 Finite Size Effects of the Impurity Problem

As one can see in figure 3-1, the energy of an impurity particle is significantly altered as it is not only interacting with one but N particles. An interesting question arises in an intermediate regime: How does the energy evolve for small numbers N? What happens for $N = 3$, $N = 10$, $N = 100$? This question might help understand the discrepancy between [16] and [40] in the determination of the critical density imbalance σ_c, above which the superfluid state is quenched. For better comparison with experiment, these calculations [88] have been performed for harmonic confinement. In the spirit of Chevy's wavefunction, a minority particle in an unperturbed harmonic potential plus elementary excitations in the majority, one can determine the energy

of the system [88][2]. The energy is shown in Fig. 3-6. The energies for a few particular values are $\epsilon_4 \simeq -0.0289\epsilon_F$, $\epsilon_{10} \simeq -0.135\epsilon_F$, $\epsilon_{1000} \simeq -0.51\epsilon_F$ and $\epsilon_{100,000} \simeq -0.59\epsilon_F$ in the case of an isotropic potential. For an anisotropic potential these mesoscopic effects become more pronounced, e.g. for an aspect ratio of 35 $\epsilon_{100,000} \simeq -0.56\epsilon_F$, 10% from its homogeneous value. Since the critical imbalance for the formation of a superfluid phase directly depends on the energy of the normal phase compared to that of the superfluid phase, the above results need to be borne in mind when experimental phase diagrams are compared to the homogeneous case using the local density approximation. In the case of the experiments performed at BEC1 at MIT the typical atom number is a few 10^6 and a typical aspect ratio $\alpha < 10$ the expected discrepancy is below 1% and therefore below our experimental resolution.
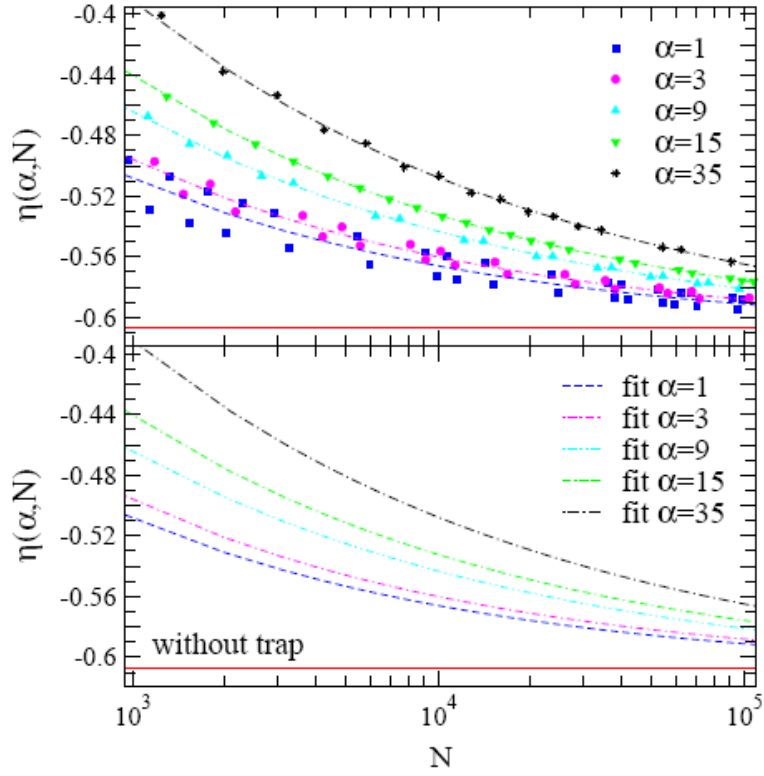
Figure 3-6: Energy $\eta(\alpha, N)$ as a function of majority particle number N for various aspect ratios α, compared to $\eta = 0.607$ for the uniform system [94] (horizontal lines).

---

[2]Pairing states beyond the variational Ansatz, such as the formation of trimers [92, 93], are naturally not included in this treatment and might not provide an accurate measure for the true ground state.

3.6 Applicability of Fermi Liquid Theory to the N+1 Body System

The treatment of Fermi liquid theory in textbooks is usually restricted to:

1. Repulsive interactions, as attractive interactions result in the Cooper-instability [5].

2. High enough temperatures such that the system does not undergo a phase transition into a superfluid or magnetic state, mediated by more subtle (attractive) interaction mechanisms (eg. phonons).

3. Low enough temperatures such that Pauli blocking results in a long enough quasiparticle lifetime for them to be treated as eigenstates of the system.

In metals this results in a temperature range of a few Kelvin up to thousands of Kelvin. For He^3 the range of validity is typically a few mK up to 1K. In our experimental system at hand, entering the superfluid phase is rendered impossible due to the number imbalance of $|\downarrow\rangle$ particles and $|\uparrow\rangle$ particles, see [95, 96] and figure 2-5. In this case, the system is guaranteed to be in the normal phase even at zero temperature. Typically, our experiments were performed at a normalized temperature of $T/T_F \simeq 0.15$ and a Fermi energy of $\epsilon_F \approx 25$kHz, resulting in a scattering rate of $(\frac{T}{T_F})^2 \epsilon_F \approx 1$kHz much smaller than ϵ_F, therefore validating a Fermi liquid approach.

It is worth noticing that our experiments constitute the first realization of a Fermi liquid with attractive interactions.

3.7 Experimental Results: Radiofrequency Spectroscopy of the Polaron

After the above theoretical preparations, let us now turn to the comparison with experiment.

As can be seen from equation 1.9, radiofrequency spectroscopy probes the single-particle excitation spectrum and is therefore ideally suited to determine the impurity binding energy with the level of precision commonly achievable employing radiofrequency spectroscopy. Furthermore, by comparing majority and minority spectra we can distinguish between the free part in equation 3.23 producing a δ-peak in the spectrum and the particle-hole excitations producing an incoherent background, see

also section 3.4.1. This allows us to determine the probability of free propagation of the minority particle, the quasiparticle residue $|\phi_0|^2 = Z$. A direct result of this is the possibility to identify a critical interaction strength, beyond which the minority forms a molecule upon encounter with a majority particle and hence $Z = 0$.

3.7.1 Preparation and Parameters

The creation of a strongly interacting degenerate Fermi gas of ^{6}Li has been described in section 1.4. For the highly number imbalanced samples on the order of $P = \frac{N_\uparrow - N_\downarrow}{N_\uparrow + N_\downarrow} > 90\%$ in this experiment we have used a two-photon Landau-Zener sweep from state $|1\rangle$ to $|3\rangle$: Using a frequency splitter in reverse, two radiofrequencies are fed into an antenna. One of the frequencies was red-detuned by 40kHz from the $|1\rangle$-$|2\rangle$ transition. The other frequency was swept over a range of 5kHz, centered around the $|2\rangle$-$|3\rangle$ transition frequency plus 40kHz. This gave a stability of the minority number characterized by fluctuations smaller than 20%. In comparison, preparation of the system using two subsequent single-photon Landau-Zener sweeps resulted in fluctuations of the minority number by a factor of 2.

The high number imbalance of $P > 90\%$ resulted in less efficient thermalization of the system than in a balanced system [19] and the temperatures we have achieved range from $T \simeq 0.12 T_F$ to $T \simeq 0.17 T_F$.

After evaporation, a radiofrequency pulse around the $|1\rangle \rightarrow |2\rangle$ ($|3\rangle \rightarrow |2\rangle$) transition frequency was applied for 500μs, resulting in a spectral resolution of 2kHz or $0.1 E_{F\uparrow}$. The power of the radiofrequency pulse was adjusted so that the maximum population transfer was $\sim 30\%$. An image was taken immediately after the radiofrequency pulse.

The two-dimensional density distribution was elliptically averaged and the three-dimensional density profile was reconstructed using the inverse Abel transform[3][66]. The local response to the radiofrequency excitation was recorded as a function of detuning from the bare hyperfine transition frequency.

Due to the inhomogeneous trapping profile the minority density varied from a maximum density to zero for almost constant density of the majority atoms. Therefore, we were able to determine the polaron energy and quasiparticle residue not only approaching the limit of a single impurity but also for higher impurity concentrations.

Typical radiofrequency spectra for low impurity concentration are shown in figure 3-7 along with the spectra of the majority component. The bulk of the majority

---

[3]The inverse Abel transform is given by $f(x,z) = -\frac{1}{\pi} \int_x^\infty dy \frac{\frac{\mathrm{d} n_{2D}(y,z)}{\mathrm{d}y}}{\sqrt{y^2 - x^2}}$, where n_{2D} is the column density.
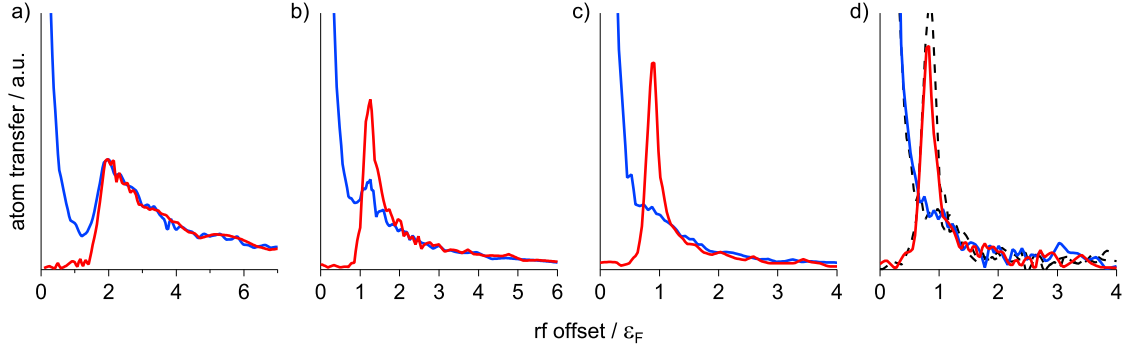
Figure 3-7: Radiofrequency spectroscopy of polarons. Shown are spatially resolved, 3D reconstructed radiofrequency spectra of the majority (blue, state $|1\rangle$) and impurity (red, state $|3\rangle$) component in a highly imbalanced spin-mixture. a) Molecular limit, b), c) Emergence of the polaron, a distinct peak exclusively in the minority component. d) At unitarity, the polaron peak is the dominant feature in the impurity spectrum, which becomes even more pronounced for $1/k_F a < 0$ (not shown). For the spectra shown as dashed lines in d) the roles of states $|1\rangle$ and $|3\rangle$ are exchanged. The local impurity concentration was $x = 5(2)\%$ for all spectra, the interaction strengths $1/k_F a$ were a) 0.76(2) b) 0.43(1) c) 0.20(1), d) 0 (Unitarity).

spectrum is found at zero offset, corresponding to the free (Zeeman plus hyperfine) energy splitting between states $|1\rangle$ and $|2\rangle$. However, interactions between impurity and majority particles lead to a spectral contribution that is shifted: The radiofrequency photon must supply additional energy to transfer a particle out of its attractive environment into the final, non-interacting state [23]. In figure 3-7a, impurity and majority spectra above zero offset exactly overlap, signalling two-body molecular pairing. The steep threshold gives the binding energy, the high-frequency wings arise from molecule dissociation into fragments with non-zero momentum [23, 10].

As the attractive interaction is reduced, however, a narrow peak appears in the impurity spectrum that is not matched by the response of the majority particles (figure 3-7b,c,d). This narrow peak, emerging from a broad incoherent background, signals the formation of the Fermi polaron. The narrow width and long lifetime are expected: At zero temperature the zero momentum polaron has no phase space for decay and is stable. At finite kinetic energy or finite temperature T it may decay into particle-hole excitations [87], but phase space restrictions due to the spin up Fermi sea and conservation laws imply a decay rate $\propto (T/T_F)^2 \sim 1\%$ in units of the Fermi energy. Indeed, the width of the polaron peak is consistent with a delta function within the experimental resolution. The full width at half maximum (FWHM) is shown in figure 3-8. On the molecular side the width of this fully incoherent disso-

ciation spectrum is a measure of the molecule size [46], but in the unitary limit and towards the BCS side of the Feshbach resonance the width of this peak approaches the experimental resolution of the radiofrequency pulse.
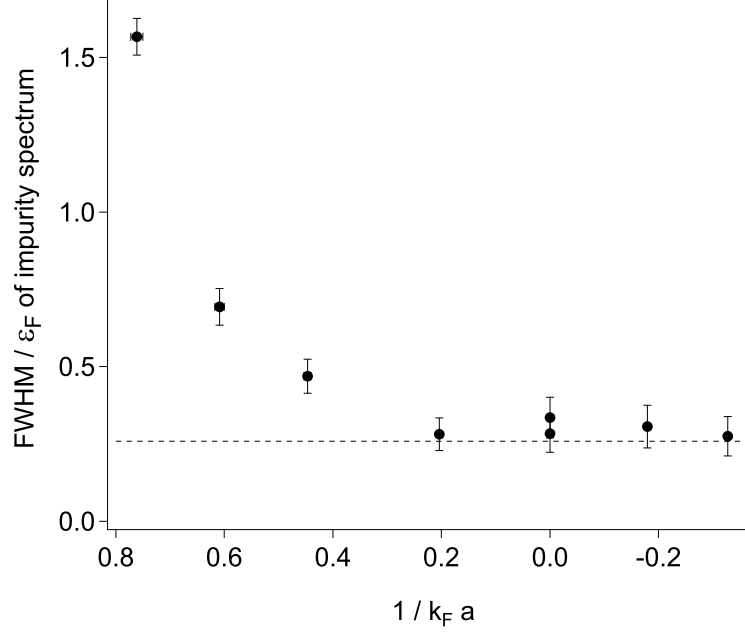
Figure 3-8: FWHM of spectra of the type shown in Fig.3-7 as a function of interaction strength. The dashed line shows the Fourier limit of a 500μs pulse.

In general, one might expect the width of the coherent polaron peak to increase with increasing impurity concentration as the polarons might be rendered unstable by interactions and have shorter lifetimes. Figure 3-9 shows a series of spectra for various impurity concentrations. Therefore, if the broadening effect is present, it is masked by our finite experimental resolution, see figure 3-8.

The incoherent background is perfectly matched by the radiofrequency spectrum of the majority particles. This is expected at high radiofrequency energies $\hbar\omega \gg \epsilon_F$ that are probing high momenta $k \gg k_F$ and thus distances short compared to the interparticle spacing. Here, an impurity particle will interact with only one majority particle, leading to overlapping spectra. We will return to this point below in chapter 3.7.4, in which we will give an estimate of the contact coefficient C.
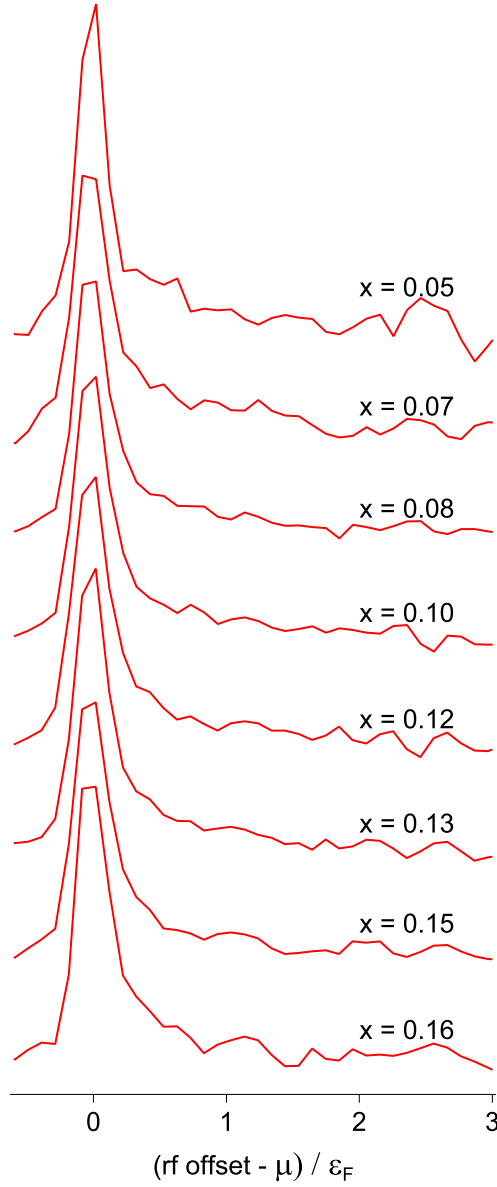
Figure 3-9: Normalized polaron spectra as a function of radiofrequency for various impurity concentrations $x = n_\downarrow/n_\uparrow$.

3.7.2   Results I:

Chemical Potential $\mu_\downarrow$ of the $N + 1$-body System

To measure the polaron energy $E_\downarrow = \mu_\downarrow$, we determine the peak position of the impurity spectrum as a function of the local interaction strength $1/k_F a$. The data for an
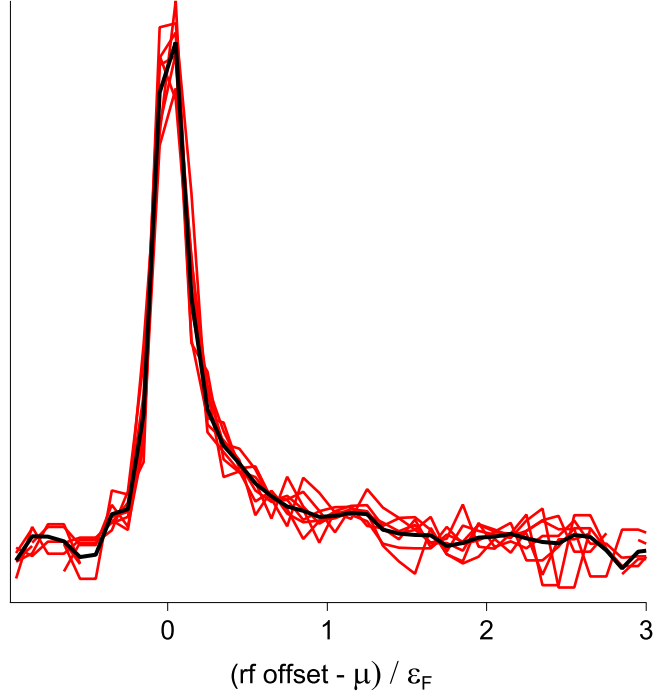
Figure 3-10: The averaged spectrum (black line) overlaps well with the individual spectra from figure 3-9 (red lines).

impurity concentration of $x = 5\%$ are shown in figure 3-11, along with the variational upper bound given by the wavefunction equation 3.23 and the diagrammatic Monte Carlo calculation of [87]. As final state interactions are weak, they can be included as a simple repulsive mean field shift $4\pi\hbar^2 a_{\mathrm{fe}} n_\uparrow / m$, with a_{fe} the scattering length between the final state and the majority atoms [65]. Polaron energies have been predicted via the variational Ansatz in equation 3.23 [78], the T-matrix approach [97, 91, 98, 99], the $1/N$ expansion [86], fixed node Monte Carlo [74, 73] and diagrammatic Monte Carlo [87]. With the exception of the $1/N$ expansion, these all agree with each other and with the present experiment to within a few percent. In particular, in the unitary limit where $1/k_F a = 0$ we find a polaron energy of $E_\downarrow = -0.64(7)\epsilon_F$ $(-0.72(9)\epsilon_F)$ when state $|3\rangle$ $(|1\rangle)$ serves as the impurity. This agrees well with the diagrammatic MC calculation, $-0.615\epsilon_F$ [100], and the analytical result $-0.6156(2)\epsilon_F$ [98]. Analysis of experimental density profiles yields a value of $-0.58(5)\epsilon_F$ [101].

The relatively large value for $E_\downarrow$ directly implies that the normal state, modeled as a Fermi sea of weakly interacting polarons, is favored over the superfluid state up to a critical concentration (44%), much higher than that predicted by mean field theories (4%) [70], see figures 2-1 and 2-2. These neglect interactions in the normal

63
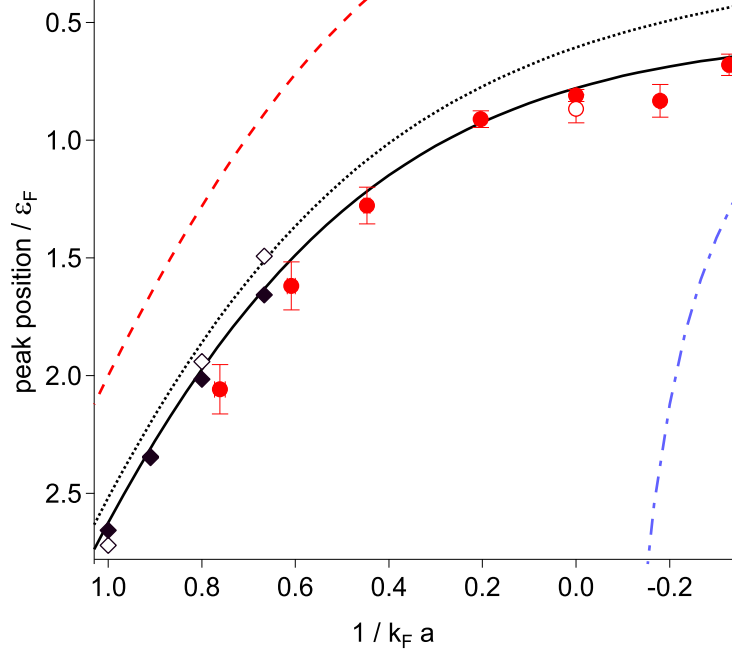
Figure 3-11: Peak position of the impurity spectrum as a measure of the polaron energy $E_\downarrow$ for various interaction strengths in the limit of low concentration $x = 5(2)\%$ (solid circles). Open circle: Reversed roles of impurity and environment. Dotted line: polaron energy from variational Ansatz equation 3.23 [78], the solid line including weak final state interactions. Dashed line: Energy of a bare, isolated molecule in vacuum. Blue dash-dotted line: Mean field limit for the energy of an impurity atom. Solid (open) diamonds: Diagrammatic Monte Carlo energy of the polaron (molecule) [87].

state and therefore imply a polaron binding energy of zero.

3.7.3   Results II: Quasiparticle Residue Z of the Polaron

The spectral weight of the polaron peak directly gives the quasiparticle residue Z. Experimentally, we determine the area under the impurity peak that is not matched by the majority's response and divide by the total area under the impurity spectrum, see figure 3-12.

Figure 3-13 presents Z as a function of interaction strength and impurity concentration x. Figure 3-14 shows Z for an impurity concentration of $x = 5\%$. As expected, Z approaches 100% for weak attractive interaction $k_F a \to 0^-$, where the bare impurity only rarely recoils off majority atoms. As the mean free path shortens and the bare impurity starts to surround itself with environment atoms Z decreases.
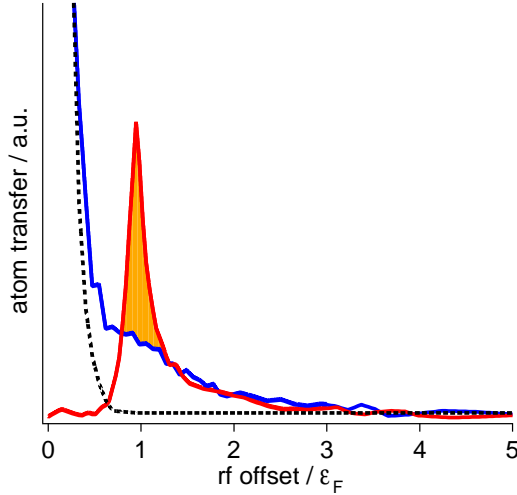
Figure 3-12: Determination of the quasiparticle residue Z. Impurity spectrum (red), majority spectrum (blue) and spectral response of non-interacting atoms (black dashed), folded over from negative radiofrequency offsets.

On resonance, we find $Z = 0.39(9)$ for $x = 5\%$, with only a weak dependence on x (figure 3-13). Theoretical values for Z vary: Ansatz Eq.(3.23) predicts $Z = 0.78$ for a single impurity, while Ref. [86] predicts $Z = 0.47$ (0.30) for vanishing (5%) impurity concentration. Our procedure might yield a lower bound on the actual value of Z, as the incoherent part of the impurity spectrum might be depleted around threshold. We have also determined an upper bound to the quasiparticle residue Z, which has been extracted under the assumption that the incoherent part of the impurity spectrum is completely depleted, see figure 3-14.

Eventually, for strong attraction between the impurity and the majority particles, Z vanishes and we observe complete overlap of the impurity and environment spectra. This signals the formation of a two-body bound state between the impurity and exactly one majority atom. For a spin down concentration of $x = 5\%$ we determine the critical interaction strength where the polaron peak vanishes to be $1/(k_F a)_c = 0.76(2)$. This is in good agreement with the independently determined critical interaction $1/k_F a = 0.74(4)$ beyond which one finds a superfluid even for the smallest impurity concentration [80]. This is a multicritical point [102, 73, 87] where a Fermi liquid of weakly interacting polarons undergoes a phase transition into a Bose liquid of molecular impurities. Fixed-node Monte Carlo calculations place this transition at a value of $1/k_F a = 0.73$ for $x \to 0$ [73]. Our $1/(k_F a)_c$ is lower than the value $0.90(2)$ from diagrammatic MC [87] for a single impurity. The Ansatz in equation 3.23 does

65
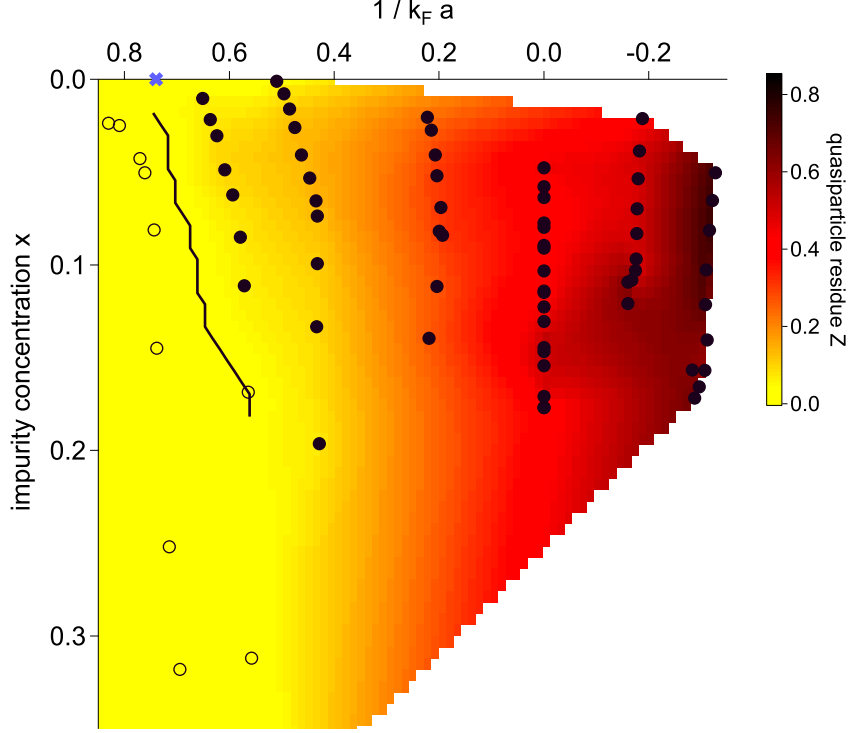
Figure 3-13: Quasiparticle residue Z as a function of interaction strength and impurity concentration. The color coding indicates the magnitude of Z and is an interpolation of the data points shown in the graph. Open circles: Data points consistent with zero ($Z < 0.03$), solid circles: $Z > 0.03$, the solid line marking the onset of Z. This defines a line of critical concentration x_c as a function of interaction strength. Blue cross: Critical interaction strength for the Fermi liquid - molecular BEC transition for $x \to 0$ [73].

not predict a transition, as it does not test for the formation of molecules. In figure 3-13, the color coding reveals where molecular behavior is observed (yellow), and where the spectra show polaronic behavior (red to black). It can be seen that the critical interaction strength for the formation of molecules depends only weakly on the impurity concentration x.

It is an interesting question what the effect of the finite temperature of $T/T_F \simeq 0.15$ is when we determine the critical interaction strength: If the polaron and the molaron state were coupled, the polaron state would exist as a thermal excitation of the molaron state for $(1/k_F a)_c > 0.76$, and vice versa. The result would be an overestimate of the critical interaction strength as there is no complete overlap if
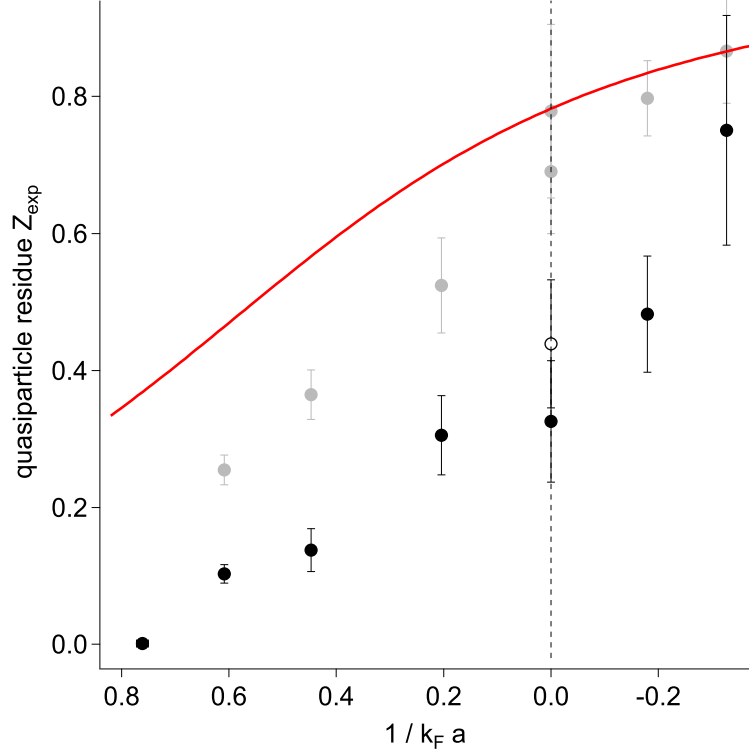
Figure 3-14: Quasiparticle residue Z as a function of interaction strength in the limit of low impurity concentration $x = 5(2)\%$. Solid black circles: State $|3\rangle$ impurity in $|1\rangle$ majority Fermi sea. Open circle: Reversed roles, state $|1\rangle$ impurity in a $|3\rangle$ majority Fermi sea. Solid grey circles: Upper limit of the quasiparticle residue determined by a Gaussian fit to the polaron peak normalized by the spectral weight of the minority. The red line is the quasiparticle residue as calculated from the variational Ansatz in equation 3.23.

part of the minority is polaronic and therefore its wavefunction delocalized. A simple estimate by much one would overestimate the critical interaction strength would consist of a comparison of our temperature to the energy difference between the two states, see the diamond data points from diagrammatic Monte Carlo calculations in figure 3-11, and would shift the critical interaction strength down by ~ 0.2 to $(1/k_F a)_c \simeq 0.56$, which is not consistent with theoretical and other experimental predictions, see previous paragraph.

However, the thermal population of the excited polaron state might evolve on a very slow time scale if the population requires breaking the molaron before formation of a polaron. This picture is similar to an endothermic chemical reaction with a large activation energy. In this case our temperature would have to be compared to the binding energy of the molaron which is several ϵ_F, see figure 3-11. Hence, the

thermal population of the polaron state would be negligible and our determination of the critical interaction strength $(1/k_F a)_c > 0.76$ unaffected by temperature.

Another caveat with respect to the determination of the critical interaction strength is the finite impurity concentration. We have shown experimentally that there is only a weak dependence on the impurity concentration. However, the phase transition from the phase separated polarized superfluid phase to the fully polarized normal phase is expected to be first order, see chapter 2.3 and figure 2-2. The minority density would therefore *jump* from a finite value to zero, making the true molaron phase inaccessible for our experiments[4].

The phase diagram revisited The black line of critical concentration x_c as a function of interaction strength has been added to figure 2-4 and validates the extrapolation of our previous study of the phase diagram based on trapped density distributions.

3.7.4   Results III: The Contact Coefficient C

After concentrating on the coherent quasiparticle peak, let us now investigate the incoherent background spectrum. At the end of chapter 3.7.1 we have given a physical interpretation of why the majority and minority spectra overlap at high radiofrequency: High energy corresponds to the large momentum components and therefore to short distances, where we expect one minority atom to interact with only one majority atom.

It can be generally shown [103] for a Fermi system interacting through a zero-range potential that the momentum distribution behaves like $n_k = \frac{C}{k^4}$, with the so-called contact coefficient C [104, 69]. This distribution at large momenta is independent of the phase or temperature[5] and is completely determined by the contact coefficient C, which is the same for both spin states, see also figure 3-3. Tan [104, 69] has derived an "adiabatic sweep theorem" which relates the contact coefficient C to the derivative of the energy of the system to the interaction strength:

$$\frac{\hbar^2 C}{4\pi m} = -\frac{\mathrm{d}u}{\mathrm{d}(1/a)} \tag{3.39}$$

with the energy density $u = E/V$. The fact that the energy of the ground state

---

[4]This argument is true only for zero temperature. In the experimentally relevant case of finite temperature, a polarized superfluid probably exists even in the limit $P \to 1$, see also figure 2-5

[5]The value of C *does* depend on the state of the system, of course.

(and the excited states) is related to C highlights the importance of the contact coefficient. The role of the contact coefficient can be further elucidated by calculating the derivative of the energy density in equation 3.39. Let us consider the general form of the Hamiltonian with contact interactions characterized by the coupling constant g:

$$H = \sum_\sigma \frac{\hbar^2}{2m} \nabla \psi_\sigma^\dagger \cdot \nabla \psi_\sigma + g\, \psi_1^\dagger \psi_2^\dagger \psi_2 \psi_1 \tag{3.40}$$

If we plug this Hamiltonian into the adiabatic sweep theorem in equation 3.39, we arrive at the following relation for the contact coefficient C:

$$
\begin{aligned}
\frac{\hbar^2}{4\pi m} C &= \frac{\mathrm{d}u}{\mathrm{d}(-1/a)} \\
&= \frac{\mathrm{d}u}{\mathrm{d}(-1/g)} \\
&= g^2 \frac{\mathrm{d}u}{\mathrm{d}g} \\
&= g^2 \left\langle \frac{\mathrm{d}H}{\mathrm{d}g} \right\rangle \\
&= g^2 \langle \psi_1^\dagger \psi_2^\dagger \psi_2 \psi_1 \rangle
\end{aligned}
\tag{3.41}
$$

where, in the second-to-last equation, we have used the Feynman-Hellman theorem [105, 106, 107, 108]. From the above equation it is clear that C can be interpreted as as the probability that an $|\uparrow\rangle$ and a $|\downarrow\rangle$ particle are close to each other, which has been formally shown by the authors of [109], hence the name contact coefficient. In general it can be shown, see [110] and references therein, that C is related to the short distance behavior of the pair correlation function $G_{\uparrow\downarrow}^{(2)}(r)$:

$$G_{\uparrow\downarrow}^{(2)}(r \to 0) \simeq \frac{C}{(4\pi)^2} \frac{1}{r^2} \tag{3.42}$$

From this one can calculate the total number of pairs of particles of opposite spin which are separated by a distance smaller than r_p:

$$
\begin{aligned}
N_{\mathrm{pair}}(r_p) &= \int_{r<r_p} \mathrm{d}^3 r\, G_{\uparrow\downarrow}^{(2)}(r) \\
&= \frac{C}{4\pi} r_p
\end{aligned}
\tag{3.43}
$$

This way, one can connect the contact coefficient to the probability of Feshbach molecules to be in the closed channel [111]. This probability has been determined by the Rice group using photoassociation spectroscopy [112].

With relation 3.39 one can immediately determine the contact coefficient for the Fermi polaron knowing the energy as a function interaction strength, see figure 3-11. As it involves a derivative of experimental data, one might get a more accurate measure by taking advantage of the high frequency wings of the polaron radiofrequency spectra, which in linear response can be calculated using Fermi's Golden Rule 1.10:

$$I(\omega \to \infty) \longrightarrow 2\pi\hbar\Omega_R^2 \sum_k \frac{C}{k^4} \delta(\hbar\omega - 2\epsilon_k + \mu) \tag{3.44}$$

where Ω_R is the Rabi frequency for the radiofrequency transfer. A comment on energy conservation in the formula above: One ϵ_k has to be "paid" for creating a particle in the final state at momentum $\mathbf{k}$. Since the radiofrequency radiation is exciting the ground state of the system, see figure 3-2 for the polaron case, removing a particle of momentum $\mathbf{k}$ out of its environment constitutes an excitation of energy $\epsilon_k - \mu$, where ϵ_k is the free particle kinetic energy. This is true only for momenta $k \gg k_F$.

Now the spectrum can be readily calculated. In order to simplify the final result, we calculate the normalized spectrum as a function of the reduced frequency $\hbar\omega \to \hbar\omega/\epsilon_F$, as they are represented in figure 3-7. We have also defined the dimensionless quantity $s = C\, k_{F\uparrow}\, k_{F\downarrow}^3$ and we measure the radiofrequency from the chemical potential μ, see also [113, 85, 114]:

$$\frac{I(\omega)}{\int I(\omega)\,\mathrm{d}\omega} = \frac{\sqrt{2}}{3} \frac{s}{(\hbar\omega)^{3/2}} \tag{3.45}$$

The generic decay of the spectra as $\omega^{-3/2}$ has already been encountered in the derivation of equal density radiofrequency spectra in the BEC-BCS crossover, see chapter 1.5.3. The normalized experimental spectra multiplied by $(\hbar\omega)^{3/2}$ should saturate at high momenta at the value of the dimensionless contact coefficient s. The results for various interaction strengths are shown in figure 3-15.

In order to increase the signal-to-noise ratio in the wings of the radiofrequency spectra we have taken advantage of the negligible change in the shape of the radiofrequency spectra as a function of position in the trap, see figure 3-10, and averaged over the normalized local minority spectra corresponding to different minority concentrations. We were thus able to extract the contact coefficient from the plateau
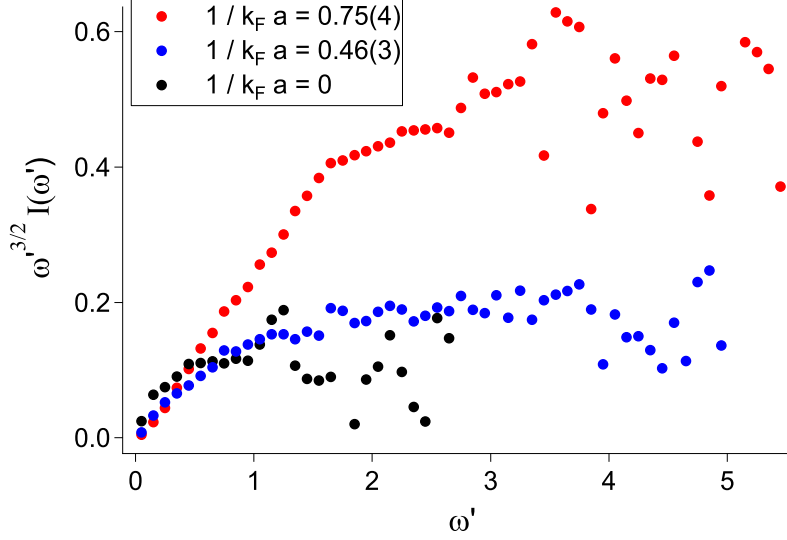
Figure 3-15: Spectra multiplied by $\omega^{3/2}$ for various interaction strengths. The tails are expected to decay as $C/\omega^{-3/2}$ with the contact coefficient C. A plateau at high ω therefore allows direct access to the contact coefficient C.

regions shown in figure 3-15 as a function of the interaction strength. The result is shown in figure 3-16. These values for the contact coefficient can be compared to the result from the model presented above 3.4. s can be readily calculated by inserting equation 3.29 into equation 3.39. The result is also shown in figure 3-16.

Our experimental data appear to be systematically below the theoretical prediction. A possible explanation is the small spectral weight in the high frequency wings, e.g. at unitarity the signal-to-noise ratio beyond $\hbar\omega/\epsilon_F = 3$ is too small for a determination of C and we have relied on the plateau $\epsilon_F < \hbar\omega < 2.6\epsilon_F$ for a determination of C. Figure 3-17 shows the comparison of the minority spectrum based on the Chevy Ansatz and the asymptotic behavior of equation 3.45.

According to the Chevy Ansatz shown in figure 3-17 one would not expect the asymptotic behavior below $\hbar\omega/\epsilon_F \simeq 4$. The spectra in figure 3-7, however, indicate perfect overlap between majority and minority components already at lower radiofrequencies on the order of $\hbar\omega/\epsilon_F \simeq 1$, which one would expect only in the high momentum limit, see also figure 3-3.

We do not expect the finite temperature of $T \simeq 0.15 T_F$ in the experiment to significantly change our extracted value of the contact coefficient as it was shown to be only weakly dependent on temperature for $T < 0.3 T_F$ due to the phonon contribution of
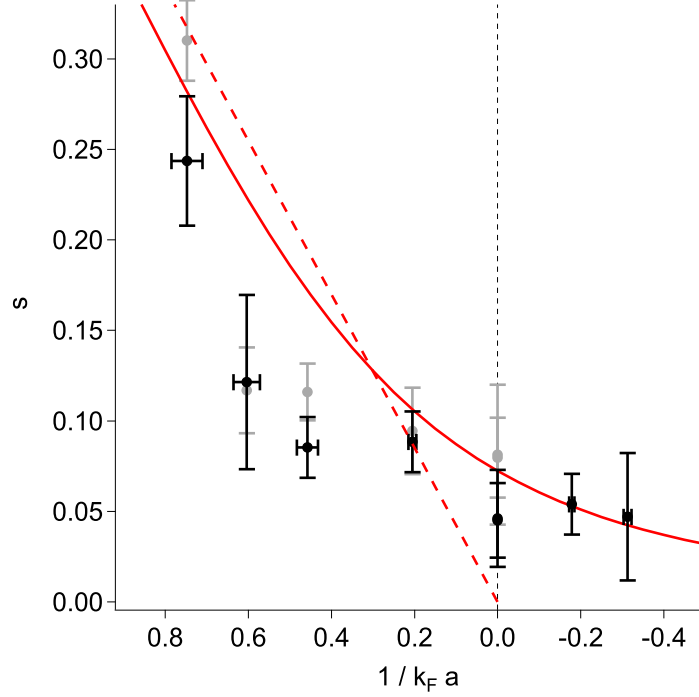
Figure 3-16: Dimensionless contact coefficient s extracted from figure 3-15 as a function of interaction strength. Solid black circles: C extracted from the high frequency wings of the minority spectra. Solid grey circles: C extracted from the high frequency wings of the majority spectra. The signal-to-noise ratio does not allow for an extraction of s on the BCS side. Solid red line: prediction according to Ansatz 3.23. Dashed red line: Contact coefficient in the BEC limit.

T^4 to the free energy [115].

It is interesting to consider the contact coefficient in the weakly interacting limits: In the deep BCS limit the energy is simply given by the mean field $U_{\mathrm{MF}} = \frac{4\pi\hbar^2 a}{m} n_\uparrow$. With equation 3.39 the dimensionless contact coefficient can immediately be determined to be $s = \frac{4}{9\pi^2}(k_F a)^2$. In the deep BEC limit with the energy given by the two-body binding energy $U = 2 E_b = \frac{2\hbar^2}{ma^2}$, the dimensionless contact coefficient is $s = \frac{4}{3\pi}\frac{1}{k_F a}$. It is also shown in figure 3-16. The predicted value for unitarity using the Chevy-Ansatz is $s = 0.072$.

In the case of a balanced system at $T = 0$, in order to find the contact coefficient, one might try to use the mean-field result for the energy as a function of the interaction strength, see chapter 1.3, and use the adiabatic sweep theorem 3.39. The result is $s = \frac{\Delta^2}{4\epsilon_F^2}$. In the BEC limit, one would expect the result to be identical to the impurity scenario as the superfluid is composed of tightly bound dimers. In the BEC limit $\Delta = \sqrt{\frac{16}{3\pi}\frac{\epsilon_F}{\sqrt{k_F a}}}$ and therefore $s = \frac{4}{3\pi}\frac{1}{k_F a}$, as in the impurity case above.
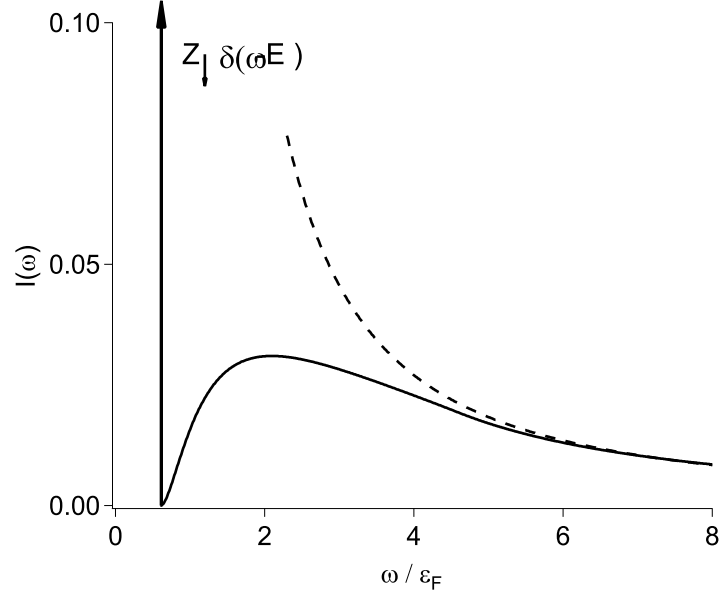
Figure 3-17: The minority spectrum calculated from the variational Ansatz equation 3.23. The incoherent background can be seen to approach the $\omega^{-3/2}$ behavior at high frequencies. One would expect this for frequencies higher than $\hbar\omega/\epsilon_F \simeq 4$.

With the general expression for the contact coefficient above, one would expect s to be exponentially small in the BCS limit. This, however, is an artefact of the shortcomings of the mean-field theory, see chapters 1.3 and 4.1. The leading order correction to this result yields $s = \frac{4}{9\pi^2}(k_F a)^2$ as in the impurity case.

At unitarity, the contact coefficient for a balanced superfluid at zero temperature is $s \simeq 0.1$ [91][113]. This is a larger value than for the polaron system, where $s = 0.072$, as the polaron has a delocalized component characterized by the quasiparticle residue Z.

To date, there are few radiofrequency spectroscopy experiments from which one could determine the contact coefficient. Early experiments using ^{40}K [116] have studied the short-range correlation between fermion pairs performing experiments in the high frequency tails of radiofrequency spectra. In early radiofrequency experiments using ^{6}Li [13, 20, 22], the high frequency tail was suppressed due to final state interactions. It has been shown [117] that the high frequency tail of the spectrum in fact decays as $\omega^{-5/2}$ instead of $\omega^{-3/2}$. This behavior is also reflected in the average clock shift [118, 91]

$$\bar{\omega} = \int \mathrm{d}\omega \, \omega I(\omega) \left/ \int \mathrm{d}\omega \, I(\omega) \right.$$

$$= \left(\frac{1}{g} - \frac{1}{g_f} \right) \frac{1}{n} \frac{\mathrm{d}(u)}{\mathrm{d}(1/g)}$$

$$= s \cdot \frac{4\epsilon_F^2}{n} \left(\frac{1}{g} - \frac{1}{g_f} \right) \qquad (3.46)$$

where $g_i = \frac{4\pi\hbar^2 a_i}{m}$, the a and a_i are the scattering lengths for the initial and final state, respectively, n is the density and where we have used the adiabatic sweep theorem 3.39 and $C = s \cdot k_F^4$ for the balanced system.

In atomic ^{6}Li, a system with a weakly interacting final state and therefore access to the contact coefficient has only recently become available [46, 44, 119]. Since the final state interactions are small but non-zero, the $\omega^{-5/2}$ behavior of the high-frequency tails in the radiofrequency spectrum will show up eventually at high enough energy. We can estimate this energy by comparing the bound state energy of the initial state E_b with the bound state energy of the final state $E_{b'}$. More precisely, based on the Franck-Condon factor describing the wavefunction overlap, it has been shown [117] that the dissociation spectrum in equation 1.11 must be modified to include the energy dependent factor $(\hbar\omega + E_b - E_{b'})^{-1}$. This factor only alters the shape of the dissociation spectrum if $\hbar\omega$ is on the order of $E_b - E_{b'}$. With $E_{b'} = \frac{\hbar^2}{ma^2}$, the bound state energy of the final state of a $|1\rangle$-$|2\rangle$ ($|1\rangle$-$|3\rangle$) molecule at 690G is on the order of 300kHz $> 10\epsilon_F$ and therefore not relevant for the spectra shown in figure 3-15. Recently [120], high-momentum transfer Bragg spectroscopy has been used to access the contact coefficient from the structure factor.

3.7.5 Results IV: Effective Mass m^* and Quasiparticle Interactions

We have so far considered the limit of few impurities. By increasing their density, we can study the effect of interactions between polarons. In figure 3-18 we show that the quasiparticle peak position depends only weakly on the impurity concentration in the unitarity limit, see also figure 3-9. Polarons are thus weakly interacting quasiparticles, despite the strong interactions between the bare impurity and its environment.

The peak position could be modified due to the effective mass m^* of polarons, larger than the mass of the bare impurity. Transfer of a moving polaron into the free final state then requires additional kinetic energy. This leads to an upshift and

a broadening on the order of the Fermi energy difference between initial and final state, $x^{2/3}\epsilon_F \left(1 - \frac{m}{m^*}\right)$. On resonance, this is $0.04\epsilon_F$ for $x = 0.1$. The effect could be partially masked by the predicted weak repulsion between polarons [73] that would downshift the resonance frequency by $-0.02\epsilon_F$ for $x = 0.1$.
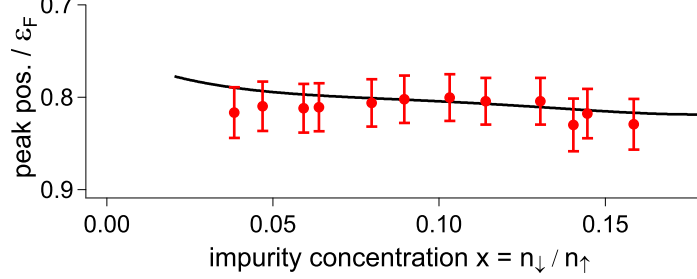
Figure 3-18: Peak position at unitarity ($1/k_F a = 0$) as a function of impurity concentration (solid circles). The line shows the expected peak position (see equation 2.7), $\hbar\omega_p/\epsilon_F = A + (1 - \frac{m}{m^*})x^{2/3} - \frac{6}{5}Fx + \frac{4}{3\pi}k_F a_{\text{fe}}$, using the Monte Carlo value $A = 0.615$ [87], the analytic result $m^* = 1.2$ [98], the weak repulsion between polarons with $F = 0.14$ [73] and weak final state interactions with scattering length a_{fe}.

3.8   Experimental Results: Collective Oscillations

As discussed at the end of chapter 3.5.2 and in previous chapter, the effect of the effective mass m^* on the radiofrequency spectrum is below our experimental resolution and one has to resort to different methods of determining m^*. Since the effective mass is a kinetic property of the system, collective excitations are a natural choice to try to experimentally access the effective mass of the polaron.

If the confining potential is harmonic $V(r) = \frac{m}{2}\omega_r^2 r^2$, in the local density approximation the effective potential experienced by the minority particle is modified due to the attraction from the majority particles:

$$W(r) = V(r) - A\epsilon_{F\uparrow}(r) \tag{3.47}$$

$$= (1 - A)V(r) \tag{3.48}$$

with the local majority Fermi energy $\epsilon_{F\uparrow}(r) = \mu - V(r)$ and $A \equiv E_\downarrow/\epsilon_F \simeq -0.6$. The attractive van der Waals interaction increases the depth of the potential seen by

the minority atom. In addition, the effective mass of the quasiparticle is modified due to the dressing with majority particles. The effective potential can be written as:

$$W(r) = \frac{m^*}{2}\omega_r^2(1+A)r^2 \tag{3.49}$$

$$\equiv \frac{m}{2}\omega'^2 r^2 \tag{3.50}$$

with the new oscillation frequency $\omega' = \omega_r\sqrt{\frac{m}{m^*}(1+A)}$. At unitarity where one expects $A \simeq 0.6$ and $m^* \simeq 1.17$, the resulting effective dipole oscillation frequency would deviate from the bare oscillation frequency ω by about 20% and should observable in experiments. There are several ways to excite this dipole oscillation:

3.8.1 Optical Potential, I

One might displace the majority cloud using a sheet of an attractive or repulsive optical potential to excite a relative motion between majority and minority. This is a relatively "violent" excitation and typically distorts the density distribution and result in a non-harmonic potential experienced by the minority atoms.

3.8.2 Optical Potential, II

One can circumvent the problem of exciting a relative motion between the two spin states if the minority cloud is created already with relative momentum. This can be done using Raman spectroscopy: Two laser beams far-detuned from the atomic transition ($\sim 1\text{GHz}$) intersect each other at the position of the atoms. The resonance condition is now momentum dependent: Only if the detuning δ between the Laser beams is chosen such that $\hbar\delta = \hbar\omega_{HF} + E_\downarrow + \frac{\hbar^2\Delta k^2}{2m}$ ($\Delta\mathbf{k}$ being the difference of the wavevectors of the lasers), atoms will be transferred into state $|2\rangle$. Therefore, minority atoms are created in state $|2\rangle$ in momentum state $\Delta\mathbf{k}$. The results are shown for the weakly interacting limit in Fig.3-19. Even for weak interactions of $k_F a \simeq 0.05$ strong damping can be observed. This might point to too a high temperature resulting in a decay of the polaron into particle-hole excitations. However, efficient cooling is notoriously difficult in this scheme as there is only a short time window for evaporative cooling after the creation of a minority cloud with momentum.
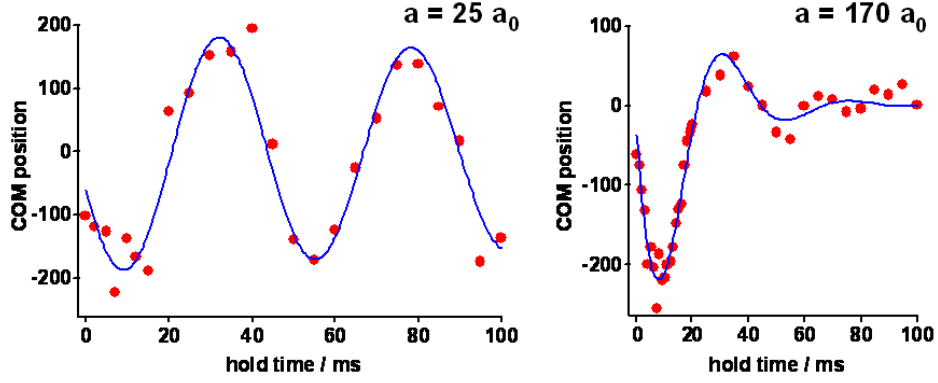
Figure 3-19: Dipole oscillations of in the weakly interacting limit.

3.8.3 Magnetic Gradient, I

The external magnetic field can be ramped to a lower value where the magnetic moments between states $|1\rangle$ and $|3\rangle$ are different enough, see figure 1-10, to initiate a relative motion between majority and minority. This method does not distort the density distribution and allows for evaporative cooling before the dipole excitation. This method has been used recently to completely separate two atomic clouds and to study the subsequent spin transport in strongly interacting Fermi systems [121]. The result for a small relative displacement is shown in figure 3-20: The oscillation can be seen to be overdamped, as the center-of-mass relaxation time is an order of magnitude higher than the oscillation frequency. This, again, might be due to the temperature of the sample being too high. We have observed that ramping the magnetic field over too wide a range tends to heat up the clouds such that it is difficult to achieve temperatures below $T/T_F \simeq 0.2$ even for equal spin mixtures.

There is an additional complication in this and the previous scheme: The majority and minority atoms are on the repulsive branch of the Feshbach resonance, see figure 1-6, and must decay into the metastable ground state first. This also presents a feature: This system can be regarded as an excited state of the polaron and it is interesting how this new state relates to the weakly interacting limits: On the molecular side, the excited state should indeed consist of two free atoms. The energy is shifted by the mean-field repulsion, see equation 3.38, of the molecules. Similarly, the energy should be mean-field shifted above the Feshbach resonance.
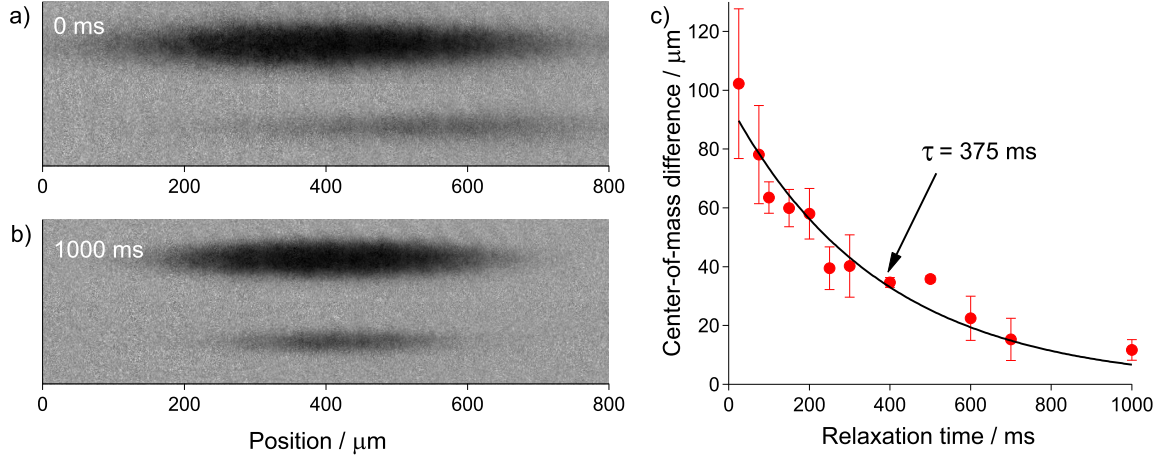
Figure 3-20: Overdamped spin dipole oscillation of an impurity particle strongly interacting with a Fermi sea. a) Initial condition: Minority cloud $\sim 130\mu$m displaced from majority center-of-mass. b) After 1000ms the minority cloud has migrated to the center. c) The center-of-mass difference of majority and minority clouds shows a slow relaxation on the time scale of several hundred milliseconds [121].

3.8.4 Magnetic Gradient, II

The problem of ramping the magnetic field over too wide a range and the complication mentioned above of excited polarons can be overcome by associating molecules by ramping the magnetic field below the Feshbach resonance and applying a magnetic field gradient. In the deep molecular limit all the minority atoms are bound in molecules in the singlet state, with zero magnetic moment and therefore not sensitive to the magnetic field gradient to first order. Dissociating the molecules by ramping above the Feshbach resonance yields polarons with a finite momentum. A complication in this scheme is that in order for the magnetic moment of the molecules to significantly differ from that of the free atoms, the molecules are so strongly bound that three-body collision are no longer Pauli-blocked. This causes loss of atoms and heating of the cloud. By completion of this thesis, we have not yet found a viable window of parameters.

3.8.5 Magnetic Gradient, III

Another method has been used recently to experimentally determine the effective mass m^*: Exciting a quadrupole oscillation by suddenly changing the magnetic field and its curvature [77]. The effect is twofold: The sudden change in the confinement,
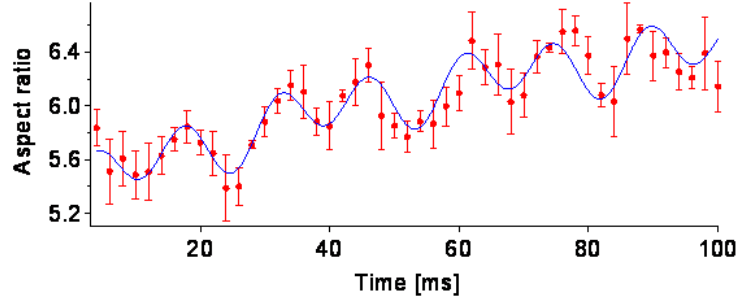
Figure 3-21: Aspect ratio of the minority cloud as a function of time after excitation of the quadrupole oscillation mode. The excitation was created by suddenly changing the scattering length

due to a change in curvature of the magnetic field, excites in an in-phase oscillation and the sudden change in the scattering length between majority and minority excites out-of-phase oscillations. The in-phase excitation is overdamped and the minority cloud size slowly relaxes whereas the out-of-phase excitation shows oscillatory behavior and allows to extract the effective mass. From the frequency of collective oscillations, Nascimbène et al. were thus able to extrapolate to the limit of high imbalance with a value for the effective mass of $m^* = 1.17(10)m$. Recently, our group has also realized these quadrupole oscillations, see figure 3-21. This method overcomes all problems mentioned above: High temperature, excited polaronic state, three-body relaxation.

3.8.6   Size Measurement

As is indicated in equation 3.50, the confining potential seen by the minority atoms is affected by the presence of the majority atoms. The attractive interaction quenches the minority cloud volume - the minority cloud is sucked into the center of the trap. For a given particle number N, in an isotropic system at $T = 0$ the minority radius is determined by $\epsilon_F \equiv \hbar\omega(6N)^3 = \frac{m}{2}\omega^2 R^2$. As a result:

$$\begin{aligned}
\frac{R_\downarrow}{R_{\downarrow 0}} &= \sqrt{\frac{m\omega}{m^*\omega'}} \\
&= \sqrt{\frac{m}{m^*}}\sqrt{\frac{m^*}{m}\frac{1}{1+A}} \\
&= \left(\frac{m}{m^*}\frac{1}{1+A}\right)^{1/4}
\end{aligned} \qquad (3.51)$$

where $R_\downarrow$ is the interacting minority Fermi radius and $R_{\downarrow 0}$ is the non-interacting minority Fermi radius for a given atom number, the bare/effective mass is m/m^* and the bare/effective dipole oscillation frequency is ω/ω' (see previous chapter).

As can be seen in equation 3.51 the size is not very sensitive to A, m^* and therefore not well suited for an accurate measurement.

Chapter 4

Quasiparticle Spectroscopy

4.1 Quantitative Studies of the BEC-BCS Crossover

We have already learned in chapter 1.3 that mean-field theories predict the correct qualitative feature but fail when put to the test of quantitative comparison. Let us briefly discuss the shortcomings of the mean-field treatment in chapter 1.3: The only simplification[1] that has been made consisted of neglecting interactions between pairs of non-zero momentum by setting $\mathbf{q} = 0$ in 1.2. This, however, has wide-ranging results: As $q = 0$, the magnitude and the phase of the gap are spatially homogeneous and therefore do not allow for density fluctuations. It has been shown in the BCS limit [122] that density fluctuations induce an interaction between the fermions in the medium, similar to the van-der Waals interaction between neutral atoms, in which the fluctuating dipole moment of one atom can induce a dipole moment in a nearby atom. The effect can be calculated to modify the interaction coefficient $V_{0,\text{eff}} = V_0 + V_0^2 N(0)\frac{1+2ln(2)}{3}$ in the BCS Hamiltonian in equation 1.2. Since $V_0 < 0$ in the BCS regime, the effective interaction strength is reduced. This lowers the value for the superfluid gap to $\Delta/E_\mathrm{F} = (2/e)^{7/3}\exp(-\pi/2k_\mathrm{F}a)$. Compared to the BCS value of $\Delta/E_\mathrm{F} = 8/e^2\exp(-\pi/2k_\mathrm{F}a)$ the value is reduced by a factor of ~ 2.2 and is known as the Gorkov Melik-Barkhudarov reduction [123] of BCS theory[2]. While the validity of the Gorkov Melik-Barkhudarov theory was originally limited to the BCS limit, when blindly applied to the unitary limit it yields a value for the superfluid gap of $\Delta \simeq 0.49\epsilon_F$, surprisingly close to the recent theoretical and experimental values

---

[1]We have also assumed a variational wavefunction, see equation 1.1. It can be shown, however, that this is the ground state wavefunction of the BCS Hamiltonian.

[2]In neutral superfluids the Gorkov Melik-Barkhudarov reduction of the superfluid gap can be significant [122], in charged superfluids the frequency at which the correction becomes important is pushed up to the Plasma frequency due to the strong Coulomb interaction [124].

[30]. Recently, the Gorkov Melik-Barkhudarov theory has been extended throughout the BEC-BCS crossover [125].

Also, in close connection to the previous point, interactions in the normal phase are not captured by equation 1.2. This has important consequences for the discussion of imbalanced Fermi gases in chapter 2 as mean-field theories overestimate the energy of the normal state. As a result, the superfluid state becomes energetically more favorable relative to the normal state and the system remains superfluid even for high density imbalances.

In general, it remains a difficult challenge to theorists to produce a quantitatively accurate model due to the absence of a small parameter in the unitary regime. The above mentioned Gorkov Melik-Barkhudarov calculation presents the second term in an expansion series that does not necessarily converge. In the unitary regime one often has to resort to Monte Carlo techniques which however suffer from the infamous sign-problem or convergence problems.

This highlights the importance of accurate quantitative experiments. In this chapter we will present a method to determine the superfluid gap using radiofrequency spectroscopy. To this end, we have identified and quantified the Hartree self-energy, which plays a crucial role in the quantitative interpretation of radiofrequency spectra. Finally, in this chapter we will make the connection between the normal polaronic phase for high imbalance and the superfluid phase for zero imbalance.

4.2 Extracting the Superfluid Gap from Radiofrequency Spectra

In this chapter we present a quantitative analysis of the spectral peaks in the superfluid phase for small density imbalance. This will allow us to determine the superfluid gap Δ at very low temperatures. Earlier work [13, 22] tried to determine the gap from the onset of the pair dissociation spectrum. However, the radiofrequency spectra are not only sensitive to final state interactions, see discussion in chapter 1.5.1, they are also shifted by Hartree energies, as we show below. Furthermore, radiofrequency spectroscopy can excite all fermions, even deep in the Fermi sea, see eg. [23]. Therefore, the onset of the pair dissociation spectrum occurs for atoms with momentum $k = 0$ and, in the BCS limit depends quadratically on the gap parameter ($\omega_{th} = \frac{\Delta^2}{2\epsilon_F}$). The excitation gap can be directly observed if quasiparticles near the dispersion minimum are *selectively* excited, as in tunneling experiments.

Since final state interactions and Hartree terms create line shifts, two peaks are needed for the analysis, the dissociation peak and the quasiparticle peak in our case. In essence, it is the separation between the peaks in spectra like fig. 4-4b, which allows us to determine Δ.

4.3   BCS Theory: Quasiparticles

We have encountered the excitation spectrum of the generalized BCS state in chapter 1.3, see figure 1-9 and have called it the quasiparticle excitation spectrum. Let us elucidate the role of quasiparticles by diagonalizing the Hamiltonian 1.2 instead of using the variational wavefunction. We will start by simplifying the interaction term and find the "best" two particle operator from the four particle operator (known as incomplete Wick contraction):

$$
\begin{aligned}
\sum_{k,k'} c_{k\uparrow}^{\dagger} c_{-k\downarrow}^{\dagger} c_{k'\downarrow} c_{-k'\uparrow} \;\rightarrow\; & \sum_{k,k'} \langle c_{-k\downarrow}^{\dagger} c_{k'\downarrow} \rangle\, c_{k\uparrow}^{\dagger} c_{k'\uparrow} \;+\; \langle c_{k\uparrow}^{\dagger} c_{-k'\uparrow} \rangle\, c_{-k\downarrow}^{\dagger} c_{k'\downarrow} \\
& -\sum_{k,k'} \langle c_{k\uparrow}^{\dagger} c_{k'\downarrow} \rangle\, c_{-k\downarrow}^{\dagger} c_{-k'\uparrow} - \langle c_{-k\downarrow}^{\dagger} c_{-k'\uparrow} \rangle\, c_{k\uparrow}^{\dagger} c_{k'\downarrow} \\
& +\sum_{k,k'} \langle c_{k\uparrow}^{\dagger} c_{-k\downarrow}^{\dagger} \rangle\, c_{k'\downarrow} c_{-k'\uparrow} + \langle c_{k'\downarrow} c_{-k'\uparrow} \rangle\, c_{k\uparrow}^{\dagger} c_{-k\downarrow}^{\dagger} \\
\equiv\; & \sum_{k} U\, (c_{k\uparrow}^{\dagger} c_{k\uparrow} + c_{k\downarrow}^{\dagger} c_{k\downarrow}) \\
& +\sum_{k} \left(\Delta\, c_{k\uparrow}^{\dagger} c_{-k\downarrow}^{\dagger} + \Delta^{*}\, c_{-k\downarrow} c_{k\uparrow} \right) \qquad (4.1)
\end{aligned}
$$

with $U = \langle c_{k\uparrow}^{\dagger} c_{k\uparrow} \rangle = \langle c_{k\downarrow}^{\dagger} c_{k\downarrow} \rangle$ and $\Delta = \sum_{k'} \langle c_{k'\uparrow}^{\dagger} c_{-k'\downarrow}^{\dagger} \rangle$. The first term is the Hartree energy, usually absorbed into the chemical potential in condensed matter systems. The second is the signature of the superfluid phase. The Fock term is zero in our case as the energies of our states $|1\rangle$ and $|3\rangle$ are not degenerate. By neglecting the quartic terms in the above contraction we have explicitly neglected fluctuations and quasiparticle interactions and we have entered the realm of the mean-field description[3]. Now the Hamiltonian is quadratic and the standard Bogoliubov

---

[3]Actually, density fluctuations have already been neglected by choosing the simplified Hamiltonian 1.2, see discussion above 4.1.

transform can be applied to diagonalize the Hamiltonian:

$$\gamma_{\mathbf{k}\uparrow} \equiv u_{\mathrm{k}}c_{\mathbf{k}\uparrow} - v_{\mathrm{k}}c^{\dagger}_{-\mathbf{k}\downarrow} \tag{4.2}$$

$$\gamma^{\dagger}_{\mathbf{k}\downarrow} \equiv u_{\mathrm{k}}c^{\dagger}_{-\mathbf{k}\downarrow} + v_{\mathrm{k}}c_{\mathbf{k}\uparrow} \tag{4.3}$$

Where the u_k, v_k must be chosen such that the $\gamma_{\mathrm{k}\uparrow}, \gamma^{\dagger}_{-\mathrm{k}\downarrow}$ obey the usual fermionic commutation rules, which results in the previous $u_k^2 + v_k^2 = 1$. Now the Hamiltonian takes the form (with $U = \sum_{\mathrm{k}} U_{\mathrm{k}}$):

$$H - \mu N + UN = \sum_{\mathbf{k},\sigma} E_{\mathbf{k}} \gamma^{\dagger}_{\mathbf{k}\sigma} \gamma_{\mathbf{k}\sigma} \tag{4.4}$$

It is indeed diagonal in the new basis $\{\gamma_{\mathrm{k}\uparrow}, \gamma^{\dagger}_{-\mathrm{k}\downarrow}\}$, where the $\gamma^{\dagger}$ are quasiparticle creation operators with the eigenenergy $E_{\mathrm{k}} = \sqrt{\Delta^2 + (\epsilon_k - (\mu - U))^2}$. It should be noted that the superfluid ground state is the quasiparticle vacuum: $\gamma_{\mathrm{k}\uparrow}|BCS\rangle = \gamma_{\mathrm{k}\downarrow}|BCS\rangle = 0$ and that a single excess particle creates a quasiparticle:

$$u_k c^{\dagger}_{\mathrm{k}\uparrow}|BCS\rangle = \left(u_k c^{\dagger}_{\mathrm{k}\uparrow} - v_{\mathrm{k}}c_{-\mathrm{k}\downarrow} \right)|BCS\rangle \tag{4.5}$$

$$= \gamma^{\dagger}_{\mathrm{k}\uparrow}|BCS\rangle \tag{4.6}$$

For very high momenta $k \gg k_F$ it can be seen from equation 1.5 that $v_k \ll 1$ and the quasiparticle is essentially a free particle, unaffected by the pairing gap, as is expected. For $k \ll k_F$ the opposite is true and the quasiparticle is essentially a free hole. At $k \simeq k_F$, the quasiparticle is a coherent superposition of a particle and a hole. At $k = k_F$, the excitation energy has a minimum and assumes the value Δ. This can be understood from a different angle: If a quasiparticle, or an excess fermion, occupies momentum state k, this momentum state is not available for Cooper pairing, raising the energy of the system by Δ. For the same reason excess fermions in an imbalanced fermion system in an inhomogeneous potential are expelled out of the superfluid in the trap center. This leads to phase separation into a balanced superfluid and a polarized normal phase, up to a critical polarization, see chapter 2.

4.3.1 Radiofrequency Spectroscopy of Quasiparticles

Let us revisit chapter 1.5.3 and consider the case of a single quasiparticle present in a BCS superfluid in a homogeneous potential. In this case the BCS spectrum should be essentially unaltered except for deviations on the order of $1/N$. The quasiparticle spectrum can be calculated easily. Energy conservation now requires $\hbar\omega_{\mathrm{RF}} \equiv -E_k +$
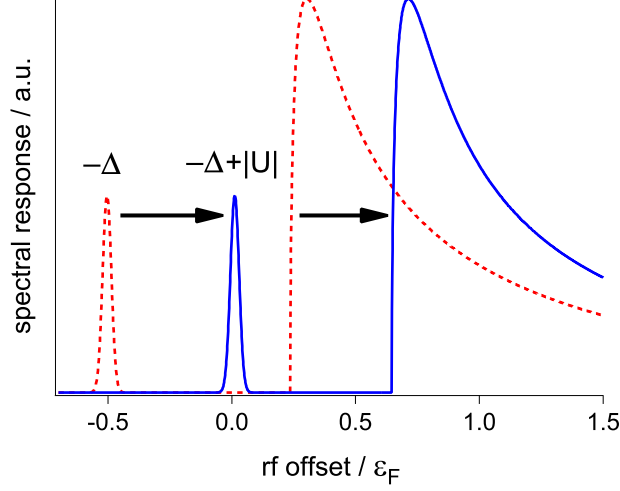
Figure 4-1: Radiofrequency spectrum with a quasiparticle at $k = k_\mathrm{F}$. The RF spectrum consists of a quasiparticle peak at a negative frequency $-\Delta$ and the pair dissociation spectrum at positive frequencies (red dotted line), see equation 4.7 and 1.11. The Hartree contribution U acts as a momentum independent effective attraction and hence shifts the entire spectrum into the positive direction (solid blue line), see equation 4.9.

$\epsilon_k - \mu$: The quasiparticle is immersed in the repulsive environment of the superfluid, hence is its energy $-E_k - \mu$ measured relative to the Fermi energy. In addition a free particle is created in the (non-interacting) final state with energy ϵ_k. The lowest energy quasiparticle has a momentum of k_F and its radiofrequency spectrum is given by:

$$I_\mathrm{QP}(\omega) \propto \delta(\hbar\omega - (-\Delta)) \tag{4.7}$$

Therefore, in the limit of small quasiparticle population, the spectral peak should *directly* reveal the superfluid gap Δ, see figure 4-1

Moreover, as quasiparticles are fermions, a finite but small population of quasiparticles should, in principle, allow to reconstruct the dispersion relation E_k around the minimum at k_F for a given temperature[4].

---

[4]For a given temperature T, the quasiparticle spectrum is given by (see equation 1.10)

$$\begin{aligned} I_{QP}(\omega) &= \int_k \mathrm{d}k\, k^2\, n_k^{QP}\, \delta(\omega - \omega_k) \\ &= \frac{f'(\omega)f^2(\omega)}{1 + \exp^{\beta\,(f^2(\omega)-\omega-\mu+h)}} \end{aligned}$$

where n_k^{QP} is the Fermi-Dirac distribution of the fermionic quasiparticles, $f^{(-1)}(k) \equiv \omega_k$ is the

Closing the Gap:
Tunneling vs Radiofrequency Spectroscopy

It is insightful to compare radiofrequency spectroscopy to tunneling experiments used to study superconducting systems: In radiofrequency spectroscopy, by flipping the spin of an atom it has been essentially removed from the system by transferring it into a non-interacting state, therefore creating a quasiparticle, see equation 4.6. In tunneling experiments, this corresponds to the transfer of an electron from the superconducting region into the normal conductor at a sufficiently high voltage of Δ/e, where e is the electron charge. As opposed to tunneling experiments the minimum energy required for the radiofrequency transition process is not Δ, but rather $\Delta^2/2E_{\mathrm{F}}$ in the BCS limit, see chapter 4.2 above[5]. Therefore, radiofrequency spectroscopy does not measure the gap Δ directly but a more complicated quantity in the BEC-BCS crossover.

The opposite process of injecting a particle into the superfluid can not be done easily in radiofrequency experiments since the final state is empty. However, in tunneling experiments an electron tunnels into the superconductor when a voltage of $-\Delta/e$ is applied, again creating a quasiparticle. Performing radiofrequency spectroscopy of quasiparticles at low concentrations, however, allows us to close this gap between tunneling and radiofrequency spectroscopy: We extract the gap not by creating a quasiparticle at k_{F} (Stokes process), but by injecting a particle at k_{F} and subsequently removing it at the cost of $-\Delta$ (Anti-Stokes process).

4.3.2　"Cold Infusion" of Quasiparticles or: The Importance of Being Imbalanced

As can be seen from the phase diagram in figure 2-5 and from the fact that the superfluid ground state is the quasiparticle vacuum, no quasiparticles will be present at $T = 0$. The quasiparticle population can be interpreted as a measure for the temperature. One might therefore be tempted to increase the temperature until a spectral signature of quasipartcles, see equation 4.7, can be observed. In a recent publication of our group [46] low temperature ($T/T_F \simeq 0.1$) radiofrequency spectra did not show

---

inverse function of f and satisfies energy conservation $f^{(-1)}(k) = -E_k + \epsilon_k - (\mu - h)$, with the Zeeman field h, see chapter 2.1. This defines a highly non-linear differential equation for $f(\omega)$ from which the quasiparticle dispersion E_k can, in principle, be deduced using the experimental spectrum $I_{QP}(\omega)$. In practice, however, even a numerical solution is difficult to find for the current experimental signal-to-noise.

[5]The reason is that the electrons of the metal in the normal state occupy all energy levels up to the Fermi energy, in cold atom experiments the final state is typically empty.
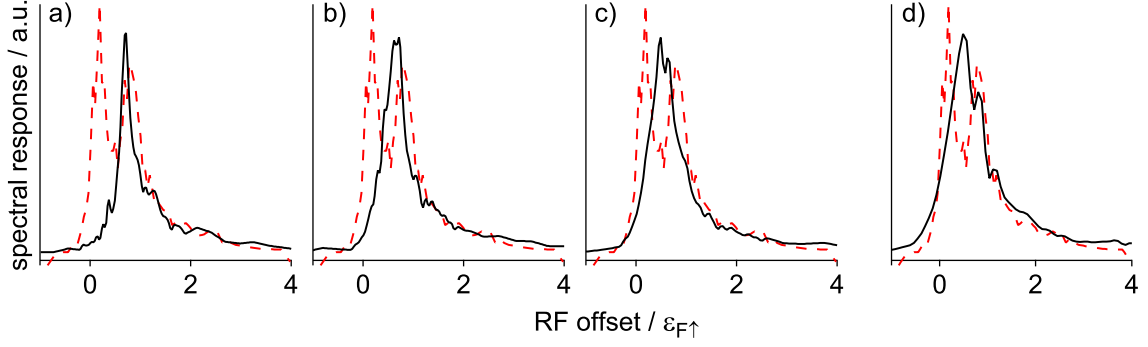
Figure 4-2: Local radiofrequency spectra of an equal spin mixture for various normalized local temperatures $T/T_{F\uparrow}$ (solid black line). a) $T/T_{F\uparrow} \simeq 0.20$, b) $T/T_{F\uparrow} \simeq 0.22$, c) $T/T_{F\uparrow} \simeq 0.34$, d) $T/T_{F\uparrow} \simeq 0.55$. No local double peak spectrum can be resolved in the radiofrequency spectrum. For comparison, the double peak spectrum of an imbalanced mixture with $T/T_{F\uparrow} \simeq 0.06$ is added (red dashed line).

any signature of the presence of quasiparticles. Using BCS theory, we can give an estimate of the temperature for which we expect a sizeable quasiparticle population: For a thermal population of quasiparticles the temperature has to be on the order of the gap Δ. In BCS theory, the temperature dependence of the gap is given by $\frac{\Delta(T)}{\Delta_0} = 1.74\sqrt{1 - \frac{T}{T_c}}$, with Δ_0 the superfluid gap at zero temperature. At unitarity, $\Delta_0/T_c \simeq 3$ (both for the mean-field treatment and Monte Carlo calculations). Therefore, one would expect to populate quasiparticles only very close to the transition temperature $T/T_c \simeq 0.95$, when the gap is only one third of its low-temperature value. The experimental results in figure 4-2 show a decrease of the spectral gap with increasing temperature, but no local double peak structures could be resolved for any temperature.

Our solution to this problem was the creation of a density imbalanced Fermi mixture at the lowest temperature we can achieve in the experiment $T/T_F < 0.1$. The associated Zeeman field h results in a splitting of the dispersion relation into two branches see equation 2.2 - the majority dispersion is given by: $E(\mathbf{k}) \to E(\mathbf{k}) - h$, see also figure 4-3. In this case the temperature needed for a sizeable quasiparticle population is decreased from Δ to $\Delta - h$. In our experiment, $\Delta - h < 0.1\epsilon_F$ and we have therefore created "cold" quasiparticles. Of course, the Zeeman field h must be smaller than the critical field $h_{c1}/\mu \simeq 0.96$ [74], beyond which the normal state becomes energetically favorable over the superfluid state. This is called the Clogston-Chandrasekhar limit [95, 96, 16] and in the BCS limit is given by $\Delta/\sqrt{2}$.
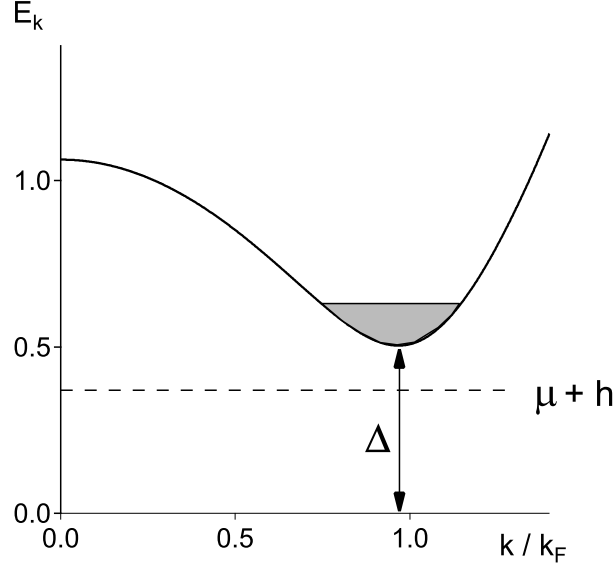
Figure 4-3: Creation of "cold" quasiparticles. The population imbalance thermally generates quasiparticles even at low temperatures on the order of $\Delta - h$, where h is the Zeeman field characterizing the number imbalance P. $\mu_\uparrow$ is defined as $\mu + h$, see equation 2.2.

4.3.3 Experimental Results and a Surprise in the Lab

Radiofrequency spectra for an imbalanced system are shown in figure 4-4. The inhomogeneous trapping profile allows us to probe the single-particle excitation spectrum in different physical regimes within a single sample by recording the local response of three-dimensional reconstructed density profiles in the final state immediately after application of the radiofrequency pulse. The spectra in figure 4-4 reveal a gradual change in the nature of the pairing correlations. The balanced superfluid is characterized by identical spectral responses of majority and minority particles and has been the subject of previous studies, see chapter 1.5.1 and the review articles [23, 126, 127] and references therein. In the polarized superfluid region [19, 70] (and references therein) the minority spectrum perfectly matches the pairing peak of the majority spectrum, locally coexisting with the quasiparticle spectral contribution, resulting in a local double peak structure of the majority spectrum, see figures 4-4b and 4.3.1.

As the local imbalance is further increased beyond the superfluid to normal (SF-N) transition [19], see figure 4-4d, the majority spectrum no longer shows a local double-peak structure. This is consistent with theoretical work [99, 128] attributing the double peak structure in the normal phase in previously reported radiofrequency spectra [13, 20] to the inhomogeneous density distribution. For increasing spin polar-
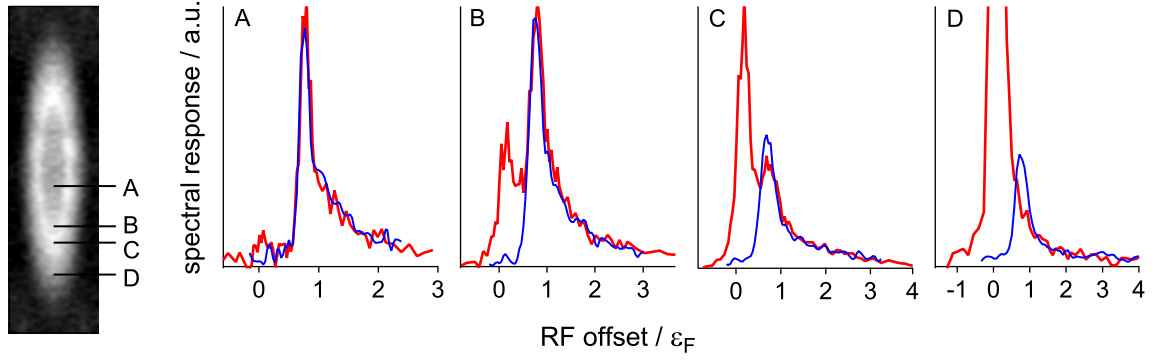
Figure 4-4: Tomographically reconstructed radiofrequency spectra for various regions of the atomic sample at unitarity. a) Balanced superfluid, b) polarized superfluid, c) moderately polarized transition region and d) highly polarized normal region. The panel on the left shows a phase contrast image of the atomic cloud before radiofrequency excitation. The positions of the spectra a) to d) are marked in the phase contrast image and by the arrows in figure 4-5. Red: Majority spectrum, blue: Minority spectrum. Local polarizations σ_{loc} and local temperature T/T_F, respectively: a) -0.04(2), 0.05(1), b) 0.03(1), 0.06(1)c) 0.19(1), 0.06(2), d) 0.64(4), 0.10(2). The negative value in a) implies that the local polarization as inferred from phase-contrast imaging underestimates σ_{loc} by up to 0.05.

ization the majority and minority pairing peaks lose spectral overlap. This missing overlap can be interpreted as indication that the minority atoms are no longer bound in pairs, each of them interacting with more than one majority atom. This is the polaronic phase which has been investigated in chapter 3. At unitarity, within our experimental resolution, the overlap starts to decrease at the superfluid-to-normal interface, see figure 4-4c.

Even when the spectral overlap decreases, there is still equal response to the radiofrequency excitation in the high frequency tails, see figure 4-4c and figure 4-4d. These tails correspond to large momentum components in the interparticle wave function and hence address the short range physics. The magnitude and functional form of the high-frequency tail are characterized by the contact coefficient C. According to the adiabatic sweep theorem, discussed in chapter 3.7.4, the contact coefficient C carries much information about the many-body state of the system. From the wings of the polaron spectra in chapter 3 we were able to estimate the contact coefficient. It is predicted to be $\approx 10\%$ larger in the superfluid state as the polaron is characterized by a delocalized component in the wavefunction, see equation 3.23. Unfortunately, in this experiment we did not explore high enough frequencies to determine the contact coefficient in the balanced superfluid the spectra multiplied by $\hbar\omega^{3/2}$ did not show a

plateau as they do in the polaron spectra, see figure 3-15.

As can be seen in figures 4-4 and 4-5 these physically very different regimes are smoothly connected across the critical density imbalance [22], see above.

A two-dimensional summary of all our results in the unitary limit is shown in figure 4-5.
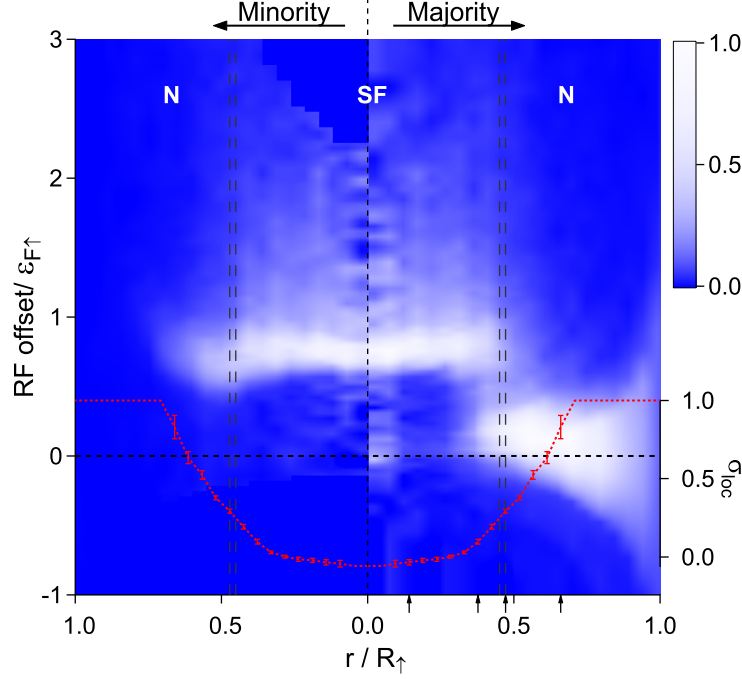
Figure 4-5: Spatially resolved RF spectra of an imbalanced Fermi gas at unitarity. a) The right half shows the majority spectra as a function of position in the trap expressed in terms of the majority Fermi radius $R_\uparrow$, the left half displays the minority spectra. The superfluid to normal transition region is marked by the gray dashed vertical lines. The local polarization σ_{loc} is given by the dashed red line. The error bars are the standard deviation of the mean value. The arrows indicate the position of the four spectra shown in figure 4-4. The image is a bilinear interpolation of 2500 data points, each plotted data point in the image is the average of three measured data points. The spatial resolution of the image is $0.045 \cdot R_\uparrow$

In figure 4-6a the position of the peaks of majority and minority spectra are plotted normalized by $\epsilon_{F\uparrow}$ as a function of position in the trap in the unitary limit. The peak positions are proportional to the local Fermi energy inside the superfluid region within our experimental resolution. In the polarized superfluid phase the spectra show local double peaks. The position of the two peaks in the limit of small polarization is depicted in figure 4-6b for various interaction strengths.
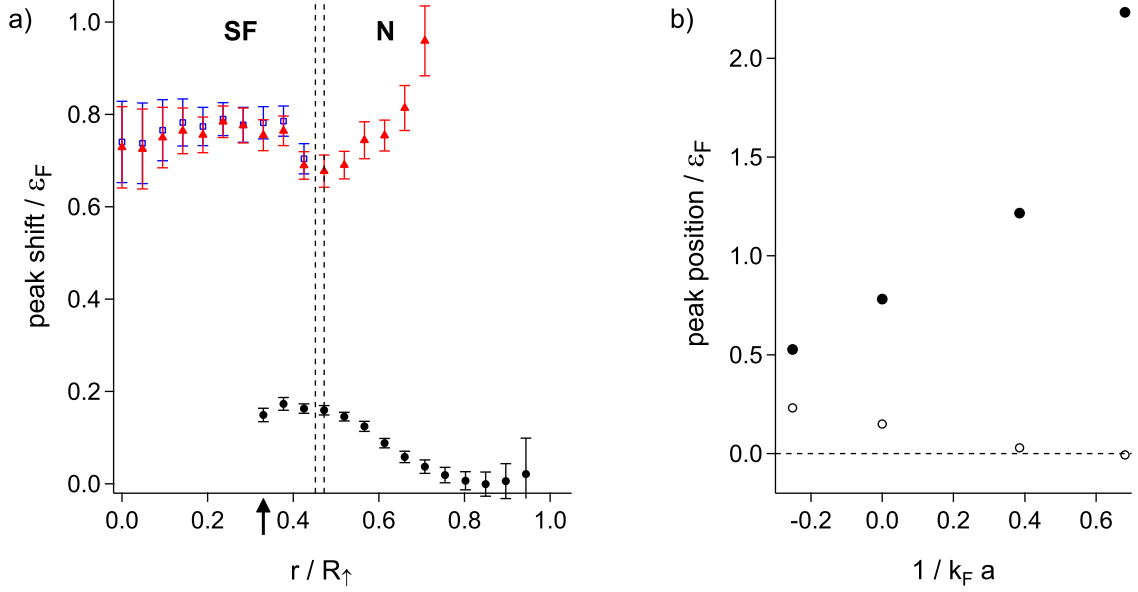
Figure 4-6: a) Normalized peak positions of pairing peaks and quasiparticle peak at unitarity as a function of position in the trap. The superfluid-to-normal boundary (cusp in column density difference, see appendix D, is marked by the dashed vertical lines. The arrow indicates the limit of low quasiparticle population relevant for b). Majority: blue open squares (pairing peak) and solid black circles (quasiparticle peak), Minority: solid red triangles. b) Pairing peak and quasiparticle peak positions as a function of the local interaction strength $1/k_F a$ in the limit of small local imbalance (see arrow in a). Pairing peak: Solid circles, quasiparticles peaks: Open circles.

One striking and initially unexpected feature of the data presented above is the position of the quasiparticle peak at positive frequencies (relative to the atomic transition frequency) - instead of being repelled out of the superfluid they seem to be attracted by it! This picture is, of course, wrong and is caused by the presence of Hartree terms, resulting in an *overall* shift of the systems energy and the radiofrequency spectrum, see below in chapter 4.3.4. In the weakly interacting limits, the Hartree term reduces to a simple mean field shift. In the strongly interacting regime one has to resort to Monte Carlo calculations [129, 74, 42] for a numerical value of U.

4.3.4   Hartree: Cause and Effect

We have seen the origin of the Hartree energy U in chapter 4.3. Let us now show what effect they have on the radiofrequency spectrum. The Hartree energy is momentum independent and can be shown to simply result in an overall shift of the spectrum.

The quasiparticle peak is located at $\hbar\omega_{\mathrm{QP}} = -E_{\mathbf{k}} + \epsilon_{\mathbf{k}} - \mu$, see chapter 4.3.1, such that the minimum is now at $\epsilon_{\mathbf{k}} = \mu - U$. It follows that the minimum excitation energy now occurs not at $k = \frac{\sqrt{2m\mu}}{\hbar}$ but rather at $k = \frac{\sqrt{2m(\mu-U)}}{\hbar}$ such that:

$$I_{\mathrm{QP}}(\omega) \propto \delta(\hbar\omega - (-\Delta + U)) \tag{4.8}$$

It is straightforward to show that with the modified dispersion the dissociation spectrum retains its functional form (equation 1.11) with a frequency axis shifted by U:

$$I(\omega') \propto \frac{\sqrt{\omega' - \omega'_{\mathrm{th}}}}{\omega'^2} \sqrt{1 + \frac{\omega'_{\mathrm{th}}}{\omega'} + \frac{\mu}{\hbar\omega'}} \tag{4.9}$$

where $\omega' = \omega + U$, $\omega'_{th} = \omega_{th} + U$ and $\mu' = \mu - U$. The maximum of the dissociation spectrum occurs at

$$\hbar\omega_{\mathrm{max}} = \frac{4}{3}\left(\sqrt{\mu'^2 + \frac{15}{16}\Delta^2} - \mu'\right) - U \tag{4.10}$$

$$\simeq \frac{4}{3}\omega_{th} - U \tag{4.11}$$

where $\mu' = \mu - U$ and ω_{th} is the dissociation threshold (which is at momentum $k = 0$).

Determination of the Superfluid Gap and the Hartree Energy

We determined the superfluid gap Δ and the Hartree energy U from the peak positions in the limit of small density imbalance ($\sigma \simeq 0.03$). At unitarity with the chemical potential $\mu = 0.42\,\epsilon_{F\uparrow}$, we obtained:

$$\Delta_{\mathrm{unit}} = 0.44(3)\,\epsilon_{\mathrm{F}\uparrow}$$
$$\text{and}$$
$$U_{\mathrm{unit}} = -0.43(3)\,\epsilon_{\mathrm{F}\uparrow} \tag{4.12}$$

in excellent agreement with the predicted values $\Delta_t = 0.45\,\epsilon_{F\uparrow}$ and $U_t = -0.43\,\epsilon_{F\uparrow}$ from Quantum Monte Carlo calculations [41]. Our determined values for Δ and U values suggest the minimum of the quasiparticle dispersion curve to occur at $k_{\mathrm{min}} \simeq 0.9k_F$. Table 4.1 shows the gap and Hartree energy for various interaction strengths. Away from unitarity we relied on Quantum Monte Carlo calculations for the chemical

Table 4.1: Superfluid gap Δ, Hartree term U and final state interaction E_{final} in terms of the Fermi energy $\epsilon_{F\uparrow}$ for various interaction strengths $1/k_F a$.

$1/k_F a$	Δ	U	E_{final}
-0.25	0.22	-0.22	0.22
0	**0.44**	**-0.43**	**0.16**
0.38	0.7	-0.59	0.14
0.68	0.99	-0.87	0.12

potential μ [33].

For an accurate quantitative comparison final state interactions, also listed in table 4.1, had to be taken into account. The effect of final state interactions is an overall mean field shift of $E_{\text{final}} = \frac{4\pi\hbar^2 a_{\text{fe}}}{m} n$. This shift affects both the quasiparticle peak and the pairing peak equally.

4.3.5 Why Should That Work?!

Above we have presented the extraction of the superfluid gap Δ and the Hartree energy U based on two assumptions: a) The quasiparticle dispersion relation is given by the mean-field result $E_k = \sqrt{\Delta^2 + (\epsilon_k - (\mu - U))^2}$, see 4.3.4, and b) the chemical potential is given by the Monte Carlo result $\mu = 0.42\epsilon_F$ [33]. This immediately raises two questions:

- The above treatment is obviously non-self-consistent as we use the dispersion from mean-field theory (which yields $\mu = 0.59$) but the chemical potential from Monte Carlo calculations $\mu = 0.42$. We have, however, stressed before that mean-field theory correctly produces qualitative features but fails for quantitative comparison, 2.2. The formula $E_k = \sqrt{\Delta^2 + (\epsilon_k - (\mu - U))^2}$ can therefore be regarded as a valid *parametrization* of the quasiparticle dispersion relation with the free parameters Δ and U.

- The exact value for the chemical potential is still under discussion and ranges from $0.32\epsilon_F$ to $0.49\epsilon_F$ [30, 31, 32, 33, 34, 35, 38, 39, 14, 40, 36, 37] at zero temperature . Moreover, this value is temperature dependent. How much does this uncertainty affect the extraction of Δ and U? Figure 4-7 shows the extracted superfluid gap and Hartree energy as a function of the value used for the chemical potential. Obviously, the dependence is weak and the variation with μ is

within the error bar. The reason for the robustness is that the value for the superfluid gap is essentially determined by the *distance* between the quasiparticle and the dissociation peak and does therefore not rely on the precise knowledge of the chemical potential. Since the quasiparticle peak is located at $-\Delta - U$, the stability of $-\Delta$ makes U stable also.
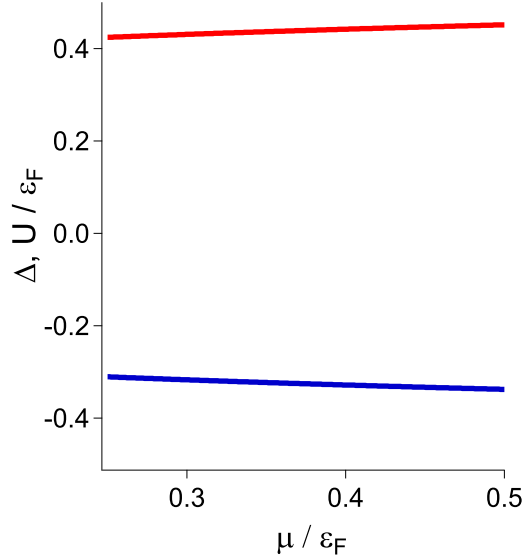
Figure 4-7: Dependence of the extracted values for Δ (red line) and U (blue line) on the assumed value for the chemical potential μ

In addition, it has to be mentioned that our determination of Δ and U is naturally not for zero temperature but for the finite local normalized temperature of $T/T_{\mathrm{F}} \simeq 0.06$. However, there is indication from finite temperature Quantum Monte Carlo calculations [42] that Δ is only weakly temperature dependent for $T/T_F < 0.15$ and that U is only weakly temperature dependent for $T/T_F < 0.3$.

Comment: Resolution / Experimental broadening For an accurate determination of the peak positions, Fourier broadening of the spectra must be taken into account: The peak of an asymmetric distribution is shifted upon convolution with the pulse duration. For comparison with the theoretical spectrum, we have modeled the radiofrequency pulse of $T = 200\mu$s length as a square pulse. This results in a FWHM of the radiofrequency spectral power of $\Delta\nu = 2 \cdot \frac{1}{2\pi} 1.39 \frac{2}{T} \simeq 4.4$kHz. The theoretical spectrum consists of the dissociation term including the Hartree energy, equation 4.9 and the quasiparticle peak modeled as a narrow (FWHM = 1 kHz) Lorentzian. This

spectrum was convolved with the Fourier transform of a square pulse $f(\omega) \propto \frac{\sin^2 \frac{\omega T}{2}}{\left(\frac{\omega T}{2}\right)^2}$.
Figure 4-8 shows that the theoretical spectrum reproduces our data quite well. The deviation in 4-8b) might be attributed to additional broadening mechanisms like finite quasiparticle lifetime, finite temperature and atomic diffusion during the duration of the radiofrequency pulse. The convolution causes a shift of $0.05\,\epsilon_{F\uparrow}$ in the spectral peak position of the dissociation spectrum and has been accounted for in the determination of Δ and U.
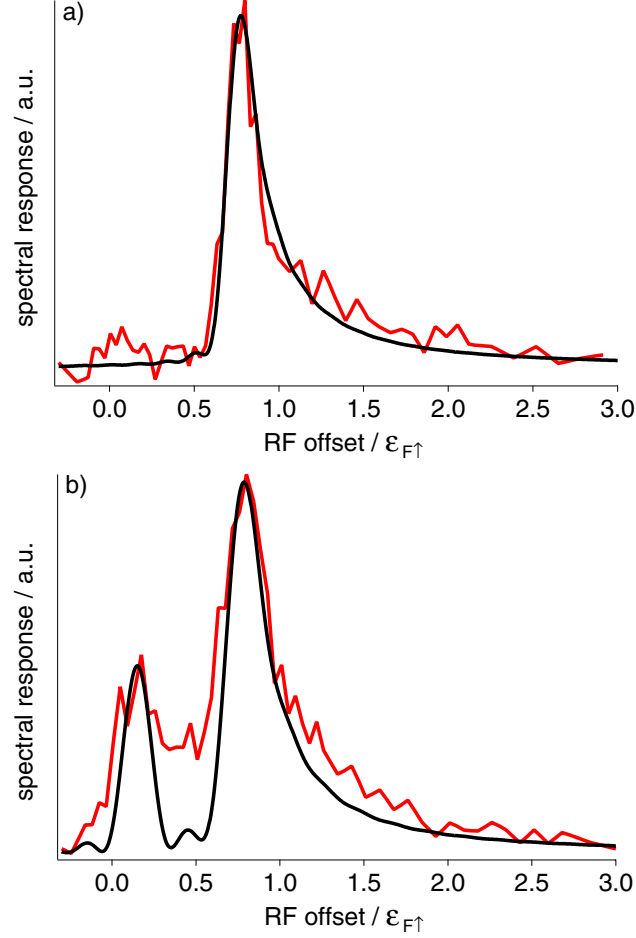
Figure 4-8: Comparison of experimental (red) and theoretical (black) line shapes for spectra a) and b) in figure 4-4. The theoretical curve is obtained from a BCS-Leggett mean field description including the Hartree term and a convolution with the experimental resolution of $\simeq 4.4$kHz (the amplitude of the spectra have been left as free fitting parameters). The values for Δ and U as calculated from the peak positions lead to a reasonable agreement with the data.

4.4 Connecting the Polaron Phase to the Superfluid Phase

So far we have focused on the balanced phase. However, the inhomogeneous trapping profile presents a cut through the phase diagram and we realize different physical regimes: Apart from the balanced superfluid core, we have realized a polarized superfluid phase for various interaction strengths (bear in mind that the experiment is not performed at zero temperature). We have identified the polarized normal region with the limiting cases of the polaronic phase and the fully spin polarized regime of an ideal Fermi gas.

One figure of merit that can be identified to distinguish the different phases is the spectral overlap, see figure 4-4. In the previous chapter 3 we have presented the quasiparticle residue Z of the polaron as a measure of the dressing of the minority particles with its surroundings. We will generalize this concept to characterize the pairing also in the moderately polarized normal region and the superfluid region and, for lack of a better word, continue to refer to it as the quasiparticle residue.

The quasiparticle residue has been extracted in the same way as for the polaronic phase, see figure 3-12 and is plotted in figure 4-9 as a function of the local polarization σ for various interaction strengths.

The two physical limits are smoothly connected. The quasiparticle residue does not change appreciably until the polarization approaches its respective critical value, suggesting that the theoretical description presented in chapter 3.4 remains accurate even away from the highly polarized limit.

Determination of the Critical Imbalance Using the Quasiparticle Residue
In chapter 2.4 we have presented a method to determine the phase boundary separating the normal phase and the phase separated superfluid phase based on the density distribution in an inhomogeneous potential. Here we will show that we can achieve very similar results by considering the local polarization σ at which the quasiparticle residue Z assume a finite value. The according data points based on the data in figure 4-9 are added to figure 2-4 and can be seen to agree well with the density profile analysis. Both of these methods yield a phase boundary at lower polarization than the zero-temperature Monte Carlo calculations, see figure 2-2. The discrepancy might be explained by the finite temperature in the experiment $T/T_F \simeq 0.1$ and a comparison should be made with finite temperature calculations, see also chapter 2.5.
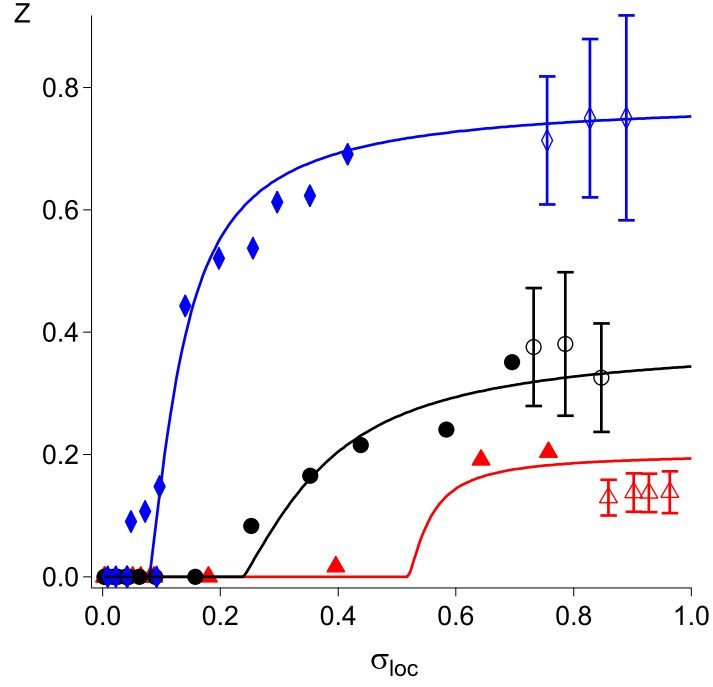
Figure 4-9: Generalized quasiparticle residue Z as a function of the local polarization $\sigma_{\mathrm{loc}} = \frac{(n_\uparrow - n_\downarrow)}{(n_\uparrow + n_\downarrow)}$ for various interaction strengths. Solid black circles: Unitary limit. Solid blue diamonds: $-0.36 < 1/k_F a < -0.24$ (BCS side). Solid red triangles: $0.34 < 1/k_F a < 0.43$ (BEC side). The open symbols represent the limit of the polaronic phase for comparable interactions strengths from the more accurate measurements of the polaron energy and the quasiparticle residue, see chapter 3. The lines are a guide to the eye and were used as a rough estimate for the critical polarizations σ_{rmloc} shown in figure 2-4.

Chapter 5

The Equation of State of a Strongly Interacting Fermi Gas at Finite Temperature

5.1 Introduction: Equation of State of a Balanced Fermi Mixture

As discussed in the previous chapters, reliable quantitative theories remain elusive in the strongly interacting regime due to the absence of a small parameter when the gas parameter na^3 diverges. However, a significant simplification arises in the unitary regime: As the scattering length diverges, it is no longer a relevant quantity for the system and all physical quantities show universal behavior, independent of the nature of the interactions. At zero temperature, the only energy scale left in the system is the chemical potential or Fermi energy $\epsilon_F = \frac{\hbar^2 k_F^2}{2m} = \frac{\hbar^2}{2m}(6\pi^2 n)^{2/3}$, where n is the density of a single component. In the universal regime energies scale as ϵ_F, times scale as $1/\epsilon_F$, velocities scale as k_F and so forth. This is called the "universality hypothesis" [130]. At finite temperature, two parameters completely describe the system, the temperature T and the chemical potential μ.

Therefore, the phase space density can be written as:

$$n\lambda^3 = f(\beta\mu) \tag{5.1}$$

with the thermal wavelength $\lambda = \sqrt{\frac{2\pi\hbar^2}{mk_BT}}$ and $\beta = 1/k_BT$ describes *any* strongly

interacting system[1] employing the universal function $f(\beta\mu)$. Equation 5.1 represents the equation of state relating the density n to the temperature T and the chemical potential μ. Starting from this equation many thermodynamic quantities can be derived. For example the pressure can be obtained using the Gibbs-Duham relation $dP = n\,d\mu + s\,dT$, which for constant temperature yields:

$$p(\mu_0) = \int_{-\infty}^{\mu_0} n\,d\mu \tag{5.2}$$

In this chapter we will present an experimental study towards a high precision determination of the Equation of State of a unitary Fermi gas at arbitrary temperature.

5.2   Inhomogeneous Potential

In the local density approximation the system can be described as locally homogeneous with a spatially dependent chemical potential $\mu_{\mathrm{loc}} = \mu - V(\mathbf{r}) = \mu - \sum_i \frac{m}{2}\omega_i^2 r_i^2$. This provides the density distribution in a harmonic trap, given the temperature T and the chemical potential μ (for simplicity, let us assume an isotropic potential $\omega_i = \omega$):

$$n(r) = \frac{1}{\lambda^3}\, f\left(\beta\mu - \beta\frac{m}{2}\omega^2 r^2\right) \tag{5.3}$$

Equivalently, if the temperature, the chemical potential and the potential profile are known, one can directly determine the equation of state $f(x)$ by inversion of the above relation:

$$f(x) = \lambda^3\, n\left(\sqrt{\frac{2}{m\omega^2}(\mu - k_B T\ x)}\right) \tag{5.4}$$

This looks more complicated than it is: Given the density distribution $n(r)$, one simply has to rescale the x-axis by finding the local $x = \beta\mu_{\mathrm{loc}}$ at position r and multiply the y-axis by λ^3.

Using equation 5.2, similar relations hold for the local pressure of the unitary Fermi gas:

---

[1]It has to be borne in mind, however, that this is only true for zero-range interactions, see also chapter 3.7.4. In cold atom experiments the effective range r_{eff} is on the order of the range of the van der Waals interaction r_0, which for alkali atoms is on the order of $50 - 100\,a_0$ and for ^{6}Li it is $r_0 = 63\,a_0$ and therefore much smaller than any other length scale.

$$p(r) = \frac{k_B T}{\lambda^3} \, F\left(\beta\mu - \beta\frac{m}{2}\omega^2 r^2\right) \qquad (5.5)$$

with the universal function $F(\beta\mu)$ being related to the function $f(\beta\mu)$ defined above: $F(x) = \int_{-\infty}^{x} \mathrm{d}(x') f(x')$. The above equation yields the formula for F:

$$F(x) = \frac{\lambda^3}{k_B T} \, p\left(\sqrt{\frac{2}{m\omega^2}(\mu - k_B T \, x)}\right) \qquad (5.6)$$

where the pressure follows from equation 5.2[2].

5.3   Temperature Measurement at Unitarity

In principle, the above determination of the equation of state is straightforward and poses no problem. Experimentally, the main challenge consists of a reliable determination of the temperature and the chemical potential. Thermometry of strongly interacting ultracold Fermi gases is a notoriously difficult problem in experiments. Different approaches have been taken to solve this problem: In imbalanced Fermi gases the shape of the non-interacting wings of the majority component have been used to determine the temperature [16, 23]. This method is obviously not applicable to the case of a balanced Fermi mixture. In balanced gases, the temperature has been determined by thermal contact with a weakly interacting bosonic bath whose temperature can be well characterized [131]. Another approach relied on fitting a non-interacting density profile to the strongly interacting profiles and rescaling of the resulting temperature. This quantity is a measure of the temperature but yields the true temperature of the system only under a series of assumptions [14]. Yet another method of temperature measurement relies on determination of the temperature in the weakly interacting limit by fitting a non-interacting density profile before adiabatically bringing the mixture into the unitary regime, see for instance [12]. Again, this only yields a quantity characterizing the temperature but not the true temperature, which changes during an adiabatic sweep. Here we will present a different approach based on the virial expansion of the equation of state.

---

[2]For a harmonic potential, $\mu = \mu_0 - \frac{m}{2}\omega^2 r^2$. The pressure then can be written as $p(r) = \frac{m}{2}\omega^2 \int_r^\infty \mathrm{d}r \, 2r \, n(r)$ and is basically given by the one-dimensional density distribution.

5.3.1 Virial Expansion

At high temperatures $T \gg \mu$ or $\beta\mu \ll 1$, quantum statistics can be neglected and every gas looks like an ideal gas. The phase space density is simply given by the Boltzmann distribution $e^{\beta\mu}$ and the equation of state is $n(r) = e^{\beta\mu}/\lambda^3$ independent of statistics or interactions. This is the first term in an expansion in powers of the fugacity $e^{\beta\mu}$:

$$n\lambda^3 = f(\beta\mu) \equiv \left(e^{\beta\mu} + 2\, b_2\, e^{2\beta\mu} + 3\, b_3\, e^{3\beta\mu} + ... \right) \tag{5.7}$$

where the coefficients b_i are the virial coefficients. Bear in mind that that the phase space density is small at high temperatures $n\lambda^3 \ll 1$, and hence the chemical potential negative $\mu < 0$. Therefore, the value of the fugacity for which the series expansion in equation 5.7 converges, is restricted to $0 < e^{\beta\mu} < 1$.

Similarly, for the pressure we have the expansion:

$$p\frac{\lambda^3}{k_B T} = F(\beta\mu) \equiv \left(e^{\beta\mu} + b_2\, e^{2\beta\mu} + b_3\, e^{3\beta\mu} + ... \right) \tag{5.8}$$

The virial coefficients for the unitary Fermi gas are $b_2 = \frac{2\sqrt{2}}{8}$ [132, 133] and $b_3 = 0.29095295$ [134]. Therefore, equation 5.7 provides a robust method to fit the wings of a balanced Fermi gas. Care has to be taken that the fitting range entails only regions of a sufficiently negative chemical potential as the virial expansion up to third order is expected to be valid only for $\beta\mu_{\mathrm{loc}} < -0.8$. At this point, the virial expansion deviates from the diagrammatic Monte Carlo calculation [135] by more than 1%. For the integrated density, yielding the pressure, see equation 5.2, it is expected to be valid up to $\beta\mu_{\mathrm{loc}} < -0.4$. The value of the *local* $\beta\mu_{\mathrm{loc}}$ of course depends on the fit yielding the *global* $\beta\mu$ and $\beta\mu$ has to be determined self-consistently.

5.3.2 Effects of the Trap: Harmonic vs Gauss

All data in cold atom experiments consist of projection images of an atom cloud. The two-dimensional density distribution $n_{2D}(x, z)$ is given by the integral of the three-dimensional density $n_{3D}(x, y, z)$ along the imaging axis, here denoted as the y-axis.

Harmonic Potential

In the case of a harmonic potential, the temperature determination using the virial expansion 5.7 is a straightforward Gaussian integral:

$$n_{2D}(x,z) \;=\; \int_{-\infty}^{\infty} \mathrm{d}y \; n_{3D}(x,y,z) \tag{5.9}$$

$$\;=\; \frac{1}{\lambda^2}\frac{k_B T}{\hbar\omega_y}\sum_k b_k \sqrt{k}\; e^{k\beta\left(\mu - \frac{m}{2}(\omega_x^2 x^2 + \omega_z^2 z^2)\right)} \tag{5.10}$$

$$n_{1D}(r) \;=\; \frac{1}{\lambda^2}\frac{(k_B T)}{\hbar\omega_y}\sum_k b_k \sqrt{k}\; e^{k\beta\left(\mu - \frac{m}{2}\omega_r^2 r^2\right)} \tag{5.11}$$

The last equality holds for an elliptically averaged density distribution.

Gaussian Potential

Typically, see chapter 1.4, in order to access a Feshbach resonance to enter the unitary regime, the atoms are radially trapped in the potential well created by a focussed laser beam red-detuned from the dominant atomic transition. The laser beam emanates from an optical fiber and is well characterized as a TEM_{00} mode. The potential well experienced by the atoms can therefore be written as:

$$V(x,y) = V_0\left(1 - e^{-2\frac{x^2+y^2}{w^2}}\right) \tag{5.12}$$

where the trap depth V_0/k_B is typically on the order of a few μK and in our setup the waist[3] is $w = 70.5\mu$m. Along the third axis, the atoms are trapped by a magnetic curvature[4] characterized by a trapping frequency of $\omega_z = 2\pi \cdot 22.83$Hz. As a typical Fermi energy is on the order of 1μK, anharmonicities play a significant role for this high precision study, see figure 5-1.

Since we typically operate at trap filling factors $0.2 < \eta < 0.5$, we can not neglect the effects of anharmonicity. Therefore, in order to determine the temperature and the chemical potential from the virial expansion in equation 5.7, one has to do one of the following:

---

[3]The power of the infrared laser beam was measured before entering the chamber through a penny window and after leaving the chamber through the opposite penny window. The total power loss was 13% so that the laser power at the position of the atoms was 93.3%. The waist was determined using a beam profiler at the position of the image of the ODT focus outside the chamber, close to the position of the CCD camera chip.

[4]In equation 5.12 we have neglected the confinement along the z-direction resulting from the optical potential, which is given by $V(z) = V_0(1 - \frac{1}{1+\frac{z^2}{z_R^2}})$ with the Rayleigh range $z_R = \frac{\pi w_0^2}{\lambda}$. In our case with a waist of $w_0 = 70.5\mu$m and a wavelength of $\lambda = 1064$nm, the Rayleigh range is $z_R \simeq 14$mm, resulting in a typical trapping frequency of $\omega_{z,ODT} = \sqrt{\frac{2V_0}{mz_R^2}} \simeq 2\pi \cdot 1$Hz. This changes the trapping frequency of the magnetic potential along the z-axis by less than one per mille.
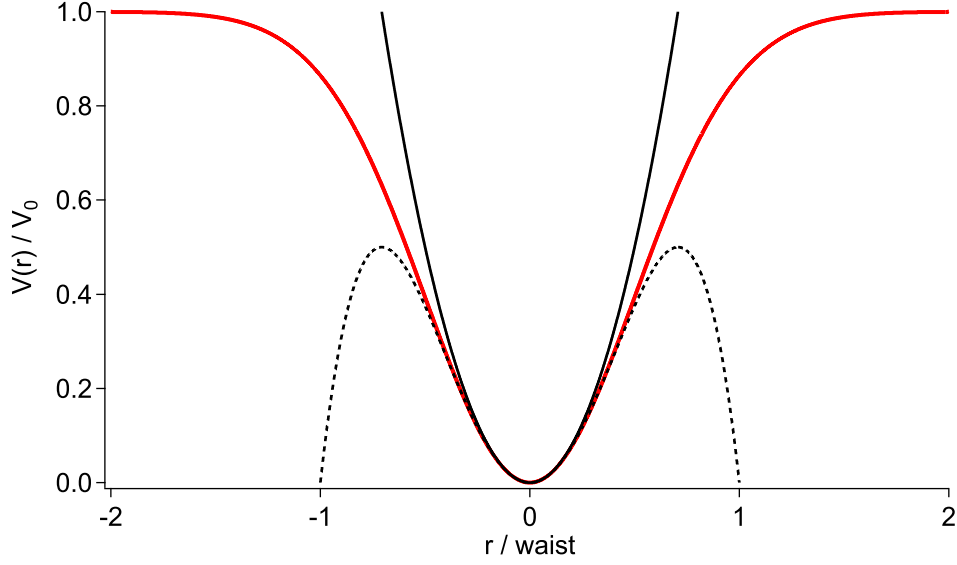
Figure 5-1: Comparison of the radial trapping potential to the harmonic approximation and the quartic correction.

Method I: Integrate the virial expansion 5.7 along the imaging axis and use the two-dimensional fitting function to $n_{2D}(x, z)$:

$$n_{2D}(x, z)\lambda^3 \quad = \quad \int_{-\infty}^{\infty} dy \, n_{3D}(x, y, z) \tag{5.13}$$

$$= \quad \int_{-\infty}^{\infty} dy \sum_k k \, b_k \, e^{k\beta\mu - k\beta\frac{m}{2}\omega_z^2 z^2} e^{-k\beta V_0\left(1 - e^{-2\frac{x^2+y^2}{w^2}}\right)} \tag{5.14}$$

$$\equiv \quad \sum_k k \, b_k \, e^{k\beta\mu - k\beta\frac{m}{2}\omega_z^2 z^2} \, S_k(\beta, x) \tag{5.15}$$

While this can be done, it has a few disadvantages. Two-dimensional fits are less robust as the final fit tends to depend on the initial guess for the fitting parameters. Also, the integral along the imaging direction $S_k(\beta, x)$ has to be done numerically in each step of the fitting procedure, resulting in slow fitting routines.

Method II: Reconstruct the three-dimensional density $n_{3D}(x, y, z)$ from the two-dimensional density $n_{2D}(x, z)$ using the inverse Abel transform[5][66]. A potential disadvantage is the loss of signal-to-noise in the data since the inverse Abel transform

---

[5]If a function $f(r, z)$ is cylindrically symmetric, the inverse Abel transform is given by $f(x, z) = -\frac{1}{\pi} \int_x^{\infty} dy \frac{\frac{dn_{2D}(y,z)}{dy}}{\sqrt{y^2 - x^2}}$, where $n_{2D}(y, z)$ is the column density.

involves a derivative of experimental data. This can be alleviated by performing an appropriate averaging procedure over equipotential lines[6]. One has to average all pixels in an image belonging to the same three-dimensional potential, see figure 5-2.
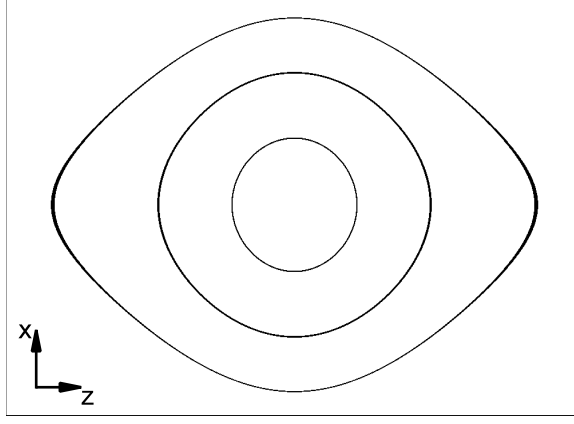
Figure 5-2: Equipotential lines for a hybrid potential: Harmonic confinement along the x-axis, Gaussian confinement along the z-axis.

We can thus "collapse" all pixels in the image into a one-dimensional form, whose high-energy wings can be fit independently of the actual trapping potential by the simple fitting function based on the virial expansion:

$$n(V) = \frac{1}{\lambda^3} \left(\sigma_{\text{loc}} + 2\, b_2\, \sigma_{\text{loc}}^2 + 3\, b_3\, \sigma_{\text{loc}}^3 \right) \tag{5.16}$$

with the local fugacity $\sigma_{\text{loc}} \equiv e^{\beta\mu - \beta V}$.

Method III: An improved signal-to-noise ratio can be obtained by an integration over the density distribution, yielding the pressure $p = \frac{k_B T}{\lambda^3} F(\beta\mu)$, see equations 5.2 and 5.8. One can now employ partial integration to avoid taking the derivative of experimental data in the inverse Abel transform and instead take the derivative of the potential [136]:

$$p(\rho_0, z) = \frac{1}{\pi} \int_{\rho_0}^{\infty} \mathrm{d}y \; n_{2D}(y, z) \left[\frac{\frac{\partial V}{\partial \rho}(y, z)}{\sqrt{y^2 - \rho_0^2}} + \int_{\rho_0}^{y} \mathrm{d}\rho \, \frac{\rho \frac{\partial V}{\partial \rho}(y, z) - y \frac{\partial V}{\partial \rho}(\rho, z)}{(y^2 - \rho^2)^{(3/2)}} \right] \tag{5.17}$$

For the case of the Gaussian potential from equation 5.12, this equation becomes:

---

[6]This can *not* be done before the reconstruction procedure due to the Gaussian potential.

$$p(\rho_0, z) = \frac{1}{\pi} \frac{4V_0}{w^2} e^{(-2\frac{\rho_0^2}{w^2})} \int_0^\infty du \, n_{2D} \left(\sqrt{u^2 + \rho_0^2}, z \right) \left(1 - 2\sqrt{2}\frac{u}{w} D \left(\sqrt{2}\frac{u}{w} \right) \right) \quad (5.18)$$

with the definition $D(x) = e^{-x^2} \int_0^\infty du \, e^{u^2}$ for the Dawson function and V_0 and w characterizing the optical trapping potential[7].

With the above equation for the two-dimensional pressure, one can now perform the appropriate averaging procedure described above and depicted in figure 5-1 to arrive at the one-dimensional pressure $p(V)$, whose high-energy wings can be fit by the simple fitting function based on the virial expansion:

$$p(V) = \frac{k_B T}{\lambda^3} \left(\sigma_{\text{loc}} + b_2 \, \sigma_{\text{loc}}^2 + b_3 \, \sigma_{\text{loc}}^3 \right) \quad (5.19)$$

with the local fugacity $\sigma_{\text{loc}} \equiv e^{\beta\mu - \beta V}$.

We have employed all three methods successfully to extract the temperature and the chemical potential, with the second and third method being more robust and less time consuming. The third method has the advantage of a higher signal-to-noise ratio and the virial expansion being valid for higher values of $\beta\mu$, see chapter 5.3.1. In the following chapter we will present the results for a unitary Fermi gas.

5.3.3   Determination of the Temperature

Figure 5-3 shows a typical pressure curve $p(V)$ as a function of the potential V, see previous chapter. The zoom-in shows the region in which the virial expansion equation 5.19 is valid.

The local value of $\beta\mu_{\text{loc}}(z) = \beta\mu - \beta V$ depends on the fitted values for $\beta\mu$ and β. Therefore, the fitting range has to be determined self-consistently. This is done by performing the fit indiscriminately in each interval $\{n \cdot \Delta z, z_{\text{last}}\}$, $n < z_{\text{end}}/\Delta z$. For each of the $(z_{\text{end}} - 1)$ fits we extract $\beta\mu$ and β. The result for $\beta\mu$ as a function of fitting range is shown in figure 5-4. The equivalent values of the temperature are not shown here but show a similar behavior.

For a perfect signal-to-noise ratio of the data and a perfect characterization of our experimental parameters, $\beta\mu$ in figure 5-4b would be a flat line until the local

---

[7]The magnetic saddle potential results in an additional anticonfining term which has to be taken into account in the analysis of experimental data. If this antitrapping potential is characterized by the "trapping frequency" ω_A, one has to add the following term to the right hand side of equation 5.18: $U = -\frac{1}{\pi} m\omega_A^2 \int_0^\infty du \, n_{2D} \left(\sqrt{u^2 + \rho_0^2}, z \right)$.
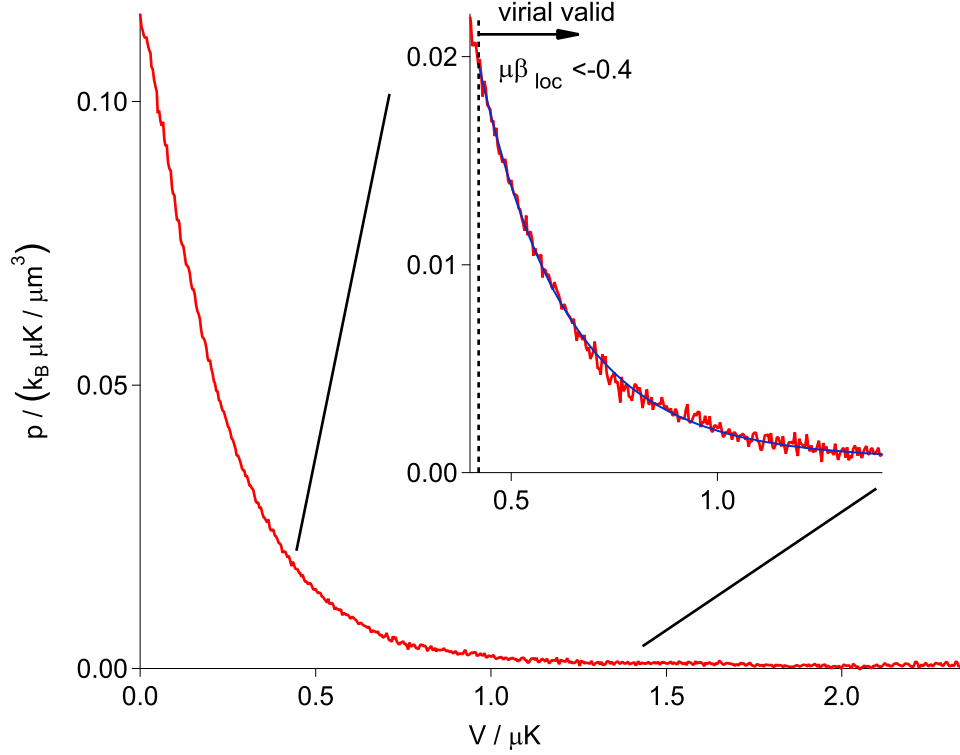
Figure 5-3: Pressure profile vs potential (solid red line). The profile demonstrates typical signal-to-noise ratio in our data. Shown is also a zoom into the region, in which the virial fit (solid blue line) is applicable. The fitting region is marked by the dashed vertical line.

$\beta\mu_{\mathrm{loc}}(z) < -0.4$, at which point the virial fit deviates from the theoretical calculations by more than 1%. This can be verified in figure 5-4b: For values $\beta\mu_{\mathrm{loc}}(z) > -0.4$, the fitted value for $\beta\mu$ becomes unreliable. Eventually, as the fitting region is restricted to low density wings, where $\beta\mu_{\mathrm{loc}} < -1$ for the particular data from the profile shown in figure 5-4a, the signal-to-noise ratio does not allow a reliable extraction of $\beta\mu$ any more. We therefore extract $\beta\mu$ at the point where $\beta\mu_{\mathrm{loc}} \simeq -0.4$. For this particular profile, $\beta\mu = 1.37(3)$, $T = 236(2)$nK and $\mu = 325(7)$nK. The error bars represent the statistical uncertainty of the fit shown in the inset of figure 5-3 and do not include potential systematic errors.

With this method we can assign values of $\beta\mu$ and T to each profile and determine the equation of state from equation 5.6. This can be done for an arbitrary number of density profiles, allowing us to suppress the statistical error and obtain a high precision determination of the equation of state.
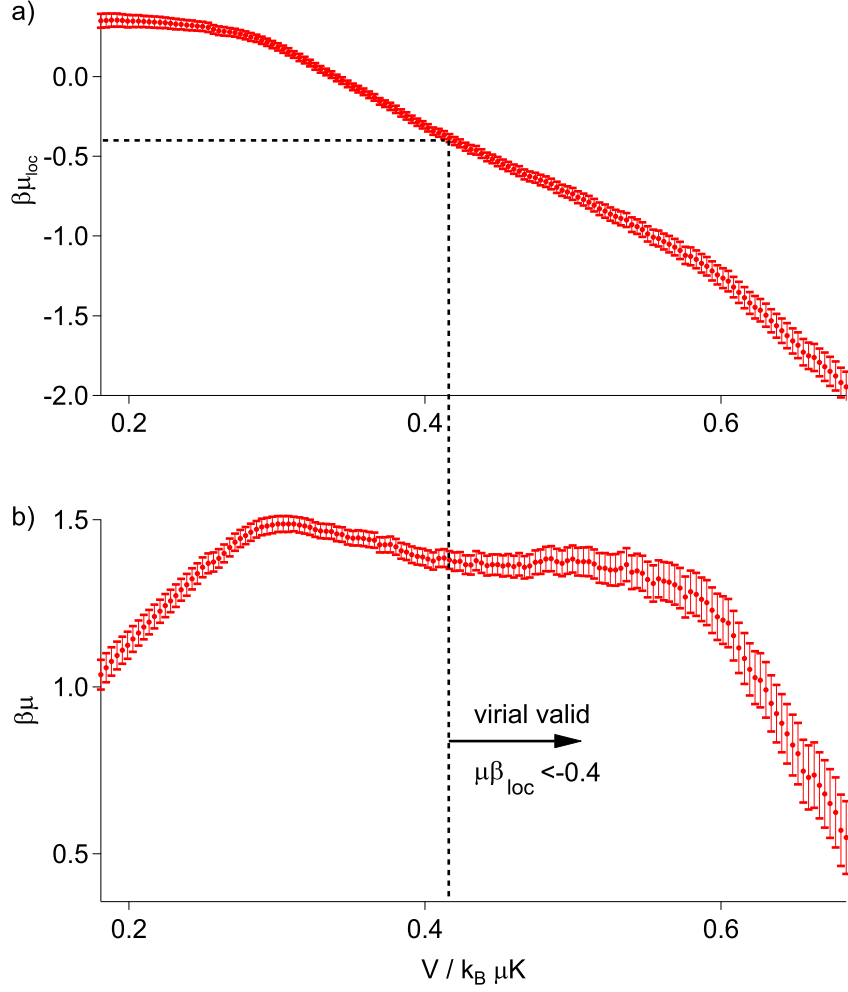
Figure 5-4: Determination of $\beta\mu$. Shown are a) the local value $\beta\mu_{\mathrm{loc}}$ as a function of the fitting range, see text, and b) the value of $\beta\mu$ as a function of the fitting range. The dashed lines show the restriction of the valid fitting range.

5.4 Preparation: Equation of State of the Non-Interacting Fermi gas

As the fit to the virial expansion in equation 5.19 requires precise knowledge of the absolute value of the density at a certain potential V, it is crucial to carefully calibrate the imaging system. Many factors determine the relation between the observed optical density for absorption and the true atomic density, such as polarization of the imaging light, linewidth of the imaging laser, off-resonant light in the imaging path, alignment of magnetic fields, magnification factor of the imaging system, etc. Here we chose a different route: We created a system for which we know the equation of state
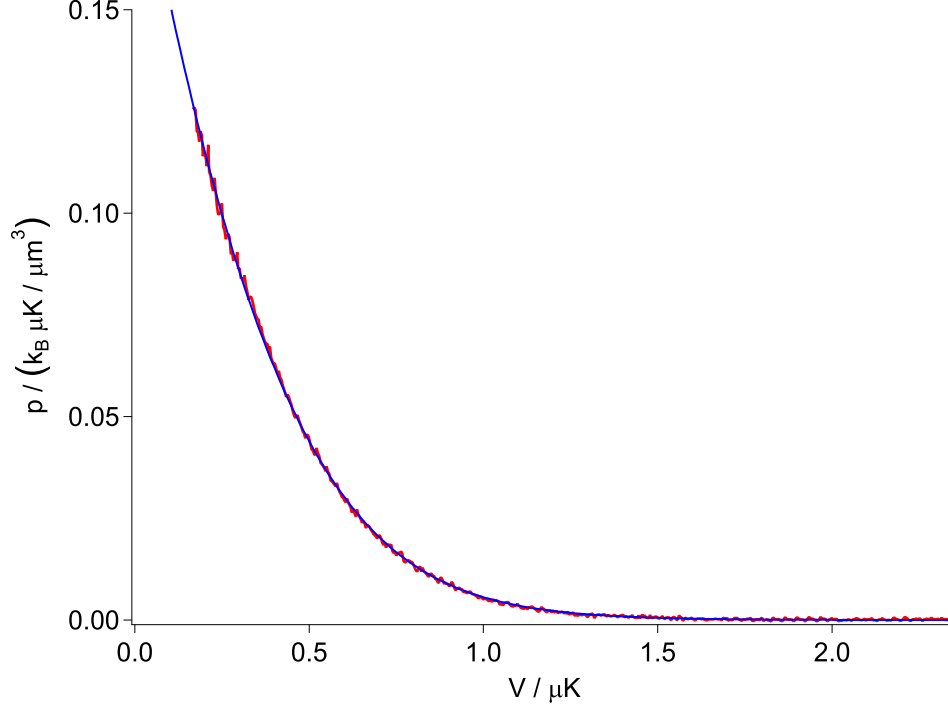
Figure 5-5: Equation of state of a non-interacting Fermi gas for calibration. Solid blue line: Polylogarithm from equation 5.20. Solid red line: Experimental data, equation of state from a single profile.

and adjusted the prefactor to calibrate imaging. Our calibration system is the non-interacting Fermi gas.

A non-interacting Fermi gas can be easily produced experimentally as there is a zero-crossing of the scattering length a at 534G [137]. An experimental complication arises from the fact that a non-interacting Fermi gas by definition does not thermalize - the "true" density distribution will therefore never be reached. We can, however, create a weakly interacting Fermi gas, whose density distribution should closely resemble a non-interacting Fermi gas if the mean-field interaction energy is much smaller than the Fermi energy. In the case discussed here, $U_{\mathrm{MF}} \simeq \epsilon_F/100$, so that interaction effects should be negligible.

The pressure of a non-interacting Fermi gas can be derived in the local density approximation by setting $\mu_{\mathrm{loc}}(r) = \mu - V(r)$ and carrying out the integration of the Fermi-Dirac distribution over the momentum components and μ, resulting in [23]:

$$p(V) = -\frac{k_B T}{\lambda^3} \mathrm{Li}_{5/2}(-e^{\beta(\mu-V)}) \tag{5.20}$$

where $\text{Li}_{5/2}(z) = \sum_{k=1}^{\infty} \frac{z^k}{k^{5/2}}$ is polylogarithm of order 5/2. Based on this series expansion, the virial coefficients, see equation 5.19, can be seen immediately: $b_1 = 1, b_2 = -\frac{\sqrt{2}}{8}, b_3 = \frac{\sqrt{3}}{27}, b_4 = \frac{1}{32}$.

Figure 5-5 shows the non-interacting equation of state, see equation 5.20 with $\beta\mu$, T and a numerical prefactor characterizing the imaging system as fitting parameters. The experimental data are well fit by the polylogarithm.

5.5 The Equation of State of the Unitary Fermi Gas I
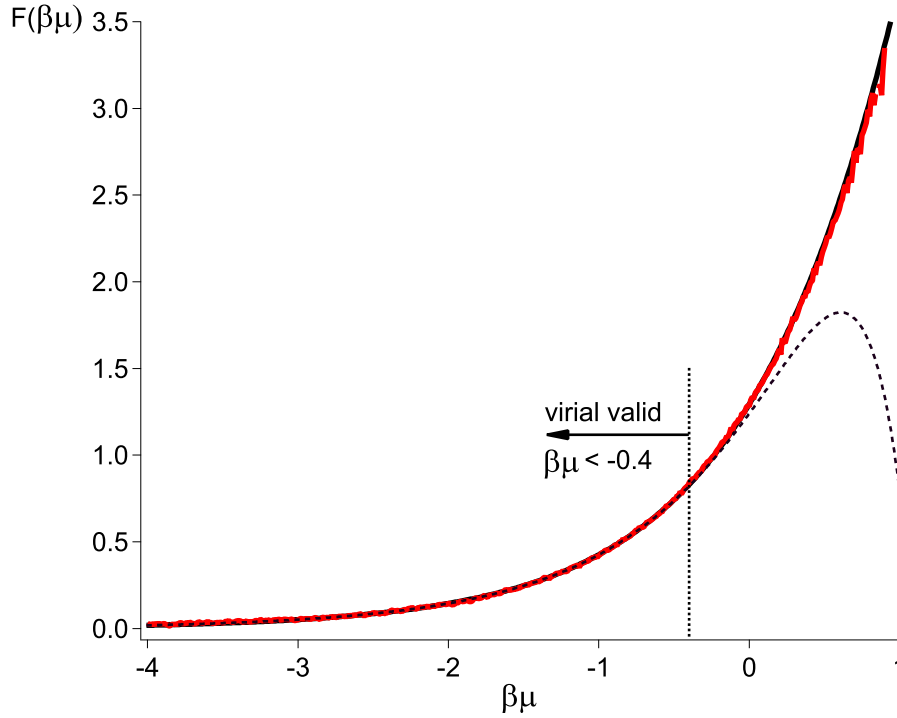
Figure 5-6: Equation of state $F(\beta\mu)$ of a unitary Fermi gas. Solid black line: Diagrammatic Monte Carlo calculation [135]. Dashed black line: Third order virial expansion, valid for $\beta\mu < -0.4$. Solid red line: Experimental equation of state averaged over 10 profiles.

After these preparations, let us now turn to the equation of state $F(\beta\mu)$, see equation 5.6, of a unitary Fermi gas.

The results are shown in figure 5-6. Also shown in the graph is the result of diagrammatic Monte Carlo calculations [135].

We can thus experimentally produce an equation of state from experimental data with very high accuracy and can verify state-of-the-art Monte Carlo calculations. At the time when this thesis was written, Diagrammatic Monte Carlo calculations [135] were available up to $\beta\mu = 1$.

5.6 The Equation of State of the Unitary Fermi Gas II (preliminary)

We can now use the equation of state in figure 5-6 to fit pressure profiles at lower temperature since a wider fitting range is available. This will allow us to obtain the equation of state for larger values of $\beta\mu$. The result is shown in figure 5-7, in which we determine the equation of state up to $\beta\mu \simeq 2.6$.
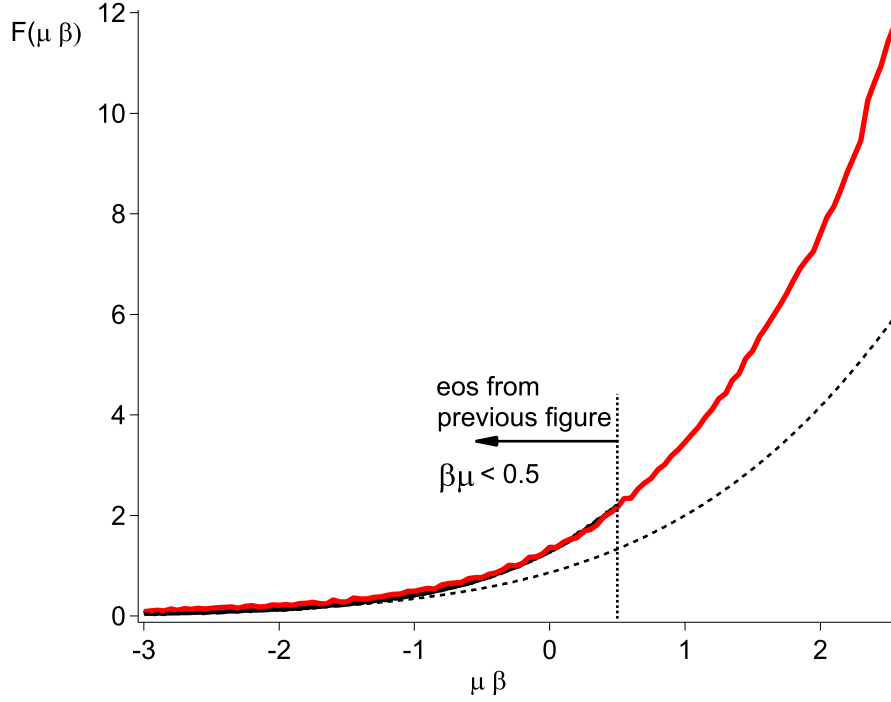
Figure 5-7: Equation of state $F(\beta\mu)$ of a unitary Fermi gas. Solid black line: Equation of state from figure 5-6 used for fitting. Solid red line: Experimental equation of state up to $\beta\mu \simeq 2.6$ averaged over 2 profiles. Dashed black line: Equation of state of the non-interacting Fermi gas shown for comparison.

Future Work   According to the universality hypothesis, see chapter 5.1, when approaching the limit of zero temperature ($T \ll \mu$ or $\beta\mu \gg 1$), the equation of state

is given by a Fermi-distribution with a renormalized chemical potential $\mu = \xi\,\epsilon_F$, see chapter 4.3.5. Therefore, for a given atom number, and $g(\beta\mu) \equiv \frac{f(\beta\mu)}{-Li_{3/2}\left(-e^{\beta\mu}\right)}$, $\lim_{\beta\mu\to\infty} g(\beta\mu) = \xi^{-3/2}$. For the previously mentioned range in chapter 4.3.5 of the chemical potential, this results in $2.7 < \xi^{-3/2} < 5.5$. Therefore, knowledge of the equation of state at low temperature will allow an accurate determination of the universal parameter ξ. From figure 5-7 it can be seen that $g(\beta\mu = 2.5) \simeq 2$. Since the phase transition to the superfluid state is expected to occur at $\beta\mu \simeq 3$, it will be interesting to determine $g(\beta\mu)$ for lower temperatures using the above method.

Chapter 6

Conclusion and Outlook

Experimental studies of ultracold atomic Fermi gases have matured over the years. Testament is given to this by the questions addressed in experiments - until a few years ago, many of the open questions were of qualitative nature. Nowadays, many questions being addressed and waiting to be addressed are of quantitative nature, such as the precise value of the chemical potential, the superfluid gap or the contact coefficient, the critical interaction strength for phase transitions or the effective mass of a polaron.

The temperature dependence of these parameters presents a challenging problem for theory and experiments alike. In fact, even the equation of state of a balanced unitary Fermi mixture has only recently been addressed in experiments, and a precise and convincing experimental and theoretical determination of the critical temperature for superfluidity remains elusive.

However, the results presented in this thesis dealt with the simplest non-trivial realization of an ultracold atomic Fermi gas: A mixture of two fermion species of equal mass in a single potential well characterized by s-wave interactions. But the field is moving forward fast and many new systems have recently been developed including ultracold atoms in lower dimensions and optical lattices, particles with p-wave or higher order angular momentum interactions, formation of dipolar bosonic and fermionic molecules, three- and four-particle bound states, and Fermi mixtures with unequal masses.

The following sentence can be found at the end of many a thesis in the field of ultracold atoms and is still true: Exciting times lie ahead of us...

Appendix A

Realization of a Strongly Interacting Bose-Fermi Mixture from a Two-Component Fermi Gas

This appendix contains a reprint of Ref. [80]: Yong-il Shin, André Schirotzek, Christian H. Schunck, and Wolfgang Ketterle, *Realization of a Strongly Interacting Bose-Fermi Mixture from a Two-Component Fermi Gas*, Phys. Rev. Lett. **101**, 070404 (2008).

P H Y S I C A L   R E V I E W   L E T T E R S

Realization of a Strongly Interacting Bose-Fermi Mixture from a Two-Component Fermi Gas

Yong-il Shin,* André Schirotzek, Christian H. Schunck, and Wolfgang Ketterle

Department of Physics, MIT-Harvard Center for Ultracold Atoms, and Research Laboratory of Electronics,
Massachusetts Institute of Technology, Cambridge, Massachusetts 02139, USA
(Received 5 May 2008; published 14 August 2008)

We show the emergence of a strongly interacting Bose-Fermi mixture from a two-component Fermi mixture with population imbalance. By analyzing *in situ* density profiles of ^{6}Li atoms in the BCS-BEC crossover regime, we identify a critical interaction strength, beyond which all minority atoms pair up with majority atoms and form a Bose condensate. This is the regime where the system can be effectively described as a boson-fermion mixture. We determine the dimer-fermion and dimer-dimer scattering lengths and beyond-mean-field contributions. Our study realizes a gedanken experiment of bosons immersed in a Fermi sea of one of their constituents, revealing the composite nature of the bosons.

PACS numbers: 03.75.Ss, 03.75.Hh, 67.60.Fp

Fermions are the fundamental building blocks of ordinary matter, whereas bosons emerge as composite particles. One of the simplest physical systems to study the emergence of bosonic behavior is a two-component fermion mixture, where the composite boson is a dimer of the two different fermions. A dramatic manifestation of bosonic behavior is Bose-Einstein condensation, representing the low-temperature phase of a gas of bosons. One way to reveal the composite nature of the bosons is to immerse such a Bose-Einstein condensate (BEC) into a Fermi sea of one of its constituents. The degeneracy pressure due to the Pauli exclusion principle affects the structure of the composite boson, resulting in a zero-temperature quantum phase transition to a normal state where Bose-Einstein condensation is quenched.

In this Letter, we observe this transition experimentally. We identify the regimes where a two-component Fermi gas can be described as binary mixture of bosons and fermions, and where the composite nature of the boson becomes essential. The validity of a Bose-Fermi (BF) description requires that all minority fermions become bound as bosons and form a BEC. We determine the critical value of $1/k_{F\uparrow}a$ for the onset of superfluid behavior in the limit of large population imbalance. Here, a is the fermion-fermion scattering length, and $k_{F\uparrow}$ is the Fermi wave number characterizing the depth of the majority Fermi sea. Of course, for an equal mixture, the zero-temperature ground state is always a superfluid in the BEC-BCS crossover. It has been shown previously that a crossover superfluid can be quenched by population imbalance, also called the Chandrasekhar-Clogston (CC) limit of superfluidity [1,2]. In this work, we determine the critical point where superfluidity can no longer be quenched by population imbalance; i.e., the CC limit becomes 100%.

In the limit of a BF mixture [3], we observe repulsive interactions between the fermion dimers and unpaired fermions. They are parameterized by an effective dimer-fermion scattering length of $a_{bf} = 1.23(3)a$. This value is in reasonable agreement with the exact value $a_{bf} = 1.18a$ which has been predicted over 50 years ago for the three-

fermion problem [4], but has never been experimentally confirmed. The boson-boson interactions were found to be stronger than the mean-field prediction in agreement with the Lee-Huang-Yang prediction [5].

The system for this study is a variable spin mixture of the two lowest hyperfine states $|\uparrow\rangle$ and $|\downarrow\rangle$ of ^{6}Li atoms (corresponding to the $|F = 1/2, m_F = 1/2\rangle$ and $|F = 1/2, m_F = -1/2\rangle$ states at low magnetic field) in an optical dipole trap as described in Refs. [1,2]. A broad Feshbach resonance, located at 834 G [6], strongly enhances the interactions between the two spin states. The final evaporative cooling was performed at 780 G by lowering the trap depth. Subsequently, the magnetic-bias field B is adjusted to a target value with a ramp speed of ≤ 0.4 G/ms, changing the interaction strength adiabatically. At the end of the preparation, our sample was confined in an effective three-dimensional harmonic trap with cylindrical symmetry. The axial (radial) trap frequency was $\omega_z/2\pi = 22.8$ Hz ($\omega_r/2\pi = 140$ Hz).

The phase diagram for the fermion mixture was obtained from the analysis of *in situ* density profiles of the majority (spin ↑) and minority (spin ↓) components. The profiles were recorded using a phase-contrast imaging technique [2]. Under the local density approximation (LDA), low-noise column-density profiles were obtained by averaging the optical signal along equipotential lines (refer to Ref. [2] for a full description of the image processing). For typical conditions, the temperature of a sample was $T/T_{F0} \lesssim 0.05$, determined from the outer region of the cloud [2], where $T_{F0} \approx 1.0$ μK is the Fermi temperature of the majority component measured as $k_B T_{F0} = m\omega_z^2 R_\uparrow^2/2$ (k_B is the Boltzmann's constant, m is the atom mass, and $R_\uparrow$ is the axial radius of the majority cloud).

Figure 1 displays density profiles of imbalanced Fermi mixtures for various magnetic fields, showing how the spatial structure of a trapped sample evolves in the crossover regime. Near resonance, as reported in Ref. [2], three distinctive spatial regions are identified: (I) a superfluid core, (II) an intermediate region of a partially polarized normal (N_{pp}) phase, and (III) a fully-polarized, outer wing.
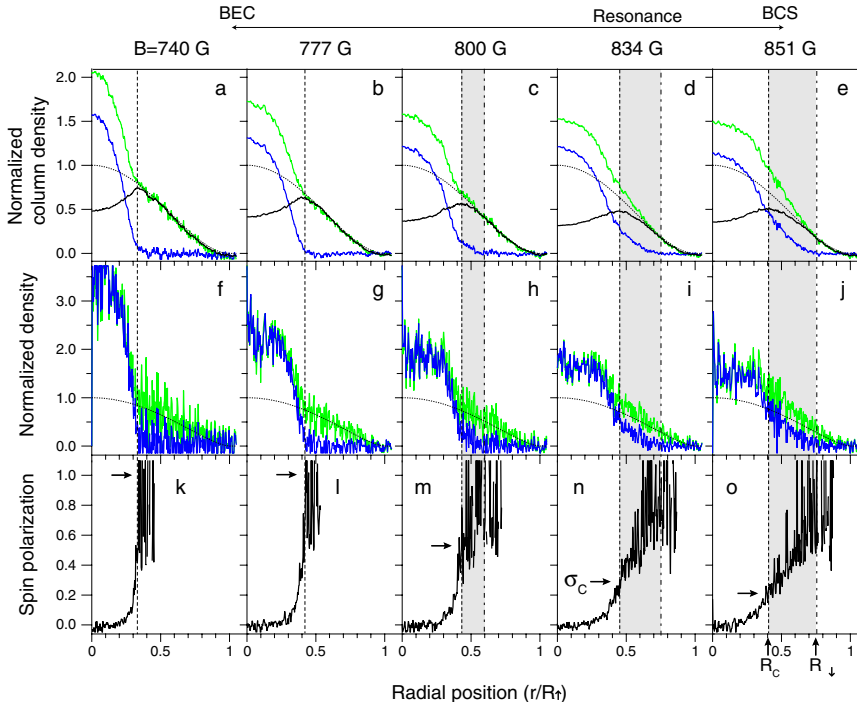
FIG. 1 (color online). Density profiles of imbalanced Fermi mixtures in a harmonic trap. The top row (a)–(e) shows the averaged column-density profiles for various magnetic fields [gray (green): majority, dark gray (blue): minority, black: difference]. The black dotted line is a zero-temperature Thomas-Fermi distribution fit to the majority wing ($r > R_\downarrow$). The middle row (f)–(j) and the bottom row (k)–(o) show the reconstructed three-dimensional density distributions and the spin polarizations obtained from the profiles in the top row. The critical polarizations σ_c at the phase boundary $r = R_c$ are indicated by the right arrows. The values for $R_\uparrow$ (in μm), $R_c/R_\uparrow$, and $R_\downarrow/R_\uparrow$ were respectively: for (a), (f), (k), 381, 0.33, 0.33; for (b), (g), (l), 380, 0.33, 0.33; for (c), (h), (m), 362, 0.35, 0.59; for (d), (i), (n), 371, 0.44, 0.72; for (e), (j), (o), 367, 0.41, 0.76. $T/T_{F0} \lesssim 0.05$, and $T_{F0} \approx 1.0 \mu$K (see the text for definitions).

The core radius R_c was determined as the peak position in the column-density difference profile and the majority (minority) radius $R_\uparrow$ ($R_\downarrow$) was determined from the fit of the outer region, $r > R_\uparrow$ ($r > R_c$) of the majority (minority) column-density profile to a zero-temperature Thomas-Fermi distribution. The local spin polarization is defined as $\sigma(r) \equiv (n_\uparrow - n_\downarrow)/(n_\uparrow + n_\downarrow)$, where $n_\uparrow$ and $n_\downarrow$ are the local majority and minority density, respectively.

Further on the BEC side, the sample has a more compressed superfluid core, a narrower intermediate normal region (gray region in Fig. 1) and a higher critical spin polarization at the phase boundary $\sigma_c = \sigma(R_c)$. Eventually, when $B < 780$ G, there is no noticeable intermediate region, implying that every minority atom pairs up with a majority atom in the superfluid core. In Fig. 2, we determine the critical point for the disappearance of the partially polarized normal phase in two different ways. Figure 2(a) shows the phase diagram for the N_{pp} phase in the plane of interaction strength $1/k_{F\uparrow}a$ and spin polarization σ. An extrapolation of the critical line to $\sigma_c = 1$ yields $1/k_{F\uparrow,c}a = 0.74(4)$. Another implication of the absence of an N_{pp} phase is that the size of the minority cloud $R_\downarrow$ approaches the radius R_c of the superfluid core. This extrapolation is conveniently done using the dimensionless parameter $\kappa = (R_\uparrow^2 - R_\downarrow^2)/(R_\uparrow^2 - R_c^2)$ [7], resulting in a value of $1/k_{F\uparrow,c}a = 0.71(5)$. These values are in good agreement with recent quantum Monte Carlo (QMC) calculations [10].

The critical point marks the onset of the emergence of a BF mixture from the two-component Fermi system. One may suspect that near the critical point, the equation of state of the BF mixture is complex, but we show now that a very simple equation of state is sufficient to quantitatively

account for the observed profiles. Because of the external trap potential, the local chemical potential varies form zero at the edge of a cloud to a maximum value in the center. Therefore, knowledge of the three-dimensional density profiles of a single cloud is sufficient to obtain the equation of state [2,3,8,9,11].

For a zero-temperature mixture of bosonic dimers with density $n_b = n_\downarrow$ and mass $m_b = 2m$ and unpaired fermions with density $n_f = n_\uparrow - n_\downarrow$ and mass $m_f = m$, the energy density $\mathcal{E}$ can be decomposed as $\mathcal{E} = \mathcal{E}_{bb} + \mathcal{E}_{bf} + \mathcal{E}_f$, where $\mathcal{E}_{bb}(n_b)$ and $\mathcal{E}_{bf}(n_b, n_f)$ are the boson-boson and
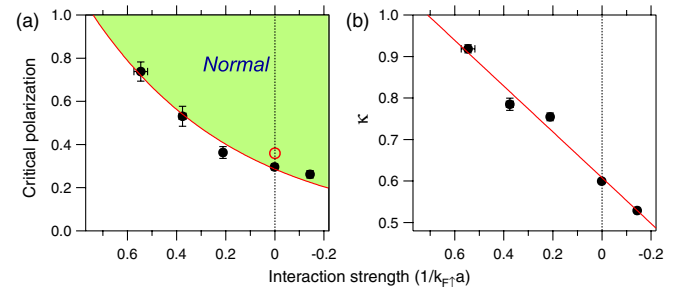
FIG. 2 (color online). Emergence of a Bose-Fermi mixture in the phase diagram for a two-component Fermi gas. (a) The critical polarization σ_c as a function of the interaction strength $1/k_{F\uparrow}a$ at the phase boundary. The open circle indicates the previously measured critical value on resonance, $\sigma_{c0} = 0.36$ [2]. (b) $\kappa = (R_\uparrow^2 - R_\downarrow^2)/(R_\uparrow^2 - R_c^2)$. The solid (red) lines are (a) an exponential fit and (b) a linear fit to the data points. $\sigma_c = 1$ and $\kappa = 1$ (i.e., $R_\downarrow = R_c$) imply the absence of minority fermions in the normal phase. Each data point consists of 9 to 23 independent measurements, and the error bars indicate only the statistical uncertainty.

boson-fermion interaction energies, respectively, and $\mathcal{E}_f = (3/5)\alpha n_f^{5/3}$ is the kinetic energy of fermions [$\alpha = (6\pi^2)^{2/3}\hbar^2/2m_f$ and $\hbar$ is the Planck's constant divided by 2π]. Here, we assume that the effective mass of a fermion in a dilute mixture is the same as its bare mass [12]. Under the LDA, the densities $n_b(r)$ and $n_f(r)$ in the harmonic trap should satisfy

$$\mu_{f0} = \alpha n_f^{2/3} + \frac{\partial \mathcal{E}_{bf}}{\partial n_f} + \frac{1}{2} m_f \omega_z^2 r^2, \tag{1}$$

$$\mu_{b0} = \frac{d\mathcal{E}_{bb}}{dn_b} + \frac{\partial \mathcal{E}_{bf}}{\partial n_b} + \frac{1}{2} m_b \omega_z^2 r^2, \tag{2}$$

where μ_{f0} and μ_{b0} are the global chemical potentials of fermions and bosons, respectively, referenced to the trap bottom.

For the determination of the boson-fermion scattering length a_{bf}, we use a mean-field expression for the boson-fermion interaction energy $\mathcal{E}_{bf,M} = (2\pi\hbar^2/m_{bf})a_{bf}n_b n_f$ with $m_{bf} = m_b m_f/(m_b + m_f) = (2/3)m$. Since $\mu_{f0} = m\omega_z^2 R_\uparrow^2/2$, Eq. (1) gives the relation, $a_{bf}(r) = [\mu_{f0}(1 - r^2/R_\uparrow^2) - \alpha n_f^{2/3}]/(\frac{3\pi\hbar^2}{m}n_b)$. We obtained a value for a_{bf} by averaging $a_{bf}(r)$ over a mixed region ($r < R_c$ with $n_{b,f} > 0.1n_0$). Here, n_0 is the reference density defined as $n_0 = (\mu_{f0}/\alpha)^{3/2}$. In this analysis, the noninteracting outer wing provides absolute density calibration [9].

The scattering length ratio a_{bf}/a turns out to be almost constant over the whole range, 700 G $< B <$ 780 G, where we could study BF mixtures [Fig. 3(a)]. For even lower magnetic fields, severe heating occurred, probably due to molecular relaxation processes. By averaging a total of 89 measurements, we obtain $a_{bf} = 1.23(3)a$, close to the exact value $a_{bf} = 1.18a$ calculated for the three-fermion problem [4]. Our finding excludes the mean-field prediction $a_{bf} = (8/3)a$. The detailed behavior above 750 G requires further investigation.

We now turn to the determination of the boson-boson scattering length a_{bb} which parameterizes the boson-boson mean-field energy $\mathcal{E}_{bb,M} = (2\pi\hbar^2/m_b)a_{bb}n_b^2$. For a given a_{bf}, the effective potential for bosons in the presence of fermions is $V_b(r) = m\omega_z^2 r^2 + (3\pi\hbar^2/m)a_{bf}n_f(r)$. Then, Eq. (2) gives $\mu_{b0} - (2\pi\hbar^2/m)a_{bb}n_b(r) = V_b(r)$. By fitting the data in the core region ($0.1R_\uparrow < r < R_c$ and $n_b > 0.1n_0$) to this equation with μ_{b0} and a_{bb} as two free parameters, we obtained a value for a_{bb}. We used the value a_{bf} determined from the corresponding profiles.

The effective mean-field values for a_{bb}/a show a strong increase by a factor of about 2, as the system approaches the critical point [Fig. 3(b)]. We attribute this behavior to strong boson-boson interactions causing non-negligible quantum depletion in the BEC. In this regime, the equation of state has to include beyond-mean-field corrections, with the leading term given by Lee, Huang, and Yang (LHY) [5] as

$$\mathcal{E}_{LHY} = \frac{2\pi\hbar^2 a_{bb}n_b^2}{m_b}\left[1 + \frac{128}{15}\sqrt{\frac{a_{bb}^3 n_b}{\pi}}\right]. \tag{3}$$

Inclusion of the LHY correction leads to smaller fitted values for a_{bb}/a, which are now almost constant over the whole range of magnetic fields with an average value of $a_{bb} = 0.55(1)a$. The exact value for weakly bound dimers is $a_{bb} = 0.6a$ [13]. For $k_{F,b}a = 1$, the LHY correction is $0.3\mathcal{E}_{bb,M}$, i.e., a 30% correction to the mean-field approximation. Here, $k_{F,b} = (6\pi^2 n_b)^{1/3}$. Recently, the LHY cor-

FIG. 3 (color online).   Characterization of a strongly interacting Bose-Fermi mixture. (a) The scattering length for dimer-fermion interactions a_{bf} and (b) for dimer-dimer interactions a_{bb} in units of the fermion-fermion scattering length a. Black solid circles were determined using mean-field theory and open (red) circles including the LHY correction for a strongly interacting Bose gas. The dashed lines indicate the calculated values $a_{bf} = 1.18a$ [4] and $a_{bb} = 0.6a$ [13]. Each data point represents 7 to 17 measurements, and the error bars indicate only the statistical uncertainty.

FIG. 4 (color online).   Observed profiles of strongly interacting Bose-Fermi mixtures compared to calculated profiles without any adjustable parameter. (a)–(c) Density profiles of bosonic dimers [dark gray (blue)] and unpaired excess fermions [gray (green)] for various magnetic fields. The numerically obtained density profiles (d)–(f) for bosons and (g)–(i) for fermion use $a_{bb} = 0.6a$ and $a_{bf} = 1.18a$ (dashed line: mean-field description, solid line: including the LHY correction). The horizontal dotted lines in (d)–(f) indicate the boson density corresponding to $1/k_{F,b}a = 1$. The values for $R_\uparrow$ (in μm) and $R_c/R_\uparrow$ were respectively: for (a), 393 and 0.29; for (b), 381 and 0.33; for (c), 366 and 0.35.
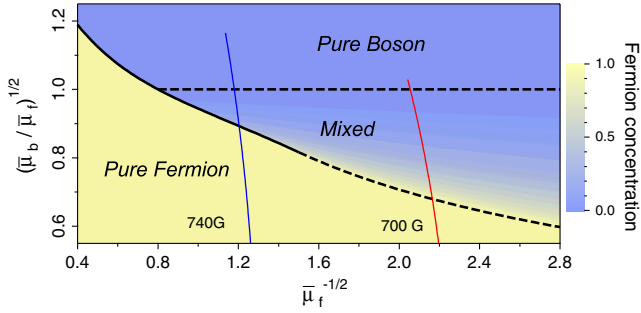
FIG. 5 (color online). Mean-field phase diagram of a dilute Bose-Fermi mixture. $\bar{\mu}_f$ and $\bar{\mu}_b$ are the chemical potentials for fermions and bosons in units of $\frac{\hbar^2}{2m_f}(6\pi^2\bar{n}_f)^{2/3}$ and $\frac{4\pi\hbar^2 a_{bb}}{m_b}\bar{n}_b$, respectively, where $\bar{n}_f = \frac{9\pi}{2}\frac{a_{bb}^3}{a_{bf}^6}\frac{m_b^3 m_f^3}{(m_b+m_f)^6}$ and $\bar{n}_b = \frac{9\pi}{4}\frac{a_{bb}^2}{a_{bf}^5}\frac{m_b^3 m_f^2}{(m_b+m_f)^5}$ (see Ref. [18]). The thick lines indicate the phase transitions (solid line: first-order, dashed line: second-order). The thin lines represent typical cuts through the phase diagram realized in our trapped samples.

rections have been observed via the upshift of collective oscillation frequencies for a strongly interacting BEC [14].

Our results show that a two-component Fermi mixture beyond the critical point can be effectively described as a strongly interacting BF mixture. In Fig. 4, we compare our experimental data with numerically obtained density profiles [15] without any adjustable parameter, showing excellent agreement. After including the LHY correction, small discrepancies are visible only at the highest boson densities exceeding $k_{F,b}a = 1$, where one would expect unitarity corrections. It is surprising that we did not need any beyond-mean-field corrections for the boson-fermion interaction. Such corrections have been calculated for a system of point bosons and fermions [16]. However, including them into our fit function degraded the quality of the fit. Recent QMC simulations have shown that the equation of state of a polarized Fermi gas on the BEC side is remarkably close to $\mathcal{E} = \mathcal{E}_{LHY} + \mathcal{E}_{bf,M} + \mathcal{E}_f$ with $a_{bb} = 0.6a$ and $a_{bf} = 1.18a$ down to $1/k_{F\uparrow}a > 0.5$ [10,17] in agreement with our findings. It appears that the beyond-mean-field term is offset by other corrections, possibly due to the composite nature of the bosons. Further studies of this rich system could address beyond-mean-field terms, characterize the breakdown of the BF description close to the critical point, and look for finite temperature effects.

One motivation for the realization of BF mixtures is to extend studies of ^{3}He -^{4}He mixtures. With tunable interactions near Feshbach resonances, cold atom systems can access a wider regime of the phase diagram. Predicted phenomena include phase separation and miscibility [11,18], boson-mediated, effective fermion-fermion coupling [12,19], and novel collective excitations [20,21]. The density profiles in Fig. 4 show a sharper boundary for higher magnetic fields. This is consistent with Fig. 5 which predicts that in the same magnetic field range, the transition from full miscibility to phase separation has taken place.

An interacting BF system has been also realized in ^{87}Rb-^{40}K mixtures [22,23]. The ^{6}Li system studied here has the advantages of using a single atomic species and much longer lifetimes of several seconds, but cannot access attractive boson-fermion interactions.

In conclusion, a two-component Fermi gas with population imbalance is a realization of a long-lived strongly interacting BF mixture. This is a new BF system with tunable interactions. Furthermore, it offers intriguing possibilities to study the emergence of bosonic behavior from a mixture of fermions.

*yishin@mit.edu
[1] M. W. Zwierlein *et al.*, Science **311**, 492 (2006); M. W. Zwierlein *et al.*, Nature (London) **442**, 54 (2006); Y. Shin *et al.*, Phys. Rev. Lett. **97**, 030401 (2006).
[2] Y. Shin *et al.*, Nature (London) **451**, 689 (2008).
[3] D. E. Sheehy and L. Radzihovsky, Phys. Rev. Lett. **96**, 060401 (2006); P. Pieri and G. C. Strinati, *ibid.* **96**, 150404 (2006); M. Iskin and C. A. R. Sá de Melo, Phys. Rev. A **77**, 013625 (2008).
[4] G. V. Skorniakov and K. A. Ter-Martirosian, Zh. Eksp. Teor. Fiz. **31**, 775 (1956) [Sov. Phys. JETP **4**, 648 (1957)].
[5] T. D. Lee, K. Huang, and C. N. Yang, Phys. Rev. **106**, 1135 (1957).
[6] M. Bartenstein *et al.*, Phys. Rev. Lett. **94**, 103201 (2005).
[7] κ is almost independent of the total population imbalance near the resonance [8,9].
[8] F. Chevy, Phys. Rev. A **74**, 063628 (2006).
[9] Y. Shin, Phys. Rev. A **77**, 041603(R) (2008).
[10] S. Pilati and S. Giorgini, Phys. Rev. Lett. **100**, 030401 (2008).
[11] K. Mølmer, Phys. Rev. Lett. **80**, 1804 (1998).
[12] J. Bardeen, G. Baym, and D. Pines, Phys. Rev. **156**, 207 (1967).
[13] D. S. Petrov, C. Salomon, and G. V. Shlyapnikov, Phys. Rev. Lett. **93**, 090404 (2004).
[14] A. Altmeyer *et al.*, Phys. Rev. Lett. **98**, 040401 (2007).
[15] For a given $\mathcal{E}$, the density profiles were numerically obtained to be self-consistent with Eqs. (1) and (2).
[16] W. F. Saam, Ann. Phys. (N.Y.) **53**, 239 (1969); A. P. Albus *et al.*, Phys. Rev. A **65**, 053607 (2002); L. Viverit and S. Giorgini, *ibid.* **66**, 063604 (2002).
[17] N. Prokof'ev and B. Svistunov, Phys. Rev. B **77**, 020408(R) (2008).
[18] L. Viverit, C. J. Pethick, and H. Smith, Phys. Rev. A **61**, 053605 (2000).
[19] M. J. Bijlsma, B. A. Heringa, and H. T. C. Stoof, Phys. Rev. A **61**, 053601 (2000).
[20] S. K. Yip, Phys. Rev. A **64**, 023609 (2001).
[21] D. H. Santamore, S. Gaudio, and E. Timmermans, Phys. Rev. Lett. **93**, 250402 (2004).
[22] S. Ospelkaus *et al.*, Phys. Rev. Lett. **97**, 120403 (2006).
[23] M. Zaccanti *et al.*, Phys. Rev. A **74**, 041605(R) (2006).

Appendix B

Phase diagram of a two-component Fermi gas with resonant interactions

This appendix contains a reprint of Ref. [19]: Yong-il Shin, Christian H. Schunck, Andre Schirotzek and Wolfgang Ketterle, *Phase diagram of a two-component Fermi gas with resonant interactions*, Nature **451**, 689 (2008).

LETTERS

Phase diagram of a two-component Fermi gas with resonant interactions

Yong-il Shin[1], Christian H. Schunck[1], André Schirotzek[1] & Wolfgang Ketterle[1]

The pairing of fermions lies at the heart of superconductivity and superfluidity. The stability of these pairs determines the robustness of the superfluid state, and the quest for superconductors with high critical temperature equates to a search for systems with strong pairing mechanisms. Ultracold atomic Fermi gases present a highly controllable model system for studying strongly interacting fermions[1]. Tunable interactions (through Feshbach collisional resonances) and the control of population or mass imbalance among the spin components provide unique opportunities to investigate the stability of pairing[2–4]—and possibly to search for exotic forms of superfluidity[5,6]. A major controversy has surrounded the stability of superfluidity against an imbalance between the two spin components when the fermions interact resonantly (that is, at unitarity). Here we present the phase diagram of a spin-polarized Fermi gas of ^{6}Li atoms at unitarity, experimentally mapping out the superfluid phases versus temperature and density imbalance. Using tomographic techniques, we reveal spatial discontinuities in the spin polarization; this is the signature of a first-order superfluid-to-normal phase transition, and disappears at a tricritical point where the nature of the phase transition changes from first-order to second-order. At zero temperature, there is a quantum phase transition from a fully paired superfluid to a partially polarized normal gas. These observations and the implementation of an *in situ* ideal gas thermometer provide quantitative tests of theoretical calculations on the stability of resonant superfluidity.

When the two spin components resonantly interact, the behaviour of the system becomes independent of the nature of the interactions. This case of unitarity has become a benchmark for experimental and theoretical studies over the last few years. However, there is an ongoing debate about the stability of resonant superfluidity, reflected in major discrepancies in predicted transition temperatures for the balanced spin mixture[7–9], and an even more dramatic discrepancy for the critical imbalance of the two spin components, called the Chandrasekhar–Clogston limit of superfluidity[2,3]. Recent quantum Monte Carlo calculations predicted that superfluidity would be quenched by a density imbalance around 40% (ref. 10), whereas other studies predicted a critical imbalance above 90% (refs 11–16). Our earlier work[17–19] suggested the lower limit but other experiments[20,21] were interpreted to be consistent with the absence of the Chandrasekhar–Clogston limit. This huge discrepancy reveals that even qualitative aspects, such as the role of interactions in the normal phase, are still controversial. The lack of reliable thermometry for strongly interacting systems limits the full interpretations of experimental results.

Here we resolve this long-standing debate by presenting the phase diagram of a spin-polarized Fermi gas at unitarity. We observe that the normal-to-superfluid phase transition changes its nature. At low temperature, the phase transition occurs with a jump in the spin polarization as the imbalance increases, which we interpret as a first-order phase transition. The local spin polarization or local density imbalance is defined as $\sigma = (n_\uparrow - n_\downarrow)/(n_\uparrow + n_\downarrow)$, where $\uparrow$ and $\downarrow$ refer to the two spin components with densities $n_{\uparrow,\downarrow}$. At high temperature, the phase transition is smooth and therefore of second order. The two regimes are connected by a tricritical point[4,22] and we estimate its position to be $(\sigma_{tc}, T_{tc}/T_{F\uparrow}) \approx (0.2, 0.07)$, where $k_B T_{F\uparrow} = \hbar^2(6\pi^2 n_\uparrow)^{2/3}/2m$ is the Fermi energy of the majority component of density $n_\uparrow$ (k_B is the Boltzmann constant, $\hbar$ is the Planck constant divided by 2π and m is the atomic mass of ^{6}Li). Our low-temperature results confirm a zero-temperature quantum phase transition at a critical polarization $\sigma_{c0} \approx 36\%$.

This work required the introduction of several techniques. A tomographic reconstruction of local Fermi temperatures and spin polarization allowed us to obtain the phase diagram for the homogeneous system, no longer affected by the inhomogeneous density of the trapped samples. Furthermore, absolute temperatures were obtained using *in situ* thermometry applied to the non-interacting fully polarized Fermi gas in the outer part of the trapped samples, an ideal thermometer with exactly known thermal properties. Unlike previous work[18,23], this is a direct measurement without any approximations.

Our experiments are carried out in a trapping potential $V(\mathbf{r})$. The local chemical potential of each spin component is given as $\mu_{\uparrow,\downarrow}(\mathbf{r}) = \mu_{\uparrow 0,\downarrow 0} - V(\mathbf{r})$, where $\mu_{\uparrow 0,\downarrow 0}$ are the global chemical potentials. When $\mu_{\uparrow 0} \neq \mu_{\downarrow 0}$, owing to imbalanced populations, the chemical potential ratio $\eta(\mathbf{r}) = \mu_\downarrow/\mu_\uparrow$ varies spatially over the trapped sample and so, under the local density approximation, the trapped inhomogeneous sample is represented by a line in the phase diagrams of the homogeneous system. Figure 1 illustrates the spatial structure of a strongly interacting Fermi mixture in a harmonic trap. In the inner region, where η is closer to unity, a superfluid with zero (or small) spin polarization will form at zero (or low) temperatures, having a sharp phase boundary against the partially polarized normal gas in the outer region. The spin polarization shows a discontinuity at the boundary of the superfluid core at $r = R_c$, a signature of the phase separation of a superfluid and a normal gas[24]. The critical polarization $\sigma_c = \lim_{r \to R_c^+} \sigma(r)$ represents the minimum spin polarization for a stable normal gas; $\sigma_s = \lim_{r \to R_c^-} \sigma(r)$ represents the maximum spin polarization for a stable superfluid gas. At higher temperatures, the discontinuity in the density imbalance disappears. The main result of this paper is the observation and quantitative analysis of such density profiles. Because we have no experimental evidence, we are not discussing the exotic partially polarized phases[25] which could exist only in the transition layer between the superfluid core and the normal outer region.

We prepared a variable spin mixture of the two lowest hyperfine states of ^{6}Li atoms, labelled $|\uparrow\rangle$ and $|\downarrow\rangle$, at a magnetic field of 833 G. A

[1]Department of Physics, MIT-Harvard Center for Ultracold Atoms, and Research Laboratory of Electronics, MIT, Cambridge, Massachusetts, 02139, USA.

broad Feshbach resonance at 834 G enhances the interactions between the two spin states. Our sample was confined in a three-dimensional harmonic trap with cylindrical symmetry. The *in situ* density distributions of the majority (spin ↑) and minority (spin ↓) components were determined using a phase-contrast imaging technique[19] (Fig. 2). We obtained the low-noise profiles $\bar{n}$ by averaging the column density distribution along the equipotential line and determined the three-dimensional density profiles $n(r)$ using the inverse Abel transformation of the column densities $\tilde{n}(r)$ (see Methods Summary). Most of our measurements were performed at a total population imbalance of $\delta \approx 50\%$, where $\delta = (N_\uparrow - N_\downarrow)/(N_\uparrow + N_\downarrow)$ refers to the total numbers of atoms in the sample, $N_\uparrow$ and $N_\downarrow$ of the spin ↑ and ↓ components, respectively.

Figure 3 displays the radial profiles of the densities $n_{\uparrow,\downarrow}(r)$ and the corresponding spin polarization $\sigma(r)$ for various temperatures. The discontinuity in the spin polarization, clearly shown at very low temperatures, demonstrates the phase separation of the inner superfluid of low polarization and the outer normal gas of high polarization. At low temperature, the core radius R_c is determined as the kink (and/or peak) position in the column density difference profile. At high temperature (but still in the superfluid regime), the discontinuity in $\sigma(r)$ disappears. At our lowest temperature, the radii of the minority cloud and the core region were measured as $R_\downarrow = 0.73(1)R_\uparrow$ and $R_c = 0.430(3)R_\uparrow$ (at $\delta = 44(4)\%$), respectively, and these values agree with recent theoretical calculations[10,25] within the experimental uncertainties due to the determination of δ. Here, $R_\uparrow$ is the radius of

the majority cloud, and the uncertainty of the final digit is indicated by parentheses.

We determined temperature from the *in situ* majority wing profiles. The outer part of the majority component, forming a non-interacting Fermi gas, fulfils the definition of an ideal thermometer, namely a substance with exactly understood properties in contact with the target sample. This new *in situ* method avoids the modification of the ideal gas profile caused by the collision with the inner core during ballistic expansion (ref. 18, see Supplementary Information). The outer part of the averaged column density difference profile ($r > R_\downarrow$) was fitted to a finite temperature Fermi–Dirac distribution in a harmonic trap (Fig. 4) and the relative temperature $T' \equiv T/T_{F0}$ was determined, where $k_B T_{F0} = h^2(6\pi^2 n_0)^{2/3}/2m$ is the Fermi energy of the non-interacting Fermi gas, which has the same density distribution in the outer region as the majority cloud (n_0 is the central density of the non-interacting Fermi gas at zero temperature). We verified that anharmonicity of the trapping potential does not affect the fitted temperature (see Methods).

The critical lines of the phase diagram of a homogeneous spin-polarized Fermi gas were obtained by determining the local temperature and spin polarization at the phase boundary. The local relative temperature $T'_{local} \equiv T/T_{F\uparrow}$ was derived from the local density $n_\uparrow(R_c)$ according to $T'(R_c) = T/T_{F0} \times (n_0/n_\uparrow(R_c))^{2/3}$. Because we observe no jump in the majority density within our resolution, $T_{F\uparrow}$ is well-defined at the boundary. The critical polarizations σ_c and σ_s were measured as $\sigma_c = \sigma(R_c)$ and $\sigma_s = \sigma(R_c - 0.05R_\uparrow)$ (this criterion for σ_s was more robust than a fitting procedure, but excludes the possibility that σ_s will be equal to σ_c at high temperature. Therefore, the measured σ_s should be regarded as a lower bound for the polarization of
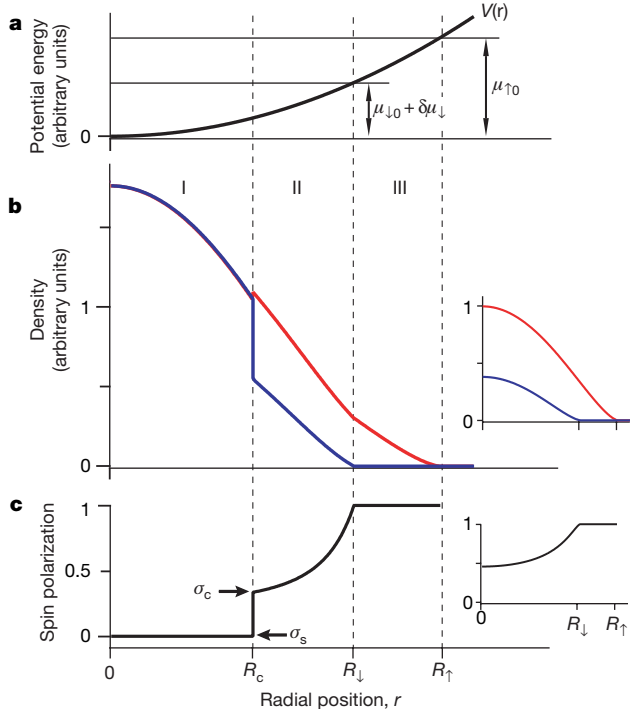
Figure 1 | Schematic of spatial structure of a strongly interacting Fermi gas in a harmonic trap. a, A two-component (spin ↑ and ↓) Fermi mixture is confined in an external potential $V(r) \propto r^2$ with the chemical potential $\mu_{\uparrow 0, \downarrow 0}$ of each spin component ($\delta\mu_\downarrow$ is the shift for the spin ↓ component owing to interactions). **b**, Density distributions of the majority component $n_\uparrow(r)$ (red line) and the minority component $n_\downarrow(r)$ (blue line). **c**, Spin polarization $\sigma(r) = (n_\uparrow - n_\downarrow)/(n_\uparrow + n_\downarrow)$. At zero temperature, the sample has a three-layer radial structure: (I), the core region ($0 \leq r < R_c$) of a fully paired superfluid with $n_\uparrow = n_\downarrow$; (II), the intermediate region ($R_c < r < R_\downarrow$) of a partially polarized normal gas; and (III), the outer region ($R_\downarrow < r < R_\uparrow$) of a fully polarized normal gas. The critical polarization σ_c (or σ_s) is defined as the minimum (or maximum) spin polarization of the normal (or superfluid) region. The non-interacting case is shown in the insets. The insets have the same axes as the main figure.
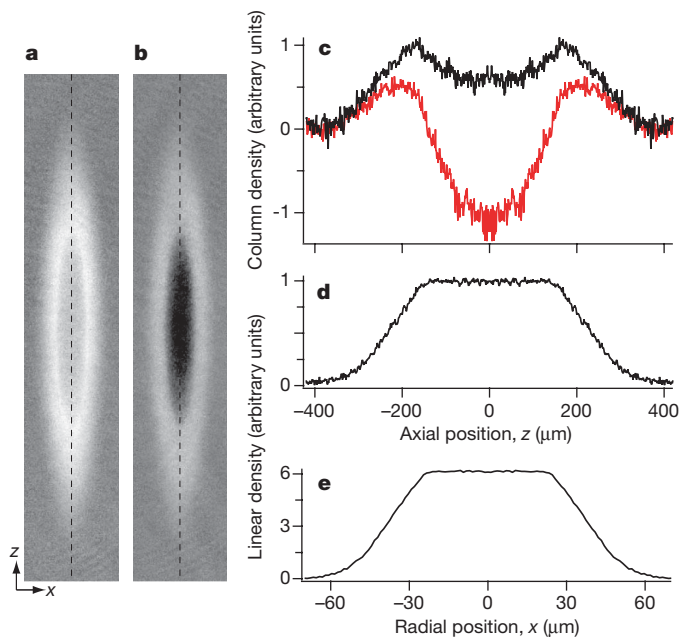
Figure 2 | Double *in situ* phase-contrast imaging of a trapped Fermi mixture. Two phase-contrast images of one sample were taken using different probe frequencies of the imaging beam, measuring the density difference $n_{d1} = n_\uparrow - n_\downarrow$ (**a**) and the weighted density difference $n_{d2} = 0.76 n_\uparrow - 1.43 n_\downarrow$ (**b**), respectively. The images show the two-dimensional distribution of the column density difference, $\tilde{n}_{d1,2}(x,z) \equiv \int n_{d1,2}(\mathbf{r})dy$, owing to the line-of-sight integration. The field of view for each image is 150 μm × 820 μm. **c**, The distributions of the column density difference $\tilde{n}_{d1}$ (black line) and $\tilde{n}_{d2}$ (red line) along the central line (the dashed lines in **a** and **b**). The profiles of the integrated linear density difference, $\bar{n}_{d1,z} \equiv \int \tilde{n}_{d1}(x,z)dx$ (**d**) and $\bar{n}_{d1,x} \equiv \int \tilde{n}_{d1}(x,z)dz$ (**e**), show the identical flat-top feature except scaling. The aspect ratio of the trapping potential was $\lambda = 6.15$, the majority atom number was $N_\uparrow = 5.9(5) \times 10^6$, the population imbalance was $\delta = 44(4)\%$, and the relative temperature was $T' = T/T_{F0} = 0.03(1)$ (see text for definitions).
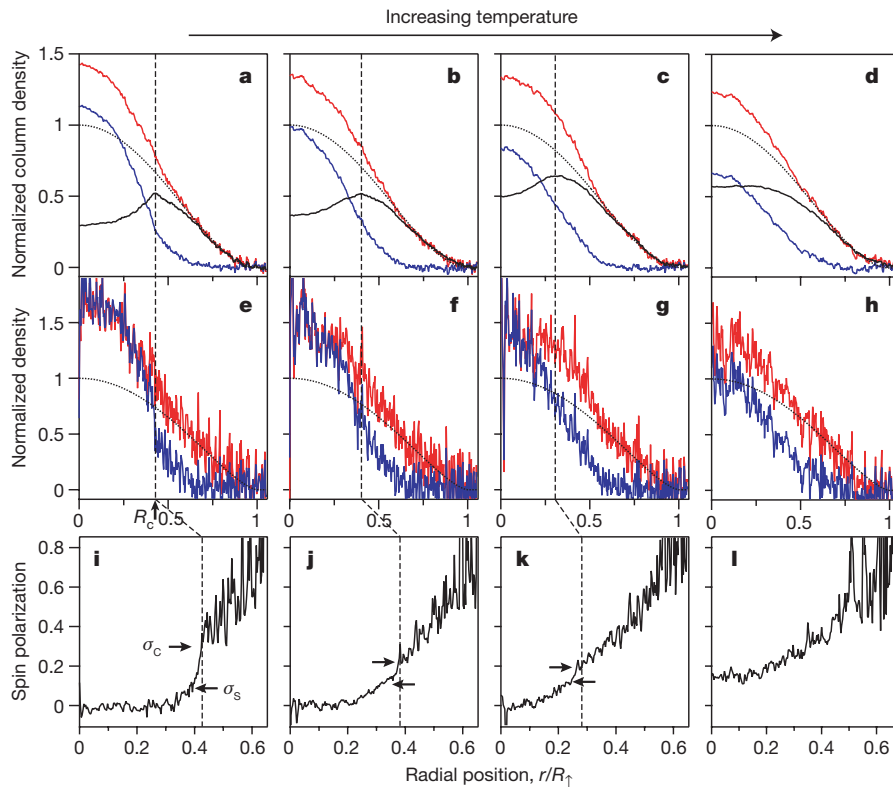
Figure 3 | Density profiles of trapped Fermi mixtures with imbalanced populations. The top row (**a–d**) shows the averaged column density profiles for various temperatures (red, majority; blue, minority; black, difference). The majority radius $R_\uparrow$ was determined from the outer region ($r > R_\downarrow$, where $R_\downarrow$ is the radius of the minority cloud) of the majority profiles using a fit to a zero-temperature Thomas–Fermi distribution (black dotted lines). The column densities are normalized by the central value of the fitted Thomas–Fermi distribution. The middle row (**e–h**) and the bottom row (**i–l**) show the reconstructed three-dimensional profiles and the spin polarization profiles $\sigma(r)$ corresponding to the profiles in **a–d**. The core radius R_c was determined as the peak (and/or kink) position in the column density difference (only for **a–c**), indicated by the vertical dashed lines. The two spin polarizations σ_c at $r = R_c$ and σ_s at $r = R_c - 0.05R_\uparrow$ are marked by the right and left arrows, respectively. The values for T', σ_c, $R_c/R_\uparrow$, $R_\uparrow$ (in µm), $N_\uparrow$, δ (in %) and λ were, respectively: for **a, e** and **i**, 0.03(1), 0.34, 0.43, 385, $5.9(5) \times 10^6$, 44(4), 6.15; for **b, f** and **j**, 0.05(2), 0.24, 0.39, 416, $1.0(1) \times 10^7$, 48(4), 6.5; for **c, g** and **k**, 0.07(1), 0.21, 0.29, 443, $1.2(2) \times 10^7$, 54(4), 6.5; for **d, h** and **l**, 0.10(1), not determined, not determined ($\sigma_{r=0} = 0.15$ and condensate fraction = 2(1)%), 398, $5.3(4) \times 10^6$, 54(4), 7.7.

the superfluid at the boundary). The discontinuity in the spin polarization profile implies that there is a thermodynamically unstable window, $\sigma_s < \sigma < \sigma_c$, leading to a first-order superfluid-to-normal phase transition. As the temperature increases, the unstable region reduces with decreasing σ_c and increasing σ_s. For high temperature when the bimodal feature in the spin polarization profile disappears, we recorded the condensate fraction as an indicator of superfluidity, using the rapid field-ramp technique[17]. As the temperature decreases, the condensate fraction gradually increases with a finite central polarization[19]. Such smooth variations of the density profile and condensate fraction across the phase transition are characteristic of a second-order phase transition.

The phase diagram is characterized by three distinct points: the critical temperature T_{c0} for a balanced mixture, the critical polarization σ_{c0} of a normal gas at zero temperature, and the tricritical point (σ_{tc}, T_{tc}) at which the nature of the phase transition changes. Owing to the lack of a predicted functional form for the phase transition line in the σ–T plane, we apply a linear fit to the measured critical points, suggesting $T_{c0}/T_{F\uparrow} \approx 0.15$, $\sigma_{c0} \approx 0.36$ and (σ_{tc}, $T_{tc}/T_{F\uparrow}$) $\approx$ (0.20, 0.07). The value for σ_{c0} agrees well with the prediction (from the quantum Monte Carlo calculation) of 0.39 (ref. 10). The extrapolation of the phase diagram to $\sigma = 0$ is tentative, because the *in situ* thermometry could not be applied to small population imbalances owing to the narrowness of the non-interacting outer region.

The Chandrasekhar–Clogston limit reflects the energetic competition between a superfluid state and a partially polarized normal state, and occurs at a critical value of $2h_c$ for the chemical potential difference $\delta\mu = \mu_\uparrow - \mu_\downarrow$. In Bardeen–Cooper–Schrieffer theory, which is valid for weak interactions, $h_c = \Delta/\sqrt{2}$ (ref. 3). Here, Δ is the pairing gap. With the assumption of no interactions in a normal gas, quantum Monte Carlo studies predict $h_c = 1.00(5)\Delta \approx 1.2\mu$ at unitarity[11], where $\mu = (\mu_\uparrow + \mu_\downarrow)/2$. The condition $\mu_{\downarrow c} = \mu - h_c < 0$ requires $n_\downarrow = 0$ for a non-interacting normal gas, implying the absence of a partially polarized normal phase and consequently $\sigma_{c0} = 100\%$. Mean-field approaches[12–16], which cannot treat the interactions in the normal phase accurately, also predict a high critical imbalance $\sigma_{c0} > 90\%$. Strong interactions in the normal phase,

however, have been observed through the compressed shape of the minority cloud[18] and the shift in the radio frequency excitation spectrum[26]. The data in Fig. 5 clearly establish a zero-temperature Chandrasekhar–Clogston limit for σ_{c0} in the range 30% to 40%. By analysing the *in situ* density profiles[25,27], we obtained $h_c \approx 0.95\mu$ (see Methods). Since theory clearly predicts $\mu < \Delta$ at unitarity[9,11], we have $h_c < \Delta$. If h_c were larger than Δ, polarized quasi-particles would have negative energies and would already form at zero temperature. Therefore, up to our observed value of h_c, the fully paired
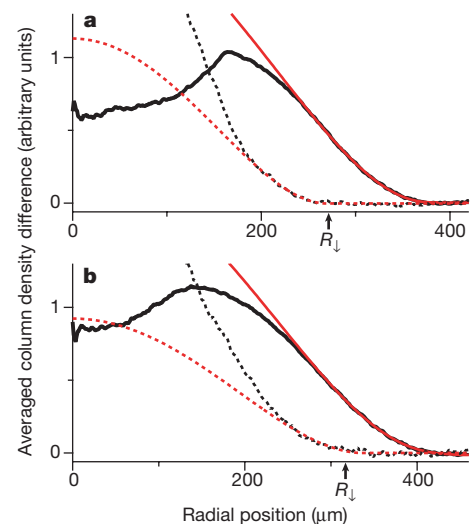
Figure 4 | Temperature determination using *in situ* density profiles. The relative temperature $T' = T/T_{F0}$ (see text for definition) was determined from the outer region ($r > R_\downarrow$) of the averaged column density difference profile (black line) fitted to a finite temperature Fermi–Dirac distribution (red line). The radius of the minority cloud $R_\downarrow$ was determined from a fit of the wing profile of the minority component (black dashed line) to a zero-temperature Thomas–Fermi distribution (red dashed line). **a**, $T' = 0.03(1)$ and $\delta = 44(4)\%$. **b**, $T' = 0.08(1)$ and $\delta = 46(4)\%$.

691

superfluid state is stable, and a polarized superfluid exists only at finite temperature.

The interface between two immiscible fluids involves a surface energy, leading to at least a small violation of the local density approximation. However, the observed sharp interface along an equipotential line and the flat-top structure of the linear density difference profiles (Fig. 2d and e) imply that corrections to the local density approximation are smaller than the resolution of our experiment. These observations are inconsistent with the interpretations given for the experimental results reported in refs 20 and 21, where it has been shown that highly elongated small samples are deformed by surface tension[28,29]. The scaling of those surface effects to our parameters predicted a deviation of the aspect ratio of the superfluid core of about 15% from the trap aspect ratio[29], whereas our data gives an upper bound of 2%. We note that surface tension would add energy in the phase-separated superfluid regime and would shift the Chandrasekhar–Clogston limit to smaller values. Refs 20 and 21 concluded that the Chandrasekhar–Clogston limit should be $\delta_{c0} > 95\%$, which is ruled out by our observations. We are not aware of any suggested effect that can reconcile the data of refs 20 and 21 with our phase diagram for a resonant superfluid. To identify this

finite size effect and to understand fully the nature of the normal state[26], more work on imbalanced Fermi gases is needed.

In conclusion, we have established the phase diagram of a homogeneous spin-polarized Fermi gas with resonant interactions in the $\sigma–T$ plane. This includes the identification of a tricritical point at which the critical lines for first-order and second-order phase transitions meet, and the final confirmation of a zero-temperature quantum phase transition—the Chandrasekhar–Clogston limit of superfluidity—for a gas at unitarity. So far, predicted exotic superfluid states such as the breached-pair state in a stronger coupling regime (Bose–Einstein condensate side)[13] and the Fulde–Ferrell–Larkin–Ovchinnikov state in a weaker coupling regime (Bardeen–Cooper–Schrieffer side)[5,6,12,16,30] have not been observed, but the novel methods of tomography and thermometry will be important tools in the search for those states.

METHODS SUMMARY

The experimental procedure has been described in our previous publications[17–19]. A degenerate Fermi gas of ^{6}Li atoms was first prepared in an optical trap, using laser cooling and sympathetic cooling with ^{23}Na atoms. A variable spin mixture of the two lowest hyperfine states $|\uparrow\rangle$ and $|\downarrow\rangle$ (corresponding to the $|F=1/2, m_F=1/2\rangle$ and $|F=1/2, m_F=-1/2\rangle$ states at low magnetic field) was created at a magnetic field $B = 885$ G. The final evaporative cooling was achieved by lowering the trap depth and all measurements were performed at $B = 833$ G. The temperature of the cloud was controlled by the lowest value of the trap depth in the evaporative cooling process. The oscillation frequency in the axial direction was $f_z = 23$ Hz. The two transverse oscillation frequencies f_ρ are equal to within less than 2%. Two phase-contrast images of the same sample were taken consecutively with different probe frequencies, ν_1 and ν_2 (Fig. 2). The time interval between the two images was 10 μs, and the pulse duration of each probe beam was 15 μs. Because the probe beam was off-resonant, no heating effect of the first pulse was observed in the second image. The trapped sample was observed to have an elliptical shell structure of the same aspect ratio $\lambda = f_\rho/f_z$ as the trapping potential over our entire temperature range, and we obtained low-noise profiles $\tilde{n}$ by averaging the column density distribution along the equipotential line defined as $\lambda^2 x^2 + z^2 = r^2$ for a given radial position r. The region for averaging was restricted depending on the type of analysis. Deviations from the trap aspect ratio were only found for the outer thermal wings. Details of the phase-contrast imaging technique and the data analysis are given in Methods and Supplementary Information.

Full Methods and any associated references are available in the online version of the paper at www.nature.com/nature.

Figure 5 | The $\sigma–T$ phase diagram for a homogeneous spin-polarized Fermi gas with resonant interactions. The critical polarizations σ_c (black solid circles and square) and σ_s (grey solid circles) are displayed along the local $T/T_{F\uparrow}$ at the phase boundary. The yellow area ($\sigma_s < \sigma < \sigma_c$) represents a thermodynamically unstable region, leading to the phase separation. Above the tricritical point, the phase transition in the centre of the cloud was observed by the onset of pair condensation. For this, a cloud was evaporatively cooled, until it crossed the phase transition on a trajectory almost perpendicular to the phase transition line (see Supplementary Information). The critical spin polarization and temperature were obtained by interpolating between points without and with small condensates (black solid square). The linear fit to the σ_c values is shown as a guide to the eye for the normal-to-superfluid phase transition line. Each data point consists of five independent measurements and error bars indicate standard deviation. The blue open symbols show theoretical predictions for the critical temperature of a homogeneous equal mixture[7–9] and the critical polarization at zero temperature[10]. The blue solid square is the measured critical temperature of ref. 23, multiplied by $\sqrt{\xi}$ with $\xi = 0.42$ (ref. 11) to obtain local T/T_F at the centre. Finite temperature correction may increase the effective value of ξ.

1. Giorgini, S., Pitaevskii, L. P. & Stringari, S. Theory of ultracold Fermi gases. Preprint at ⟨http://arxiv.org/abs/0706.3360⟩ (2007).
2. Chandrasekhar, B. S. A note on the maximum critical field of high-field superconductors. *Appl. Phys. Lett.* **1**, 7–8 (1962).
3. Clogston, A. M. Upper limit for the critical field in hard superconductors. *Phys. Rev. Lett.* **9**, 266–267 (1962).
4. Sarma, G. On the influence of a uniform exchange field acting on the spins of the conduction electrons in a superconductor. *J. Phys. Chem. Solids* **20**, 1029–1032 (1963).
5. Fulde, P. & Ferrell, R. A. Superconductivity in a strong spin-exchange field. *Phys. Rev.* **135**, A550–A563 (1964).
6. Larkin, A. I. & Ovchinnikov, Y. N. Inhomogeneous state of superconductors. *Sov. Phys. JETP* **20**, 762–769 (1965).
7. Bulgac, A., Drut, J. E. & Magierski, P. Spin 1/2 fermions in the unitary regime: a superfluid of a new type. *Phys. Rev. Lett.* **96**, 090404 (2006).
8. Burovski, E., Prokofev, N., Svistunov, B. & Troyer, M. Critical temperature and thermodynamics of attractive fermions at unitarity. *Phys. Rev. Lett.* **96**, 160402 (2006).
9. Haussmann, R., Rantner, W., Cerrito, S. & Zwerger, W. Thermodynamics of the BCS-BEC crossover. *Phys. Rev. A.* **75**, 023610 (2007).
10. Lobo, C., Recati, A., Giorgini, S. & Stringari, S. Normal state of a polarized Fermi gas at unitarity. *Phys. Rev. Lett.* **97**, 200403 (2006).
11. Carlson, J. & Reddy, S. Asymmetric two-component fermion systems in strong coupling. *Phys. Rev. Lett.* **95**, 060401 (2005).
12. Sheehy, D. E. & Radzihovsky, L. BEC-BCS Crossover in "magnetized" Feshbach-resonantly paired superfluids. *Phys. Rev. Lett.* **96**, 060401 (2006).
13. Yi, W. & Duan, L.-M. Phase diagram of a polarized Fermi gas across a Feshbach resonance in a potential trap. *Phys. Rev. A* **74**, 013610 (2006).
14. Gubbels, K. B., Romans, M. W. & Stoof, H. T. Sarma phase in trapped unbalanced Fermi gases. *Phys. Rev. Lett.* **97**, 210402 (2006).
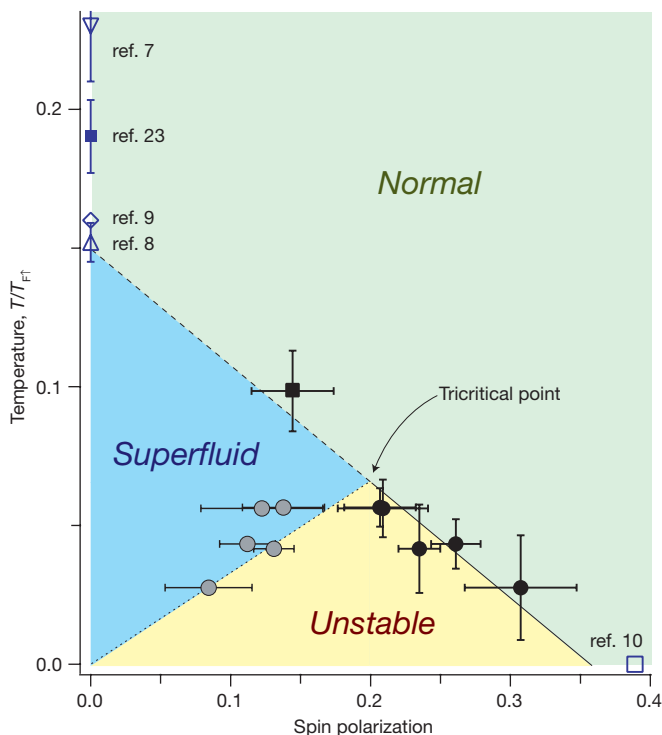
15. Chien, C.-C., Chen, Q., He, Y. & Levin, K. Superfluid phase diagrams of trapped Fermi gases with population imbalance. *Phys. Rev. Lett.* **98**, 110404 (2007).
16. Parish, M. M., Marchetti, F. M., Lamacraft, A. & Simons, B. D. Finite-temperature phase diagram of a polarized Fermi condensate. *Nature Phys.* **3**, 124–128 (2007).
17. Zwierlein, M. W., Schirotzek, A., Schunck, C. H. & Ketterle, W. Fermionic superfluidity with imbalanced spin populations. *Science* **311**, 492–496 (2006).
18. Zwierlein, M. W., Schunck, C. H., Schirotzek, A. & Ketterle, W. Direct Observation of the superfluid phase transition in ultracold Fermi gases. *Nature* **442**, 54–58 (2006).
19. Shin, Y., Zwierlein, M. W., Schunck, C. H., Schirotzek, A. & Ketterle, W. Observation of phase separation in a strongly interacting imbalanced Fermi gas. *Phys. Rev. Lett.* **97**, 030401 (2006).
20. Partridge, G. B., Li, W., Karmar, R. I., Liao, Y. & Hulet, R. G. Pairing and phase separation in a polarized Fermi gas. *Science* **311**, 503–505 (2006).
21. Partridge, G. B., Li, W., Karmar, R. I., Liao, Y. & Hulet, R. G. Deformation of a trapped Fermi gas with unequal spin populations. *Phys. Rev. Lett.* **97**, 190407 (2006).
22. Griffiths, R. B. Thermodynamics near the two-fluid critical mixing point in He^3-He^4. *Phys. Rev. Lett.* **24**, 715–717 (1970).
23. Luo, L., Clancy, B., Joseph, J., Kinast, J. & Thomas, J. E. Measurement of the entropy and critical temperature of a strongly interacting Fermi gas. *Phys. Rev. Lett.* **98**, 080402 (2007).
24. Bedaque, P. F., Caldas, H. & Rupak, G. Phase separation in asymmetrical fermion superfluids. *Phys. Rev. Lett.* **91**, 247002 (2003).

25. Bulgac, A. & Forbes, M. M. Zero-temperature thermodynamics of asymmetric Fermi gases at unitarity. *Phys. Rev. A* **75**, 031605(R) (2007).
26. Schunck, C. H., Shin, Y., Schirotzek, A., Zwierlein, M. W. & Ketterle, W. Pairing without superfluidity: the ground state of an imbalanced Fermi mixture. *Science* **316**, 867–870 (2007).
27. Chevy, F. Universal phase diagram of a strongly interacting Fermi gas with unbalanced spin populations. *Phys. Rev. A* **74**, 063628 (2006).
28. De Silva, T. N. & Mueller, E. J. Surface tension in unitary Fermi gases with population imbalance. *Phys. Rev. Lett.* **97**, 070402 (2006).
29. Haque, M. & Stoof, H. T. C. Trapped fermionic clouds distorted from the trap shape due to many-body effects. *Phys. Rev. Lett.* **98**, 260406 (2006).
30. Machida, K., Mizushima, T. & Ichioka, M. Generic phase diagram of fermion superfluids with population imbalance. *Phys. Rev. Lett.* **97**, 120407 (2006).

METHODS

Phase-contrast imaging. The optical signal in the phase-contrast imaging is proportional to the net phase shift of the imaging beam passing through a Fermi mixture, that is, it is proportional to $n_\uparrow/(v - v_\uparrow^0) - n_\downarrow/(v - v_\downarrow^0)$, where v is the probe frequency of the imaging beam, and $v_\uparrow{}^0$ and $v_\downarrow{}^0$ are the resonance frequencies of the optical transition for the states $|\uparrow\rangle$ and $|\downarrow\rangle$, respectively. When the probe beam is tuned to the middle of the two transitions, that is, to $v = v_0 = (v_\uparrow^0 + v_\downarrow^0)/2$, the optical signal reflects the density difference $n_d = n_\uparrow - n_\downarrow$. In our experiment, two phase-contrast images of the same sample were taken consecutively with different probe frequencies, v_1 and v_2 (Fig. 2). The two images record the density difference $n_{d1} = n_\uparrow - n_\downarrow$ and the weighted density difference $n_{d2} = \alpha_\uparrow n_\uparrow - \alpha_\downarrow n_\downarrow$. The first probe frequency v_1 was determined by zeroing the optical signal with an equal mixture and $\alpha_{\uparrow,\downarrow}$ was determined by the signal ratio between the first and the second image for a highly imbalanced Fermi mixture with $|\delta| > 95\%$ (an almost fully polarized gas). Finally, we obtained $n_\uparrow = (\alpha_\downarrow n_{d1} - n_{d2})/(\alpha_\downarrow - \alpha_\uparrow)$ and $n_\downarrow = (\alpha_\uparrow n_{d1} - n_{d2})/(\alpha_\downarrow - \alpha_\uparrow)$. The difference between v_1 and v_2 was chosen to lie between 8 and 13 MHz.

Data analysis. Low-noise profiles were obtained by averaging the column density distribution of phase-contrast images along elliptical equipotential lines ($\lambda^2 x^2 + z^2 = r^2$). For the measurement of the critical spin polarization, the averaging region was restricted to $|x| < 12\,\mu m$ to preserve the sharp features at the phase boundary. The diffraction limit for our imaging system was about $2\,\mu m$. For the determination of local quantities in the profiles, we averaged over $\pm 5\,\mu m$ around a given position. For temperature determination, the averaging region was restricted to an axial sector of $\pm 60°$ to avoid corrections due to transverse anharmonicities (see below). The relative temperature T' is determined as $T' \equiv T/T_{F0} = (-6\mathrm{Li}_3(-\zeta))^{-1/3}$, where ζ is the fugacity obtained from the fit ($\mathrm{Li}_s(z) \equiv \sum_{k=1}^{\infty} z^k/k^s$ is the polylogarithmic function of order s).

Anharmonicity of the trapping potential. For the determination of temperatures from the spatial *in situ* profiles it was necessary to address the anharmonicity of the trapping potential. Our trap is generated by a weakly focused (beam waist $w \approx 125\,\mu m$) infrared gaussian laser beam (wavelength 1,064 nm) near the saddle point of a magnetic potential. The total trapping potential is given as

$$V(\rho,z) = U_0 \exp\left(-\frac{2\rho^2}{w^2}\right) + \frac{m(2\pi f_z)^2}{2}\left(-\frac{\rho^2}{2} + z^2\right),$$

where $\rho^2 = x^2 + y^2$. We note that gravity has been compensated by a magnetic field gradient. The axial confinement comes mainly from the magnetic potential

with oscillation frequency of $f_z = 23$ Hz. The transverse magnetic potential is anti-trapping and limits the trap depth according to:

$$U = \frac{1}{4}m(2\pi f_\rho)^2 w^2 \left[1 - \frac{f_z^2}{2f_\rho^2}\ln\left(\frac{2f_\rho^2 + f_z^2}{f_z^2}\right)\right] \tag{1}$$

where f_ρ is the transverse oscillation frequency in the central harmonic region. When the trap depth is comparable to the Fermi energy of a sample, the transverse anharmonicity will affect the shape of the cloud. Although in our experiments the inner core and the outer cloud had the same aspect ratio as the trapping potential, anharmonicities were not negligible in the spatial wings used to determine the temperature.

This issue was addressed by adjusting the angular averaging region (Supplementary Fig. 3). Because the trapping potential is only anharmonic for large ρ, we could reduce the effect by decreasing the angle of the averaging sector around the axial z-direction. Both the experimental data and an exact simulation for an ideal Fermi gas show that the fitted temperature remains almost constant up to a certain angle and then increases when the averaging sector includes more of the transverse outer region. In our temperature determination, we chose the averaging sector to be $\pm 60°$, which was large enough to create low-noise profiles, but kept the effect of the anharmonicities to below 10%. The one-dimensional fit to angularly averaged profiles was computationally more efficient than a two-dimensional fit to a selected region of the image. In a two-dimensional fit, one could also include anharmonic terms in the fitting function.

Critical chemical potential ratio η_c. In a harmonic trap, the chemical potential of the majority and minority components are given as $\mu_\uparrow(r) = \mu_{\uparrow 0}(1 - r^2/R_\uparrow^2)$ and $\mu_\downarrow(r) = \mu_{\uparrow 0}(\eta_0 - r^2/R_\uparrow^2)$, respectively. At unitarity, the global chemical potential of a fully paired superfluid in the core is given as $\mu_{s0} = \xi \varepsilon_F = \xi \hbar^2 (6\pi^2 n_{s0})^{2/3}/2m$ where $n_{s0} = n_{\uparrow,\downarrow}(r = 0)$ is the central density. The thermodynamic equilibrium requires $\mu_{s0} = (\mu_{\uparrow 0} + \mu_{\downarrow 0})/2$, where $\mu_{\uparrow 0} = \hbar^2(6\pi^2 n_0)^{2/3}/2m$. From $\mu_{s0}/\mu_{\uparrow 0} = \xi(n_{s0}/n_0)^{2/3}$, we obtain the chemical potential ratio as:

$$\eta(r) = \frac{\eta_0 - r^2/R_\uparrow^2}{1 - r^2/R_\uparrow^2} = 2\frac{\xi(n_{s0}/n_0)^{2/3} - 1}{1 - r^2/R_\uparrow^2} + 1$$

In our coldest sample ($\delta \approx 44\%$), the normalized central density and the radius for the phase boundary were measured to be $n_{s0}/n_0 = 1.72(4)$ and $R_c/R_\uparrow = 0.430(3)$, respectively, yielding the critical chemical potential ratio $\eta_c = \eta(R_c) \approx 0.03$ with $\xi = 0.42$ (ref. 11). The critical difference is $h_c/\mu = (1 - \eta_c)/(1 + \eta_c) \approx 0.95$.

Phase diagram of a two-component Fermi gas with resonant interactions

Yong-il Shin, Christian H. Schunck, André Schirotzek & Wolfgang Ketterle

Supplementary Information

Supplementary Figures
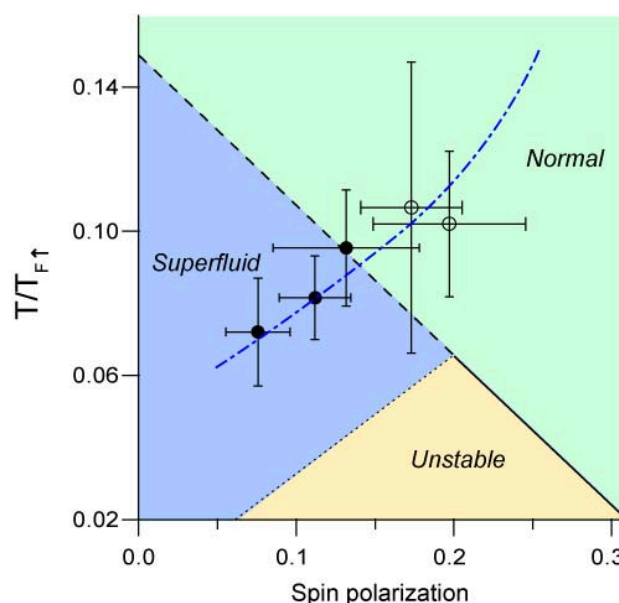
Supplementary Figure 1: (Color online) Trajectory of the center of a cloud in the phase diagram during the cooling process. Above the tricritical point, the normal-to-superfluid phase transition was observed by the onset of pair condensation in the evaporative cooling process. The local spin polarization and temperature at the center of the cloud was measured (black solid (open) circles with (without) condensate fraction), and the critical point was obtained by linearly interpolating with the condensate fraction. The dashed-dot line shows a guide line for the trajectory of the cloud center. The population imbalance of the sample was $\delta \approx 55\%$. A non-interacting mixture with this imbalance has a spin polarization $\sigma \approx 30\%$ at the center at zero temperature.
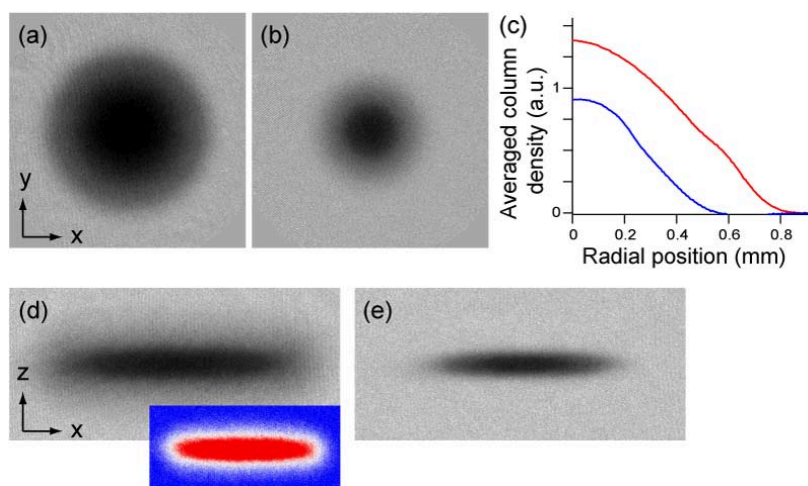
Supplementary Figure 2: (Color online) Expansion of a population-imbalanced Fermi mixture. The absorption images of (a, d) the majority and (b, e) minority components were taken along (a, b) the axial z and (d, e) transverse y directions after expansion. (c) The azimuthally averaged column density profiles of the majority (red) and the minority (blue) cloud are obtained from (a) and (b), respectively. The excess majority atoms in the outer region interact with the core during expansion. The contour lines of the outer part of the majority cloud (color inset) are not elliptical and have the shape of a horse-track. This shows that the minority cloud pushes the outer majority atoms in the transverse direction, which is also indicated by the hump of the majority profile at the edge of the minority cloud. The population imbalance was $\delta \approx 55\%$
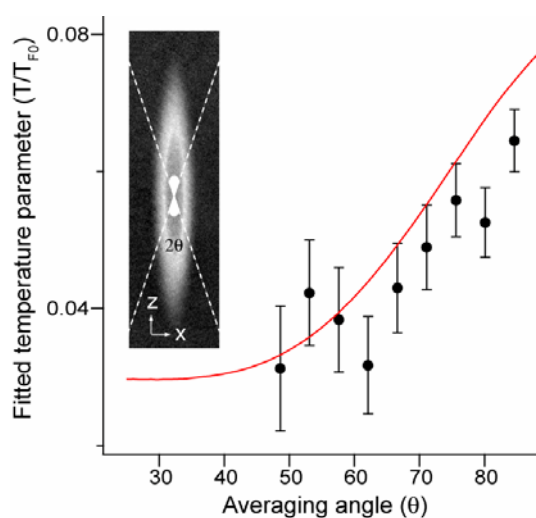
Supplementary Figure 3: (Color online) The temperature of the cloud was determined for various angles θ of the averaging sector. For a large angle, the large-x region is included in the averaged profile, resulting in a broadening of the spatial wings and consequently higher value of the fitted temperature. The red line shows the results of a simulation using the same parameters as the experiment ($\lambda = f_\rho/f_z = 6.15$, $T_{F0} = 1$ μK and the trap depth $U / k_B = 2$ μK).

Supplementary Discussion

Thermometry of ultracold Fermi gases
In our previous work[1,2], temperatures have been determined by fitting the spatial wings of the majority component after expansion. However, we found that one can neglect collisions with the minority atoms in the core only for large population imbalances. In a simplified picture, one can regard collisions with the inner core as collisions with a moving wall, which moves outward radially and inward axially (due to the magnetic trapping potential). This results in different average kinetic energies (transversely and axially) of the free majority atoms in the outer region. Figure S2 shows the density distribution of the majority and minority components after expansion. Although the temperature has been overestimated by only 20% for typical experimental conditions ($\delta \approx 60\%$) in refs [1,2], we do not regard this technique as well-calibrated absolute thermometry.

One other concept for thermometry determines temperature as the derivative of entropy with energy. So far, this concept could be implemented only for balanced fermion mixtures with certain approximations, and due to the need of determining a derivative, could only be used to obtain temperatures averaged over a certain range[3].

Polarized superfluid at finite temperature
When the two spin components have a chemical potential difference $2h$, the BCS-type superfluid has two branches of quasiparticles with excitation energies $\sqrt{(\varepsilon_k - \mu)^2 + \Delta^2} \pm h$ where $\varepsilon_k = \hbar^2 k^2 / 2m$. At finite temperature, the superfluid is polarized due to the large thermal population of the lower branch compared to the upper branch. An interesting situation arises when h becomes larger than Δ, i.e. the lower branch has negative energy quasiparticles, implying that even at zero temperature the superfluid state would have a finite polarization. Our experiments show $h_c < \Delta$ at very low temperature, suggesting that a polarized superfluid state exists only at finite temperature. The breached-pair state with $h_c > \Delta$ at zero temperature has been predicted in a stronger coupling regime (on the BEC side of the Feshbach resonance). Since Δ gradually decreases with higher temperature, it might be possible to have $h_c > \Delta$ at finite temperature, at least in the weakly-interacting BCS limit where Δ smoothly approaches zero at a second order phase transition point. One interesting problem is identifying this gapless region of $h > \Delta$ in the phase diagram for various coupling regimes.

Supplementary Notes
1. Zwierlein, M. W., Schunck, C. H., Schirotzek, A. & Ketterle, W. Direct Observation of the superfluid phase transition in ultracold Fermi gases. *Nature* **442**, 54-58 (2006).

2. Shin, Y., Zwierlein, M. W., Schunck, C. H., Schirotzek A. & Ketterle, W. Observation of phase Separation in a strongly interacting imbalanced Fermi gas. *Phys. Rev. Lett.* **97**, 030401 (2006).

3. Luo, L., Clancy, B., Joseph, J., Kinast, J. & Thomas, J. E. Measurement of the entropy and critical temperature of a strongly interacting Fermi gas. *Phys. Rev. Lett.* **98**, 080402 (2007).

Appendix C

Observation of Fermi Polarons in a Tunable Fermi Liquid of Ultracold Atoms

This appendix contains a reprint of Ref. [119]: Andre Schirotzek, Cheng-Hsun Wu, Ariel Sommer, and Martin W. Zwierlein, *Observation of Fermi Polarons in a Tunable Fermi Liquid of Ultracold Atoms*, Phys. Rev. Lett. **102**, 230402 (2009).

Ⓟ Selected for a Viewpoint in *Physics*
PHYSICAL REVIEW LETTERS

☙

Observation of Fermi Polarons in a Tunable Fermi Liquid of Ultracold Atoms

André Schirotzek, Cheng-Hsun Wu, Ariel Sommer, and Martin W. Zwierlein

Department of Physics, MIT-Harvard Center for Ultracold Atoms, and Research Laboratory of Electronics,
Massachusetts Institute of Technology, Cambridge, Massachusetts 02139, USA
(Received 17 February 2009; revised manuscript received 9 April 2009; published 8 June 2009)

We have observed Fermi polarons, dressed spin-down impurities in a spin-up Fermi sea of ultracold atoms. The polaron manifests itself as a narrow peak in the impurities' rf spectrum that emerges from a broad incoherent background. We determine the polaron energy and the quasiparticle residue for various interaction strengths around a Feshbach resonance. At a critical interaction, we observe the transition from polaronic to molecular binding. Here, the imbalanced Fermi liquid undergoes a phase transition into a Bose liquid, coexisting with a Fermi sea.

The fate of a single impurity interacting with its environment determines the low-temperature behavior of many condensed matter systems. A well-known example is given by an electron moving in a crystal lattice, displacing nearby ions and thus creating a localized polarization. The electron, together with its surrounding cloud of lattice distortions, phonons, forms the lattice polaron [1]. It is a quasiparticle with an energy and mass that differ from that of the bare electron. Polarons are central to the understanding of colossal magnetoresistance materials [2], and they affect the spectral function of cuprates, the parent material of high-T_C superconductors [3]. Another famous impurity problem is the Kondo effect, where immobile spin impurities give rise to an enhanced resistance in metals below the Kondo temperature [4]. In contrast to the electron moving in a phonon bath, a bosonic environment, in the latter case the impurity interacts with a fermionic environment, the Fermi sea of electrons.

Here we study a small concentration of spin-down impurities immersed in a spin-up Fermi sea of ultracold atoms. This system represents the limiting case of spin-imbalanced Fermi gases and has been recognized to hold the key to the quantitative understanding of the phase diagram of imbalanced Fermi mixtures [5–16]. Unlike in liquid ^{3}He, the *s*-wave interaction potential between the impurities and the spin-up atoms in this novel spin-imbalanced Fermi liquid is attractive. The vicinity of a Feshbach resonance allows tuning of the interaction strength at will, characterized by the ratio of the interparticle distance $\sim 1/k_F$ to the scattering length a, where k_F is the spin-up Fermi wave vector [17]. Figure 1 depicts the scenario for a single impurity: For weak attraction $(1/k_F a \ll -1)$ the impurity propagates freely in the spin-up medium of density $n_\uparrow = k_F^3/6\pi^2$ [Fig. 1(a)]. It merely experiences the familiar attractive mean field energy shift $E_\downarrow = 4\pi\hbar^2 an_\uparrow/m < 0$. However, as the attractive interaction grows, the impurity can undergo momentum changing collisions with environment atoms, and thus starts to attract its surroundings. The impurity "dressed" with the localized cloud of scattered fermions constitutes

the Fermi polaron [Fig. 1(b)]. Dressing becomes important once the mean free path $\sim 1/n_\uparrow a^2$ of the bare impurity in the medium becomes comparable to the distance $\sim 1/k_F$ between environment particles or when $(k_F a)^2 \sim 1$. Collisions then reduce the bare impurity's probability of free propagation, the quasiparticle residue Z, from unity. The dressed impurity can instead move freely through the environment, with an energy $E_\downarrow$ shifted away from the simple mean field result. This polaronic state is stable until, for strong attraction $(1/k_F a \sim 1)$, equivalent to a deep effective potential well, the spin-down impurity will bind exactly one spin-up atom, thus forming a tightly bound molecule [Fig. 1(c)]. This molecule is itself a dressed impurity, albeit a bosonic one [13].

To prepare and observe Fermi polarons, we start with a spin-polarized cloud of ^{6}Li atoms in the lowest hyperfine state $|1\rangle$ (spin-up), confined in a cylindrically symmetric optical trap (125 μm waist, 145 Hz/22.3 Hz radial/axial trapping frequency) at a magnetic field of 690 G [17]. A two-photon Landau-Zener sweep transfers a small fraction into state $|3\rangle$ (spin-down), and further cooling results in a cloud containing 2% $|3\rangle$ impurities immersed in a degenerate Fermi gas of 5×10^6 $|1\rangle$ atoms at a temperature $T = 0.14(3)T_F$, where T_F is the Fermi temperature. A 100 G wide Feshbach resonance for scattering between these states is centered at 690 G. For various fields around the

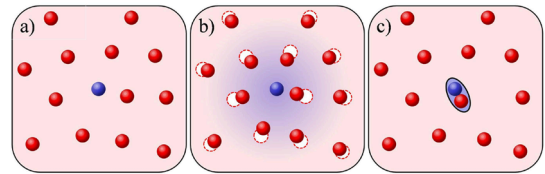FIG. 1 (color online). From polarons to molecules. (a) For weak attraction, an impurity (blue) experiences the mean field of the medium (red). (b) For stronger attraction, the impurity surrounds itself with a localized cloud of environment atoms, forming a polaron. (c) For strong attraction, molecules of size a form despite Pauli blocking of momenta $\hbar k < \hbar k_F \ll \hbar/a$ by the environment.

resonance, we perform rf spectroscopy on the impurity species $|3\rangle$ and on the environment particles in $|1\rangle$ by transferring atoms into the empty state $|2\rangle$, accessible to either hyperfine state. This state is sufficiently weakly interacting with the initial states to allow a direct interpretation of the resulting spectra [18]. As in previous work, spectra are spatially resolved and tomographically 3D reconstructed [19] via an inverse Abel transform, and are thus local and free from broadening due to density inhomogeneities. In addition, phase contrast images yield the *in situ* density distribution $n_\uparrow$, $n_\downarrow$ and thus the local Fermi energy ϵ_F of the environment atoms and the local impurity concentration $x = \frac{n_\downarrow}{n_\uparrow}$. The Rabi frequencies Ω_R for the impurity and environment rf transitions are measured (on fully polarized samples) to be identical to within 5%.

Figure 2 shows the observed spectra of the spin-down impurities and that of the spin-up environment at low local impurity concentration. The bulk of the environment spectrum is found at zero offset, corresponding to the free (Zeeman plus hyperfine) energy splitting between states $|1\rangle$ and $|2\rangle$. However, interactions between impurity and spin-up particles lead to a spectral contribution that is shifted: The rf photon must supply additional energy to transfer a particle out of its attractive environment into the final, noninteracting state [17]. In Fig. 2(a), impurity and environment spectra above zero offset exactly overlap, signaling two-body molecular pairing. The steep threshold gives the binding energy, the high-frequency wings arise from molecule dissociation into remnants with nonzero momentum [17,20,21]. As the attractive interaction is reduced, however, a narrow peak appears in the impurity spectrum that is not matched by the response of the environment [Figs. 2(b)–2(d)]. This narrow peak, emerging from a broad incoherent background, signals the formation of the Fermi polaron, a long-lived quasiparticle. The narrow width and long lifetime are expected: At zero temperature the zero momentum polaron has no phase space for decay and is stable. At finite kinetic energy or finite temperature T it may decay into particle-hole excitations [13], but phase space restrictions due to the spin-up Fermi sea and conservation laws imply a decay rate $\propto (T/T_F)^2 \sim$

1% in units of the Fermi energy. Indeed, the width of the polaron peak is consistent with a delta function within the experimental resolution, as calibrated by the spectra of fully polarized clouds. The background is perfectly matched by the rf spectrum of the environment. This is expected at high rf energies $\hbar\omega \gg \epsilon_F$ that are probing high momenta $k \gg k_F$ and thus distances short compared to the interparticle spacing. Here, an impurity particle will interact with only one environment particle, leading to overlapping spectra.

Chevy has provided an instructive variational wave function [5,9] that captures the essential properties of the polaron, even on a quantitative level [16] when compared with Monte Carlo (MC) calculations [6,12,13]:

$$|\Psi\rangle = \varphi_0 |0\rangle_\downarrow |FS\rangle_\uparrow + \sum_{|\mathbf{q}|<k_F<|\mathbf{k}|} \varphi_{\mathbf{kq}} c_{\mathbf{k}\uparrow}^\dagger c_{\mathbf{q}\uparrow} |\mathbf{q}-\mathbf{k}\rangle_\downarrow |FS\rangle_\uparrow \quad (1)$$

The first part describes a single impurity with a well-defined wave vector ($\mathbf{k}_\downarrow = \mathbf{0}$) that is not localized and free to propagate in the Fermi sea of up spins $|FS\rangle_\uparrow$. In the second part the impurity particle recoils off environment particles that are scattered out of the Fermi sea and leave holes behind. This describes the dressing of the impurity with particle-hole excitations. The probability of free propagation is given by the first, unperturbed part, $Z = |\varphi_0|^2$. According to Fermi's golden rule [11,15,17,22], the two portions of $|\Psi\rangle$ give rise to two distinct features of the impurity rf spectrum $\Gamma(\omega)$ (ω is the rf offset from the bare atomic transition):

$$\Gamma(\omega) = 2\pi\hbar\Omega_R^2 Z\delta(\hbar\omega + E_\downarrow) + \Gamma^{\text{inc}}(\omega). \quad (2)$$

The first part in $|\Psi\rangle$ contributes a coherent narrow quasiparticle peak to the minority spectrum. Its position is a direct measure of the polaron energy $E_\downarrow$, its integral gives the quasiparticle residue Z. The particle-hole excitations in the second part give rise to a broad, incoherent background $\Gamma^{\text{inc}}(\omega) \propto \sum_{\mathbf{q,k}} |\varphi_{\mathbf{qk}}|^2 \delta(\hbar\omega - \epsilon_{\mathbf{q-k}} - \epsilon_{\mathbf{k}} + \epsilon_{\mathbf{q}} + E_\downarrow)$: The polaron energy $E_\downarrow$ is released as the impurity at momentum $\mathbf{q} - \mathbf{k}$ is transferred into the final state, leaving behind an
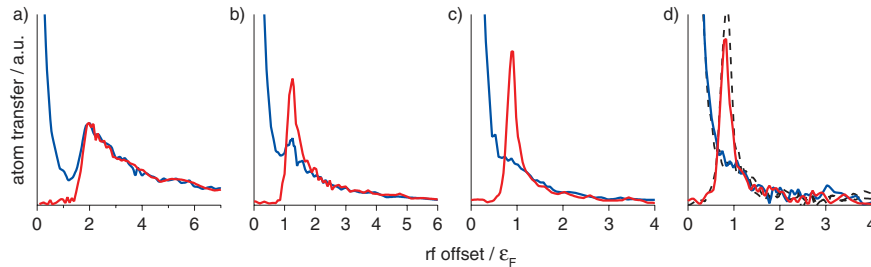
FIG. 2 (color online). rf spectroscopy on polarons. Shown are spatially resolved, 3D reconstructed rf spectra of the environment (blue, state $|1\rangle$) and impurity (red, state $|3\rangle$) component in a highly imbalanced spin-mixture. (a) Molecular limit; (b),(c) Emergence of the polaron, a distinct peak exclusively in the minority component. (d) At unitarity, the polaron peak is the dominant feature in the impurity spectrum, which becomes even more pronounced for $1/k_F a < 0$ (not shown). For the spectra shown as dashed lines in (d) the roles of states $|1\rangle$ and $|3\rangle$ are exchanged. The local impurity concentration was $x = 5(2)\%$ for all spectra, the interaction strengths $1/k_F a$ were (a) 0.76(2), (b) 0.43(1), (c) 0.20(1), and (d) 0 (unitarity).

environment particle in **k** above and a hole within the Fermi sea at **q** [22]. These two spectral features are recovered in theoretical rf spectra for a finite number of impurities, i.e., a Fermi liquid [15,23]. For our analysis we do not rely on a theoretical fit to the spectra.

To measure the polaron energy $E_\downarrow$, we determine the peak position of the impurity spectrum as a function of the local interaction parameter $1/k_F a$. The data for 5% impurity concentration are shown in Fig. 3(a), along with the variational upper bound given by the wave function Eq. (1) [22] and the diagrammatic MC calculation of [13]. As final state interactions are weak, they can be included as a simple repulsive mean field shift $4\pi\hbar^2 a_{\rm fe} n_\uparrow/m$, with $a_{\rm fe}$ the scattering length between the final state and the environment atoms [24]. Polaron energies have been predicted via the variational ansatz [5], the T-matrix approach [9,10,15,16], the $1/N$ expansion [11], fixed-node MC [6,12] and diagrammatic MC calculations [13]. With the exception of the $1/N$ expansion, these all agree with each other and with the present experiment to within a few percent. In particular, in the unitary limit where $1/k_F a = 0$ we find a polaron energy of $E_\downarrow = -0.64(7)\epsilon_F$ ($-0.72(9)\epsilon_F$) when state $|3\rangle$ ($|1\rangle$) serves as the impurity [25]. This agrees well with the diagrammatic MC calculation, $-0.615\epsilon_F$ [14], and the analytical result $-0.6156(2)\epsilon_F$ [16]. Analy-
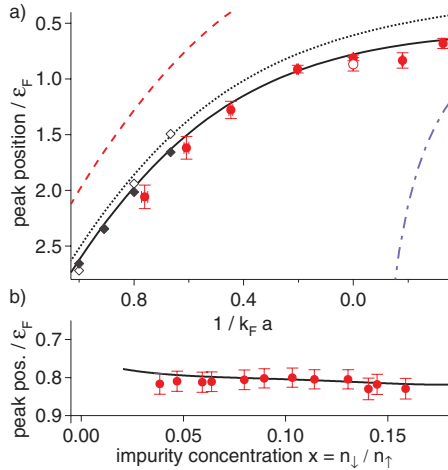
sis of experimental density profiles yields a value of $-0.58(5)\epsilon_F$ [26].

The relatively large value for $E_\downarrow$ directly implies that the normal state, modeled as a Fermi sea of weakly interacting polarons, is favored over the superfluid state up to a critical concentration (44%), much higher than that predicted by mean field theories (4%) [27]. These neglect interactions in the normal state and therefore imply a polaron binding energy of zero.

We have so far considered the limit of few impurities. By increasing their density, we can study the effect of interactions between polarons. In Fig. 3(b) we show that the quasiparticle peak position depends only weakly on the impurity concentration in the unitarity limit. Polarons are thus weakly interacting quasiparticles, despite the strong interactions between the bare impurity and its environment.

The peak position could be modified due to the effective mass m^* of polarons, larger than the mass of the bare impurity. Transfer of a moving polaron into the free final state then requires additional kinetic energy. This leads to an upshift and a broadening on the order of the Fermi energy difference between initial and final state, $x^{2/3}\epsilon_F(1 - \frac{m}{m^*})$. On resonance, this is $0.04\epsilon_F$ for $x = 0.1$. The effect could be partially masked by the predicted weak repulsion between polarons [12] that would downshift the resonance frequency by $-0.02\epsilon_F$ for $x = 0.1$.

The spectral weight of the polaron peak directly gives the quasiparticle residue Z, a defining parameter of a Fermi liquid. Experimentally, we determine the area under the impurity peak that is not matched by the environment's

FIG. 3 (color online).   Peak position of the impurity spectrum as a measure of the polaron energy $E_\downarrow$. (a) peak position for various interaction strengths in the limit of low concentration $x = 5(2)\%$ (solid circles). Open circle: Reversed roles of impurity and environment. Dotted line: polaron energy from variational ansatz Eq. (1) [5], the solid line including weak final state interactions. Dashed line: Energy of a bare, isolated molecule in vacuum. Blue dash-dotted line: Mean field limit for the energy of an impurity atom. Solid (open) diamonds: Diagrammatic MC energy of the polaron (molecule) [13]. (b) Peak position at unitarity ($1/k_F a = 0$) as a function of impurity concentration (solid circles). The line shows the expected peak position, $\hbar\omega_p/\epsilon_F = A + (1 - \frac{m}{m^*})x^{2/3} - \frac{6}{5}Fx + \frac{4}{3\pi}k_F a_{\rm fe}$, using the MC value $A = 0.615$ [13], the analytic result $m^* = 1.2$ [16], the weak repulsion between polarons with $F = 0.14$ [12] and weak final state interactions with scattering length $a_{\rm fe}$.

FIG. 4 (color online).   Quasiparticle residue Z as a function of interaction strength and impurity concentration. The color coding indicates the magnitude of Z and is an interpolation of the data points shown in the graph. Open circles: Data points consistent with zero ($Z < 0.03$), solid circles: $Z > 0.03$, the solid line marking the onset of Z. Blue cross: Critical interaction strength for the Fermi liquid—molecular BEC transition for $x \to 0$ [12]. Inset: Z as a function of interaction strength in the limit of low impurity concentration $x = 5(2)\%$. Open circle: Reversed roles, $|1\rangle$ impurity in $|3\rangle$ environment. The spectrum in the inset illustrates the determination of Z [22].

response and divide by the total area under the impurity spectrum (see spectrum in Fig. 4 and [22]). Figure 4 presents Z as a function of interaction strength and impurity concentration x, the inset shows Z for $x = 5\%$. As expected, Z approaches 100% for weak attractive interaction $k_F a \rightarrow 0^-$, where the bare impurity only rarely recoils off environment atoms. As the mean free path shortens and the bare impurity starts to surround itself with environment atoms Z decreases. On resonance, we find $Z = 0.39(9)$ for $x = 5\%$, with only a weak dependence on x (Fig. 4). Theoretical values for Z vary: ansatz Eq. (1) predicts $Z = 0.78$ for a single impurity, while Ref. [11] predicts $Z = 0.47 (0.30)$ for vanishing (5%) impurity concentration. Our procedure might yield a lower bound on the actual value of Z, as the incoherent part of the impurity spectrum might be depleted around threshold. Eventually, for strong attraction between the impurity and particles of the medium, Z vanishes and we observe complete overlap of the impurity and environment spectra. This signals the formation of a two-body bound state between the impurity and exactly one environment atom. For a spin-down concentration of 5% we determine the critical interaction strength where the polaron peak vanishes to be $1/(k_F a)_c = 0.76(2)$. This is in good agreement with the independently determined critical interaction $1/k_F a = 0.74(4)$ beyond which one finds a superfluid even for the smallest impurity concentration [28]. This is a multicritical point [12,13,29] where a Fermi liquid of weakly interacting polarons undergoes a phase transition into a Bose liquid of molecular impurities. Fixed-node MC calculations place this transition at a value of $1/k_F a = 0.73$ for $x \rightarrow 0$ [12]. Our $1/(k_F a)_c$ is lower than the value $0.90(2)$ from diagrammatic MC [13] for a single impurity. Ansatz Eq. (1) does not predict a transition, as it does not test for the formation of molecules. In Fig. 4, the color coding reveals where molecular behavior is observed (yellow), and where the spectra show polaronic behavior (red to black). It can be seen that the critical interaction strength for the formation of molecules depends only weakly on the impurity concentration x.

In conclusion, we have observed Fermi polarons in a novel, attractive Fermi liquid of spin-down impurity atoms immersed in a spin-up Fermi sea. The energy and residue of this quasiparticle was determined and interactions between quasiparticles were found to be weak. Polarons thus emerge as the quasiparticles of a Landau Fermi liquid description of this strongly interacting Fermi mixture. To study first the impurity limit of $N + 1$ interacting particles before dealing with the full $N + M$ many-body system will be a fruitful approach for other strongly correlated systems realized with cold atoms. An intriguing question is how the limit of a weakly interacting polaron liquid containing few impurities connects to the physics of a hydrodynamic, balanced Fermi gas containing Cooper pair fluctuations above the critical temperature for superfluidity. In light of our findings, fermion pair condensation could be viewed as condensation of pairs of polarons with opposite spin. This is also suggested by the large normal state interaction measured by quasiparticle spectroscopy on the superfluid state [30].

[1] L. Landau, Phys. Z. Sowjetunion **3**, 644 (1933).
[2] N. Mannella *et al.*, Nature (London) **438**, 474 (2005).
[3] P. A. Lee, N. Nagaosa, and X.-G. Wen, Rev. Mod. Phys. **78**, 17 (2006).
[4] J. Kondo, Prog. Theor. Phys. **32**, 37 (1964).
[5] F. Chevy, Phys. Rev. A **74**, 063628 (2006).
[6] C. Lobo *et al.*, Phys. Rev. Lett. **97**, 200403 (2006).
[7] C. Schunck *et al.*, Science **316**, 867 (2007).
[8] A. Bulgac and M. M. Forbes, Phys. Rev. A **75**, 031605(R) (2007).
[9] R. Combescot *et al.*, Phys. Rev. Lett. **98**, 180402 (2007).
[10] M. Punk and W. Zwerger, Phys. Rev. Lett. **99**, 170404 (2007).
[11] M. Veillette *et al.*, Phys. Rev. A **78**, 033614 (2008).
[12] S. Pilati and S. Giorgini, Phys. Rev. Lett. **100**, 030401 (2008).
[13] N. V. Prokof'ev and B. V. Svistunov, Phys. Rev. B **77**, 020408(R) (2008).
[14] N. V. Prokof'ev and B. V. Svistunov, Phys. Rev. B **77**, 125101 (2008).
[15] P. Massignan, G. M. Bruun, and H. T. C. Stoof, Phys. Rev. A **78**, 031602(R) (2008).
[16] R. Combescot and S. Giraud, Phys. Rev. Lett. **101**, 050404 (2008).
[17] W. Ketterle and M. Zwierlein, in *Proceedings of the International School of Physics "Enrico Fermi", Course CLXIV*, edited by M. Inguscio, W. Ketterle, and C. Salomon (IOS Press, Amsterdam, 2008), p. 95.
[18] C. H. Schunck *et al.*, Nature (London) **454**, 739 (2008).
[19] Y. Shin *et al.*, Phys. Rev. Lett. **99**, 090403 (2007).
[20] C. A. Regal *et al.*, Nature (London) **424**, 47 (2003).
[21] We do not observe Pauli blocking effects proposed in [15].
[22] See EPAPS Document No. E-PRLTAO-102-040923. For more information on EPAPS, see http://www.aip.org/pubservs/epaps.html.
[23] W. Schneider, V. B. Shenoy, and M. Randeria, arXiv:0903.3006.
[24] The next order correction due to incoherent scattering, where a_{fe} is replaced by the full real part of the scattering amplitude, is of order $(k_F a_{\text{fe}})^2 \approx 5\%$ and thus negligible.
[25] Switching roles of states $|1\rangle$ and $|3\rangle$ tests for the influence of final state interactions. They contribute $E_f = 0.17(1)\epsilon_F$ $[0.13(1)\epsilon_F]$ to the peak position when state $|3\rangle$ ($|1\rangle$) serves as the impurity.
[26] Y. Shin, Phys. Rev. A **77**, 041603(R) (2008).
[27] D. E. Sheehy and L. Radzihovsky, Ann. Phys. (N.Y.) **322**, 1790 (2007).
[28] Y. Shin *et al.*, Phys. Rev. Lett. **101**, 070404 (2008).
[29] S. Sachdev and K. Yang, Phys. Rev. B **73**, 174504 (2006).
[30] A. Schirotzek *et al.*, Phys. Rev. Lett. **101**, 140403 (2008).

Supplemental Material: "Observation of Fermi Polarons in a Tunable Fermi Liquid of Ultracold Atoms"

André Schirotzek, Cheng-Hsun Wu, Ariel Sommer, and Martin W. Zwierlein

Department of Physics, MIT-Harvard Center for Ultracold Atoms, and Research Laboratory of Electronics,
Massachusetts Institute of Technology, Cambridge, Massachusetts 02139, USA

(Dated: May 1, 2009)

In this supplemental material we state, starting with the variational Ansatz by Chevy, key properties of the polaron, such as the energy $E_\downarrow$ and the quasiparticle residue Z, and we calculate its RF spectrum using Fermi's Golden Rule. We connect this approach and its implication for finite impurity concentration to the results of Fermi liquid theory and the T-matrix formalism used in [1–4]. Furthermore, details are provided about the extraction of the quasiparticle residue Z.

Polaron wavefunction, energy and quasiparticle residue

We start with the hamiltonian for a dilute two component mixture of fermionic atoms interacting via the van-der-Waals potential $V(\mathbf{r})$ [5]. Thanks to the diluteness of the system, the potential is of short range R compared to the interparticle distance $1/k_F$, so $k_F R \ll 1$. Its Fourier transform $V(\mathbf{k})$ is thus essentially constant, g_0, below k_F and rolls off to zero at a momentum on the order of $1/R \gg k_F$. The many-body Hamiltonian for the system is then

$$\hat{H} = \sum_{\mathbf{k},\sigma} \epsilon_{\mathbf{k}} c^\dagger_{\mathbf{k}\sigma} c_{\mathbf{k}\sigma} + \frac{g_0}{\mathcal{V}} \sum_{\mathbf{k},\mathbf{k}',\mathbf{q}} c^\dagger_{\mathbf{k}+\frac{\mathbf{q}}{2}\uparrow} c^\dagger_{-\mathbf{k}+\frac{\mathbf{q}}{2}\downarrow} c_{\mathbf{k}'+\frac{\mathbf{q}}{2}\downarrow} c_{-\mathbf{k}'+\frac{\mathbf{q}}{2}\uparrow} \tag{1}$$

Here, the label σ denotes the spin state $\uparrow,\downarrow$, $\epsilon_{\mathbf{k}} = \hbar^2 k^2/2m$, $\mathcal{V}$ is the volume of the system and the $c^\dagger_{k\sigma}, c_{k\sigma}$ are the usual creation and annihilation operators for fermions with momentum $\mathbf{k}$ and spin σ. The trial wavefunction for the Fermi polaron with zero momentum proposed by F. Chevy in [6] is

$$|\Psi\rangle = \varphi_0 |\mathbf{0}\rangle_\downarrow |FS\rangle_\uparrow + \sum_{q<k_F}^{k>k_F} \varphi_{\mathbf{kq}} c^\dagger_{\mathbf{k}\uparrow} c_{\mathbf{q}\uparrow} |\mathbf{q}-\mathbf{k}\rangle_\downarrow |FS\rangle_\uparrow \tag{2}$$

The energy is then minimized under variation of the parameters φ_0 and $\varphi_{\mathbf{kq}}$, with the constraint of constant norm $\langle\Psi|\Psi\rangle = |\varphi_0|^2 + \sum_{q<k_F}^{k>k_F} |\varphi_{\mathbf{kq}}|^2 = 1$. That is, the quantity to minimize is $\langle\Psi|\hat{H}|\Psi\rangle - E_\downarrow \langle\Psi|\Psi\rangle$. The derivation can be found in [6], here we quote the result for the particle-hole excitation amplitudes $\varphi_{\mathbf{kq}}$, the quasiparticle weight $|\varphi_0|^2 = Z$, and the energy $E_\downarrow$ due to addition of the down spin impurity:

$$\varphi_{\mathbf{kq}} = \varphi_0 \frac{1}{\mathcal{V}} \frac{f(E_\downarrow, \mathbf{q})}{E_\downarrow - \epsilon_{\mathbf{k}} + \epsilon_{\mathbf{q}} - \epsilon_{\mathbf{q}-\mathbf{k}}} \tag{3}$$

$$\frac{1}{|\varphi_0|^2} \equiv \frac{1}{Z} = \left(1 - \frac{\partial}{\partial E} \frac{1}{\mathcal{V}} \sum_{q<k_F} f(E,\mathbf{q})\right)_{E=E_\downarrow} \tag{4}$$

$$E_\downarrow = \frac{1}{\mathcal{V}} \sum_{q<k_F} f(E_\downarrow, \mathbf{q}) \tag{5}$$

These all depend on the function $f(E,\mathbf{q})$ with

$$f^{-1}(E,\mathbf{q}) = \frac{1}{g_0} + \frac{1}{\mathcal{V}} \sum_{k>k_F} \frac{1}{\epsilon_{\mathbf{k}} - \epsilon_{\mathbf{q}} + \epsilon_{\mathbf{q}-\mathbf{k}} - E} \tag{6}$$

It is a measure of the interaction strength between spin up and spin down, modified by the presence of the spin up Fermi sea. As usual, g_0 can be replaced by the physically observable scattering length a for collisions between spin up and down via [5] $\frac{1}{g_0} = \frac{m}{4\pi\hbar^2 a} - \frac{1}{\mathcal{V}}\sum_{\mathbf{k}} \frac{1}{2\epsilon_{\mathbf{k}}}$.

$$f^{-1}(E,\mathbf{q}) = \frac{mk_F}{2\pi^2\hbar^2}\left(\frac{\pi}{2k_F a} - 1\right) + \tag{7}$$
$$\frac{1}{\mathcal{V}} \sum_{k>k_F} \left(\frac{1}{\epsilon_{\mathbf{k}} - \epsilon_{\mathbf{q}} + \epsilon_{\mathbf{q}-\mathbf{k}} - E} - \frac{1}{2\epsilon_k}\right)$$

The integral in above expression is convergent and gives

$$f^{-1}(E,\mathbf{q}) = \frac{mk_F}{2\pi^2\hbar^2}\left\{\frac{\pi}{2k_F a} - 1 + I\left(\frac{E}{E_F}, \frac{q}{k_F}\right)\right\} \tag{8}$$
$$I(\epsilon, y) = \int_1^\infty dx \left(\frac{x}{2y} \ln\left(\frac{2x^2 + 2xy - \epsilon}{2x^2 - 2xy - \epsilon}\right) - 1\right)$$

An analytic expression for the integral exists but does not provide additional insight. The equation for $E_\downarrow$ becomes

$$\frac{E_\downarrow}{E_F} = -2 \int_0^1 dy \frac{y^2}{1 - \frac{\pi}{2k_F a} - I\left(\frac{E_\downarrow}{E_F}, y\right)} \tag{9}$$

This implicit equation for $E_\downarrow$ can be easily solved numerically. The result is shown as the dashed line in Fig. 3 of the main paper. Clearly, $E_\downarrow$ is negative due to the attractive interactions with the medium. In the weakly interacting limit $1/k_F a \to -\infty$, we can neglect the integral in the denominator and immediately obtain $E_\downarrow = \frac{2}{3}\frac{2k_F a}{\pi} E_F = 4\pi\hbar^2 a n_\uparrow/m$, which is the mean field result [7].

The approach turns out to be equivalent to a T-Matrix description, as shown in [7]. In that language, $f(E,\mathbf{q})$

is (up to a constant) the scattering amplitude in the medium (i.e. the vertex) for the scattering process with total energy and momentum E and q of the colliding particles. $\Sigma(\mathbf{0}, E) \equiv \frac{1}{V} \sum_{q<k_F} f(E_\downarrow + E, \mathbf{q})$ is the self-energy at zero momentum and frequency $E/\hbar$. It is real in this approximation. The expression for the quasiparticle residue Z of a *single* spin down impurity in Eq. 4 is immediately seen to be equivalent to the well-known relation [3]

$$Z_\downarrow^{-1} = \left(1 - \frac{\partial}{\partial E} \mathrm{Re}\Sigma(k_{F\downarrow}, E)\right)_{E=0} \quad (10)$$

for a spin down quasiparticle on top of a spin down Fermi sea, in the limit of vanishing Fermi momentum $k_{F\downarrow}$.

RF spectrum from the variational Ansatz

Fermi's Golden Rule allows us to directly predict the shape of the impurity RF spectrum. This topic has been studied in detail since the early days of RF spectrosocpy, and for the problem of highly imbalanced Fermi gases in [1–4], among others. Chevy's wavefunction offers a simple way of calculating the RF spectrum of a single impurity.

The RF operator $\hat{V} = \hbar\Omega_R \sum_k c_{k,f}^\dagger c_{k,\downarrow} + h.c.$ promotes the impurity into the free final state $|f\rangle$ (energy E_f) without momentum transfer [5]. In the experiment, the final internal state is the second lowest hyperfine state of ^{6}Li. Fermi's Golden Rule for the impurity starting in state $|\Psi\rangle$ is

$$\Gamma(\omega) = \frac{2\pi}{\hbar} \sum_f \left|\left\langle f|\hat{V}|\Psi\right\rangle\right|^2 \delta(\hbar\omega - (E_f - E_\downarrow)) \quad (11)$$

Where ω is the RF offset from the bare atomic transition frequency between the internal states labeled by $\downarrow$ and f. One possible final state is $|0\rangle \equiv |\mathbf{0}\rangle_f |FS\rangle_\uparrow$, i.e. a zero momentum particle in the final state plus a perfect Fermi sea of up spins, with energy $E_{|0\rangle} = 0$ relative to the Fermi energy E_F of the environment. Other possible final states are $|\mathbf{q}, \mathbf{k}\rangle \equiv |\mathbf{q} - \mathbf{k}\rangle_f c_{\mathbf{k}\uparrow}^\dagger c_{\mathbf{q}\uparrow} |FS\rangle_\uparrow$ with $q < k_F$ and $k > k_F$, i.e. a particle with momentum $\mathbf{q} - \mathbf{k}$ in the final state and a Fermi sea with a hole at $\mathbf{q}$ and an excited environment particle above the Fermi sea at $\mathbf{k}$. The energy of these states is $E_{|\mathbf{q},\mathbf{k}\rangle} = \epsilon_\mathbf{k} - \epsilon_\mathbf{q} + \epsilon_{\mathbf{q}-\mathbf{k}}$ relative to the environment Fermi energy E_F. The matrix elements are

$$\left\langle 0\left|\hat{V}\right|\Psi\right\rangle = \hbar\Omega_R\, \varphi_0$$
$$\left\langle \mathbf{q}, \mathbf{k}\left|\hat{V}\right|\Psi\right\rangle = \hbar\Omega_R\, \varphi_{\mathbf{k}\mathbf{q}}$$

This leaves us with two components in the RF spectrum:

$$\Gamma(\omega) = 2\pi\hbar\Omega_R^2 \Bigg(Z\delta(\hbar\omega + E_\downarrow) + \quad (12)$$
$$\sum_{q<k_F}^{k>k_F} |\varphi_{\mathbf{k}\mathbf{q}}|^2\, \delta(\hbar\omega + E_\downarrow - \epsilon_\mathbf{k} + \epsilon_\mathbf{q} - \epsilon_{\mathbf{q}-\mathbf{k}}) \Bigg)$$

The first part is a delta-peak shifted by the quasiparticle energy. As $E_\downarrow < 0$, it is shifted to higher frequencies: The RF photon has to supply additional energy to transfer the impurity out of its attractive environment. The weight of this peak is Z, the quasiparticle residue, allowing the experimental determination of Z by simply integrating the area under the prominent peak. Such a delta-peak is typically called "coherent", as a broadband excitation around this energy would not dephase over time. The second part of the spectrum is incoherent, it consists of a broad continuum of frequencies. Broadband excitations of this continuum would rapidly dephase, over a timescale given by the inverse width of the continuum.

RF spectrum in Fermi Liquid theory

This structure of the RF spectrum is a generic feature of quasiparticle spectra. In Fermi liquid theory, the propagator of a quasiparticle is approximated as a pole at energy $E(k) > 0$ (relative to the ground state energy), lifetime $1/\gamma(k)$ and residue Z plus an incoherent spectrum [3, 8]

$$G_-^R(\mathbf{k}, \omega) = \frac{Z}{\hbar\omega + E(k) + i\hbar\gamma(k)} + G_-^{R,\mathrm{inc}}(\mathbf{k}, \omega) \quad (13)$$

The spectral function is given by $A_-(\mathbf{k}, \omega) = -\frac{1}{\pi}\mathrm{Im}G_-^R(\mathbf{k}, \omega) = Z\frac{1}{\pi}\frac{\hbar\gamma(k)}{(\hbar\omega+E(k))^2+\hbar^2\gamma(k)^2} + A_-^{\mathrm{inc}}(\mathbf{k}, \omega)$ which tends to

$$A_-(\mathbf{k}, \omega) = Z\delta(\hbar\omega + E(k)) + A_-^{\mathrm{inc}}(\mathbf{k}, \omega) \quad (14)$$

in the limit of small damping of the quasiparticle. $A_-(\mathbf{k}, \omega)$ measures the probability that removing a particle with momentum $\mathbf{k}$ will cost an energy $-\hbar\omega$. The RF spectrum in linear response is given by [2]

$$\Gamma(\omega) = 2\pi\hbar\Omega_R^2 \sum_k A_-(\mathbf{k}, \epsilon_\mathbf{k} - \mu - \hbar\omega) n_F(\epsilon_\mathbf{k} - \mu - \hbar\omega) \quad (15)$$

where μ is the chemical potential of the quasiparticle and $n_F(x) = 1/(e^{\beta x} + 1)$ is the Fermi function that tends to $\theta(-x)$ at zero temperature. This is intuitively understood: For a given momentum $\mathbf{k}$, the RF photon with energy $\hbar\omega$ has to provide the energy $\epsilon_\mathbf{k} - \mu$ (relative to the initial chemical potential μ) to create a free particle in the final state. The rest, $\hbar\omega - \epsilon_\mathbf{k} + \mu$, is used to remove a particle from the initial state (probability $A_-(\mathbf{k}, \epsilon_\mathbf{k} - \mu - \hbar\omega)$) if there exists such a particle (factor

$n_F(\epsilon_\mathbf{k} - \mu - \hbar\omega))$. Eq. 15 is equivalent to Fermi's Golden Rule Eq. 11 [9]. In the case where the spectral function is dominated by a quasiparticle peak, the spectrum becomes

$$
\begin{aligned}
\Gamma(\omega) \;=\; & 2\pi\hbar\Omega_R^2 Z \sum_k \delta(\epsilon_\mathbf{k} + E(k) - \mu - \hbar\omega) \\
& \times\, n_F(\epsilon_\mathbf{k} - \mu - \hbar\omega) + \Gamma^{\rm inc}(\omega)
\end{aligned}
\tag{16}
$$

Connecting to our case of a single quasiparticle with $\mu = E_\downarrow$ and $k = 0$, this directly gives

$$
\Gamma(\omega) = 2\pi\hbar\Omega_R^2 Z \delta(\hbar\omega + E_\downarrow) + \Gamma^{\rm inc}(\omega)
\tag{17}
$$

identical to the prediction via the trial wavefunction.

Polaron spectral function

To connect the single particle and the Fermi liquid description, we calculate the propagator $G_-^R(\mathbf{k}, \omega)$ for the removal of a single spin down impurity from the wavefunction $|\Psi\rangle$. By definition,

$$
iG_-^R(\mathbf{k}, t) \;=\; \langle\Psi| c_{\mathbf{k}\downarrow}^\dagger e^{i\hat{H}t/\hbar} c_{\mathbf{k}\downarrow} |\Psi\rangle\, \theta(t)
\tag{18}
$$

Inserting a complete set of eigenstates, this gives

$$
iG_-^R(\mathbf{k}, t) \;=\; \sum_f |\langle f| c_{\mathbf{k}\downarrow} |\Psi\rangle|^2 \, e^{iE_f t/\hbar}\theta(t)
\tag{19}
$$

The state $c_{\mathbf{k}\downarrow}|\Psi\rangle$ is void of any spin down impurity and has non-vanishing matrix elements only with either the unperturbed spin up Fermi sea, $|FS\rangle_\uparrow$ (if $\mathbf{k} = \mathbf{0}$), or with particle-hole excitations $|\mathbf{q}, \mathbf{k}'\rangle = c_{\mathbf{k}'\uparrow}^\dagger c_{\mathbf{q}\uparrow} |FS\rangle_\uparrow$ (in the case $\mathbf{k} = \mathbf{q} - \mathbf{k}'$). These matrix elements are $\varphi_0 = \sqrt{Z}$ and $\varphi_{\mathbf{k}'\mathbf{q}}$ resp., the corresponding energies $E_f = 0$ and $E_f = \epsilon_{\mathbf{k}'} - \epsilon_\mathbf{q}$ relative to E_F. So one has:

$$
iG_-^R(\mathbf{k}, t) = (Z\delta_{\mathbf{k},\mathbf{0}} + \sum_{q<k_F}^{k'>k_F} \delta_{\mathbf{k},\mathbf{q}-\mathbf{k}'} |\varphi_{\mathbf{k}'\mathbf{q}}|^2 \, e^{i(\epsilon_{\mathbf{k}'} - \epsilon_\mathbf{q})t/\hbar})\theta(t)
$$

Finally, $G_-^R(\mathbf{k}, \omega) = \frac{Z}{\hbar\omega + i\eta}\delta_{\mathbf{k},\mathbf{0}} + G_-^{R,\rm inc}(\mathbf{k}, \omega)$ with infinitesimal $\eta > 0$. This is just the Fermi liquid form of G_-^R but for a single quasiparticle with zero momentum ($E(0) = 0$ in (13)), as described by $|\Psi\rangle$. The spectral function is

$$
\begin{aligned}
A_-(\mathbf{k}, \omega) \;=\; & Z\delta(\hbar\omega)\delta_{\mathbf{k},\mathbf{0}} + \\
& \sum_{q<k_F}^{k'>k_F} \delta_{\mathbf{k},\mathbf{q}-\mathbf{k}'} |\varphi_{\mathbf{k}'\mathbf{q}}|^2 \, \delta(\hbar\omega + \epsilon_{\mathbf{k}'} - \epsilon_\mathbf{q})
\end{aligned}
$$

With Eq. 15 this exactly gives the RF spectrum of Eq. 12.

Calculation of the incoherent background

Using Eq. 3, we can write the incoherent part of the spectrum as:

$$
\Gamma^{\rm inc}(\omega) \equiv 2\pi\hbar\Omega_R^2 \sum_{q<k_F}^{k>k_F} |\varphi_{\mathbf{k}\mathbf{q}}|^2 \, \delta(\hbar\omega + E_\downarrow - \epsilon_\mathbf{k} + \epsilon_\mathbf{q} - \epsilon_{\mathbf{q}-\mathbf{k}})
$$

$$
= \frac{2\pi\Omega_R^2}{\hbar} \frac{Z}{\omega^2} \frac{1}{\mathcal{V}^2} \sum_{q<k_F}^{k>k_F} f(E_\downarrow, \mathbf{q})^2 \delta(\hbar\omega + E_\downarrow - \epsilon_\mathbf{k} + \epsilon_\mathbf{q} - \epsilon_{\mathbf{q}-\mathbf{k}})
$$

The integral over $\mathbf{k}$ exists in analytic form:

$$
\frac{1}{\mathcal{V}} \sum_{k>k_F} \delta(\hbar\omega + E_\downarrow - \epsilon_\mathbf{k} + \epsilon_\mathbf{q} - \epsilon_{\mathbf{q}-\mathbf{k}}) =
$$

$$
\frac{mk_F}{8\pi^2\hbar^2} K\left(\frac{\hbar\omega+E_\downarrow}{2E_F}, \frac{q}{k_F}\right)
$$

$$
\text{with} \quad K(\epsilon, y) = \begin{cases} \frac{y_+^2 - y_-^2}{y} & \text{for } y_- > 1, \\ \frac{y_+^2 - 1}{y} & \text{for } y_- < 1 < y_+, \\ 0 & \text{for } 1 > y_+. \end{cases}
$$

$$
\text{and} \quad y_\pm = \pm\frac{y}{2} + \sqrt{\frac{y^2}{4} + \epsilon}
\tag{20}
$$

The incoherent spectrum is then

$$
\Gamma^{\rm inc}(\omega) = \pi\Omega_R^2 \frac{ZE_F}{\hbar\omega^2} \int_0^1 {\rm d}y \frac{y^2 K\left(\frac{\hbar\omega+E_\downarrow}{2E_F}, y\right)}{\left(1 - \frac{\pi}{2k_F a} - I\left(\frac{E_\downarrow}{E_F}, y\right)\right)^2}
\tag{21}
$$

One can check that the total spectrum obeys the sum rule

$$
\int_{-\infty}^\infty {\rm d}\omega\,\Gamma(\omega) = 2\pi\hbar\Omega_R^2
\tag{22}
$$

and in particular that the total weight of the incoherent background is proportional to $1 - Z$, which is not obvious from the form in Eq. 21. For RF frequencies close to threshold $\hbar\omega + E_\downarrow \ll 2E_F$, the hole momentum $\mathbf{q}$ and the particle momentum $\mathbf{k}$ must be close to each other to fulfill energy conservation, i.e. they have to be close to the Fermi momentum. The double sum over $\mathbf{q}$ and $\mathbf{k}$ thus gives a phase space suppression on the order of $(\hbar\omega + E_\downarrow)^2$, i.e. the spectrum starts like $(\hbar\omega + E_\downarrow)^2/\omega^2$. This is in contrast to the dissociation spectrum of a molecule of binding energy E_B, where the density of states above threshold gives a spectrum proportional to $\sqrt{\hbar\omega + E_B}/\omega^2$. For large RF energies, large particle momenta $\mathbf{k}$ are involved, the suppression due to the Fermi sea becomes negligible and the spectrum behaves like $\sqrt{\hbar\omega + E_\downarrow}/\omega^2$, as for a molecule of binding energy $E_\downarrow$. This is natural as for large momenta, we are probing short-range physics which involves at most two particles, a spin up environment atom and the impurity. In particular, at RF energies $\hbar\omega \gg E_\downarrow$, we recover the $\omega^{-3/2}$ behavior of the RF spectrum that is universal for short-range interactions.

RF Spectrum of a finite concentration of impurities

Since polarons are found to be weakly interacting, they will form a Fermi sea filled up to the impurity Fermi momentum $k_{F\downarrow}$. The fact that the dispersion of polarons $E_(k) = \frac{m}{m^*}\epsilon_{\mathbf{k}}$ differs from that of a free particle due to the effective mass $m^* \neq m$ leads to broadening of the RF spectra. The RF photon has to supply the difference in kinetic energies $(1 - \frac{m}{m^*})\epsilon_{\mathbf{k}}$ between the initial and the final state, with a maximal shift $(1-\frac{m}{m^*})\hbar^2 k_{F\downarrow}^2/2m$. The spectral shape is easily obtained: The spectral function at momentum $\mathbf{k}$ will be dominated by polarons that occupy that momentum state. The coherent part of the spectral function is thus $A_-^{\mathrm{coh}}(\mathbf{k},\omega) = Z\delta(\hbar\omega + E(k))$ with $E(k) = -\hbar^2 k^2/2m^* = -\frac{m}{m^*}\epsilon_{\mathbf{k}}$ relative to the impurity Fermi energy. The coherent part of the spectrum then becomes

$$\Gamma^{\mathrm{coh}}(\omega) = 2\pi\hbar\Omega_R^2 \sum_k A_-^{\mathrm{coh}}(\mathbf{k}, \epsilon_k - E_\downarrow - \hbar\omega)$$

where the sum extends up to the impurity Fermi momentum $k_{F\downarrow}$. With the free, 3D density of states $\rho(\epsilon)$, this is

$$\begin{aligned}
\Gamma^{\mathrm{coh}}(\omega) &= 2\pi\hbar\Omega_R^2 \int_0^{E_{F\downarrow}} \mathrm{d}\epsilon\, \rho(\epsilon) Z\delta(\epsilon - E_\downarrow - \hbar\omega - \frac{m}{m^*}\epsilon) \\
&= 2\pi\hbar\Omega_R^2 \frac{Z}{1 - \frac{m}{m^*}}\rho\left(\frac{\hbar\omega + E_\downarrow}{1 - \frac{m}{m^*}}\right) \times \\
&\quad \theta\left((1 - \frac{m}{m^*})E_{F\downarrow} - \hbar\omega - E_\downarrow\right) \qquad (23)
\end{aligned}$$

This coherent part of the spectrum starts at the polaron ground state energy $\hbar\omega = |E_\downarrow|$, then grows like a square root and jumps to zero when $\hbar\omega - |E_\downarrow| = (1 - \frac{m}{m^*})E_{F\downarrow}$. On resonance, where $m^* \approx 1.2$, this occurs at $\hbar\omega - |E_\downarrow| = 0.2x^{2/3}E_{F\uparrow} \approx 0.04 E_{F\uparrow}$ for $x = 0.1$. This is still smaller than the Fourier width of the RF pulse used in the experiment of about $0.1 E_F$. The size of the jump is given by $2\pi\hbar\Omega_R^2 \frac{Z}{1-\frac{m}{m^*}}\rho(E_{F\downarrow})$ and reflects the impurity Fermi surface in the RF spectrum. This behavior of the coherent part of the spectrum was found in [1] and was discussed recently in [4]. It is intriguing that the sharpness of the Fermi surface and its discontinuity should, at least in principle, be observable in the RF spectrum.

Determination of Z from experimental spectra

In order to extract the quasiparticle residue Z, we determine the area under the peak that is not matched by the environment's response and divide by the total area under the impurity spectrum (see spectrum in the inset of Fig. 4 in the main body of the paper). Due to the Fourier width of the probe pulse, the strong response of
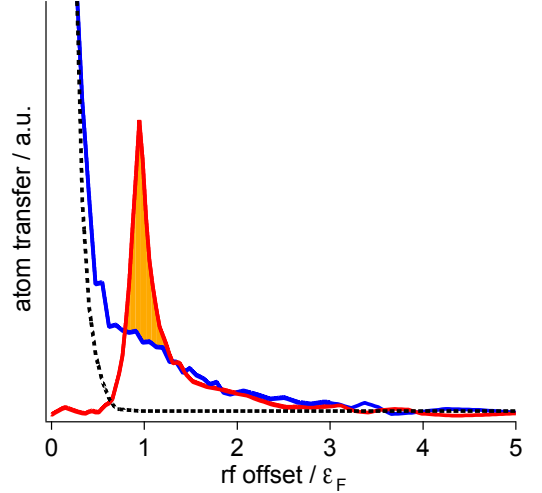
the environment around zero RF offset (the resonance for

FIG. 1: Determination of the quasiparticle residue Z. Impurity spectrum (red), environment spectrum (blue) and spectral response of non-interacting atoms (black dashed), folded over from negative RF offsets.

non-interacting atoms) adds some weight to the environment background at the position of the polaron peak. To remove this effect in the determination of Z, the part of the environment's response at negative frequency offset is folded towards the positive side (dashed line in Fig. 1) and subtracted from the environment spectrum. As it turns out, this procedure changes the value for Z by less than 5% for all spectra in Fig. 2 of the main paper.

[1] M. Punk and W. Zwerger, Phys. Rev. Lett. **99**, 170404 (2007).

[2] P. Massignan, G. M. Bruun, and H. T. C. Stoof, Phys. Rev. A **78**, 031602 (2008).

[3] M. Veillette, E. G. Moon, A. Lamacraft, L. Radzihovsky, S. Sachdev, and D. E. Sheehy, Phys. Rev. A **78**, 033614 (2008).

[4] W. Schneider, V. B. Shenoy, and M. Randeria, preprint arXiv:0903.3006 (2009).

[5] W. Ketterle and M. Zwierlein, in *Ultracold Fermi Gases, Proceedings of the International School of Physics "Enrico Fermi", Course CLXIV, Varenna, 20 - 30 June 2006*, edited by M. Inguscio, W. Ketterle, and C. Salomon (IOS Press, Amsterdam, 2008).

[6] F. Chevy, Phys. Rev. A **74**, 063628 (2006).

[7] R. Combescot, A. Recati, C. Lobo, and F. Chevy, Phys. Rev. Lett. **98**, 180402 (2007).

[8] P. Nozières, *Theory of Interacting Fermi Systems*, Advanced Book Classics (Addison-Wesley, Reading, MA, 1997).

[9] A. Fetter and J. Walecka, *Quantum Theory of Many-Particle Systems* (McGraw-Hill, New York, 1971).

Appendix D

Determination of the Superfluid Gap in Atomic Fermi Gases by Quasiparticle Spectroscopy

This appendix contains a reprint of Ref. [44]: Andre Schirotzek, Yong-il Shin, Christian H. Schunck, and Wolfgang Ketterle , *Determination of the Superfluid Gap in Atomic Fermi Gases by Quasiparticle Spectroscopy*, Phys. Rev. Lett. **101**, 140403 (2009).

Determination of the Superfluid Gap in Atomic Fermi Gases by Quasiparticle Spectroscopy

André Schirotzek, Yong-il Shin, Christian H. Schunck, and Wolfgang Ketterle

Department of Physics, MIT-Harvard Center for Ultracold Atoms, and Research Laboratory of Electronics,
Massachusetts Institute of Technology, Cambridge, Massachusetts 02139, USA

We present majority and minority radio frequency spectra of strongly interacting imbalanced Fermi gases of ^{6}Li. We observed a smooth evolution in the nature of pairing correlations from pairing in the superfluid region to polaron binding in the highly polarized normal region. The imbalance induces quasiparticles in the superfluid region even at very low temperature. This leads to a local bimodal spectral response, which allowed us to determine the superfluid gap Δ and the Hartree energy U.

Pairing and superfluidity in fermionic systems are intricately related phenomena. In BCS theory [1], describing conventional superconductors, the emergence of superfluidity is accompanied by the opening of a gap in the excitation spectrum of the superfluid. This gap can be interpreted as the minimum energy required to break a Cooper pair or, equivalently, to create an elementary excitation, a so-called quasiparticle, inside the superfluid.

However, strongly correlated systems show a more complicated behavior. There are gapless fermionic superfluid systems, e.g., high temperature superconductors [2] or for superconductors with magnetic impurities [3]. On the other hand, there are numerous examples of systems with an excitation gap in the normal state, e.g., a high temperature superconductor above its superfluid transition temperature exhibiting a pseudogap [2].

Here, we use radio frequency (rf) spectroscopy to investigate the nature of pairing and the relation between pairing and superfluidity in a strongly interacting system of ultracold atomic Fermions.

We can spectroscopically distinguish the superfluid and the polarized normal fluid by introducing excess fermions into the system. In a superfluid phase described by BCS theory, the excess particles can be accommodated only as thermally excited quasiparticles. A local double-peaked spectrum reflects the coexistence of pairs and unpaired particles. In the normal phase, at large spin polarization, the limit of a single minority particle immersed into a Fermi sea is approached, which can be identified as a polaron [4–7]. Here the system can be described in the framework of Fermi liquid theory and no stable pairs exist. We find that these different kinds of pairing correlations are smoothly connected across the critical density imbalance [8], also called the Clogston-Chandrasekhar limit of superfluidity [9,10].

The rf spectrum of a superfluid containing quasiparticles shows two peaks, which, in the BCS limit, would be split by Δ, the superfluid gap. Therefore, rf spectroscopy of quasiparticles is a direct way to observe the superfluid gap Δ in close analogy with tunneling experiments in superconductors [11]. From the observed spectrum we

can also determine a Hartree term, see Y. Castin in [12], whose inclusion turned out to be crucial.

For this study, we have combined several recently developed experimental techniques: The realization of superfluidity with population imbalance [13] leading to phase separation [8,13,14], tomographic rf spectroscopy [15], *in situ* phase-contrast imaging with 3D reconstruction of the density distributions [8]. In order to minimize final state effects [16] we have prepared an imbalanced mixture of states $|1\rangle$ and $|3\rangle$ of ^{6}Li (corresponding to $|F = 1/2, m_F = 1/2\rangle$ and $|F = 3/2, m_F = -3/2\rangle$ at low field) in an optical dipole trap at a magnetic field of $B = 690$ G, at which there is a Feshbach scattering resonance between the states $|1\rangle$ and $|3\rangle$ [16,17]. Evaporative cooling at $B = 730$ G is performed by lowering the power of the trapping light. After equilibration an rf pulse was applied for 200 μs selectively driving a hyperfine transition from state $|1\rangle$ or $|3\rangle$ to state $(|2\rangle|F = 1/2, m_F = -1/2\rangle$ at low field). Immediately after the rf pulse an absorption image was taken of the atoms transferred into state $|2\rangle$.

The spectra were correlated to the local Fermi energy $\epsilon_{F\uparrow} = \frac{\hbar^2}{2m}(6\pi n_\uparrow)^{2/3}$ of the majority density $n_\uparrow$ and to the local polarization $\sigma_{\text{loc}} = \frac{n_\uparrow - n_\downarrow}{n_\uparrow + n_\downarrow}$ which is a measure of the local excess fermion population. As in a previous publication [8] the local densities were measured using phase-contrast imaging and 3D reconstruction using the inverse Abel transformation.

The rf spectra shown in Fig. 1 reveal a gradual change in the nature of the pairing correlations. The balanced superfluid is characterized by identical spectral responses of majority and minority particles and has been the subject of previous studies, see Zwierlein, Grimm, and Regal in [12] and references therein. In the polarized superfluid region [8,18] (and references therein) the minority spectrum perfectly matches the pairing peak of the majority spectrum, locally coexisting with the quasiparticle spectral contribution, resulting in a local double-peak structure of the majority spectrum, see Fig. 1(b). The spectrum suggests that the majority population can be divided into two distinct parts: One part consisting of pairs forming the superfluid, the other part consisting of quasiparticle exci-
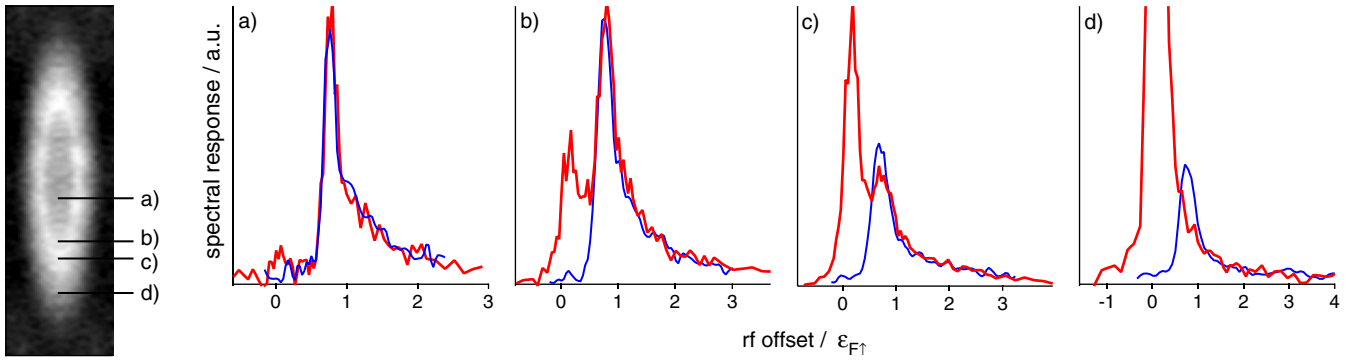
FIG. 1 (color online).   Tomographically reconstructed rf spectra for various regions of the atomic sample at unitarity. (a) Balanced superfluid, (b) polarized superfluid, (c) moderately polarized transition region, and (d) highly polarized normal region. The panel on the left shows a phase-contrast image of the atomic cloud before rf excitation. The positions of the spectra (a) to (d) are marked in the phase-contrast image and by the arrows in Fig. 2. Red: Majority spectrum, blue: Minority spectrum. Local polarizations σ_{loc} and local temperature T/T_F, respectively: (a) $-0.04(2)$, $0.05(1)$; (b) $0.03(1)$, $0.06(1)$; (c) $0.19(1)$, $0.06(2)$; (d) $0.64(4)$, $0.10(2)$. The negative value in (a) implies that the local polarization as inferred from phase-contrast imaging underestimates σ_{loc} by up to 0.05.

tations in the form of excess fermions. Therefore, a natural interpretation of the rf spectrum is to identify one peak as a Stokes process (rf creates a quasiparticle excitation) giving rise to the dissociation part of the rf spectrum and the other as an anti-Stokes process (rf destroys a quasiparticle excitation).

As the local imbalance is further increased beyond the superfluid to normal (SF-N) transition [8,19], see Fig. 1(d), the majority spectrum no longer shows a local double-peak structure. This is consistent with theoretical work [20,21] attributing the double-peak structure in the normal phase in previously reported rf spectra [22,23] to the inhomogeneous density distribution. For increasing spin polarization the majority and minority pairing peaks lose spectral overlap. We interpret the missing overlap as indication that the minority atoms are no longer bound in pairs, each of them interacting with more than one majority atom, a situation we refer to as polaronic binding. We have seen [19] that on the Bose-Einstein condensation (BEC) side of the Feshbach resonance the overlap between minority and majority spectra does not depend strongly on the presence of excess fermions as is expected in a molecular picture. At unitarity, within our experimental resolution, the overlap starts to decrease at the SF-N interface, see Fig. 1(c).

Even when the spectral overlap decreases, there is still equal response to the rf excitation in the high frequency tails, see Figs. 1(c) and 1(d). These tails correspond to large momentum components in the interparticle wave function and hence address the short range physics. We expect this part of the spectrum to be insensitive to changes in the binding at large distances.

The direct comparison between majority and minority spectra clarifies our previous experimental results on minority rf spectra in the $|1\rangle - |2\rangle$ mixture [23], in which we concluded that there is strong pairing in the normal phase. Although the previous results suffered from final state interactions [16], we confirm that the change in pairing correlations is indiscernible in the minority spectrum

alone, but shows up in the spectral overlap with the majority spectrum. As a result, the observed spectral gap in the normal phase should not be interpreted as a signature of pairing but rather as strong pairing correlations in the form of a polaron as suggested in [24–26]. Figure 2 summarizes our data in the unitary regime.
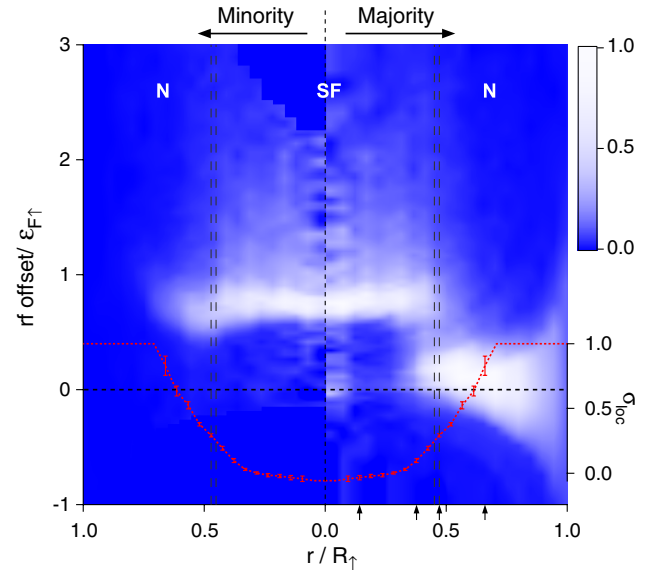
FIG. 2 (color online).   Spatially resolved rf spectra of an imbalanced Fermi gas at unitarity. (a) The right half shows the majority spectra as a function of position in the trap expressed in terms of the majority Fermi radius $R_\uparrow$, the left half displays the minority spectra. The superfluid to normal transition region is marked by the gray vertical lines. The local polarization σ_{loc} is given by the short-dashed red line. The error bars are the standard deviation of the mean value. The arrows indicate the position of the four spectra shown in Fig. 1. The image is a bilinear interpolation of 2500 data points, each plotted data point in the image is the average of three measured data points. The spatial resolution of the image is $0.045 \cdot R_\uparrow$.

We now turn to a quantitative analysis of the spectral peaks in the superfluid phase for small density imbalance, and to the determination of the superfluid gap. Earlier work [15,22] tried to determine the gap from the onset of the pair dissociation spectrum. However, the rf spectrum is not only sensitive to final state interactions, it is also shifted by Hartree energies, as we show here. Furthermore, rf spectroscopy can excite all fermions, even deep in the Fermi sea, see M. Zwierlein in [12]. Therefore, the onset of the pair dissociation spectrum occurs for atoms with momentum $k = 0$ and, in the BCS limit depends quadratically on the gap parameter ($\omega_{th} = \frac{\Delta^2}{2\epsilon_F}$). The excitation gap can be directly observed if quasiparticles near the dispersion minimum are *selectively* excited, as in tunneling experiments.

Our solution is to study not the ground state of a superfluid, but excited states where quasiparticles are present. In a simple BCS description, quasiparticles are in pure momentum states, but increase the total energy of the system because their momentum state is no longer available to the other particles for pairing. Consequently, in an excitation spectrum, quasiparticles appear at negative frequencies relative to the bare atomic transition frequency. The lowest energy quasiparticle appears at frequency $-\Delta$, see Fig. 3.

Final state interactions and Hartree terms can also create line shifts, and two peaks are needed for analysis, the dissociation peak and the quasiparticle peak in our case. In essence, it is the separation between the peaks in spectra like Fig. 1(b), which allows us to determine Δ.

Thermal population of quasiparticles requires a temperature on the order of the excitation gap Δ. At unitarity, this temperature can be estimated to be 95% of the critical temperature, away from the low temperature limit addressed in this Letter. Indeed, in samples of equal population of the spin states we were not able to spectroscopically resolve any local double-peak structures [19]. This problem can be overcome by introducing density imbalance between the constituents: The chemical potential difference between majority and minority components ($\mu_\uparrow > \mu_\downarrow$) forces a finite quasiparticle occupation into the superfluid region already at very low temperature [27]. This allows us to selectively populate quasiparticles at the minimum of the dispersion curve, see Fig. 3(a).

In Fig. 4(a) the position of the peaks of majority and minority spectra are plotted normalized by $\epsilon_{F\uparrow}$ as a function of position in the trap in the unitary limit [19]. The peak positions are proportional to the local Fermi energy inside the superfluid region within our experimental resolution. In the region of superfluidity with finite polarization the spectra show local double peaks. The position of the two peaks in the limit of small polarization is depicted in Fig. 4(b) for various interaction strengths.

It was unexpected that the quasiparticles appear at positive frequencies (relative to the atomic transition frequency). This is caused by the presence of Hartree terms, resulting in an overall shift of the systems energy and the rf spectrum [19]. In the weakly interacting limits, the Hartree term reduces to a simple mean-field shift. In the strongly interacting regime one has to resort to quantum Monte Carlo (QMC) calculations [28–30] for a numerical value of U.

In a mean-field description of the balanced superfluid starting from the BCS-Leggett ansatz for the BEC-BCS crossover, see Zwierlein in [12] taking into account the Hartree term U, the dispersion relation of the quasiparticles can be expressed as $E_k = \sqrt{\Delta^2 + (\epsilon_k + U - \mu)^2}$, see Y. Castin in [12] where $\epsilon_k = \frac{\hbar^2 k^2}{2m}$ is free particle kinetic energy and μ is the chemical potential. This mean-field formalism gives the analytic expression for the two peak positions. A quasiparticle at the minimum of the dispersion
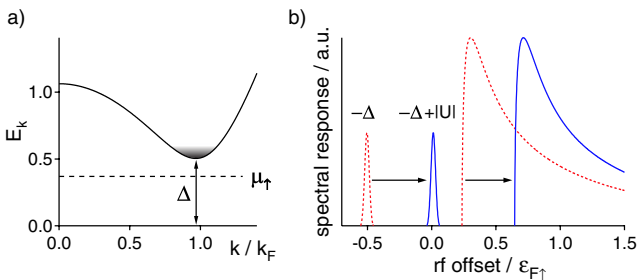

FIG. 3 (color online). Creation and spectroscopy of quasiparticles. (a) Population imbalance thermally generates quasiparticles even at low temperatures comparable to $\Delta - \mu_\uparrow$. $\mu_\uparrow$ is the chemical potential of the majority component. (b) The rf spectrum consists of a quasiparticle peak at negative frequencies and the pair dissociation spectrum at positive frequencies (dotted line). On resonance, the Hartree contribution U acts as an effective attraction and hence shifts the entire spectrum into the positive direction.
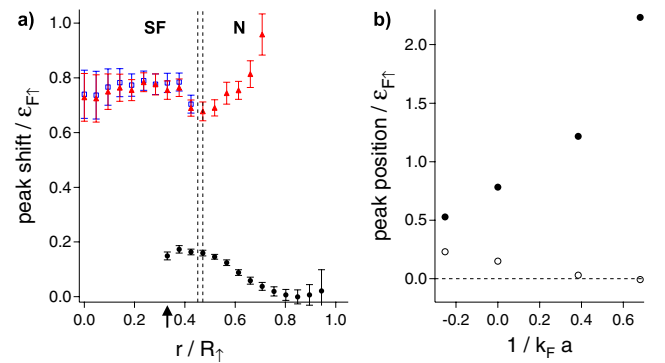
FIG. 4 (color online). (a) Normalized peak positions of pairing peaks and quasiparticle peak at unitarity as a function of position in the trap. The SF-N boundary (cusp in column density difference [19]) is marked by the dashed vertical lines. The arrow indicates the limit of low quasiparticle population relevant for (b). Majority: blue open squares (pairing peak) and solid black circles (quasiparticle peak). Minority: solid red triangles. (b) Pairing peak and quasiparticle peak positions as a function of the local interaction strength $1/k_F a$ in the limit of small local imbalance [see arrow in (a)]. Pairing peak: solid circles; quasiparticles peaks: open circles.

P H Y S I C A L R E V I E W L E T T E R S

TABLE I. Superfluid gap Δ, Hartree term U, and final state interaction E_{final} in terms of the Fermi energy $\epsilon_{F\uparrow}$ for various interaction strengths $1/k_F a$.

$1/k_F a$	Δ	U	E_{final}
-0.25	0.22	-0.22	0.22
0	**0.44**	**-0.43**	**0.16**
0.38	0.7	-0.59	0.14
0.68	0.99	-0.87	0.12

curve will respond at an rf offset of $\omega_{\text{rf}} = -E_{k_{\min}} - \mu + \epsilon_{k_{\min}} = -\Delta - U$, and the maximum of the pair dissociation spectrum occurs at $\hbar\omega_{\max} = \frac{4}{3}(\sqrt{\mu'^2 + \frac{15}{16}\Delta^2} - \mu') - U \simeq \frac{4}{3}\omega_{\text{th}} - U$, where $\mu' = \mu - U$ and ω_{th} is the dissociation threshold (which is at momentum $k = 0$).

We determined the superfluid gap Δ and the Hartree energy U from the peak positions in the limit of small density imbalance ($\sigma_{\text{loc}} \simeq 0.03$). At unitarity with the chemical potential $\mu = 0.42\epsilon_{F\uparrow}$, confirmed in previous experiments and theory, see [31] and references therein, we obtained $\Delta = 0.44(3)\epsilon_{F\uparrow}$ and $U = -0.43(3)\epsilon_{F\uparrow}$, in excellent agreement with the predicted values $\Delta_t = 0.45\epsilon_{F\uparrow}$ and $U_t = -0.43\epsilon_{F\uparrow}$ from QMC calculations [32]. Our determined values for Δ and U values suggest the minimum of the quasiparticle dispersion curve to occur at $k_{\min} \simeq 0.9k_F$. Table I shows the gap and Hartree energy for various interaction strengths. Away from unitarity we relied on QMC calculations for the chemical potential μ [33].

For an accurate quantitative comparison [19] final state interactions, also listed in Table I, had to be taken into account. The effect of final state interactions is an overall mean-field shift of $E_{\text{final}} = \frac{4\pi\hbar^2 a}{m} n$. This shift affects both the quasiparticle peak and the pairing peak equally.

In conclusion, in crossing the superfluid to normal boundary we observed a gradual crossover in the pairing mechanism by comparing majority and minority spectra. The majority spectrum shows a local double-peak spectrum in the polarized superfluid region which allowed us to determine the superfluid gap Δ and the Hartree terms U. The spectra in the normal phase are consistent with a polaron picture.

[1] J. Bardeen, L. N. Cooper, and J. R. Schrieffer, Phys. Rev. **108**, 1175 (1957).

[2] P. A. Lee, N. Nagaosa, and X.-G. Wen, Rev. Mod. Phys. **78**, 17 (2006).

[3] A. A. Abrikosov and L. Gork'ov, JETP **12**, 1243 (1961).

[4] F. Chevy, Phys. Rev. A **74**, 063628 (2006).

[5] R. Combescot, A. Recati, C. Lobo, and F. Chevy, Phys. Rev. Lett. **98**, 180402 (2007).

[6] N. Prokof'ev and B. Svistunov, Phys. Rev. B **77**, 020408 (2008).

[7] P. Massignan, G. M. Bruun, and H. T. C. Stoof, arXiv:0805.3667 [Phys. Rev. A (to be published)].

[8] Y. Shin, C. H. Schunck, A. Schirotzek, and W. Ketterle, Nature (London) **451**, 689 (2008).

[9] A. M. Clogston, Phys. Rev. Lett. **9**, 266 (1962).

[10] B. S. Chandrasekhar, Appl. Phys. Lett. **1**, 7 (1962).

[11] I. Giaever, Phys. Rev. Lett. **5**, 147 (1960).

[12] M. Inguscio, W. Ketterle, and C. Salomon, in *Ultracold Fermi Gases*, Proceedings of the International School of Physics "Enrico Fermi" Course CLXIV (IOS Press, Amsterdam, 2008).

[13] M. W. Zwierlein, A. Schirotzek, C. H. Schunck, and W. Ketterle, Science **311**, 492 (2006).

[14] G. B. Partridge *et al.*, Science **311**, 503 (2006).

[15] Y. Shin, C. H. Schunck, A. Schirotzek, and W. Ketterle, Phys. Rev. Lett. **99**, 090403 (2007).

[16] C. H. Schunck, Y. Shin, A. Schirotzek, and W. Ketterle, Nature (London) **454**, 739 (2008).

[17] M. Bartenstein *et al.*, Phys. Rev. Lett. **94**, 103201 (2005).

[18] D. E. Sheehy and L. Radzihovsky, Ann. Phys. (N.Y.) **322**, 1790 (2007).

[19] See EPAPS Document No. E-PRLTAO-101-019841 for auxiliary material. For more information on EPAPS, see http://www.aip.org/pubservs/epaps.html.

[20] P. Massignan, G. M. Bruun, and H. T. C. Stoof, Phys. Rev. A **77**, 031601 (2008).

[21] E. J. Mueller, arXiv:0711.0182v1 [Phys. Rev. A (to be published)].

[22] C. Chin *et al.*, Science **305**, 1128 (2004).

[23] C. H. Schunck *et al.*, Science **316**, 867 (2007).

[24] M. Punk and W. Zwerger, Phys. Rev. Lett. **99**, 170404 (2007).

[25] M. Veillette *et al.*, arXiv:0803.2517v1 [Phys. Rev. A (to be published)].

[26] A. Perali, P. Pieri, and G. C. Strinati, Phys. Rev. Lett. **100**, 010402 (2008).

[27] M. M. Parish, F. M. Marchetti, A. Lamacraft, and B. D. Simons, Nature Phys. **3**, 124 (2007).

[28] J. Carlson and S. Reddy, Phys. Rev. Lett. **95**, 060401 (2005).

[29] C. Lobo, A. Recati, S. Giorgini, and S. Stringari, Phys. Rev. Lett. **97**, 200403 (2006).

[30] A. Bulgac, J. E. Drut, P. Magierski, and G. Wlazlowski, arXiv:0801.1504v1.

[31] R. Haussmann, W. Rantner, and W. Zwerger, Phys. Rev. A **75**, 023610 (2007).

[32] J. Carlson and S. Reddy, Phys. Rev. Lett. **100**, 150403 (2008).

[33] J. C. G. E. Astrakharchik, J. Boronat, and S. Giorgini, Phys. Rev. Lett. **93**, 200404 (2004).

Auxiliary Material: Determination of the Superfluid Gap in Atomic Fermi Gases by Quasiparticle Spectroscopy

Determination of the superfluid boundary

It has been shown previously [1] that at unitarity the difference column density profiles serve as an indicator for the SF-N boundary. The discontinuity of the minority density results in a pronounced "cusp" in the difference profile $n_\uparrow(r) - n_\downarrow(r)$, see fig. 1. In the main body of the paper the phase boundary has been determined by this peak position. Hence, "normal" refers to spatial regions beyond the peak, "superfluid" refers to spatial regions inside.

The color coding in the graphs in fig. 1 shows where the spectral overlap (definition see below) between the majority and minority pairing peaks is lost. On resonance ($B = 690$ G) this position shows excellent agreement with the position of the cusp in the difference density profile and can therefore serve as an alternative indicator for the SF-N boundary. This coincidence breaks down away from resonance: On the BCS side ($B = 710$ G) the spectra are less "robust" against polarization and spectral overlap is lost before the column density difference shows a peak. The reverse situation occurs on the BEC side of the resonance ($B = 671$ G). Note that on the BEC side the minority cloud does not extend much further than the peak position in the column density difference.

Quantification of spectral overlap

In order to calculate the spectral overlap of a spectrum, the quasiparticle peak was fitted by a gaussian and subtracted from the majority spectrum. The overlap is then defined as one minus the difference of the integrated spectra normalized by the sum of the integrated spectra, see fig. 2. As mentioned in the main text and above, on the BEC side of the Feshbach resonance almost complete spectral overlap can be observed into the normal region. On the BCS side the reverse situation occurs.

Minority peak shift for high imbalance

Fig. 4 in the main body of the text shows the peak positions normalized by the local majority Fermi energy $\epsilon_{F\uparrow}$. Fig. 3 shows the bare peak positions as observed in the experiment.

One unexpected finding in fig. 4a in the main body of the text is the sudden increase of the minority peak position for high imbalances. This behavior can be traced back to the data in fig. 3: The minority peak position

(red) shows a change in curvature as the SF-N boundary is crossed, in contrast to the majority Fermi energy. Therefore, the ratio of minority peak and majority Fermi energy shows a sudden increase towards the edges of the cloud. The value of the peak position of $\omega_{pol} \simeq 0.9\,\epsilon_{F\uparrow}$ (where final state interactions of $E_{final} \simeq 0.05\,\epsilon_{F\uparrow}$ have been taken into account) is higher than the theoretically calculated value of $\simeq 0.6\,\epsilon_{F\uparrow}$ [2].

Quasiparticles in an equal mixture

In a previous publication [3] low temperature RF spectra did not show any signatures of quasiparticles. We have attempted to create thermally generated quasiparticles in an equal density mixture for higher temperatures $T/T_F \geq 0.20$. The experimental results in fig. 4 show a decrease of the gap parameter, but no local double peak structures could be resolved for any temperature.

We can estimate the temperature required to populate quasiparticles, assuming that the temperature has to be on the order of the gap and that $\Delta(T)$ is given by the BCS relation $\frac{\Delta(T)}{\Delta_0} = 1.74\sqrt{1 - \frac{T}{T_c}}$ [4]. At unitarity, $\Delta_0/T_c \simeq 3$. One would expect to populate quasiparticles only very close to the transition temperature $T/T_c \simeq 0.95$, when the gap is only one third of its low-temperature value.

The theoretical dissociation spectrum including the Hartree term U

Starting from a BCS-Leggett mean-field wavefunction and applying Fermi's Golden Rule, the RF spectrum can be described by (neglecting the Hartree term):

$$\Gamma(\omega) \propto \frac{\sqrt{\omega - \omega_{th}}}{\omega^2}\sqrt{1 + \frac{\omega_{th}}{\omega} + \frac{2\mu}{\omega}} \qquad (1)$$

where $\omega_{th} = \sqrt{\Delta^2 + \mu^2} - \mu$ is the dissociation threshold and μ is the chemical potential.

The corresponding quasiparticle dispersion relation is:

$$E_k = \sqrt{\Delta^2 + (\epsilon_k - \mu)^2} \qquad (2)$$

ϵ_k being the free particle dispersion $\epsilon_k = \frac{\hbar^2 k^2}{2m}$.

Hartree terms U modify the quasiparticle excitation spectrum [5, 6]:

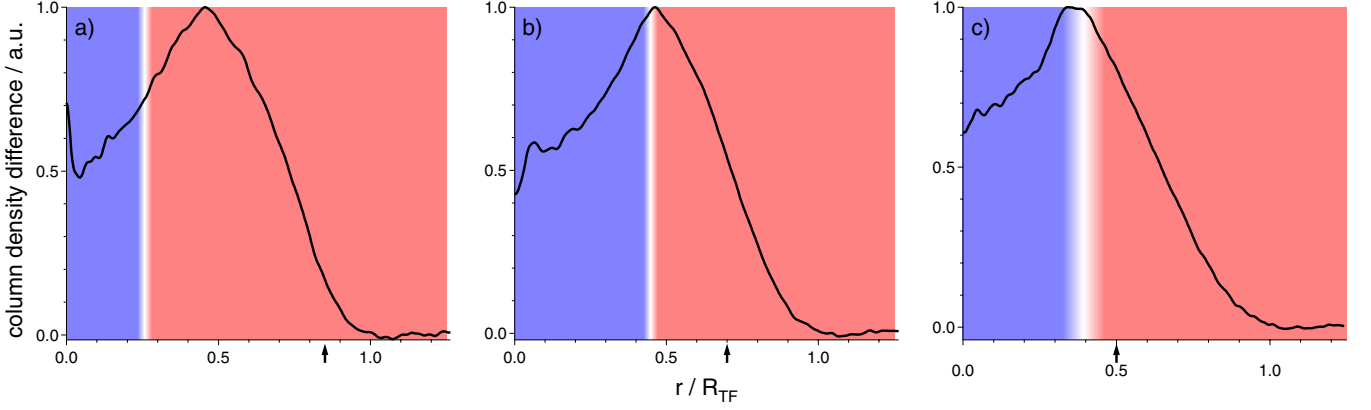$$E_k = \sqrt{\Delta^2 + (\epsilon_k - (\mu - U))^2} \qquad (3)$$

FIG. 1: (Color online) The difference column density profile $n_\uparrow(r) - n_\downarrow(r)$ (radially averaged). a) BCS side ($B = 710G$), b) Unitary limit ($B = 690G$), c) BEC side ($B = 671G$). Each profile shown is the average of 10 individual profiles. Blue marks the region of complete spectral overlap between majority and minority components, red marks the region where there is no complete spectral overlap. The black arrows at the bottom indicate the radial size of the minority component.
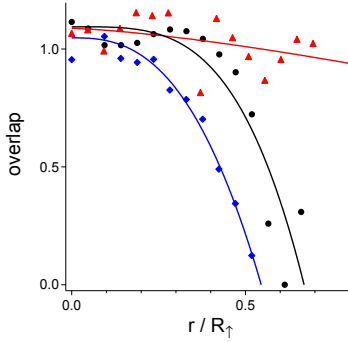

FIG. 2: (color online) Overlap of majority and minority pairing peak as a function of position in the trap for various interaction strengths. A power law was fitted to the curves as a guide to the eye. Unitary limit (black circles): $1/k_{F\uparrow}a = 0$, phase boundary at $r_c/R_\uparrow \simeq 0.46$; BEC side (red triangles): $1/k_{F\uparrow}a = 0.39(1)$, $r_c/R_\uparrow \simeq 0.45$; and BCS side (blue diamonds): $1/k_{F\uparrow}a = -0.25(1)$, $r_c/R_\uparrow \simeq 0.35$

resulting in an RF spectrum of

$$\Gamma\left(\omega'\right) \propto \frac{\sqrt{\omega' - \omega'_{th}}}{\omega'^2}\sqrt{1 + \frac{\omega'_{th}}{\omega'} + \frac{2\,\mu'}{\omega'}} \qquad (4)$$

where $\omega' = \omega + U$, $\omega'_{th} = \omega_{th} + U$ and $\mu' = \mu - U$. This demonstrates that the spectrum retains its functional form but the entire spectrum is shifted by U.

Resolution / Experimental broadening

For comparison with the theoretical spectrum, we model the RF pulse of $T = 200~\mu s$ length as a square pulse, in the frequency domain, resulting in a FWHM of the RF spectral power of $\Delta\nu = 2 \cdot \frac{1}{2\pi} 1.39 \frac{2}{T} \simeq 4.4$ kHz.
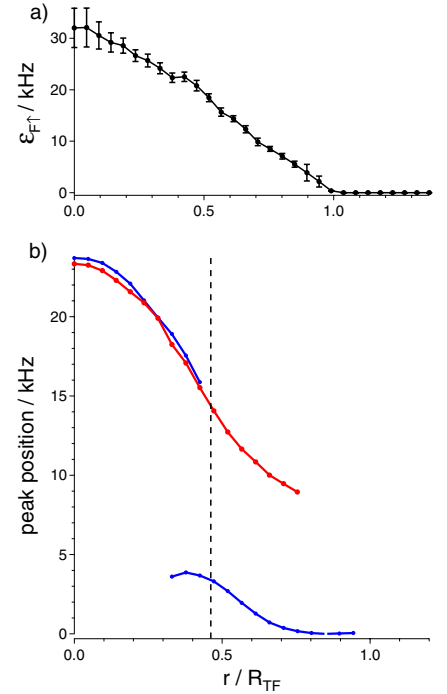
FIG. 3: (color online) a) Local majority Fermi energy in kHZ, the error bars are the standard deviation of the mean value. b) Peak positions of majority and minority in kHz. Majority (Blue): Pairing peak (higher frequencies, only discernible in the SF region) and quasiparticle peak (lower frequencies). Minority (red): The peak can be traced well into the normal region.

The theoretical spectrum consists of two parts: 1) A dissociation peak including the Hartree energy, described by eqn. 1 with Δ and U as given in table I in the main text. 2) A quasiparticle peak modeled as a narrow (FWHM = 1 kHz) Lorentzian with a peak height adjusted so that

FIG. 4: (Color online) Local RF spectra of an equal spin mixture for various normalized local temperatures $T/T_{F\uparrow}$. a) $T/T_{F\uparrow} \simeq 0.20$, b) $T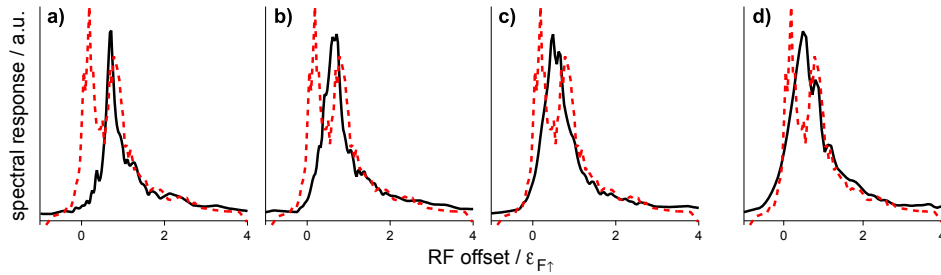/T_{F\uparrow} \simeq 0.22$, c) $T/T_{F\uparrow} \simeq 0.34$, d) $T/T_{F\uparrow} \simeq 0.55$. No local double peak spectrum can be resolved in the RF spectrum. For comparison, the double peak spectrum of an imbalanced mixture with $T/T_{F\uparrow} \simeq 0.06$ is added with a red dashed line.
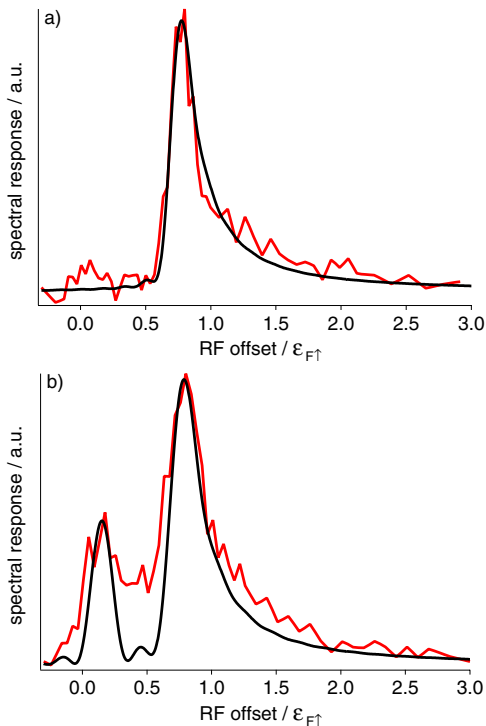

FIG. 5: (color online) Comparison of experimental (red) and theoretical (black) line shapes for spectra a) and b) of figure 1 of the main body of the paper. The theoretical curve is obtained from a BCS-Leggett mean field description including the Hartree term and a convolution with the experimental resolution of $\simeq 4.4$ kHz. The values for Δ and U as calculated from the peak positions lead to a reasonable agreement with the data.

it resembles our data. This spectrum was convolved with the Fourier transform of a square pulse $f(\omega) \propto \frac{\sin^2 \frac{\omega T}{2}}{\left(\frac{\omega T}{2}\right)^2}$.

Fig. 5 shows that the theoretical spectrum reproduces our data quite well. The deviation in 5b) might be attributed to additional broadening mechanisms like finite quasiparticle lifetime, finite temperature and atomic diffusion during the duration of the RF pulse. The convolution causes a small shift of $0.05\,\epsilon_{F\uparrow}$ in the spectral peak position due to the asymmetry of the theoretical spectrum and has been accounted for in the determination of Δ and U.

The value given above for the experimental resolution is confirmed by looking at the blurring of the sharp onset of pair dissociation. Equation 1 predicts that the threshold and peak position in the strongly interacting regime differ by less than 10% of the Fermi energy. Adjusting the experimental resolution to ~ 4 kHz accounts for the experimentally observed difference of threshold and peak position of about $0.3\,\epsilon_{F\uparrow}$.

[1] Y. Shin, C. H. Schunck, A. Schirotzek, and W. Ketterle, Nature **451**, 689 (2008).
[2] F. Chevy, Phys. Rev. A **74**, 063628 (2006).
[3] C. H. Schunck, Y. Shin, A. Schirotzek, and W. Ketterle, preprint, arXiv:0802.0341v2.
[4] M. Tinkham, *Introduction to Superconductivity* (McGraw-Hill, New York, 1975).
[5] Y. Castin (IOS Press, Amsterdam, 2008), pp. 289–350.
[6] A. Bulgac, J. E. Drut, P. Magierski, and G. Wlazlowski, preprint, arXiv:0801.1504v1.

Bibliography

[1] M. Fierz. Uber die relativistische theorie kräftefreier teilchen mit beliebigem spin. *Helvetica Physica Acta*, 12:3–37, 1939.

[2] W. Pauli. The connection between spin and statistics. *Phys. Rev.*, 58:716, 1940.

[3] W. Pauli. About quantum statistics. *Zeitschrift fur Physik*, 41:81, 1927.

[4] A. Einstein. Quantentheorie des einatomigen idealen Gases. *Sitzungsberichte der preussischen Akademie der Wissenschaften*, Bericht 22:261–267, 1924.

[5] L. N. Cooper. Bound electron pairs in a degenerate Fermi gas. *Phys. Rev.*, 104:1189–1190, 1956.

[6] J. Bardeen, L. N. Cooper, and J. R. Schrieffer. Theory of superconductivity. *Phys. Rev.*, 108:1175, 1957.

[7] K. B. Davis, M.-O. Mewes, M. R. Andrews, N. J. van Druten, D. S. Durfee, D. M. Kurn, and W. Ketterle. Bose-Einstein condensation in a gas of sodium atoms. *Phys. Rev. Lett.*, 75:3969–3973, 1995.

[8] M. H. Anderson, J. R. Ensher, M. R. Matthews, C. E. Wieman, and E. A. Cornell. Observation of Bose-Einstein condensation in a dilute atomic vapor. *Science*, 269:198–201, 1995.

[9] B. DeMarco and D. S. Jin. Exploring a quantum degenerate gas of fermionic atoms. *Phys. Rev. A*, 58:R4267, 1998.

[10] C. A. Regal, C. Ticknor, J. L. Bohn, and D. S. Jin. Creation of ultracold molecules from a Fermi gas of atoms. *Nature*, 424:47, 2003.

[11] M. W. Zwierlein, C. A. Stan, C. H. Schunck, S. M. F. Raupach, S. Gupta, Z. Hadzibabic, and W. Ketterle. Observation of Bose-Einstein condensation of molecules. *Phys. Rev. Lett.*, 91:250401, 2003.

[12] C. A. Regal, M. Greiner, and D. S. Jin. Observation of resonance condensation of fermionic atom pairs. *Phys. Rev. Lett.*, 92:040403, 2004.

[13] C. Chin, M. Bartenstein, A. Altmeyer, S. Riedl, S. Jochim, J. Hecker Denschlag, and R. Grimm. Observation of the pairing gap in a strongly interacting Fermi gas. *Science*, 305:1128, 2004.

[14] J. Kinast, A. Turlapov, J. E. Thomas, Q. Chen, J. Stajic, and K. Levin. Heat capacity of a strongly-interacting Fermi gas. *Science*, 307:1296–1299, 2005.

[15] M. W. Zwierlein, J. R. Abo-Shaeer, A. Schirotzek, C. H. Schunck, and W. Ketterle. Vortices and superfluidity in a strongly interacting Fermi gas. *Nature*, 435:1047–1051, 2005.

[16] M. W. Zwierlein, A. Schirotzek, C. H. Schunck, and W. Ketterle. Fermionic superfluidity with imbalanced spin populations. *Science*, 311:492–496, 2006. Published online on Science Express 22 December 2005 (10.1126/science.1122318).

[17] M. W. Zwierlein, C. H. Schunck, A. Schirotzek, and W. Ketterle. Direct observation of the superfluid phase transition in ultracold Fermi gases. *Nature*, 442:54–58, 2006.

[18] Y. Shin, M. W. Zwierlein, C. H. Schunck, A. Schirotzek, and W. Ketterle. Observation of phase separation in a strongly interacting imbalanced Fermi gas. *Phys. Rev. Lett.*, 97:030401, 2006.

[19] Yong-il Shin, Christian H. Schunck, André Schirotzek, and Wolfgang Ketterle. Phase diagram of a two-component fermi gas with resonant interactions. *Nature*, 451(7179):689–693, 2008. 10.1038/nature06473.

[20] C. H. Schunck, Y. Shin, A. Schirotzek, M. W. Zwierlein, and W. Ketterle. Pairing without superfluidity: The ground state of an imbalanced fermi mixture. *Science*, 316:5826, 2007.

[21] C. H. Schunck. PhD thesis, MIT, 2008.

[22] Y. Shin, C. H. Schunck, A. Schirotzek, and W. Ketterle. Tomographic rf spectroscopy of a trapped fermi gas at unitarity. *Phys. Rev. Lett.*, 99:090403, 2007.

[23] W. Ketterle and M.W. Zwierlein. Making, probing and understanding ultracold Fermi gases. In *Ultracold Fermi Gases, Proceedings of the International School of Physics.*

[24] G.-B. Jo, Y.-R. Lee, J.-H. Choi, C. A. Christensen, T. H. Kim, J. H. Thywissen, D. E. Pritchard, and W. Ketterle. Itinerant ferromagnetism in a fermi gas of ultracold atoms. *Science*, 325(5947):1521–1524, 2009.

[25] C. Cohen-Tannoudji, J. Dupont-Roc, and G. Grynberg. *Atom-Photon Interactions*. Wiley, New York, 1992.

[26] Ludovic Pricoupenko and Yvan Castin. One particle in a box: The simplest model for a fermi gas in the unitary limit. *Physical Review A*, 69(Copyright (C) 2009 The American Physical Society):051601, 2004. PRA.

[27] A. J. Leggett. Diatomic molecules and Cooper pairs. In *Modern Trends in the Theory of Condensed Matter. Proceedings of the XVIth Karpacz Winter School of Theoretical Physics, Karpacz, Poland, 1980,*, pages 13–27, Karpacz, Poland, 1980. Springer-Verlag, Berlin.

[28] P. Nozières and S. Schmitt-Rink. Bose condensation in an attractive fermion gas: from weak to strong coupling superconductivity. *J. Low Temp. Phys.*, 59:195–211, 1985.

[29] D. S. Petrov, C. Salomon, and G. V. Shlyapnikov. Weakly bound dimers of fermionic atoms. *Phys. Rev. Lett.*, 93:090404, 2004.

[30] R. Haussmann and W. Zwerger. Thermodynamics of a trapped unitary fermi gas. *Physical Review A (Atomic, Molecular, and Optical Physics)*, 78(6):063602, 2008.

[31] J. Carlson, S.-Y. Chang, V. R. Pandharipande, and K. E. Schmidt. Superfluid Fermi gases with large scattering length. *Phys. Rev. Lett.*, 91:050401, 2003.

[32] S. Y. Chang, V. R. Pandharipande, J. Carlson, and K. E. Schmidt. Quantum monte carlo studies of superfluid fermi gases. *Phys. Rev. A*, 70(4):043602, Oct 2004.

[33] G. E. Astrakharchik, J. Boronat, J. Casulleras, and S. Giorgini. Equation of state of a Fermi gas in the BEC-BCS crossover: A Quantum Monte-Carlo study. *Phys. Rev. Lett.*, 93:200404, 2004.

[34] A. Bulgac, J. E. Drut, and P. Magierski. Spin 1/2 fermions in the unitary regime at finite temperature. *Phys. Rev. Lett.*, 96:090404, 2006.

[35] E. Burovski, N. Prokof'ev, B. Svistunov, and M. Troyer. Critical temperature and thermodynamics of attractive fermions at unitarity. *Phys. Rev. Lett.*, 96:160402, 2006.

[36] A. Perali, P. Pieri, and G. C. Strinati. Quantitative comparison between theoretical predictions and experimental results for the bcs-bec crossover. *Phys. Rev. Lett.*, 93(10):100404, Sep 2004.

[37] H. Hu, X.-J. Liu, and P. D. Drummond. Equation of state of a superfluid fermi gas in the bcs-bec crossover. *EPL (Europhysics Letters)*, 74(4):574–580, 2006.

[38] M. Bartenstein, A. Altmeyer, S. Riedl, S. Jochim, C. Chin, J. Hecker Denschlag, and R. Grimm. Crossover from a molecular Bose-Einstein condensate to a degenerate Fermi gas. *Phys. Rev. Lett.*, 92:120401, 2004.

[39] T. Bourdel, L. Khaykovich, J. Cubizolles, J. Zhang, F. Chevy, M. Teichmann, L. Tarruell, S. J. J. M. F. Kokkelmans, and C. Salomon. Experimental study of the BEC-BCS crossover region in lithium 6. *Phys. Rev. Lett.*, 93:050401, 2004.

[40] G. B. Partridge, W. Li, R. I. Kamar, Y. a. Liao, and R. G. Hulet. Pairing and phase separation in a polarized Fermi gas. *Science*, 311:503, 2006. published online 21 December 2005 (10.1126/science.1122876).

[41] J. Carlson and Reddy Sanjay. Superfluid pairing gap in strong coupling. *Physical Review Letters*, 100(15):150403, 2008.

[42] Piotr Magierski, Gabriel Wlazłowski, Aurel Bulgac, and Joaquín E. Drut. Finite-temperature pairing gap of a unitary fermi gas by quantum monte carlo calculations. *Phys. Rev. Lett.*, 103(21):210403, Nov 2009.

[43] J. T. Stewart, J. P. Gaebler, and D. S. Jin. Using photoemission spectroscopy to probe a strongly interacting fermi gas. *Nature*, 454:744, 2008.

[44] André Schirotzek, Yong-il Shin, Christian H. Schunck, and Wolfgang Ketterle. Determination of the superfluid gap in atomic fermi gases by quasiparticle spectroscopy. *Phys. Rev. Lett.*, 101(14):140403, Oct 2008.

[45] Z. Hadzibabic, S. Gupta, C. A. Stan, C. H. Schunck, M. W. Zwierlein, K. Dieckmann, and W. Ketterle. Fifty-fold improvement in the number of quantum degenerate fermionic atoms. *Phys. Rev. Lett.*, 91:160401, 2003.

[46] C. H. Schunck, Y. Shin, A. Schirotzek, and W. Ketterle. Determination of the fermion pair size in a resonantly interacting superfluid. *Nature*, 454:739, 2008.

[47] A. G. Martin, K. Helmerson, V. S. Bagnato, G. P. Lafyatis, and D. E. Pritchard. rf spectroscopy of trapped neutral atoms. *Phys. Rev. Lett.*, 61:2431, 1988.

[48] H. F. Hess. Evaporative cooling of magnetically trapped and compressed spin-polarized hydrogen. *Phys. Rev. B*, 34:3476, 1986.

[49] D. E. Pritchard, K. Helmerson, and A. G. Martin. Atomic physics 11. page 179. World Scientific, Singapore, 1989.

[50] K. B. Davis, M.-O. Mewes, M. A. Joffe, M. R. Andrews, and W. Ketterle. Evaporative cooling of sodium atoms. *Phys. Rev. Lett.*, 74:5202–5205, 1995.

[51] W. Petrich, M. H. Anderson, J. R. Ensher, and E. A. Cornell. A stable, tightly confining magnetic trap for evaporative cooling of neutral atoms. *Phys. Rev. Lett.*, 74:3352, 1995.

[52] M.-O. Mewes, M. R. Andrews, D. M. Kurn, D. S. Durfee, C. G. Townsend, and W. Ketterle. Output coupler for Bose-Einstein condensed atoms. *Phys. Rev. Lett.*, 78:582–585, 1997.

[53] M. R. Matthews, D. S. Hall, D. S. Jin, J. R. Ensher, C. E. Wieman, E. A. Cornell, F. Dalfovo, C. Minniti, and S. Stringari. Dynamic response of a Bose-Einstein condensate to a discontinuous change in internal state. *Phys. Rev. Lett.*, 81:243–247, 1998.

[54] J. Stenger, S. Inouye, D. M. Stamper-Kurn, H.-J. Miesner, A. P. Chikkatur, and W. Ketterle. Spin domains in ground-state Bose-Einstein condensates. *Nature*, 396:345–348, 1998.

[55] D. M. Harber, H. J. Lewandowski, J. M. McGuirk, and E. A. Cornell. Effect of cold collisions on spin coherence and resonance shifts in a magnetically trapped ultracold gas. *Phys. Rev. A*, 66:053616, 2002.

[56] A. Görlitz, T. L. Gustavson, A. E. Leanhardt, R. Löw, A. P. Chikkatur, S. Gupta, S. Inouye, D. E. Pritchard, and W. Ketterle. Sodium Bose-Einstein condensates in the f=2 state in a large-volume optical trap. *Phys. Rev. Lett.*, 90:090401, 2003.

[57] B. DeMarco and D. S. Jin. Onset of Fermi degeneracy in a trapped atomic gas. *Science*, 285:1703–1706, 1999.

[58] A. G. Truscott, K. E. Strecker, W. I. McAlexander, G. B. Partridge, and R. G. Hulet. Observation of Fermi pressure in a gas of trapped atoms. *Science*, 291:2570–2572, 2001.

[59] F. Schreck, L. Khaykovich, K. L. Corwin, G. Ferrari, T. Bourdel, J. Cubizolles, and C. Salomon. Quasipure Bose-Einstein condensate immersed in a Fermi sea. *Phys. Rev. Lett.*, 87:080403, 2001.

[60] S. R. Granade, M. E. Gehm, K. M. O'Hara, and J. E. Thomas. All-optical production of a degenerate Fermi gas. *Phys. Rev. Lett.*, 88:120405, 2002.

[61] Z. Hadzibabic, C. A. Stan, K. Dieckmann, S. Gupta, M. W. Zwierlein, A. Görlitz, and W. Ketterle. Two species mixture of quantum degenerate Bose and Fermi gases. *Phys. Rev. Lett.*, 88:160401, 2002.

[62] G. Roati, F. Riboli, G. Modugno, and M. Inguscio. Fermi-Bose quantum degenerate ^{40}K - ^{87}Rb mixture with attractive interaction. *Phys. Rev. Lett.*, 89:150403, 2002.

[63] C. A. Regal and D. S. Jin. Measurement of positive and negative scattering lengths in a Fermi gas of atoms. *Phys. Rev. Lett.*, 90:230404, 2003.

[64] S. Gupta, Z. Hadzibabic, M. W. Zwierlein, C. A. Stan, K. Dieckmann, C. H. Schunck, E. G. M. v. Kempen, B. J. Verhaar, and W. Ketterle. Rf spectroscopy of ultracold fermions. *Science*, 300:1723–1726, 2003.

[65] M. W. Zwierlein, Z. Hadzibabic, S. Gupta, and W. Ketterle. Spectroscopic insensitivity to cold collisions in a two-state mixture of fermions. *Phys. Rev. Lett.*, 91:250404, 2003.

[66] Niels Henrik Abel. *Oeuvres Completes*. Johnson Reprint Corp., New York, 1988.

[67] S. Basu and E. J. Mueller. Final-state effects in the radio frequency spectrum of strongly interacting fermions. *Phys. Rev. Lett.*, 101:060405, 2008.

[68] N. Ramsey. *Molecular Beams*. Oxford University Press, 1956.

[69] S. Tan. Energetics of a strongly correlated fermi gas. *Annals of Physics*, 323:2952, 2008.

[70] D. E. Sheehy and L. Radzihovsky. BEC-BCS crossover, phase transitions and phase separation in polarized resonantly-paired superfluids. Preprint cond-mat/0607803.

[71] Leo Radzihovsky and Daniel E. Sheehy. Imbalanced feshbach-resonant fermi gases. *preprint 0911.1740v1*, 2009.

[72] M. M. Parish, F. M. Marchetti, A. Lamacraft, and B. D. Simons. Finite-temperature phase diagram of a polarized fermi condensate. *Nature Physics*, 3(2):124–128, 2007. TY - JOUR M3 - 10.1038/nphys520 N1 - 10.1038/nphys520.

[73] S. Pilati and S. Giorgini. Phase separation in a polarized fermi gas at zero temperature. *Physical Review Letters*, 100(3):030401, 2008.

[74] C. Lobo, A. Recati, S. Giorgini, and S. Stringari. Normal state of a polarized fermi gas at unitarity. *Physical Review Letters*, 97(20):200403, 2006.

[75] G. Baym and C.Pethick. *Landau Fermi-Liquid Theory*. John Wiley, New York, 1991.

[76] M. Punk, P. T. Dumitrescu, and W. Zwerger. Polaron-to-molecule transition in a strongly imbalanced fermi gas. *Physical Review A (Atomic, Molecular, and Optical Physics)*, 80(5):053605–10, 2009.

[77] S. Nascimbène, N. Navon, K. J. Jiang, L. Tarruell, M. Teichmann, J. McKeever, F. Chevy, and C. Salomon. Collective oscillations of an imbalanced fermi gas: Axial compression modes and polaron effective mass. *Phys. Rev. Lett.*, 103(17):170402, Oct 2009.

[78] F. Chevy. Universal phase diagram of a strongly interacting fermi gas with unbalanced spin populations. *Physical Review A*, 74(6):063628, 2006.

[79] D. S. Petrov. Three-body problem in Fermi gases with short-range interparticle interaction. *Phys. Rev. A*, 67:010703, 2003.

[80] Yong-il Shin, André Schirotzek, Christian H. Schunck, and Wolfgang Ketterle. Realization of a strongly interacting bose-fermi mixture from a two-component fermi gas. *Physical Review Letters*, 101(7):070404–4, 2008.

[81] Jun Kondo. Resistance minimum in dilute magnetic alloys. *Prog. Theor. Phys.*, 32(1):37–49, 1964.

[82] L.D. Landau. Über die bewegung der elektronen im kristallgitter. *Phys. Z. Sowjetunion*, 3:644–645, 1933.

[83] P. Nozières. *Theory of Interacting Fermi Systems*. Perseus, 1964.

[84] A. L. Fetter and J. D. Walecka. *Quantum Theory of Many-Particle Systems*. McGraw-Hill, New York, 1971. reprint appeared as Dover Edition in Dover Publications, Inc., Mineola, N.Y. (2003).

[85] William Schneider, Vijay B. Shenoy, and Mohit Randeria. Theory of radio frequency spectroscopy of polarized fermi gases. *preprint arXiv:0903.3006*, 2009.

[86] Martin Veillette, Eun Gook Moon, Austen Lamacraft, Leo Radzihovsky, Subir Sachdev, and D. E. Sheehy. Radio-frequency spectroscopy of a strongly imbalanced feshbach-resonant fermi gas. *Physical Review A*, 78(3):033614, 2008.

[87] Nikolay Prokof'ev and Boris Svistunov. Fermi-polaron problem: Diagrammatic monte carlo method for divergent sign-alternating series. *Physical Review B*, 77(2):020408, 2008.

[88] M. Ku. Master's thesis, University of British Columbia, 2009.

[89] Christophe Mora and Frédéric Chevy. Ground state of a tightly bound composite dimer immersed in a fermi sea. *Phys. Rev. A*, 80(3):033607, Sep 2009.

[90] R. Combescot, S. Giraud, and X. Leyronas. Analytical theory of the dressed bound state in highly polarized fermi gases. Preprint arXiv:0907.3197.

[91] M. Punk and W. Zwerger. Theory of rf-spectroscopy of strongly interacting fermions. *Physical Review Letters*, 99(17):170404, 2007.

[92] V. Efimov. Energy levels arising from resonant two-body forces in a three-body system. *Phys. Lett.*, 33B:563–564, 1970.

[93] V. Efimov. Weakly-bound states of three resonantly-interacting particles. *Sov. J. Nucl. Phys.*, 12:589–595, 1971.

[94] F. Chevy. Universal phase diagram of a strongly interacting Fermi gas with unbalanced spin populations. Preprint cond-mat/0605751.

[95] A. M. Clogston. Upper limit for the critical field in hard superconductors. *Phys. Rev. Lett.*, 9:266, 1962.

[96] B.S. Chandrasekhar. A note on the maximum critical field of high-field superconductors. *Applied Physics Letters*, 1:7, 1962.

[97] R. Combescot, A. Recati, C. Lobo, and F. Chevy. Normal state of highly polarized fermi gases: Simple many-body approaches. *Physical Review Letters*, 98(18):180402, 2007.

[98] R. Combescot and S. Giraud. Normal state of highly polarized fermi gases: Full many-body treatment. *Physical Review Letters*, 101(5):050404, 2008.

[99] P. Massignan, G. M. Bruun, and H. T. C. Stoof. Spin polarons and molecules in strongly interacting atomic fermi gases. *Physical Review A*, 78(3):031602, 2008.

[100] N. V. Prokof'ev and B. V. Svistunov. Bold diagrammatic monte carlo: A generic sign-problem tolerant technique for polaron models and possibly interacting many-body problems. *Physical Review B*, 77(12):125101, 2008.

[101] Yong-il Shin. Determination of the equation of state of a polarized fermi gas at unitarity. *Physical Review A (Atomic, Molecular, and Optical Physics)*, 77(4):041603–4, 2008.

[102] Subir Sachdev and Kun Yang. Fermi surfaces and luttinger's theorem in paired fermion systems. *Physical Review B*, 73(17):174504–6, 2006.

[103] L. Viverit, S. Giorgini, L.P. Pitaevskii, and S. Stringari. Momentum distribution of a trapped fermi gas with large scattering length. *Phys. Rev. A*, 69(1):013607, Jan 2004.

[104] Shina Tan. Large momentum part of a strongly correlated fermi gas. *Annals of Physics*, 323(12):2971–2986, 2008.

[105] P. Guttinger. *Zeitschrift fur Physik*, 73:169, 1932.

[106] W. Pauli. *Handbuch der Physik*. Springer, Berlin, 1933.

[107] H. Hellmann. *Einführung in die Quantenchemie*. Franz Deuticke, Leipzig, 1937.

[108] R. P. Feynman. Forces in molecules. *Phys. Rev.*, 56:340, 1939.

[109] Eric Braaten and Lucas Platter. Exact relations for a strongly interacting fermi gas from the operator product expansion. *Phys. Rev. Lett.*, 100(20):205301, May 2008.

[110] F. Werner and Y. Castin. Exact relations for quantum-mechanical few-body and many-body problems with short-range interactions in two and three dimensions. Preprint, arXiv:1001.0774v1.

[111] F. Werner, L. Tarruell, and Y. Castin. Number of closed-channel molecules in the bec-bcs crossover. *Eur. Phys. J. B*, 68(3):401–415, apr 2009.

[112] G. B. Partridge, K. E. Strecker, R. I. Kamar, M. W. Jack, and R. G. Hulet. Molecular probe of pairing in the BEC-BCS crossover. *Phys. Rev. Lett.*, 95:020404, 2005.

[113] R. Haussmann, M. Punk, and W. Zwerger. Spectral functions and rf response of ultracold fermionic atoms. Preprint arXiv:0904.1333.

[114] Schneider and Mohit Randeria. Universal short-distance structure of the single-particle spectral function of dilute fermi gases. *preprint arXiv:0910.2693*, 2009.

[115] Zhenhua Yu, Georg M. Bruun, and Gordon Baym. Short-range correlations and entropy in ultracold-atom fermi gases. *Phys. Rev. A*, 80(2):023615, Aug 2009.

[116] M. Greiner, C. A. Regal, C. Ticknor, J. L. Bohn, and D. S. Jin. Detection of spatial correlations in an ultracold gas of fermions. *Phys. Rev. Lett.*, 92(15):150405, Apr 2004.

[117] Cheng Chin and Paul S. Julienne. Radio-frequency transitions on weakly bound ultracold molecules. *Phys. Rev. A*, 71(1):012713, Jan 2005.

[118] Gordon Baym, C. J. Pethick, Zhenhua Yu, and Martin W. Zwierlein. Coherence and clock shifts in ultracold fermi gases with resonant interactions. *Phys. Rev. Lett.*, 99(19):190407, Nov 2007.

[119] André Schirotzek, Cheng-Hsun Wu, Ariel Sommer, and Martin W. Zwierlein. Observation of fermi polarons in a tunable fermi liquid of ultracold atoms. *Phys. Rev. Lett.*, 102(23):230402, Jun 2009.

[120] H. Hu, E. D. Kuhnle, X.-J. Liu, P. Dyke, M. Mark, P. D. Drummond, P. Hannaford, and C. J. Vale. Universal structure of a strongly interacting fermi superfluid. Preprint, arXiv:1001.3200v1.

[121] A. Sommer et al. To be pulished.

[122] H. Heiselberg, C. J. Pethick, H. Smith, and L. Viverit. Influence of induced interactions on the superfluid transition in dilute fermi gases. *Physical Review Letters*, 85(Copyright (C) 2009 The American Physical Society):2418, 2000. PRL.

[123] L. P. Gorkov and T. K. Melik-Barkhudarov. Contribution to the theory of superfluidity in an imperfect Fermi gas. *Zh. Eskp. Theor. Fiz.*, 40:1452, 1961.

[124] Immanuel Bloch, Jean Dalibard, and Wilhelm Zwerger. Many-body physics with ultracold gases. *Rev. Mod. Phys.*, 80(3):885–964, Jul 2008.

[125] Zeng-Qiang Yu, Kun Huang, and Lan Yin. Induced interaction in a fermi gas with a bec-bcs crossover. *Physical Review A (Atomic, Molecular, and Optical Physics)*, 79(5):053636, 2009.

[126] D. S. Jin and C. A. Regal. Fermi gas experiments. In *Ultracold Fermi Gases, Proceedings of the International School of Physics*.

[127] R. Grimm. Ultracold fermi gases in the bec-bcs crossover: A review from the innsbruck perspective. In *Ultracold Fermi Gases, Proceedings of the International School of Physics*.

[128] E. J. Mueller. Generic features of the spectrum of trapped polarized fermions. Preprint, arXiv:0711.0182v1.

[129] J. Carlson and S. Reddy. Asymmetric two-component fermion systems in strong coupling. *Phys. Rev. Lett.*, 95:060401, 2005.

[130] Tin-Lun Ho. Universal thermodynamics of degenerate quantum gases in the unitarity limit. *Physical Review Letters*, 92:090402, 2004.

[131] S. Nascimbène, N. Navon, K. J. Jiang, F. Chevy, and C. Salomon. Exploring the thermodynamics of a universal fermi gas. *preprint arXiv:0911.0747*, 2009.

[132] Tin-Lun Ho and Erich J. Mueller. High temperature expansion applied to fermions near feshbach resonance. *Physical Review Letters*, 92(Copyright (C) 2010 The American Physical Society):160404, 2004. PRL.

[133] Stefano Giorgini, Lev P. Pitaevskii, and Sandro Stringari. Theory of ultracold atomic fermi gases. *Reviews of Modern Physics*, 80(4):1215–60, 2008.

[134] Xia-Ji Liu, Hui Hu, and Peter D. Drummond. Virial expansion for a strongly correlated fermi gas. *Physical Review Letters*, 102(Copyright (C) 2010 The American Physical Society):160401, 2009. PRL.

[135] F. Werner et al. To be published.

[136] F. Werner. private communication.

[137] K. M. O'Hara, S. L. Hemmer, S. R. Granade, M. E. Gehm, J. E. Thomas, V.Venturi, E. Tiesinga, and C. J. Williams. Measurement of the zero crossing in a Feshbach resonance of fermionic ^{6}Li. *Phys. Rev. A*, 66:041401(R), 2002.